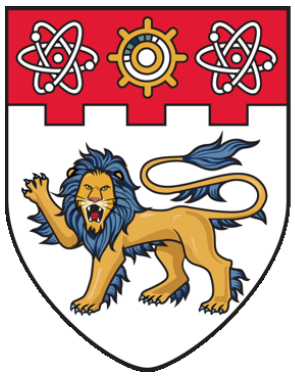

NANYANG TECHNOLOGICAL UNIVERSITY
SINGAPORE

FABRICATION AND CHARACTERISATION OF NANOSTRUCTURED AU FOR IMPROVED ELECTROCATALYTIC PERFORMANCE IN ETHANOL OXIDATION REACTION

CAO XUN

SCHOOL OF MATERIALS SCIENCE AND ENGINEERING

2020

FABRICATION AND CHARACTERISATION OF NANOSTRUCTURED AU FOR IMPROVED ELECTROCATALYTIC PERFORMANCE IN ETHANOL OXIDATION REACTION

CAO XUN

SCHOOL OF MATERIALS SCIENCE AND ENGINEERING

A thesis submitted to the Nanyang Technological University
in partial fulfilment of the requirement for the degree of
Doctor of Philosophy

2020

Statement of Originality

I hereby certify that the work embodied in this thesis is the result of original research, is free of plagiarised materials, and has not been submitted for a higher degree to any other University or Institution.

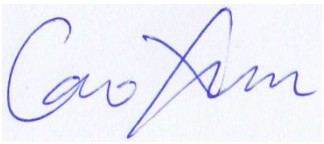

2020-8-24

. . . . . .

Date

. . . . . .

CAO XUN

Supervisor Declaration Statement

I have reviewed the content and presentation style of this thesis and declare it is free of plagiarism and of sufficient grammatical clarity to be examined. To the best of my knowledge, the research and writing are those of the candidate except as acknowledged in the Author Attribution Statement. I confirm that the investigations were conducted in accord with the ethics policies and integrity standards of Nanyang Technological University and that the research data are presented honestly and without prejudice.

2020-8-24

. . . . . .

Date

. . . . . .

A/P HUANG YIZHONG

Authorship Attribution Statement

This thesis contains material from 3 papers published in the following peer-reviewed journals in which I am listed as an author.

Chapter 4 is published as **X. Cao**, C. Li, Y. Lu, B. Zhang, Y. Wu, Q. Liu, J. Wu, J. Teng, W. Yan and Y. Huang, *Journal of Catalysis*, 2019, **377**, 389-399.

The contributions of the co-authors are as follows:

- Associate Professor Huang Yizhong provided the initial project direction and edited the manuscript drafts.
- I prepared the manuscript drafts. The manuscript was revised by Dr Li Chaojiang.
- I co-designed the study with Associate Professor Huang Yizhong and Associate Professor Teng Jiao. Mr Wu Yu performed the physical vapour deposition (PVD) of Au thin film on Si/SiO_2 substrates.
- Professor Yan Weiguo performed the self-assembly of polystyrene (PS) nanospheres on Au thin film samples.
- Professor Wu Junsheng provided the electrodes and I performed all the electrochemistry tests at Nanoelectronics Lab, School of Materials Science and Engineering (MSE). Mr Lu Yu and I analysed the data.
- I conducted the X-ray diffraction and analysed the results from the Facility for Analysis, Characterisation, Testing and Simulation (FACTS Lab).
- I conducted the scanning electron microscopy and energy dispersive X-ray (EDX) spectroscopy.
- Dr Liu Qing provided the focused ion beam (FIB) equipment (located in Microelectronics Reliability & Characterisation Lab). I prepared the transmission electron microscopy (TEM) samples using FIB.
- Dr Zhang Bowei assisted in the collection of transmission electron micrographs and elemental distribution mapping.
- Dr Li Chaojiang assisted in performing the Brunauer-Emmett-Teller (BET) tests.

Chapter 6 is published as **X. Cao**, C. Li, D. Peng, Y. Lu, K. Huang, J. Wu, C. Zhao and Y. Huang, *Journal of Physical Chemistry Letters*, 2020, **11**, 3005-3013.

The contributions of the co-authors are as follows:

- Associate Professor Huang Yizhong and Professor Zhao Chunwang provided the initial project direction.
- I prepared the manuscript drafts. The manuscript was revised by Associate Professor Huang Yizhong.
- I co-designed the study with Associate Professor Huang Yizhong. I performed the synthesis of Au nanoparticles using the precision ion polishing system (PIPS).
- Dr Li Chaojiang provided necessary consumables, including the Au grids and brass/Ti substrates.
- Professor Wu Junsheng and Mr Huang Kang provided the electrodes. I performed all the electrochemistry tests at Nanoelectronics Lab, School of Materials Science and Engineering. Mr Peng dongdong, Mr Lu Yu and I analysed the data.
- I conducted the X-ray diffraction and analysed the results from the FACTS Lab.
- I conducted the electron microscopies (SEM, FIB and TEM), including the collection of electron micrographs and elemental distribution mapping (via EDX spectroscopy).

Chapter 5 is submitted (under revision) as **X. Cao**, D. Peng, C. Wu, Y. He, C. Li, B. Zhang, C. Han, J. Wu, Z. Liu and Y. Huang, *Nano Research*, 2020.

The contributions of the co-authors are as follows:

- Associate Professor Huang Yizhong provided the initial project direction and edited the manuscript drafts.
- I prepared the manuscript drafts. The manuscript was revised by Associate Professor Huang Yizhong.
- I co-designed the study with Associate Professor Huang Yizhong and Mr Peng Dongdong.
- Mr Peng Dongdong and I performed the nanoimprint lithography of polyvinyl chloride (PVC) substrates.
- Mr Wu Cao provided the Ni grids as necessary consumables.
- Dr He Yongmin and Associate Professor Liu Zheng helped with the electron beam evaporation of Au onto the patterned PVC substrates.
- Dr Li Chaojiang provided some guidance in the explanations.
- Professor Wu Junsheng and Dr Zhang Bowei provided the electrodes. I performed all the electrochemistry tests at Nanoelectronics Lab, School of MSE. Mr Peng dongdong, Associate Professor Han Changcun and I analysed the data.
- I conducted the X-ray diffraction and analysed the results from the FACTS Lab.
- I conducted the electron microscopies (SEM/FIB and TEM), including the collection of electron micrographs and subsequent data analyses.

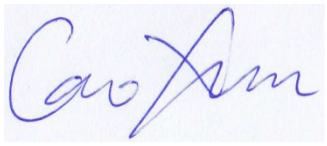

2020-8-24

. . . . . .

Date

. . . . . .

CAO XUN

Abstract

In the modern society, fossil fuels are absolutely the major energy sources in daily lives. However, the over-usage of fossil fuels not only leads to quick depletion of their reserves, but also causes environmental pollution when they are burnt. As such, apart from degradation of pollutants like hazardous chemicals and greenhouse gases, there are two key parts to counteract the current energy crisis – sourcing for alternative and renewable clean energies, as well as to develop energy storage and energy conversion systems. Although different sources of renewable energy are playing their individual role in the energy supply, electrochemical energy will be the dominant one in a long term energy scenario. A general requirement for electrochemical energy conversion and storage is to develop efficient and cost-competitive devices, such as batteries, supercapacitors and fuel cells. Ethanol, being a potential substituent fuel, has wide availability, cheap price, low toxicity and high energy density, therefore direct ethanol fuel cell (DEFC) has long been a popular research topic and ethanol oxidation reaction (EOR) is one of the key focuses. Electrochemical conversion and storage at electrodes undergo complex processes, but most of them are related to electrocatalysis process. Furthermore, electrocatalysis process is one of the best solutions to environmental pollution, as it degrades many hazardous materials into less harmful ones without too much outsourced energy supply. Therefore, development of novel electrocatalysts (electro-active materials) with low cost and high efficiency is an essential step in the advancement of pollutant degradation and next-generation electrochemical energy storage/conversion systems.

In this project, an important concept established is that there are two distinct ways to improve the electrocatalytic performance of Au in EOR, which are increasing the specific surface area and raising the surface energy. Nanostructured Au electrocatalyst was fabricated in two forms – thin films and nanoparticles (NPs). Micro-/nanostructured arrays were fabricated on Au thin films by two lithographical methods, one was a combination of nanosphere lithography (NSL) and reactive ion etching (RIE) and the other was nanoimprint lithography. Through optimisation of parameters, the ordered Au array structures could have almost 100% effective coverage area over the entire substrate.

Transmission electron microscopy (TEM) characterisation achieved direct observation of atomic-scale active sites and partial lattice rotation, which greatly contributed to the improvement of electrocatalytic performance of Au. On the other hand, Au NPs were fabricated via a non-traditional way. Under the ion bombardment in a precision ion polishing system (PIPS), homogeneous and ultra-small Au NPs were found to have single crystallinity; with a suitable set of parameters, the NPs rendered crystal twinning effect, which created localised stress centres that raised the surface energy of the NPs.

Literatures have reported that EOR may proceed via two distinct pathways (C1 and C2) with totally different end products; C1 pathway is the more desired one that causes full oxidation of ethanol and produces CO_2 as a result. In this project, the catalytic performance of Au in EOR was tested via electrochemical methods. Through cyclic voltammetry (CV) scans of the samples, Au rendered high efficiency in EOR with low energy input requirement. The CV scans were carried out under different physical parameters – such as having different pH values and ethanol concentrations in the electrolyte – to have a thorough understanding of the catalytic nature of Au in EOR. Results had shown that at extreme pH values, the electrolyte has high concentrations of mobile charge carriers that favour forward proceeding of EOR. The variation of ethanol concentrations quantified the detecting limit of ethanol, which was usually ~ 5.0 mM and with the presence of atomic-scale active site, this value could reach as low as 1.0 mM. Electrochemical impedance spectroscopy and chronoamperometry tests were also conducted to determine the double layer capacitance and the amount of active sites involved in the electrocatalysis, as well as the stability of the samples during the process. Results had demonstrated that the samples exhibited low charge transfer resistance and excellent double layer capacitance with large amount of participating active sites. Long continuous CV scans revealed that in alkaline medium, C1 pathway could become increasingly preferential over C2 pathway, and thus making nanostructured Au useful in the application of DEFC. Excellent controllability and repeatability, usage of low-hazard materials as well as cost-effective large area fabrication are the key features in this project, which creates opportunities for large-scale fabrication and industrial applications.

Lay Summary

In view of the fast depletion of fossil fuels, human beings must counteract the current energy crisis by looking for alternative energy sources. Amongst the various renewable and clean energies, as well as the energy storage and energy conversion systems, electrochemical energy will dominate in the long term. Ethanol has wide availability, cheap price, low toxicity and high energy density, thus it is becoming a good potential substituent in the form of direct ethanol fuel cell (DEFC). Ethanol oxidation reaction (EOR) is one of the key parts in the functioning of DEFC; the complex electrochemical processes require catalysis to proceed. Therefore, development of novel electrocatalysts (electro-active materials) with low cost and high efficiency is an essential step in the advancement of efficient and cost-competitive DEFC system.

In this project, an important concept established is that there are two distinct ways to improve the electrocatalytic performance of Au in EOR, which are increasing the specific surface area and raising the surface energy. Nanostructured Au electrocatalyst was fabricated in two forms – thin films and nanoparticles (NPs). Micro-/nanostructured arrays were fabricated on Au thin films; through optimisation of parameters, the ordered Au array structures could have almost 100% effective coverage area over the entire substrate. Transmission electron microscopy (TEM) characterisation achieved direct observation of atomic-scale active sites and partial rotation of the crystal lattice, which greatly contributed to the improvement of electrocatalytic performance of Au. On the other hand, Au NPs were fabricated via high-energy ion bombardment in a precision ion polishing system (PIPS). The as-fabricated Au NPs were found to be homogeneous and ultra-small single crystals; with a suitable set of parameters, the NPs rendered crystal twinning effect – high resolution TEM images displayed a distinct separation line, along which a mirror effect could be observed for the arrangement of atomic sites. Most of the stress would be concentrated along this separation line and thus the total surface energy of the NPs could be raised.

Literatures have reported that EOR may proceed via two distinct pathways (C1 and C2) with totally different end products; C1 pathway is the more desired one that causes full oxidation of ethanol and produces CO_2 as a result. In this project, the catalytic performance of Au in EOR was tested via electrochemical methods. Through cyclic voltammetry (CV) scans of the samples, Au renders high efficiency in EOR with low energy input requirement. The CV scans were carried out under different physical parameters – such as having different pH values and ethanol concentrations in the electrolyte – to have a thorough understanding of the catalytic nature of Au in EOR. Results have shown that at extreme pH values, the electrolyte has high concentrations of mobile charge carriers that favour forward proceeding of EOR. The variation of ethanol concentrations quantifies the detecting limit of ethanol, which is usually ~ 5.0 mM and with the presence of atomic-scale active site, this value could reach as low as 1.0 mM.

Electrochemical impedance spectroscopy and chronoamperometry tests were also conducted to determine the double layer capacitance and the amount of active sites involved in the electrocatalysis, as well as the stability of the samples during the process. Results have demonstrated that the samples exhibit low charge transfer resistance (speeding up the process by quicker electron flow) and excellent double layer capacitance (speeding up the process by quicker diffusion of materials) with large amount of participating active sites. Long continuous CV scans reveal that in alkaline medium, C1 pathway could become increasingly preferential over C2 pathway, and thus making nanostructured Au useful in the application of DEFC. Excellent controllability and repeatability, usage of low-hazard materials as well as cost-effective large area fabrication are the key features in this project, which creates a great opportunity for potential large-scale fabrication that favours industrial applications.

Acknowledgements

This dissertation would not have been possible without funding from the Ministry of Education (Academic Research Fund).

Sincerest gratitude is conveyed to my research project supervisor Associate Professor Huang Yizhong for his patient guidance and continual enlightenment in the past four years. Apart from the incisive recommendations concerning the scope of the research, his constructive feedbacks and enthusiastic encouragement has always been the key for me to overcome the difficulties.

I am most grateful to Dr Liu Qing and Mr Tan Jok Boon Eric, and all the technicians of the Facility for Analysis, Characterisation, Testing and Simulation, who were wonderful hosts and persevered in training me to use the characterisation instruments (FEG-SEM/FIB, XRD, FEG-SEM and FEG-TEM/STEM) and credibly interpret the results.

I was fortunate for the generosity of Professor Teng Jiao from University of Science and Technology Beijing, Professor Yan Weiguo from Tianjin Chengjian University and Professor Zhao Chunwang from Shanghai Maritime University, who graciously helped me in the initial stage of sample preparations and project direction guidance.

I would like to extend my appreciation to my peers in the research group as well as friends from other groups, for their cooperation, strong support and collaborations.

Heartfelt love and gratitude to my family members – they have given me the absolute trust, confidence, courage and support throughout the entire course of study. They are always the extraordinary source of inspiration through all the bright and gloomy days.

Table of Contents

Table Captions

Figure Captions

Figure 3.10 Schematic setup of sample preparation by PIPS: (a) for TEM characterisation and (b) for electrode preparation.

Figure 3.11 (a) Schematic illustration of the production of X-rays; (b) energy level diagram showing electron transitions from different shells and orbitals, thereby producing X-rays of different wavelengths; (c) schematic diagram of plane wave scattering by a one-dimensional chain of atoms.

Figure 3.12 Schematic illustration of the interaction of X-ray with crystal planes, for the derivation of the Bragg's law of diffraction.

Figure 3.13 Photo of Shimadzu XRD-6000 thin film XRD used in this project

Figure 3.14 Schematic illustrations of common aberrations: (a) a perfect lens; (b) with spherical aberrations and (c) with chromatic aberrations.

Figure 3.15 Schematic illustration of the beam-specimen interaction during electron microscopies and all possible signals being produced.

Figure 3.16 (a) Schematic diagram of interaction volume; (b) illustration of the production of various signals, (top) secondary electrons, (middle) backscattered electrons and (bottom) characteristic X-rays.

Figure 3.17 Photo of JEOL JSM-7800F Prime FEG-SEM used in this project

Figure 3.18 Photo of FEI Nova NanoLab 600i FEG-SEM/FIB used in this project

Figure 3.19 Schematic diagram showing the dual-beam system and the concept of eucentric height

Figure 3.20 A panoramic view of the applications of FIB technology. The techniques

used in this project are highlighted in red.

Figure 3.21 Photo of JEOL JEM-2100F FEG-TEM/STEM used in this project and the inset diagram is the schematic illustration of the instrument structure, where blue marks the electron source part; yellow marks the illumination system and green marks the imaging system.

Figure 3.22 A simplified schematic illustration of operations in (left) diffraction and (right) imaging mode

Figure 3.23 Schematic illustration of a computer-controlled electrochemical workstation with three-electrode setup, based on CH Instruments Model 600A.

Figure 3.24 Schematic illustration of Ag/AgCl reference electrode

Figure 3.25 Photo of Metrohm Autolab PGSTAT302N electrochemical workstation used in this project

Figure 4.1 52° tilted FEG-SEM images of Si/Au/PS samples at 100 k×: (a) before and (b-d) after the RIE process. The etchant gas used was (b) Ar; (c) CF_4 and (d) O_2.

Figure 4.2 POM images taken at 1 k× (top) and 52° tilted FEG-SEM images taken at 50 k× (bottom) of Si/Au/PS sample after 5 min RIE. The chamber pressure was kept at (a-a') 300 mTorr; (b-b') 120 mTorr and (c-c') 90 mTorr. The inset of (c') is a top view FEG-SEM image taken at the magnification of 50 k×.

Figure 4.3 (a-h) Top view FEG-SEM images of Si/Au/PS sample taken at 100 k×: (a) before RIE; and after RIE for 5 min at the power of (b) 10 W; (c) 20 W; (d) 30 W; (e) 50 W; (f) 80 W; (g) 120 W and (h) 150 W. (i) A diagram showing the relationship of the remaining PS spheres and feature spacing sizes with RIE power.

Figure 4.4 FEG-SEM images of Si/Au/PS sample after RIE taken using the dual-beam FIB system: (a-b) 10 k× and 100 k× top view and (c) 100 k× at 52° tilt; (d-e) 7 k× and 20 k× top view and (f) 100 k× at 52° tilt, showing contrast before and after irradiation by Ga^+ ion source at 30 kV and 0.46 nA for 30 s. The points indicated in (f) are the EDX analyses sites.

Figure 4.5 EDX spectra of different spots on the Si/Au/PS sample

Figure 4.6 XRD patterns of the Si/Au/PS sample before (black) and after (red) RIE

Figure 4.7 FEG-SEM image of Si/Au/PS samples taken under dual-beam SEM/FIB system. (a) Top view FEG-SEM images of Si/Au/PS samples, taken at a low magnification of 10 k×. (b-f) Top view FEG-SEM images of Si/Au/PS samples after different RIE durations: (b) 5.0 min; (c) 7.5 min; (d) 10.0 min; (e) 15.0 min and (f) 20.0 min, taken at the magnification of 50 k×. (Insets of b-f) 52° tilted FEG-SEM images of each sample showing one feature, taken at the magnification of 100 k×.

Figure 4.8 Schematic illustration of the formation mechanism of the Au nano-ring array, with inset being the magnified view of the boxed regions. The graphs are not drawn to scale.

Figure 4.9 TEM and HRTEM images of Au nano-ring array. (a) The cross-sectional TEM lamella made by the dual-beam SEM/FIB system. (b) TEM image of the lamella at low magnification. (Inset of b) Low magnification bright field TEM image (left) and the corresponding EDX elemental mapping (right) of the sample performed using an EDX detector integrated on the FEG-TEM. Green: Si; red: O; yellow: Au; blue: Pt. (c) Magnified TEM image of the square region in (b). (d) HRTEM image of the square region in (c), and (inset) the FFT pattern of the square region in (d).

Figure 4.10 Relationship between Au nano-ring height and etching duration, as well as a linear fit trend line.

Figure 4.11 Direct observation of active sites through TEM and HRTEM images. (a) Part of one Au nano-ring imaged under TEM showing several pyramids across the surface. (b) HRTEM image taken at the tip of pyramid 1. (c) HRTEM image of the square region in (a). (d) The FFT patterns taken from the two square regions in (c) at the zone axis of [1 0 1], in which the red spot array is reflected from the red square area in (c). There are two sets of blue spot arrays diffracted from the blue square region (i.e. the Moiré fringe region) in (c). One blue spot array is in superposition with the red spot array. The other blue spot array is rotated with respect to the first blue spot array at a small angle of ~ 6°.

Figure 4.12 Electrochemical behaviours of the Si/Au/PS samples. (a) Cyclic voltammograms. (b) The Nyquist plots obtained from EIS, as well as the equivalent circuit diagram of the experimental setup (inset). R_L: electrolyte resistance; R_P: electrochemical impedance; C_D: double layer capacitance. (c) Magnified EIS of square region in (b) showing only the arrayed samples. (d) CA graph comparing the planar and arrayed samples. All testing was carried out in an electrolyte with 0.1 M NaOH and 1.0 M ethanol.

Figure 4.13 CV curves of the samples taken under different scan rates. (a) Original without RIE; as well as after (b) 5.0 min, (c) 7.5 min, (d) 10.0 min, (e) 15.0 min and (f) 20.0 min RIE.

Figure 4.14 Cyclic voltammograms of the Si/Au/PS samples under different physical conditions. (a) All samples in 1.0 M ethanol at pH = 13; (b) the sample after 5.0 min RIE at pH = 13 with varying ethanol concentrations; (c-d) the sample after 5.0 min RIE in 1.0 M ethanol at different pH values.

Figure 4.15 The FTIR spectra of the electrolyte on KBr pellet after 5 (red spectrum) and 135 (blue spectrum) consecutive cycles of CV collected using transmission mode after the removal of background

Figure 4.16 Schematic illustration of the working mechanism when the active sites are brought in close proximity to the ethanol molecules. The reactions are proceeding via (a) C2 and (b) C1 pathways, ending up with different intermediate and final reaction products.

Figure 5.1 The thermal phase transition profile of the cleaned PVC substrate

Figure 5.2 The working profile during the NIL process

Figure 5.3 The POM and top-view FEG-SEM images of different samples. (a-e) Samples imprinted for 5 min under 8 bar pressure, at (a) 70 °C; (b) 90 °C; (c) 110 °C; (d) 130 °C and (e) 150 °C. (f-g) Samples imprinted at 150 °C under 8 bar pressure for (f) 1 min and (g) 3 min. (h-i) Samples imprinted at 150 °C for 5 min under (h) 2 bar and (i) 5 bar pressures. The inset figures of (b-i) show the top-view FEG-SEM images of a "junction" at the magnification of 2 k×, and the scale bar represents 10 μm.

Figure 5.4 Characterisations of the PVC/Au samples. (a-e) The 50× POM images of the patterned samples with (a) 50-mesh, (b) 150-mesh, (c) 200-mesh, (d) 300-mesh and (e) 400-mesh MAs; (a'-e') the corresponding top-view FEG-SEM micrographs showing a single hexagonal pillar structure; (f) FEG-SEM micrograph of a pillar at its corner, taken at an inclined angle of 52° showing its height; (g) the XRD pattern of the samples after Au-coating.

Figure 5.5 TEM characterisations of Au thin film with 400-mesh MAs. (a) Low magnification bright-field TEM image showing part of an edge. (b) The SAED pattern rendering strong diffraction of the sample. (c-d) The original HRTEM image (c) of an inner site (~ 100 nm away from the edge of sample), as well as the corresponding FFT pattern (d) of the entire HRTEM image. (e-i) The IFFT images of (d), transformed (e) in whole and (f-h) along <0 1 1>, <1 0 1> and <1 1 0> directions, respectively; (i) the RGB mapping of (f-h). (e-i) share the same scale bar as the HRTEM image shown in (c).

Figure 5.6 Marking of the atomic-scale 3D nanostructure (top), as well as the line measurement profile along the yellow line from atom #0 to atom #6 (bottom).

Figure 5.7 *In-situ* TEM observation of interactions between atomic-scale active sites. (a-g) HRTEM images of Au near the edge of sample, visualising the in-situ observation of the interactions between atomic-scale active sites; the images were consecutively captured at an interval of 30 s. The red lines in (a) mark the crystal twinning on the surface of the atomic-scale active site which keeps its existence in (a-g). (h-i) The FFT pattern (h) and the corresponding IFFT image (i) of the white square region in (g); (inset of g) the line measurement profiles of the d-spacing values of <1 1 1> and <2 0 0> crystal planes as marked in (i). (b-f) share the same scale bar as (a), while (i) shares the same scale bar as (g).

Figure 5.8 Time-resolved line measurement profiles along the twinning plane

Figure 5.9 Cyclic voltammograms of the samples in EOR showing their electrochemical behaviours. (a) Comparison of MA samples of different mesh grades against the planar sample; (b-c) performance of the sample with 400-mesh MAs in (b) alkaline and (c) acidic electrolytes of varying pH values; (d) performance of the sample with 400-mesh MAs in alkaline electrolytes (pH = 13) with different ethanol concentrations.

Figure 5.10 (a) The Nyquist plots of the samples obtained from EIS, with the enlarged plots for the samples with MAs (inset); (b) plot of WE current against scan rate for the calculation of C_D as displayed in the equivalent circuit diagram (inset); (c) plots and fitting of C_D in relationship with mesh grade and array size; (d) CA profiles of planar and MA samples with amplification of their difference (inset).

Figure 5.11 CV curves of the samples taken under different scan rates. (a) Planar sample; as well as samples with (b) 50-mesh, (c) 150-mesh, (d) 200-mesh, (e) 300-mesh

performance in EOR; (b-c) catalytic performance of the sample produced with 5 keV Ar^+ ion beam in electrolytes of different pH values; (d) catalytic performance of the sample produced with 5 keV Ar^+ ion beam in electrolytes of different ethanol concentrations. The mass loadings for Ti/Au samples and commercial Au NPs are ~ 1.9 mg/cm^2 and the graphs are plotted based on mass activities. The commercial Au NPs serve as a reference sample for comparison purpose.

Figure 6.7 (a) CA profiles of bare Ti foil and Ti/Au sample in EOR, showing their stability during electrochemical testing; (inset of a) enlarged graph showing the pitting corrosion, with an exponential fit of the rate of corrosion. (b-d) The morphology of the Ti/Au sample after CA test, with the top-view image (b) shows many pits formed across the surface and the cross-sectional images (c-d) show some of the pits formed in an enlarged view.

Figure A.1 The detailed internal structure and external attachment modules of JEOL JSM-7800F Prime FEG-SEM used in this project

Figure A.2 (a) Absorptance and (b) spherical reflectance spectra of the Si/Au/PS samples measured using UV-Vis-NIR: (black) original before RIE; (red) after 5.0 min RIE; (blue) after 7.5 min RIE; (green) after 10.0 min RIE; (orange) after 15.0 min RIE and (purple) after 20.0 min RIE.

Figure A.3 Emission profile of the arrayed Si/Au sample measured using spectrofluorophotometer, with excitation wavelength being 320 nm.

Figure A.4 (a) Raman spectra of R-6G powder and 1 ppm R-6G solution on different surfaces; (b) Raman spectra of 0.01 ppm R-6G solution on different samples.

Abbreviations

%A	Absorptance
%R	Reflectance
%T	Transmittance
ΔG	Change in Gibbs free energy
λ	Wavelength
Ag	Silver
Ar	Argon
Au	Gold
BEI	Backscatter electron imaging
BET	Brunauer-Emmett-Teller
CA	Chronoamperometry
C_D	Double layer capacitance
CF_4	Tetrafluoromethane
CFC	Chlorofluorocarbon
CO	Carbon monoxide
Cu	Copper
CV	Cyclic voltammetry
CVD	Chemical vapour deposition
DAFC	Direct alcohol fuel cell
DC	Direct current
DEFC	Direct ethanol fuel cell
$d_{(h\,k\,l)}$	Inter-atomic spacing/d-spacing of crystals on the (h k l) plane
DSSC	Dye-sensitised solar cell
E^0	Standard reduction potential
E_a	Activation energy
EBL	Electron beam lithography
ECSA	Electrochemical surface area
EDX	Energy-dispersive X-ray spectroscopy
EIS	Electrochemical impedance spectroscopy

EOR	Ethanol oxidation reaction
(FEG-)SEM	(Field emission gun) scanning electron microscope/microscopy
(FEG-)TEM	(Field emission gun) transmission electron microscope/microscopy
FIB	Focused ion beam
FTIR	Fourier-transform infrared
H_2	Hydrogen
H_2O_2	Hydrogen peroxide
H_2SO_4	Sulphuric acid
HRTEM	High resolution TEM
HSQ	Hydrogen silsesquioxane
(I)FFT	(Inverse) fast Fourier transform
JCPDS	Joint committee on powder diffraction standards
KOH	Potassium hydroxide
LB	Langmuir-Blodgett
LMIS	Liquid metal ion source
LSPR	Localised surface plasmon resonance
NaOH	Sodium hydroxide
Ni	Nickel
NIL	Nanoimprint lithography
NSL	Nanosphere lithography
O_2	Oxygen
ORR	Oxygen reduction reaction
PhL	Photolithography
PMMA	Poly(methyl methacrylate)
POM	Polarised optical microscope
PS	Polystyrene
Pt	Platinum
PVC	Polyvinyl chloride
PVD	Physical vapour deposition
RF	Radio frequency
RIE	Reactive ion etching

R_L	Solution (intrinsic) resistance
R_P	Electrochemical impedance
SAED	Selected-area electron diffraction
SAM	Self-assembled monolayer
SA/V	Surface area to volume (ratio)
SEI	Secondary electron imaging
Si	Silicon
SPL	Scanning probe lithography
SPM	Scanning probe microscope
TED	Transmission electron detector
Ti	Titanium
TOF	Turnover frequency
UV-Vis-NIR	Ultraviolet-visible light-near infrared (spectroscopy)
VLS	Vapour-liquid-solid
XRD	X-ray diffraction/diffractometer
Z	Atomic number

Chapter 1

Introduction

Ethanol has long been an integral part in our daily lives. It is cheap, safe, abundantly available, and could be applied across many fields. In modern days, over-consumption of alcoholic drinks might lead to drunk driving which causes many traffic accidents; on the other hand, fast depletion of fossil fuels is bringing significant attention to the development of clean and renewable energy. Fuel cells have a strong potential to replace fossil fuels in many fields; amongst the various types, direct ethanol fuel cell (DEFC) has the highest energy density with low fabrication cost, thus the electro-oxidation of ethanol becomes an important research. The ethanol oxidation reactions (EORs) can be applied not only in DEFC (as an alternative source of energy output from fossil fuels used in transportation and industries), but also can be used in the hand-held ethanol detectors. To date, most of the EORs are either having the participation of strong oxidative chemicals like acidified potassium dichromate (VI) solution, or catalysed by transition metals like copper (Cu). The main issues on the usage of strong oxidants are their associated pollution and environmental unfriendliness; while the problems with the latter arise from the partial catalysis and incomplete oxidation, which could release more toxic products like ethanal. Therefore, research on materials that are capable of catalysing full oxidation of ethanol – yet environmentally friendly – is now a key focus over EORs in materials science and engineering.

1.1 Hypothesis

Noble metals are well studied in catalysis due to their excellent properties and chemical resistance. In the field of electrochemical oxidation of ethanol, gold (Au) is a popular choice due to its high performance to cost ratio compared to platinum (Pt) and silver (Ag), thus making it an extraordinary candidate to catalyse in DEFC. In most cases, the Au catalyst exists in the form of nanoparticles (NPs) for high surface area to volume ratio, but this leads to the disadvantage of high fabrication cost and the small sizes of NPs might be limited by the aggregation issues arising from the chemical synthesis process. While Au could be coated as thin films for cost-effectiveness, the reduction in catalytic properties becomes a shortcoming in contrary. This project is intended to research on methods to enhance the catalytic activities of nanostructured Au in EOR.

The electrochemical performance would be improved via two distinct ways – either increasing the specific surface area, or raising the surface energy of the catalyst – or both if possible. Increasing the specific surface area might be the easier way and has more prominent effect; but in the cases which this approach is not really feasible, raising the surface energy would become the underlying reason to enhance the catalytic performance of the Au catalyst.

Synthesis of NPs and fabrication of array structures could effectively increase the specific surface area of the active materials; however, raising surface energy of the catalyst would require some special techniques, which during the process, external energy content could be transferred onto the surface of active sites. Both approaches are to be carried out and through systematic experiments, the hypothesis should be proven.

This thesis tests the hypothesis that when nanostructured Au electrocatalyst is subjected to an increase in either the specific surface area or the surface energy, they will produce more active sites or stress centres, thus the electrocatalytic performance of Au in EOR could be improved.

1.2 Objectives and Scope

The aim of this research is to improve the electrocatalytic performance of Au in EOR. As introduced in Section 1.1, this could be achieved by increasing the specific surface area or raising the surface energy of the catalyst. In this project, both methods will be carried out and the outcome will be tested through electrochemical testing.

Through a systematic set of trials using different parameters (such as feature size of mask, duration and so on), Au thin films with micro-/nano-structured arrays will be fabricated on different substrates (silicon (Si) and polyvinyl chloride (PVC)). The relationship between the geometry of ordered Au array structures and the electrochemical performance will be studied through comparison against samples without the ordered array structures. On the other hand, Au NPs will be synthesised via a non-traditional way with the use of precision ion polishing system (PIPS), so high surface energy could be feasible as a result of crystal twinning due to bombardment by energetic ion beams.

1.3 Dissertation Overview

The thesis addresses the methods to improve the electrocatalytic performance of nanostructured gold in ethanol oxidation reaction, which is a key part in direct ethanol fuel cell (DEFC) as a potential solution to the current energy crisis.

Chapter 1 provides a rationale for the research and outlines the goals and scope.

Chapter 2 reviews the literatures concerning the current solutions to the energy crisis and highlights the great potential of DEFC. Catalysed electro-oxidation of ethanol at the anode and its working principles are also reviewed. Various types of catalysts and their fabrication processes are introduced and various methods to improve the catalytic activity of gold are compared.

Chapter 3 discusses the principles underlying the synthesis, characterisation and testing

techniques employed.

Chapter 4 elaborates the first major set of results. Au nano-ring array structures were fabricated on Si substrates via nanosphere lithography (NSL) followed by reactive ion etching (RIE). High resolution transmission electron microscopy (HRTEM) characterisations have revealed the formation of atomic-scale active sites by the fabrication process. Based on the systematic electrochemical testing, a mechanism of the catalytic process has been proposed.

Chapter 5 elaborates the second major set of results. Au micro-array structures were fabricated on flexible PVC substrates via nanoimprint lithography (NIL). Atomic-scale 3D nanostructures are directly visualised with advanced electron microscopy for the first time, and *in-situ* observations unveil the interactions between the atomic-scale active sites. Electrocatalytic performance has been thoroughly tested and elaborated. Several correlations were established and simple simulation has demonstrated great potential of the approach.

Chapter 6 elaborates the third major set of results. Homogeneous and ultra-small single crystalline Au nanoparticles were synthesised using the precision ion polishing system (PIPS). Under suitable conditions, they were found to form highly strained twinned crystals. HRTEM characterisations have illustrated the stress centres and their contribution to the enhancement of electrocatalytic performance was discussed.

Chapter 7 draws together the threads of the thesis. A framework for further studies is recommended based on the findings of the current research in this project.

Appendix provides some supporting information of the thesis. Reconnaissance studies that do not warrant a complete chapter are also included.

1.4 Findings and Outcomes/Originality

This research led to several novel outcomes by:

1. Demonstrating that NSL and NIL might be the easiest, safest and most effective ways to increase the specific surface area of Au electrocatalyst by fabrication of micro-/nanostructured arrays. The theoretical 100% coverage area and potential to large-scale fabrication could lay a firm foundation for the application in DEFC.

2. Establishing the key concept that apart from increasing the specific surface area, raising the surface energy is another major contribution to the improvement of electrocatalytic performance of Au in EOR.

3. Constructing a systematic understanding of Au-catalysed EOR under various physical conditions, such as pH value and ethanol concentration in the electrolyte. The Au catalyst performs better in electrolytes with extreme pH values and can detect ethanol down to pretty low concentrations ($\leq$ 5 mM). Samples with array structures may force the reactions via C1 pathway (desired) and have excellent performance stability.

4. Directly visualising the atomic-scale 3D nanostructures, active sites and defects (such as partial lattice rotation, crystal twinning and stress centres), as well as *in-situ* observing the instantaneous interactions of the atomic-scale active sites through advanced materials characterisation techniques. Their presence has brought about great improvements in the electrocatalytic performance of the Au catalyst.

5. Showing that nanostructured Au in both forms (thin films and NPs) can perform much better EOR than the control sample. The electrocatalytic performance of Au thin films with nano-ring arrays or micrometre-scale arrays can be more than four times that of planar Au thin films. On the other hand, the electrocatalytic performance of highly strained Au NPs with crystal twinning (~ 10 nm in size) is up to about two times that of commercial Au NPs (~ 5 nm in size).

6. Correlating the key parameters in electrochemistry (like electrochemical surface area (ECSA), number of active sites and double layer capacitance (C_D)) to the

performance of Au electrocatalyst (such as turnover frequency (TOF) and working electrode current density).

Chapter 2

Literature Review

Catalysts are a special kind of substance which could modify (usually increase) the rate of chemical reactions, without themselves having any permanent change in chemical compositions throughout the process. Electrocatalysts are a special type of catalysts that participate in electrochemical reactions, and are one of the most common types utilised in the modern society. Being a noble metal, gold (Au) has the highest performance to cost ratio. Therefore in this project, the Au electrocatalyst is to be fabricated in various forms; the main focus of research will be the ways to enhance its catalytic performance, as well as to understand the mechanism behind the improvements.

2.1 Energy Crisis and Current Solutions

Since the Industrial Revolution, fossil fuels have been the main energy sources of the human civilisations. In the modern society, many key industrial sectors are heavily relied on the combustion of fossil fuels, thus leading to their fast depletion and subsequent environmental pollution. Therefore, human beings must search for alternative ways in order to maintain a sustainable development. Currently, the major approaches include harvesting of clean and renewable energy, such as wind and geothermal energies; as well as development of energy storage and energy conversion solutions, for example, batteries, supercapacitors, solar cells, fuel cells and gas storage.

2.1.1 Renewable Energies

Energies harvested from infinite sources or those can be naturally replenished in finite amount of time (on human timescale) are called renewable energies. Based on the contemporary technology, the major types include wind energy, hydro energy, geothermal energy, solar energy and so on.[1]

Wind energy is based on the fast-growing technology, which is harvested by the operation of wind turbines. The power output is a function of the cube of the wind speed, so wind energy has a great potential in meeting the global demands on power generation.[2] However, there are many restrictions, for example, the wind turbines need to be set up at ice-free rural areas which are not forested, and they are best operated at the wind speed of ~ 4-20 m/s.[3] The unpredictability of wind as a natural phenomenon, together with the low efficiency of power output, has thus limited the large-scale replacement of fossil fuels in power plants.[4]

In comparison, hydro energy comes from liquid water, which is much denser than air that brings about wind energy. The hydro energy is a matured technology that has little room for improvement;[3] its main source is associated with water in motion, which includes running rivers, waves and tides.[2, 4] An important advantage of hydropower is that turbines

can be designed to run either forwards (generating power from falling water) or backwards (using power to pump water up to a high-level reservoir), hence about 16% of the world's total energy is from hydro energy.[3, 5] By far, the contribution of hydro energy is generally limited by the availability of rivers and coastlines in countries, as well as the cost incurred in the construction of dams.[2-4]

Geothermal energy is a special type of thermal energy that originates from the Earth since the birth of the planet. The Earth has a molten core and a solid shell, between which exists a temperature gradient that drives continuous conduction of the thermal energy. Volcanic activities could also contribute to the geothermal energy through the convection of heat based on the movement of magma. Researches have shown that geothermal energy is a cost effective, reliable, and environmentally friendly energy source,[2] which can be either applied in small-scale residential heating and large-scale power plants, thus it is estimated to produce 19.8 GW power worldwide in 2050.[4] However, the mechanism of the energy resource has limited its production primarily to places near to tectonic plate boundaries.[6]

Energy from the Sun is named solar energy, it is deemed infinite in the human civilisation. Harvesting of solar energy and conversion into electrical energy is achieved by solar cells. In the photovoltaic industries, silicon is the major material used in the solar panels due to its high relative abundancy on Earth, low cost and small bandgap.[7] However, the biggest issue is that the commercial solar panels generally have low conversion efficiency (< 30%).[8] Recent studies are focusing on the development of various types of solar cells for better performance, for example, thin film solar cell, dye-sensitised solar cell, polymer solar cell and quantum dot solar cell.[9] One of the promising materials is perovskites, and in particular the organic-inorganic hybrid perovskites such as $CH_3NH_3PbX_3$.[10] They are reported to have high charge carrier mobility, complementary absorption bands in the visible light and near infrared range, and a small energy offset to minimise voltage losses.[11] There have been great progress in the researches and the conversion efficiency is expected to catch up with the commercial products, but the extensive use of lead in many materials makes them toxic, which is still the most challenging issue to solve.

2.1.2 Energy Storage

Energy can neither be created nor destroyed, but it can be stored and converted from one type to another. Renewable energies are not always available as they could be limited by various natural factors, thus the storage of energy was a dream in the ancient times. Now with technological advances, solutions have been developed and various types of energies could be stored, for instance, chemical/electrochemical energy, thermal energy and mechanical energy.

The storage of mechanical and thermal energy is usually for efficient use of energy. This is because the consumption of energy is not evenly distributed in daily lives; efficiency should be improved by storing energy during off-peak hours and releasing during peak periods. Commercial applications of flywheel energy storage (FES) and compressed air are well-known examples of mechanical energy storage solutions. In an FES system, the flywheel is accelerated by an electromotor to high speed, which stores energy in the form of angular kinetic energy (also known as rotational energy); deceleration leads to the release of stored energy in the form of electric energy. The long working life, high reliability, wide working temperature range and high energy storage efficiency (~ 90%) are the key advantages of FES systems.[12] On the other hand, compress air can be used in electric power generation and could save ~ 40% gas for the same amount of power output.[12] In contrast, the storage of thermal energy is a good management of heat. Current researches are mainly focusing on phase change materials,[12] which could regulate the excess latent heat in the surrounding environment. A classic type is thermochromic materials, which changes phase upon temperature change and thus reveal different optical properties before and after the phase change.[13-17]

In certain applications with high energy input, gaseous fuels (especially hydrogen) could be the best choice, and therefore the production and storage of gas are developed to meet such requirements. But in consideration of the wide spectrum of applications ranging from daily use to industrial production, the mainstream of energy storage solutions are for

chemical/electrochemical energies, of which the storage is achieved by devices such as batteries, capacitors and fuel cells. **Figure 2.1** compares the performance of these devices in terms of power density and energy density. It can be found that capacitors have higher power densities but small energy density; this means they can be quickly charged and discharged, but the amount of energy stored is limited. Batteries and fuel cells are in the opposite way, signifying that they require more time to charge and discharge, but the energy stored could last longer. With gasoline (which is a fossil fuel product) as the reference, fuel cells are the only type that has comparable performance, and therefore they are the most ideal substituent for fossil fuels.

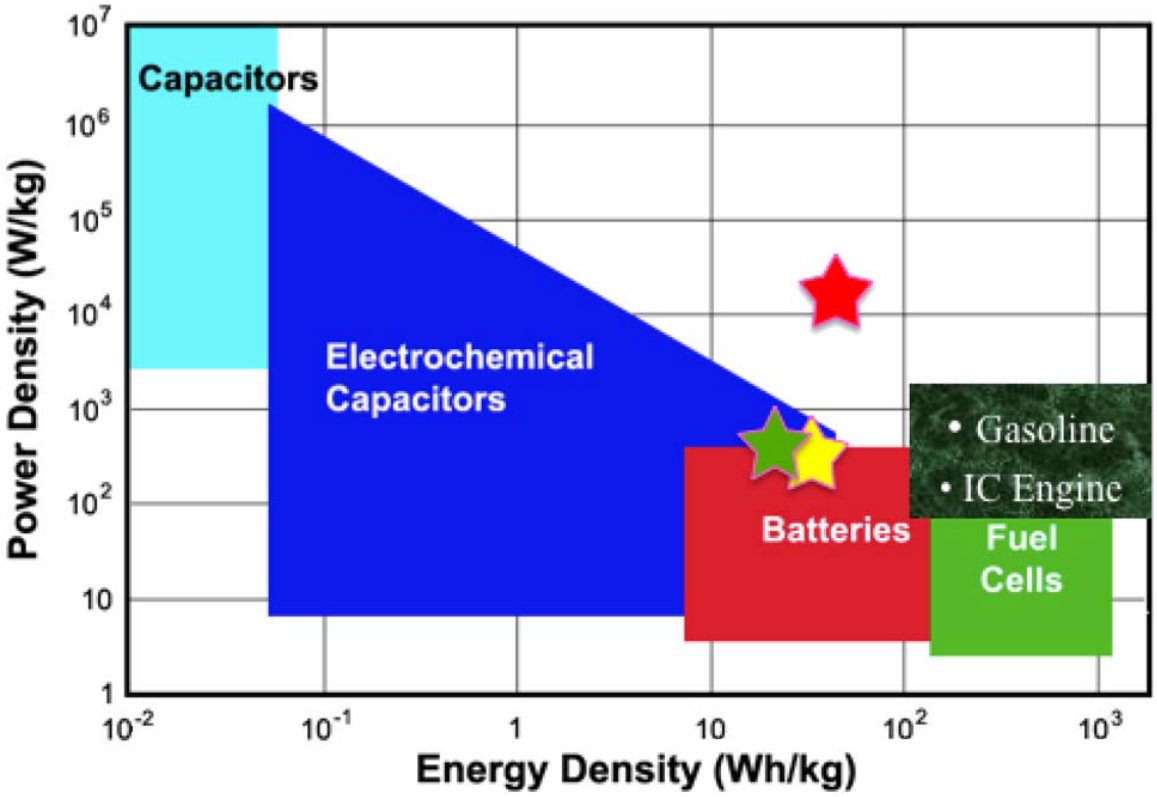

Figure 2.1 Comparison of various chemical/electrochemical energy storage devices in terms of power density and energy density.[3, 18] Three commercial examples are shown by the stars – yellow: 2008 Toyota Prius; green: BAE Bus; red: A123 Formula One race car booster.[18]

2.1.3 Hydrogen (H_2) as a Clean Fuel

Searching for alternative energy sources is not only because fossil fuels are depleting soon, but also their combustion leads to the release of large amount of greenhouse gases that causes global warming. The combustion of hydrogen (H_2) with oxygen (O_2) forms water, and large amount of energy is released from the highly exothermic process. The theoretical zero carbon emission makes it a clean fuel.[19] The current major application of H_2 fuel is the space shuttle and rocket propellant, but it has been technically demonstrated to be capable in heating, power generation and transportation.[20]

Equation 2.1 Production of hydrogen via steam reforming of methane[19]

$$CH_4 + H_2O \xrightarrow{700-1100℃} CO \uparrow + 3H_2 \uparrow$$

$$CO + H_2O \xrightarrow{360℃} CO_2 \uparrow + H_2 \uparrow$$

Equation 2.2 The water splitting reaction

$$2H_2O \xrightarrow{Energy} 2H_2 \uparrow + O_2 \uparrow$$

H_2 can be industrially produced by steam reforming of fossil resources (mostly methane),[19, 21] as given in **Equation 2.1**. By far, the majority of hydrogen production (~ 95%) is by steam reforming of natural gas, which is based on an "energy return on investment" mode. This means the production of H2 requires lots of energy input and most of the energy is still based on fossil fuels. Researchers are now working on water splitting, which is a chemical reaction that breaks down water molecules into their compositional H_2 and O_2, as given in **Equation 2.2**. Based on the reaction mechanism, this process can be classified as photochemical,[22, 23] photoelectrochemical[24, 25] and electrochemical[26, 27] water splitting, which may require different catalyst materials. In electrocatalysis, water splitting is more commonly divided into two sub-reactions, namely the hydrogen evolution reaction (HER) and oxygen evolution reaction (OER).

Currently, the use of H_2 as a clean fuel has many concerns and disadvantages. H_2 is highly flammable and can burn ferociously in air over a wide range of concentrations (~ 4% to 75%);[28] this brings about potential safety issues in the transportation and combustion of the fuel, and poses great difficulty in its leak detection.[29] Furthermore, although H_2 has high energy density on a mass basis (120 MJ/kg for H_2 vs 44 MJ/kg for gasoline), its poor volumetric energy density (0.01 MJ/L for H_2 vs 32 MJ/L for gasoline at standard temperature and pressure) is limiting the practical applications.[30, 31] Large amount of the fuel has to be stored in order to support the functioning of the motors or fuel cells, so the storage of produced H_2 has led to another field of research about gas storage. Apart from the traditional ways like compression of gas and liquefaction, more studies have been carried out to understand the mechanism of gas storage. Currently, based on the chemical storage and physical adsorption (physisorption) mechanisms, the storage of hydrogen may be achieved by various ways, for example, storing as hydrogen-rich chemicals which may be decomposed to release hydrogen, and utilising materials with cavity in their structures for physisorption processes.[32] An important type of materials from the latter is the metal-organic frameworks (MOFs),[33] which are widely investigated on the performance of gas (especially H_2) storage.

2.1.4 Fuel Cells

A fuel cell converts the chemical energy of the fuel directly into electrical energy, and this process is dependent on a pair of electrochemical redox reactions. In order for a fuel cell to work, it needs the supply of fuel, a suitable working temperature and the presence of oxidising agent. As long as the requirements are fulfilled, the fuel cell could continuously output electricity. This is one of the advantages of fuel cells over batteries, which have limited lifespan even they could be rechargeable. As such, the market of fuel cells keeps growing and their total power output is expected to reach 50 GW by 2020.

To facilitate the electrochemical redox reactions, a fuel cell is therefore comprised of a connected pair of anode and cathode, as well as an electrolyte to form a closed circuit. The fuel is oxidised at the anode; this process releases electrons that flow towards the

cathode through the external circuit and thereby produces a direct current (DC). The ions produced by the process flow towards the cathode through the electrolyte and thus balance the charges. Ions from the electrolyte and electrons from the circuit would undergo reduction reactions at the cathode (at which oxidant like is O_2 fed), so as to make the entire system a full cell. **Figure 2.2** shows the schematic illustration of a fuel cell, which comprises of its various components and the basic process principles.

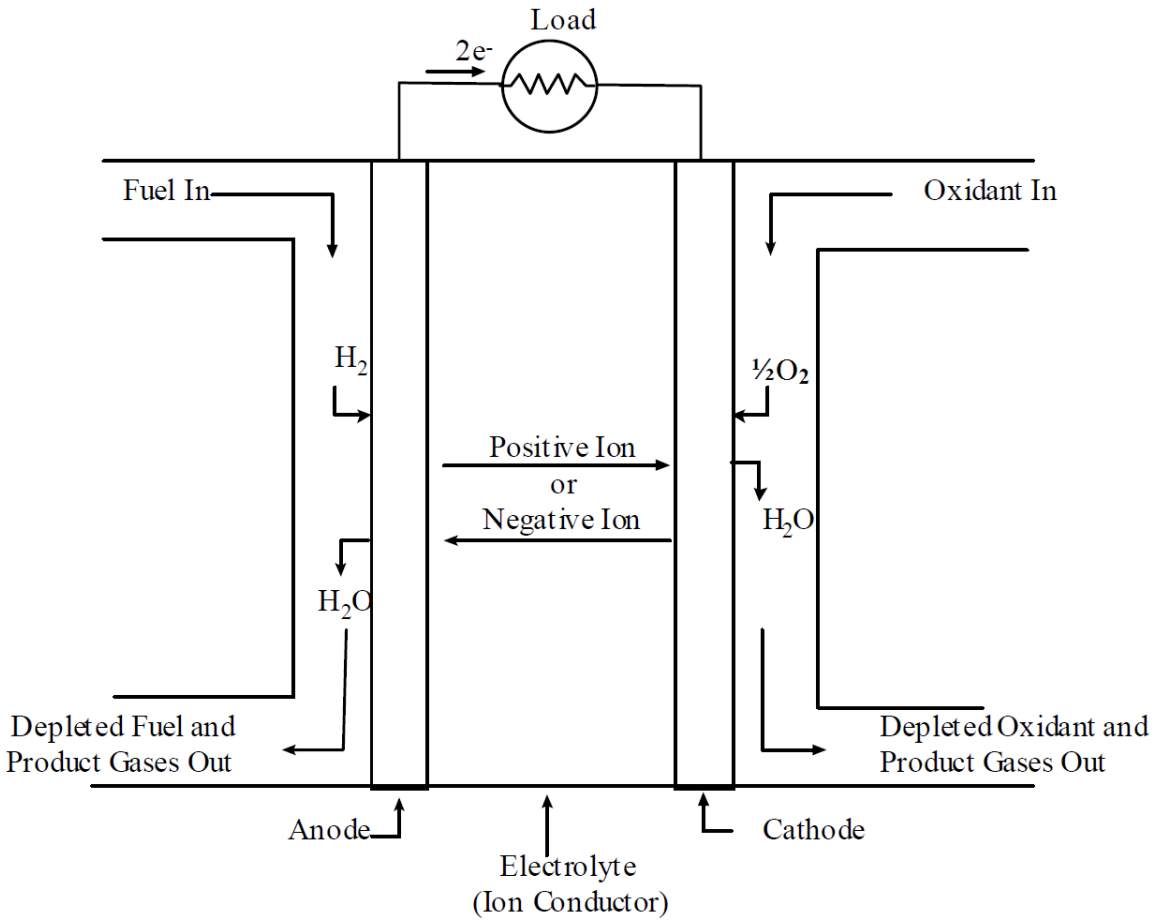

Figure 2.2 Schematic illustration of a fuel cell[34]

Fuel cells can be categorised by the type of electrolyte in the system. The common types include polymer electrolyte fuel cell (PEFC), alkaline fuel cell (AFC), phosphoric acid fuel cell (PAFC), molten carbonate fuel cell (MCFC) and solid oxide fuel cell (SOFC). Their process principles mainly differ by the state of the electrolyte (liquid or solid). As such, different catalyst materials are to be developed according to the fuel cell system, so

as to ensure the smooth proceeding of the electrochemical reactions. They provide active sites for the reactions, which are exposed to the reactants (fuel), in electrical contact with the electrode materials and in ionic contact with the electrolyte.[34] **Table 2.1** lists some key features of these systems.

Table 2.1 List of common types of fuel cell systems[34, 35]

	PEFC	**AFC**	**PAFC**	**MCFC**	**SOFC**
Common electrolyte	Hydrated polymeric ion exchange membrane	NaOH or KOH	H_3PO_4	K_2CO_3 or Li_2CO_3	Y_2O_3-stabilised ZrO_2
Ionic charge carrier	H^+	OH^-	H^+	CO_3^{2-}	O^{2-}
Electrode material	Carbon	Noble metals	Graphite	Nickel or nickel oxide	Perovskite
Catalyst material	Noble metals	Noble metals	Noble metals	Transition metals or their oxides (TMO)	Perovskite
Operating temperature	40-80 °C	20-220 °C	205 °C	650 °C	600-1000 °C

The advantages of AFCs over other types mainly include lower cost, low corrosiveness and high current densities. In this particular type, direct alcohol fuel cell (DAFC) has attracted great attention and becomes a popular research in the recent years. This is because alcohols have low fabrication cost, and when they are used as the fuel, the energy densities of the fuel cells (~ 6-8 kWh/kg) are close to those with combustion of petroleum products (~ 10-11 kWh/kg).[36] Furthermore, fuel cells working on liquid alcohols make their application in transportation industries possible.[37] Therefore, alcohols are considered as nearly perfect substituent for fossil fuels.

Methanol, ethanol, isopropyl alcohol (IPA) and ethylene glycol (EG) are the common fuels in DAFCs. Amongst them, the low energy density of EG-based fuel cells hinder their practical applications, and IPA-based fuel cells often suffer from poisoning of the catalyst materials by CO-rich intermediates.[36, 38] Therefore, methanol and ethanol are the

most commonly used fuels in DAFC researches. In comparison to methanol, ethanol is less toxic and can be fabricated from bioprocesses like fermentation of agricultural products, these are the added advantages of ethanol over methanol apart from its higher energy density.[36] Furthermore, the lower crossover rate of ethanol than methanol could bring about a better performance in fuel cells.[36]

2.1.5 Summary for Solutions to Energy Crisis

Fuel cells have comparable performance to fossil fuels in theory, and are considered as the ideal substituent energy source. Amongst the various systems and types of fuel cells, DEFC has attracted plenty amount of attention due to its versatile properties. No matter how the systems vary, a common feature is that they all require catalyst materials during the redox reactions. Therefore, the research on suitable catalysts is one of the most important parts in the development of DEFC.

2.2 Catalysis

2.2.1 Background

Apart from direct reactions, which may require harsh physical, chemical or biological conditions, catalysts offer alternative reaction pathways that are easier to be achieved. As less energy is consumed in the initiation of the reactions, the rates of reactions can also be greatly improved. A well-known process, photosynthesis in plants (**Equation 2.3**), is catalysed by the chlorophyll and a series of enzymes. It can be briefly split into two parts: a photochemical reaction catalysed by chlorophyll and enzymes, which transforms solar energy into electrical energy through electron transfer; and an electrochemical reaction catalysed by enzymes, which fixes carbon atoms and generate carbohydrate products.

Equation 2.3 Photosynthesis reaction

$$6CO_2 + 6H_2O \xrightarrow{Sunlight} C_6H_{12}O_6 + 6O_2 \uparrow$$

In environmental science, the depletion of ozone layer is largely contributed to the use of chlorofluorocarbons (CFCs), which may release harmful chlorine free radicals (Cl·). They attack ozone molecules by removing an oxygen atom, and further attack ozone molecules to get themselves recovered,[39] as shown in **Equation 2.4**:

Equation 2.4 Depletion of ozone[39]

$$Cl\cdot + O_3 \rightarrow ClO + O_2 \quad \text{(a)}$$

$$ClO + O_3 \rightarrow Cl\cdot + 2O_2 \quad \text{(b)}$$

Similarly, catalysis can be applied in many other fields, such as the disproportionation and fabrication of many chemicals (**Equation 2.5 a**), the catalytic converters in vehicles and petroleum refineries (**Equation 2.5 b**), and even food processing industries.

Equation 2.5 Disproportionation reaction and functioning of catalytic converters

$$2H_2O_2 \xrightarrow{MnO_2} 2H_2O + O_2\uparrow \quad \text{(a)}$$

$$2CO + 2NO \xrightarrow{Pt/Rh} 2CO_2\uparrow + N_2\uparrow \quad \text{(b)}$$

2.2.2 Basic Principles

All chemical reactions involve activation energy (E_a) as shown in **Figure 2.3 a**, which is the energy barrier to be overcome before a reaction can be initiated. It could determine the spontaneity of reactions under specific physical environments. Although the mechanisms are complex and vary from each other, all forms of catalyses bring about the same fact that the activation energy is reduced compared to the conventional reactions, thus the rate of reaction could be improved under the same conditions.[40] However, regardless of the reaction pathway, final products remain the same, and the total change in Gibbs free energy (ΔG) of the reaction is equivalent via all available reactions pathways. For most of the energy storage and energy conversion solutions, catalysis is one of the most important parts, as the entire process would be either made possible or accelerated due to the overcoming of E_a.

Many chemical reactions could be divided into a few steps; in catalysed reactions, the catalyst often functions in the rate-determining (slowest) step. The participation is mainly defined by the activity of the catalyst, as well as total effective active sites in contact with the reactants. The general mechanism is illustrated in **Equation 2.6**, where catalyst C attaches to or reacts with the reactants X and Y at the transition states (**Figure 2.3 b**), and produces intermediate products (XC, XYC and CZ), before the reaction ends with separation of the catalyst and the final product Z. The catalyst usually does not appear in the overall reaction equation. A classical representation is the TiO_2-catalysed water production,[41] in which hydrogen and oxygen atoms react to form intermediates (OH-O, OH-OH and OH-OH_2) before the final product $(H_2O)_2$ dimer molecules are obtained.

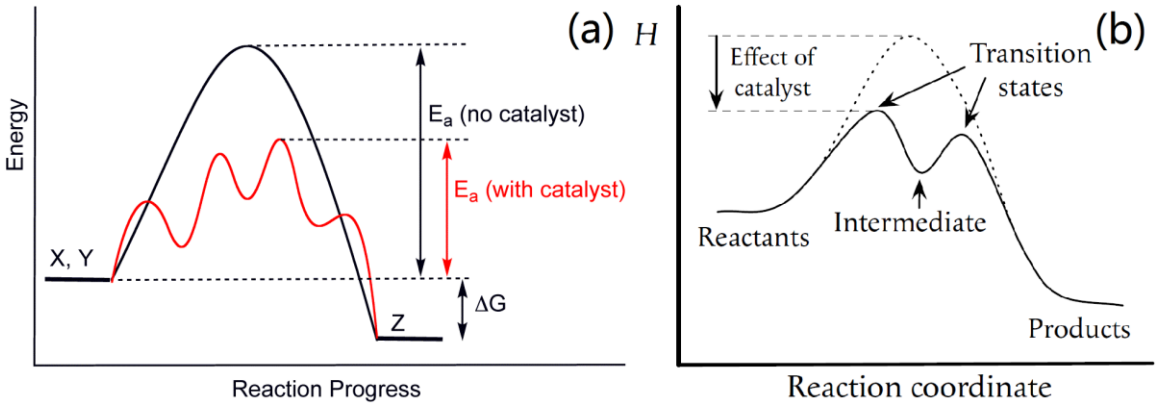

Figure 2.3 Comparison between conventional and catalysed reactions, showing: (a) the activation energy and Gibbs free energy of the reaction; and (b) the transition states and intermediate products.[40]

Equation 2.6 General mechanism of a catalysed reaction

$$X + C \rightarrow XC \qquad (1)$$

$$XC + Y \rightarrow XYC \rightarrow CZ \qquad (2)$$

$$CZ \rightarrow C + Z \qquad (3)$$

$$X + Y \rightarrow Z \qquad \text{(Overall)}$$

Catalysts do not get consumed as they are regenerated in the reactions. However, their activity might vary as the environment changes,[42] for example, enzymes could be denatured at high temperature; the active sites could be covered by side products causing

poisoning of catalysts; or the activity can be enhanced in the presence of a suitable promoter. Therefore, besides optimising the working environment, the enhancement of the catalytic performance may also come from enlarging specific surface area, so that more active sites could be formed within the same amount of catalysts used.

2.3 Types of Catalysts

Catalysts can be classified in many ways, but they are generally divided by their homogeneity. If the catalyst and the reactants are in the same phase, it is regarded as a homogeneous catalyst; otherwise it is considered to be heterogeneous. However, the nomenclatures of the known catalysts are often given either from their functions or the nature of the catalysts. According to their working principles or functionalities, catalysts may be categorised into different types. The following sub-sections will introduce some of the typical catalysts in more details.

Heterogeneous catalysts are usually solid materials like metals or metal oxides, while the reactants could be either liquids or a mixture of gases.[43] They may have different forms of active sites, such as exposed areas of bulk metals, surface areas of NPs or even specific crystallographic orientations of crystals. Therefore, reducing the size of the catalysts could help to increase their specific surface areas, and thus improving their catalytic properties through boosting the rate of reactions. Compared to bulk counterparts, nanomaterials are less likely to be free standing, so most of these catalysts are thus evenly spread and distributed on a substrate. This could help prevent aggregation of NPs during reactions, or may help create ordered arrangement of features, which largely increases the effective area for catalysing the reactions. As such, the application of the catalysts could be effective or bear a lower cost. Substrate materials are usually porous which have large surface areas, for example, alumina, zeolites, nickel foam or various kinds of activated carbon; specialised supporting materials include SiO_2, TiO_2, $CaCO_3$, $BaSO_4$, and so on.

On the other hand, homogeneous catalysts are often dissolved together with the reactants to become a solution. The working principle of homogeneous catalysts is very similar to

that of heterogeneous catalysts. Classic examples include the esterification reactions between carboxylic acids and alcohols,[44] which could be affected by the concentrations of H^+ in the solution; as well as formation of alkyl aldehydes by adding carbon monoxide to aliphatic alkenes,[45] which can then be transformed into different forms of organic products like alcohols, carboxylic acids or polyols.

2.3.1 Electrocatalysts

Typical electrochemical reactions usually involve a set of connected electrodes and an electrolyte; however, many of them are not really feasible under standard conditions or take place very slowly. Therefore, electrocatalysts become an important participant in these electrochemical reactions; at the working electrode, they assist in transferring of electrons between the electrode and reactants, and provide alternative reaction pathways by facilitating intermediate chemical transformations described by half-equations.[46] While the rate of reactions is increased, they stay unconsumed at the end of the process.

Electrocatalysts can be heterogeneous or homogeneous. Heterogeneous electrocatalysts could either simply be the surface of metallic electrodes (such as Pt), or exist as nanoparticles working at the surfaces of electrodes (such as transition metal oxides). Coordination complexes and electrically conducting enzymes are typical examples of homogeneous electrocatalysts.

A significant application of electrocatalysts is in fuel cell engineering. In fuel cells, chemical energy stored in the fuels is released through oxidation of the fuels, which is then converted into electrical energy and heat. With the participation of electrocatalysts, H^+ ions and electrons are generated at the anode in the oxidation reactions, and they flow towards the cathode either through the electrolyte or external circuit (**Figure 2.4**).[46, 47] Fuel cells are important substitutes for fossil fuels in fulfilling various demands for energy, such as power generation, fuel cell electric vehicles and portable power systems.

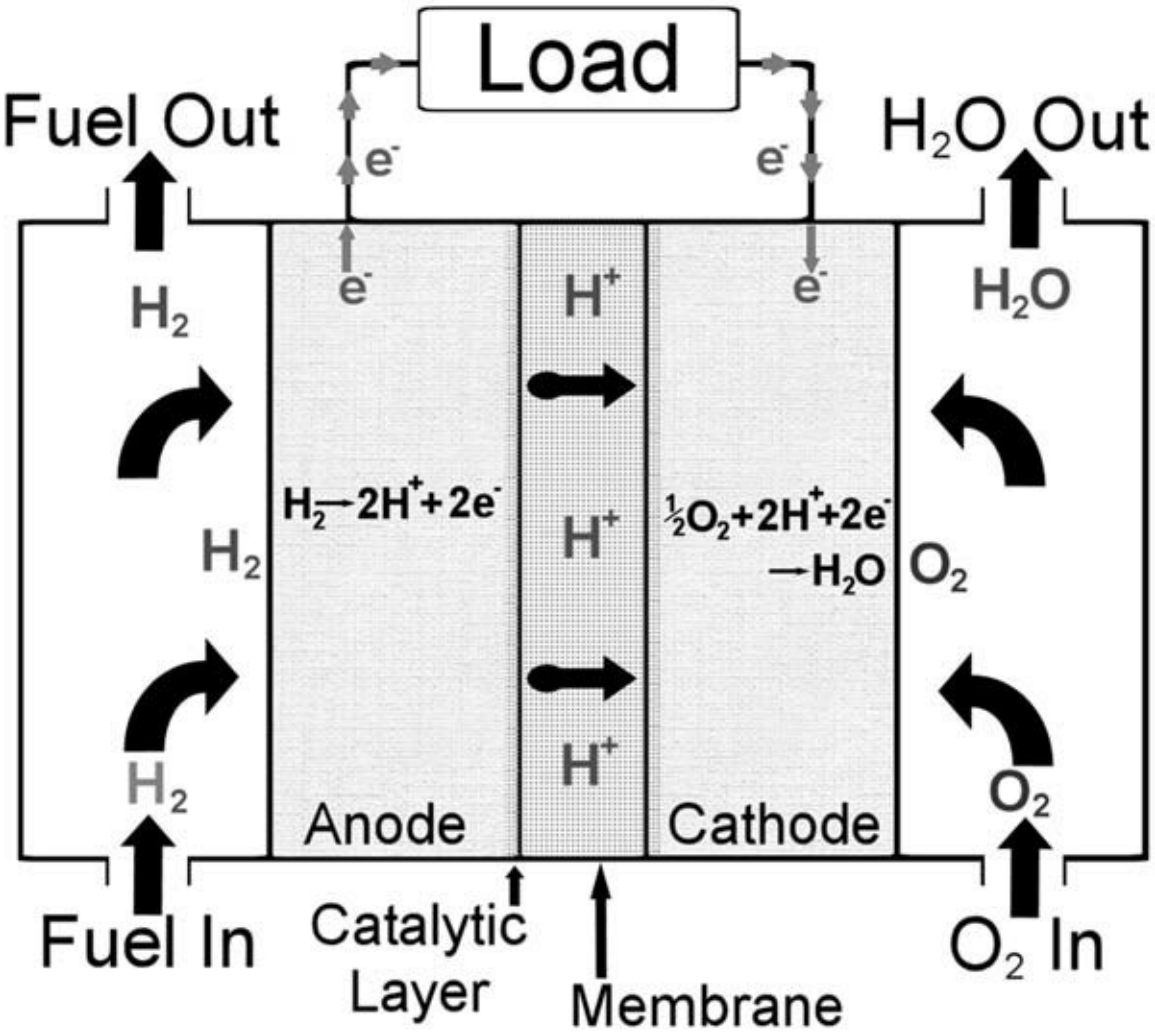

Figure 2.4 The setup of a proton exchange membrane fuel cell[48]

2.3.2 Photocatalysts

There are many reactions which have energy barriers. Usually the energy barriers have to be overcome before reactions could be initiated. To achieve this, the system must obtain energy from external sources, such as heat and light. Photocatalysts, as the name suggests, could be excited upon capturing photons from incident light. The excited photocatalysts would then interact with the reactants and undergo chemical reactions, before they return to the ground state. However, as the reactants are different materials from the photocatalysts, direct illumination on the reactants usually cannot start the reactions as the energy barrier could be at even higher level. Classic applications of photocatalysts

include water splitting (**Figure 2.5**),[49] water treatment,[50] decomposition of polyaromatic hydrocarbons, self-cleaning glasses,[51, 52] sterilisation of instruments[53] and dye-sensitised solar cells (DSSCs).

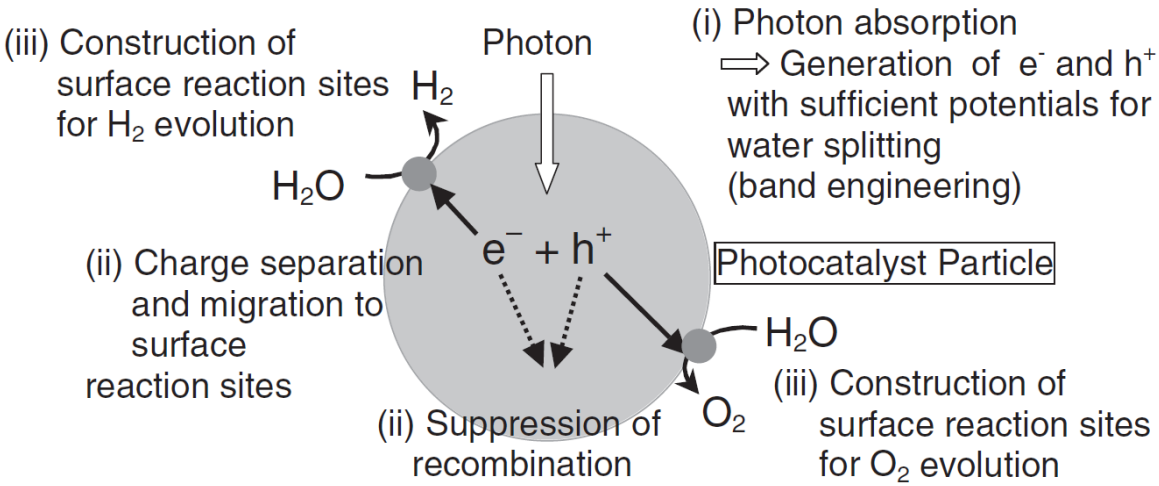

Figure 2.5 Processes in photocatalytic reactions for water splitting[49]

2.3.3 Enzymes and Biocatalysts

Many metabolic and catabolic processes in lives require the involvement of enzymes, which are made of proteins and they are the most common type of biocatalysts. They can be classified by homogeneity as well; homogenous enzymes are usually soluble, while some membrane-bound ones are considered heterogeneous. Their activities include large amount of formation and breakage of bonds in biomolecules, and are often decided by the biological environment, such as pH, working temperature, reactants and concentration.[54]

There are wide applications of biocatalysis. In human bodies, enzymes are important biocatalysts that keep our lives active; synthetic enzymes are also widely used in various industries for fabrications, including biofuels,[55] food processing,[56, 57] dairy and brewing industries,[58, 59] and even detergents[60]. Some non-protein-based biomolecules may show important performances in biocatalysis, for example, ribozymes and synthetic deoxyribozymes.[54]

2.4 Electrocatalyst Materials for DEFC

2.4.1 Basic Working Principles of DEFC

DEFCs are still under the research and development, and several prototypes have been designed based on the possible electrochemical reactions. The systems could be classified based on the type of electrolyte used, which in turn determines the flow of ionic species during the electrochemical reactions. **Figure 2.6** schematically illustrates the basic working principles of various types of DEFCs by listing the electrochemical reactions at each electrode as well as the flow of ions.[61]

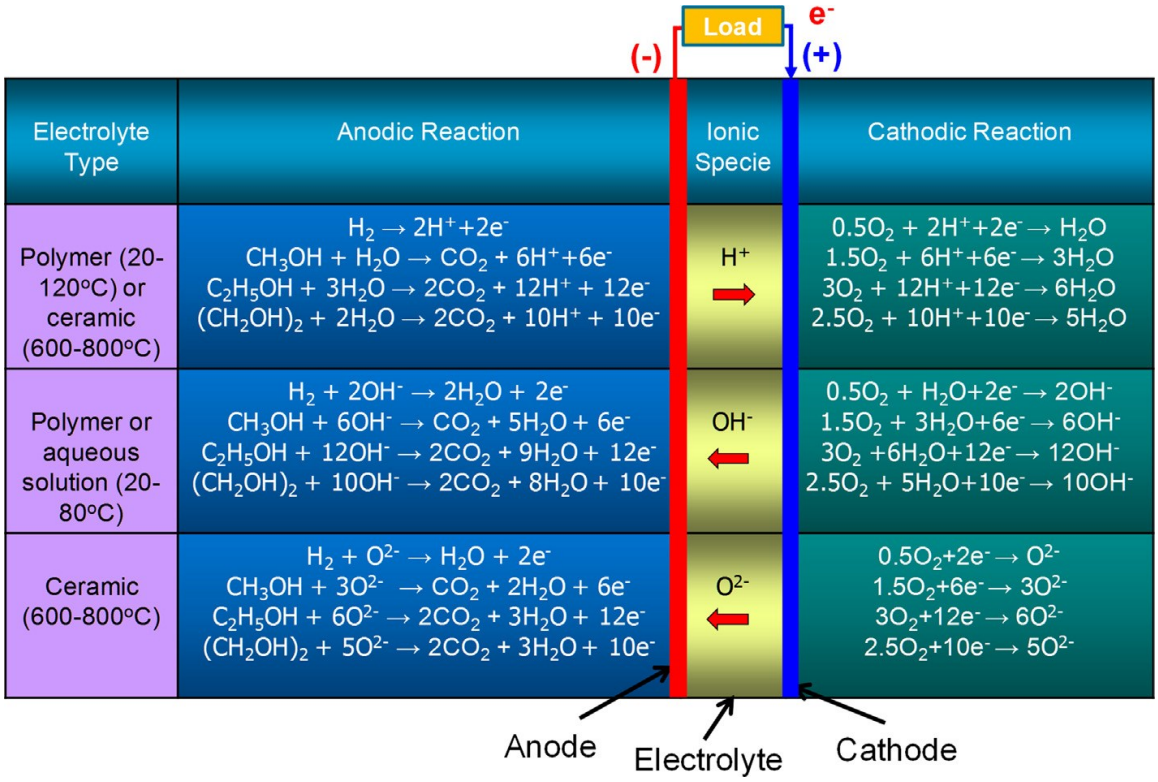

Figure 2.6 Schematic illustration of the electrochemical reactions involved in various types of DAFCs[61]

In the first row, the flow of H^+ indicates an acidic environment, and the system is thus named proton-conducting polymer electrolyte membrane (PEM) DEFC. NAFION is the most commonly used polymer electrolyte and is commercially available.[61] When the

electrolyte is an aqueous solution with the flow of OH^- (the second row), the system is an alkaline DEFC. Both PEM-DEFC and alkaline DEFC are working in a relatively low temperature range (20-120 °C) due to the nature of the system. When a higher working temperature is required, the electrolyte has to be ceramic (usually ceria (CeO2) or YSZ) and the ionic species is usually O^{2-} (the third row). Regardless of the type of DEFCs, the full oxidation of 1 mol ethanol to carbon dioxide and water involves the transfer of 12 electrons in the process. In comparison to other alcohols in DAFC systems, DEFCs could render a higher working load based on the full oxidation process.

The electrochemical oxidation of ethanol is hereafter named ethanol oxidation reaction (EOR). The EOR occurs only at the anode and could proceed in both acidic and alkaline environment. However, the EOR is not a direct reaction; they are usually proceeding in a stepwise manner with the existence of several intermediate products, or they might produce different end products according to the reaction conditions. **Equation 2.7** and **Equation 2.8** list the possible electrochemical reactions in a DEFC system with acidic and alkaline media respectively.[61-63]

Equation 2.7 Electrochemical reactions in an acidic PEM-DEFC[61-63]

C2 pathway:

$$CH_3CH_2OH \rightarrow CH_3CHO + 2H^+ + 2e^- \quad \text{(a)}$$

$$CH_3CH_2OH + H_2O \rightarrow CH_3COOH + 4H^+ + 4e^- \quad \text{(b)}$$

C1 pathway:

$$CH_3CH_2OH + 3H_2O \rightarrow 2CO_2 + 12H^+ + 12e^- \quad \text{(a)}$$

$$CH_3CH_2OH + 5H_2O \rightarrow 2HCO_3^- + 14H^+ + 12e^- \quad \text{(b)}$$

$$CH_3CH_2OH + 5H_2O \rightarrow 2CO_3^{2-} + 16H^+ + 12e^- \quad \text{(c)}$$

Assuming full oxidation via C1 pathway:

$$CH_3CH_2OH + 3H_2O \rightarrow 2CO_2 + 12H^+ + 12e^- \quad \text{(anode)}$$

$$3O_2 + 12H^+ + 12e^- \rightarrow 6H_2O \quad \text{(cathode)}$$

$$CH_3CH_2OH + 3O_2 \rightarrow 2CO_2 + 3H_2O \quad \text{(cell)}$$

Equation 2.8 Electrochemical reactions in an alkaline DEFC[61-63]

C2 pathway:

$$CH_3CH_2OH + 2OH^- \rightarrow CH_3CHO + 2H_2O + 2e^- \quad \text{(a)}$$

$$CH_3CHO + 3OH^- \rightarrow CH_3COO^- + 2H_2O + 2e^- \quad \text{(b)}$$

C1 pathway:

$$CH_3CH_2OH + xOH^- \rightarrow CH_{x,ads} + CO_{ads} + xe^- \rightarrow 2CO_{ads} \quad \text{(c)}$$

$$CO_{ads} + 2OH^- \rightarrow CO_2 + H_2O + 2e^- \quad \text{(d)}$$

Assuming full oxidation via C1 pathway:

$$CH_3CH_2OH + 12OH^- \rightarrow 2CO_2 + 9H_2O + 12e^- \quad \text{(anode)}$$

$$3O_2 + 6H_2O + 12e^- \rightarrow 12OH^- \quad \text{(cathode)}$$

$$CH_3CH_2OH + 3O_2 \rightarrow 2CO_2 + 3H_2O \quad \text{(cell)}$$

The reaction pathways shown in **Equation 2.7** and **Equation 2.8** are a good example of the stepwise reaction profile as introduced in **Section 2.2**. The reactions can never proceed to a full oxidation in a single step due to the huge amount of E_a. From the reaction mechanisms, it can be found that oxygen reduction reaction (ORR) occurs at the cathode while EOR occurs at the anode with two distinct possible pathways; both processes create an electrode/catalyst-electrolyte double layer that helps improve the charge transfer during the catalysis. Therefore, suitable catalyst materials must be used at both the anode and cathode.

2.4.2 Noble Metals as Efficient Electrocatalysts

Noble metals, as the name suggests, differentiate themselves from other metals by their extraordinary stability against corrosion and oxidation in different kinds of environment.[64] The various compounds they form with organic and inorganic molecules tend to be unstable and can be easily reverted back to elementary states, thus making them noble. In the belief of most chemists, noble metals occupy groups 8-11 and periods 5-6 in the Periodic Table of the Elements (as shown in **Figure 2.7**),[65] or namely, the platinum-group metals (Ru, Rh, Pd, Os, Ir, Pt), Au and Ag.[64, 65]

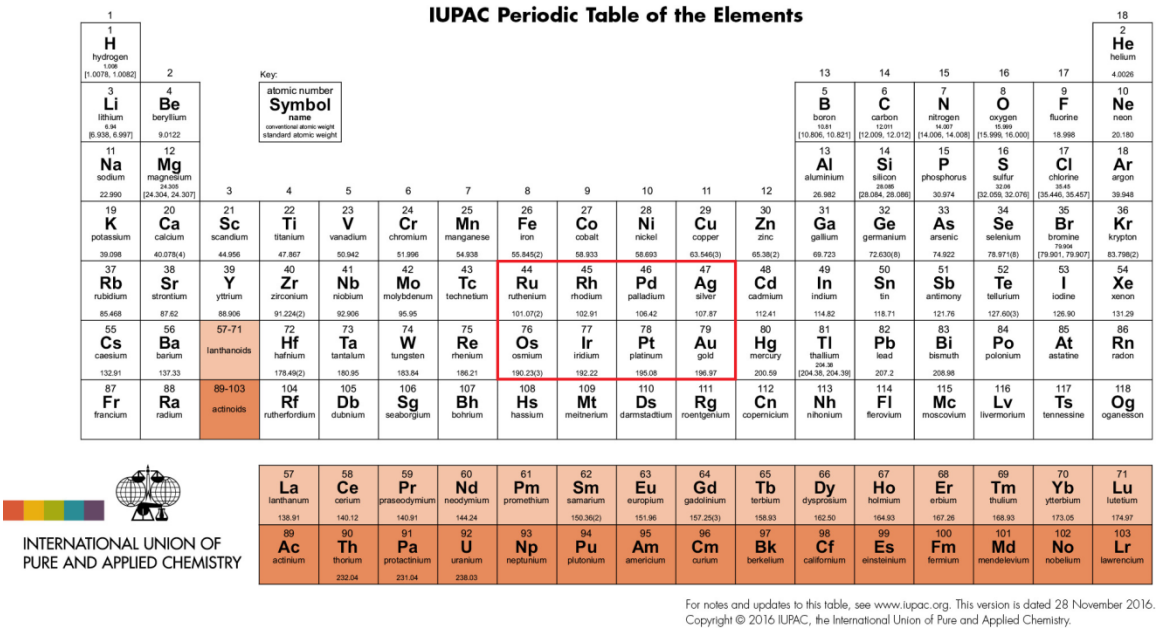

Figure 2.7 The positions of noble metals in the Periodic Table of the Elements[65]

Figure 2.8 shows the indicative prices of noble metals in January to July 2020.[66] Noble metals are not only valuable in economic and monetary means, but also very useful in many scientific and engineering fields, such as like metallurgy, mineralogy, microbiology and even clinical medicine.[64] In materials science and engineering, noble metals are perfect candidates as electrocatalysts, which could facilitate ORR,[67] hydrogen storage,[68] metal-assisted chemical etching[69] and fuel cells (including DEFC)[36, 38, 61, 70-73] and so on.

The catalytic activities of noble metals arise from their electronic configurations, in which they all have hybridised bands in the d-orbital electrons. They are currently the state-of-the-art catalysts in many reactions including the abovementioned ones. For example, Ru is commonly used for H2 production,[74] water splitting[75] and hydrogenation chemical catalyses;[76] Rh and Pd are excellent catalyst materials for chemical catalyses and their classic application is the catalytic converter for exhaust gases of vehicles;[77] Os is reported for dedicated applications in organometallic chemical catalyses[78-80] and Ir is reported to specialise in OER[81] and hydrogenation/dehydrogenation chemical catalyses.[82]

In terms of DEFC, many noble metals and their alloys could act as both the anode and cathode catalysts, and Pt-based materials have the overall best catalytic performance. In

the context of this project, the main concern is the anode catalyst material for EOR and the state-of-the-art electrocatalyst is reported as PtRuSn alloy NPs. Although Pt and Ru are currently cheaper than Au (**Figure 2.8**), they are however much more expensive from the historical perspective. Furthermore, the synthesis process and essential chemicals required are costly as well, so there is a need to look for catalyst materials with high performance to cost ratio. Amongst the noble metals, Au has relatively high abundance in the Earth's crust, high catalytic performance and moderate cost as compared to the rest, thus it becomes a preferred choice by many researchers.

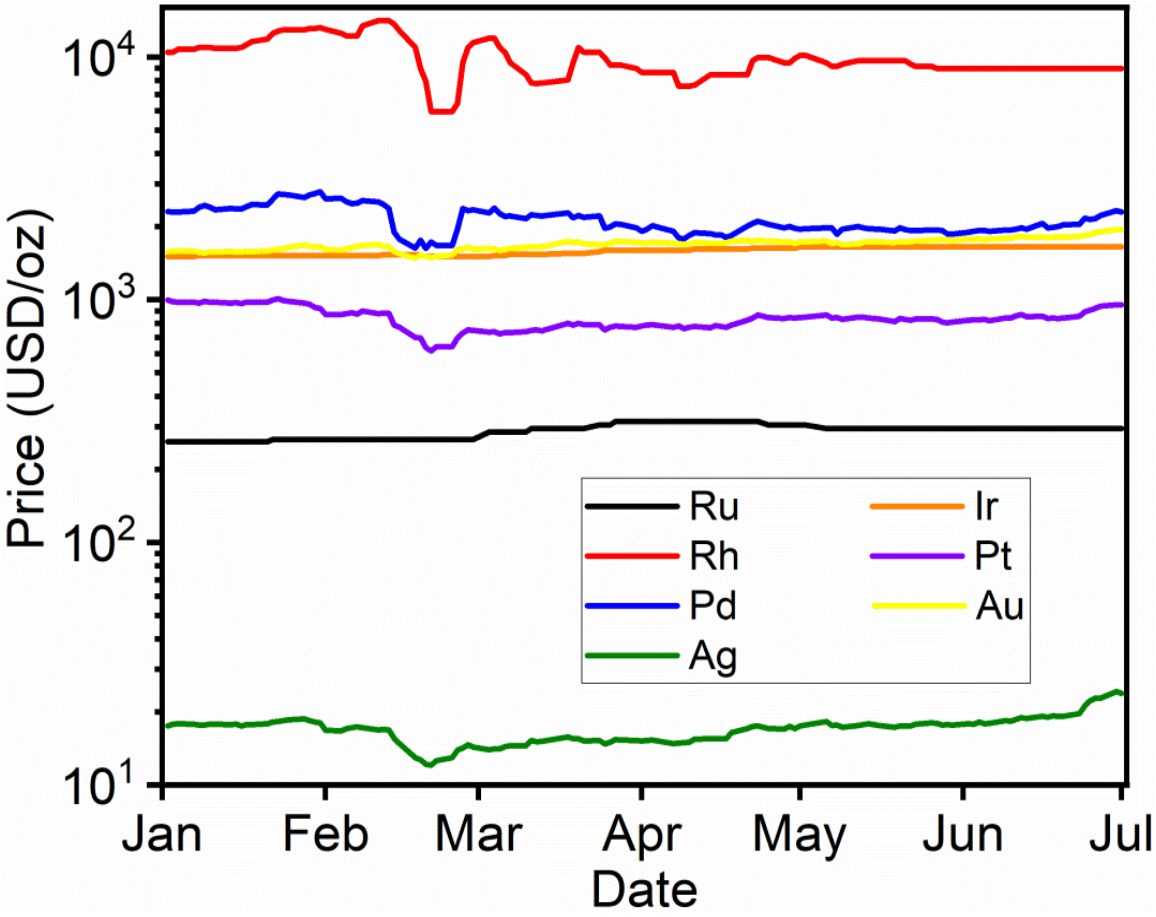

Figure 2.8 The indicative prices of noble metals in January to July 2020[66]

2.4.3 Cost-Effective Electrocatalysts

Apart from the superb catalytic performance of noble metals and their alloys, the high cost of the materials hinders their large-scale applications. Therefore, plenty of researches have been conducted to look for other cost effective electrocatalyst materials. Unfortunately, most literatures have reported that electrocatalysts without noble metals could not act as efficiently as the noble metals, because the electro-oxidation process will become two- or four-electron reactions and terminate at the intermediate stage (**Equation 2.7 a-b** and **Equation 2.8 a-b**).[70] Therefore, cost-effective electrocatalysts are only reported to catalyse ORR at the cathode.

The reported cost-effective catalysts for ORR mainly include transition metals and their compounds. Bezerra *et. al.* reviewed on the ORR catalytic activities of Fe-N/C and Co-N/C;[83] the literature listed the parameters that might affect the catalytic activities and suggested a few ways to make improvements. Mohana Reddy *et. al.* reported a Co-PPy-MWCNT catalyst with high catalytic activity and cell voltage stability.[84] Garcia *et. al.* found that $NiMnO_x$ catalyst supported on carbon have stable activity towards ORR with high tolerance of ethanol. It is emphasised that due to the reaction kinetics of ORR, an underlying factor is the adsorption of O_2 molecules onto the surface of cathode/catalyst. With multiple possible oxidation states and excellent coordination nature, transition metals and their compounds could exhibit outstanding ORR catalytic performance based on the mechanism. On the other hand, carbon-based materials (especially graphene) can act not only as catalyst support materials,[85, 86] but also as catalysts.[86-88] They have large specific surface area, excellent electrical and thermal properties and good durability;[88] these unique factors make them ideal candidates as catalyst materials.

2.4.4 Electrocatalytic Activities of Au

Being a noble metal, Au has been widely studied for its high electrocatalytic activities,[89-91] either on its own or together with one or more oxide materials.[92, 93] In gas-phase catalysis, Au has very well performance in carbon monoxide (CO) oxidation. One of the

key factors is pH; CO has weak adsorption energy on the surface of Au in an acid environment, thus its oxidation has to take place at higher over potential.[94] But in alkaline medium, it is found that the electrocatalysis of Au on CO could even exceed that of Pt.[95] Rodriguez *et. al.* reported that even if a solution is absent of CO, the CO molecules could still be chemically adsorbed on the surface of Au along (1 1 1) and (1 0 0) orientations (**Figure 2.9**),[96] which helps facilitate the oxidation of CO. Density function theory calculations predicted that adsorbed CO enhances the bonding of OH groups from alkaline medium, thus causing oxidation of CO to CO_2 by reacting with each other.

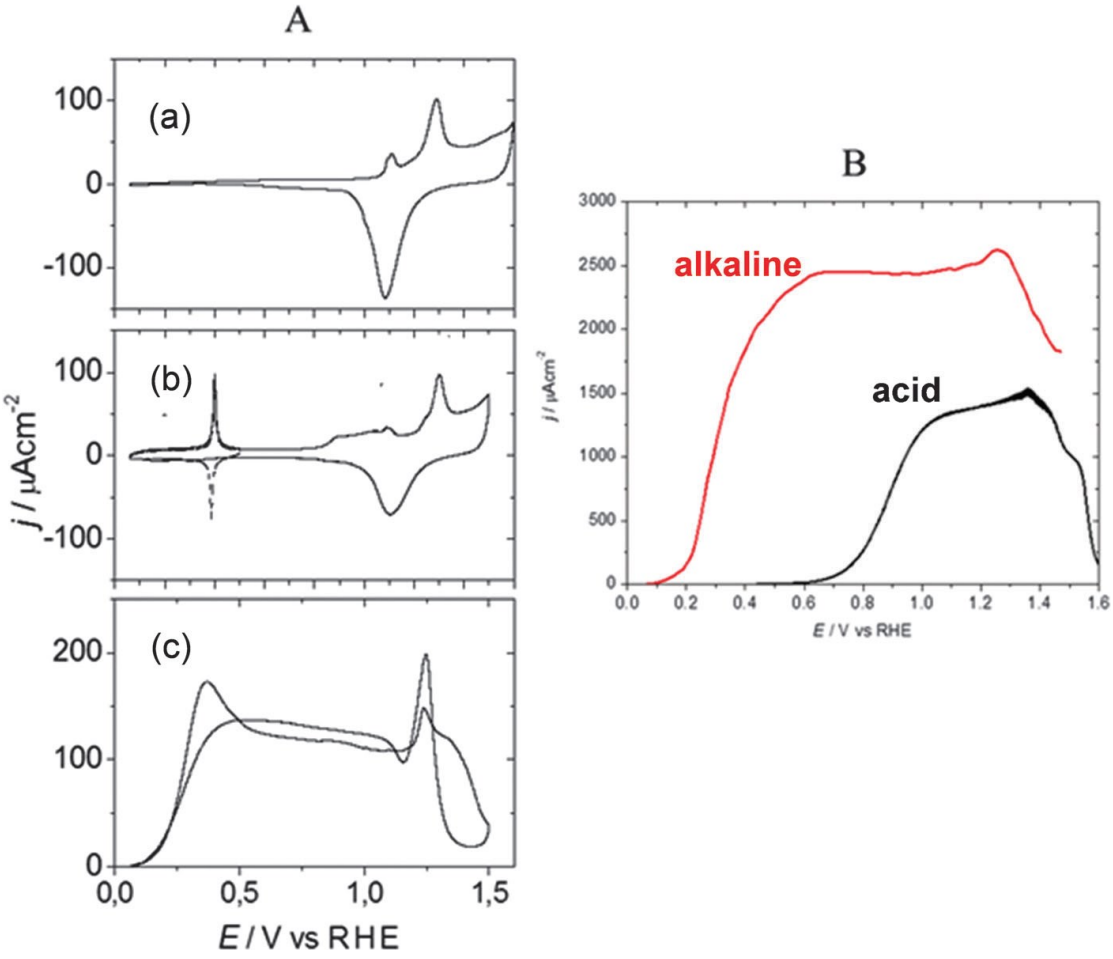

Figure 2.9 (A) Voltammetric profiles at 50 mV/s of the Au (111) electrode in 0.1 M NaOH (a) in absence of CO, (b) in presence of chemisorbed CO and (c) in presence of CO in solution.[97] (B) Hanging-meniscus rotating disk electrodes voltammograms of Au (1 1 1) in CO-saturated 0.1 M $HClO_4$ (black) and in CO-saturated 0.1 M NaOH (red). Scan rate: 50 mV/s; rotation rate: 1100 rpm.[96]

In liquid-phase catalysis, electrochemical oxidation of alcohols, sugars and organic acids has been found excellent on Au. **Figure 2.10 a** illustrates that Au could catalyse EOR well in alkaline medium and the peak occurs at the pH of 12. Alcohols deprotonates in alkaline medium according to the following mechanism: $H_\beta R\text{-}OH_\alpha \rightarrow H_\beta RO^- + H_\alpha^+$,[98] this means the reactivity of alcohol is inversely related to its pK_a value depending on the nature of R group; as a result of charge transfer on the electrode, a lower pK_a value would generally represent higher reactivity of alcohol on the surface of Au. Poly-oriented Au has three basal crystallographic planes: (1 1 1), (1 0 0) and (1 1 0), amongst which (1 1 0) is the easiest to be oxidised and (1 1 1) is the least; that explains the much higher current density from Au (1 1 1) as compared to the other two in **Figure 2.10 b**.

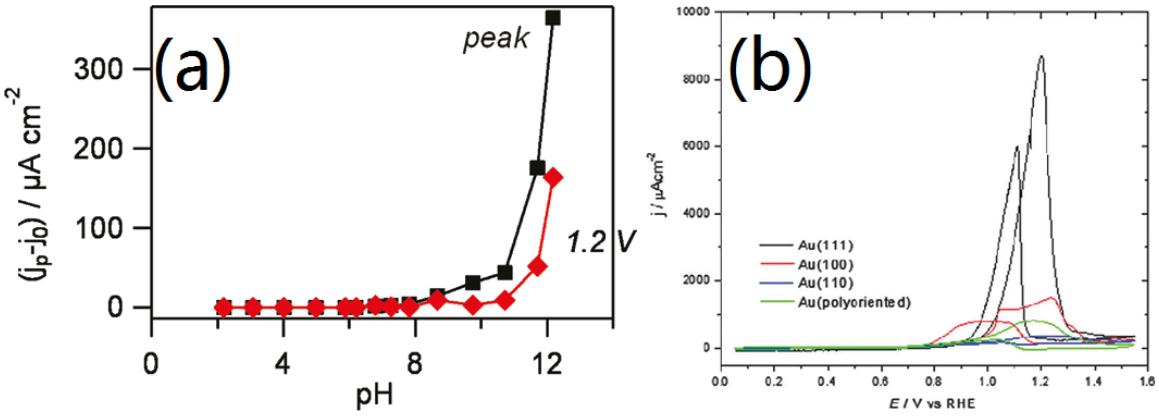

Figure 2.10 (a) Measured current j_p for 0.5 M ethanol oxidation on a gold electrode at peak potential (black curve) or at 1.2 V vs. RHE (red curve) minus the background current j_0 as a function of the electrolyte pH using 0.1 M phosphate buffers.[98] (b) Voltammetric profile of the Au (1 1 1), Au (1 0 0), Au (1 1 0) and Au (poly-oriented) electrodes in 0.1 M NaOH + 0.5 M ethanol.[96]

Tremiliosi-Filho *et. al.* reported the analyses of the reaction products of EOR on Au electrode and proposed a possible mechanism (**Figure 2.11**).[99] The EOR was carried out in both alkaline and acidic media. It suggests that hydroxyl species has to be formed on the surface of Au electrode before ethanol could be adsorbed onto Au for participation in the reaction (step 1). The subsequent reactions could be split into two pathways – one is

direct oxidation to acetic acid/acetate (steps 2-5), and the other is an indirect oxidation with the partial oxidation to aldehyde species as intermediate products (steps 1'-4').

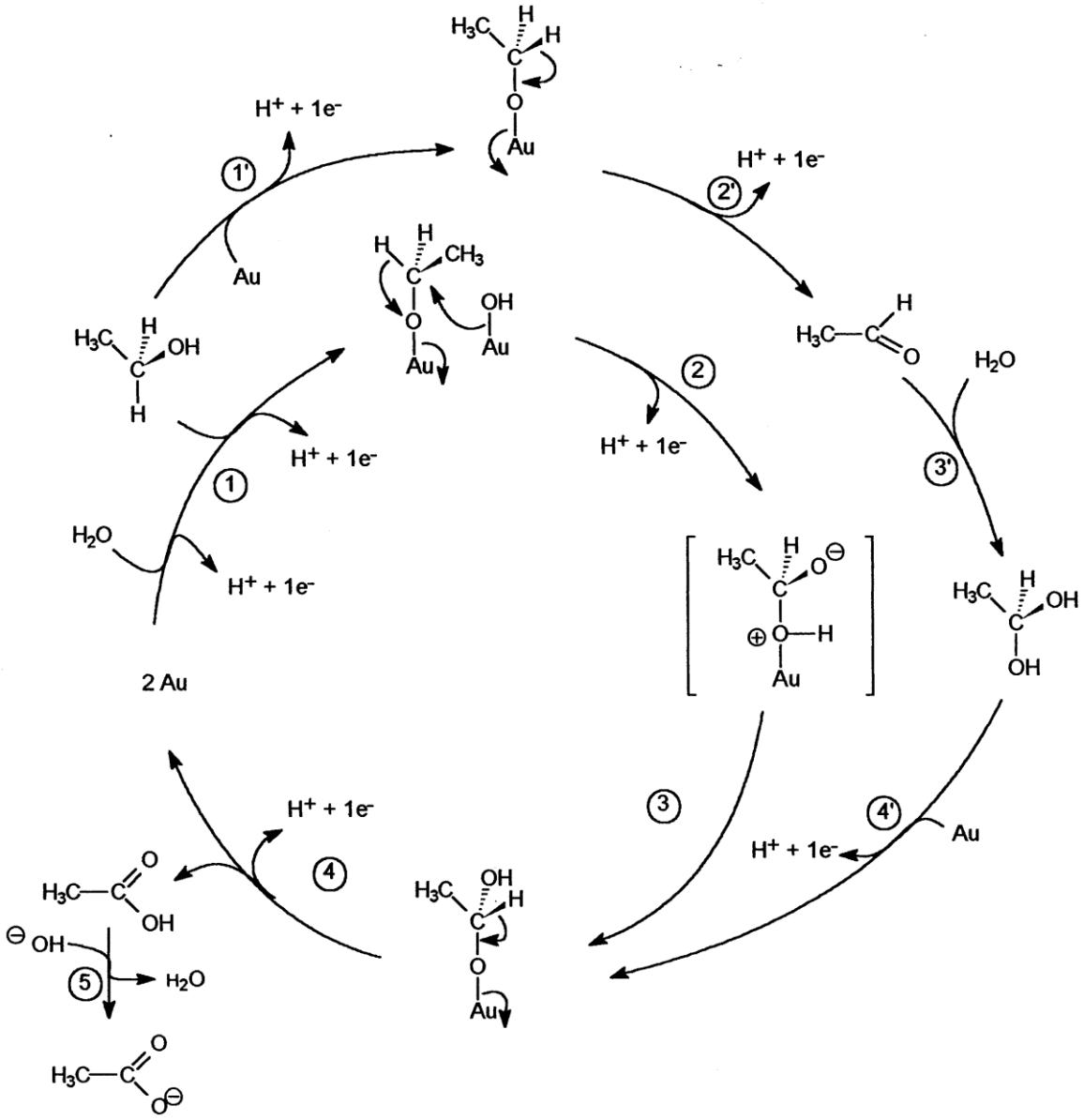

Figure 2.11 Possible reaction mechanism of EOR on Au electrode in both alkaline and acidic media[99]

In the direct oxidation pathway, the activated hydroxyl species acts as a nucleophile and attacks the adsorbed species to form a few possible intermediate products (steps 2-3). At the oxidation potential for EOR, the Au electrode is electrophilic and promotes the loss of

a proton (step 4) resulting to form a desorbed acetic acid molecule. For reactions in alkaline medium, the end product would be an acetate species (step 5). In the indirect oxidation pathway, the formation of ethanal is a simple dehydrogenation process of the adsorbed ethanol molecule (steps 1'-2'), which is hydrated in step 3' to form another intermediate product (1,1-ethanediol). At suitable oxidation potentials, 1,1-ethanediol could undergo further oxidation according to steps 4'-4. It is reported that the selectivity of reaction pathway is dependent on the pH of electrolyte during steps 1-1', and the rate of step 1' should be greater than that of step 1 in acid medium.

The abovementioned works were conducted using bulk Au electrode, but researches with nanostructured Au in EOR were rarely reported. Most of the Au-based electrocatalysts were synthesised with other noble metals, which are in the form of either alloys or with particular nanostructures. Ksar *et. al.* synthesised bimetallic nanostructures with the aid of surfactants, which comprise of an Au-rich core and a porous Pd shell.[100] Compared to the Pd-Au alloy NPs prepared by solution radiolysis, the core-shell structure has shown good electrocatalytic activity in EOR and higher stability than the alloy NPs. It is believed that the difference in reduction mechanisms leads to the formation of the two nanostructures. However, the disadvantage of the core-shell structure is that the size is much larger than the alloy NPs, which results in its lower electrocatalytic performance. Furthermore, the synthesis via radiolysis generated some inhomogeneity in morphology, which is given by the existence of pure Au NPs instead of the Au-Pd core-shell structure.

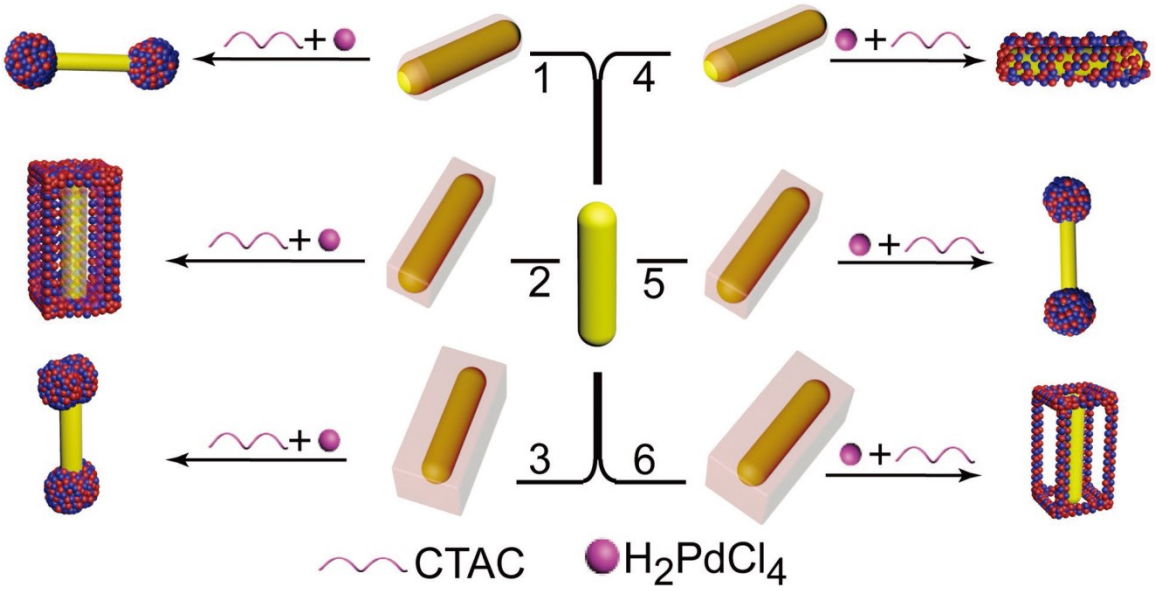

Figure 2.12 Schematic illustration of the growth mechanisms of Au/(PdAg alloy) nanocrystals with different architectures, showing the morphological evolutions under different adding sequences of H_2PdCl_4 and cetyltrimethylammonium chloride (CTAC). Routes 1-3 on the left illustrate the syntheses when CTAC was added first, while Routes 4-6 on the right are the syntheses when H_2PdCl_4 was added first.[101]

It is reported that size, shape, and architecture are some of the factors influencing the electrocatalytic performance of nanostructured noble metal catalysts. In order to study the morphology-property relationship, Fang *et. al.* performed morphology engineering on the nanostructures of Au/(PdAg alloy) catalyst.[101] Starting with Au-Ag core-shell nanocrystals, by tuning the Ag shell thickness and the sequence in addition of reactants (H_2PdCl_4 and CTAC), various morphologies including nano-dumbbells, yolk-shell nano-boxes and yolk-shell nano-frames were obtained. The growth mechanism is schematically illustrated in **Figure 2.12**. Electrochemistry testing revealed enhanced catalytic performance of the nanostructures in EOR and much better stability compared to commercial carbon-supported Pd NPs. Amongst the reported architectures, the nano-dumbbells and the yolk-shell nano-frames showed the best specific and mass activities respectively, while the nano-dumbbells had the best stability, as shown in **Figure 2.13**.

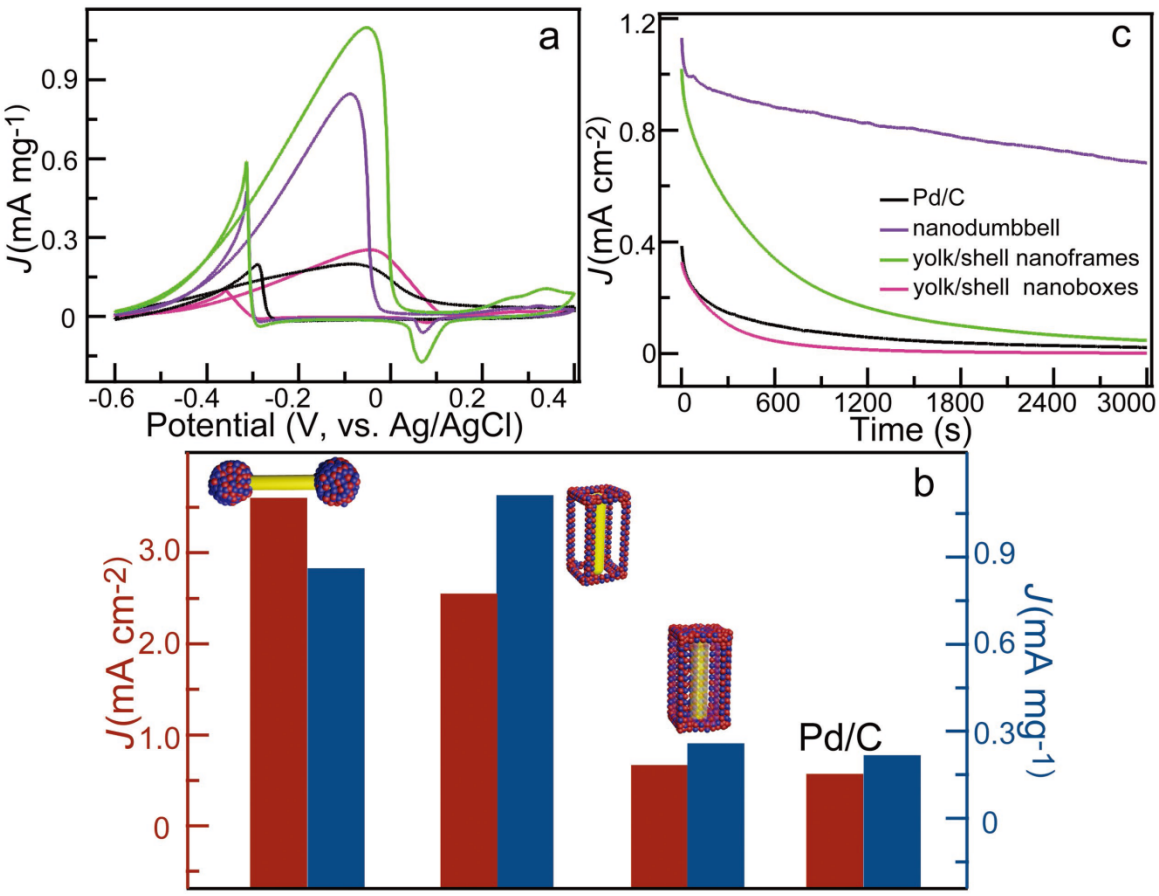

Figure 2.13 Evaluation of the Au/(PdAg alloy) nanocrystals as electrocatalysts for EOR in alkaline medium. (a) Cyclic voltammograms of the various architectures and commercial Pd/C electrocatalysts. (b) Specific and mass activities towards EOR of Au/PdAg and commercial Pd/C catalyst. c) Chronoamperometry (CA) curves for Au/PdAg and commercial Pd/C catalyst. The measurements were carried out in N_2-saturated solution of 0.3 M KOH and 0.5 M ethanol at a scanning rate of 50 mV/s.[101]

The morphology and phase engineering for nanocrystals is an effective way in improving the performance of electrocatalysts in EOR, but it is generally applied in a multi-element condition and less feasible for pure Au electrocatalyst. As another possible appearance, there is very limited research on nanostructured Au thin films. A similar work was done by Wang *et. al.*,[102] in which a polycrystalline Pt disk was subjected to electrochemical treatment and its surface was roughened to increase the effective ECSA. This brought about a stronger signal in EOR response by having a higher working electrode current density and a better stability as illustrated in **Figure 2.14**.

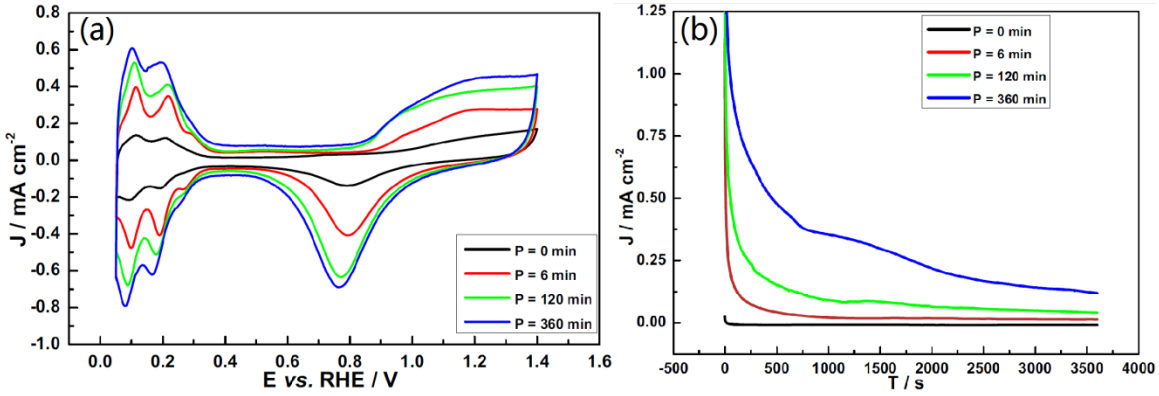

Figure 2.14 The cyclic voltammograms (a) and CA curves (b) of Pt disk electrodes after different durations of electrochemical treatment[102]

2.4.5 Current Challenges

The DEFC is still under development at the early stage. The current major challenge remains to be the EOR process – the reaction kinetics is quite sluggish and it is difficult to achieve full oxidation of ethanol with a complete 12-electron transfer; instead, the transfer of 2 or 4 electrons often takes place and leads to the incomplete oxidation of ethanol.[61, 70] The undesired early termination not only brings about Faradaic efficiency loss of the DEFC, but also may cause poisoning of the catalyst materials due to the formation of unwanted intermediate products.[61]

Another key issue is the ethanol crossover, which can be understood as the migration of ethanol molecules from the anode to the cathode through the polymer membrane. A higher ethanol crossover rate would lead to a greater amount of fuel being incompletely oxidised and thus in turn decrease the overall performance of the fuel cell. Several studies and mathematical modelling have demonstrated that ethanol concentration, operating temperature and current density are the main factors affecting this property.[61, 103] The development of anode catalyst and improvement of the catalytic performance is an urgent need to both lower the ethanol crossover rate and to lengthen the fuel cell lifetime.

2.4.6 Summary for DEFC Electrocatalyst Materials

In order to make a complete DEFC, the system must have two electrodes connected to each other. The reduction reaction occurring at the cathode is ORR and two possible reaction mechanisms were proposed by far (i.e. the associative and the dissociative mechanisms).[104] However, its process for both is generally described as adsorption → reduction → desorption as displayed in **Figure 2.15**.[104, 105] Depending on the pH value of the electrolyte, the end product may vary from H_2O in acidic environment to OH^- in alkaline environment.[106]

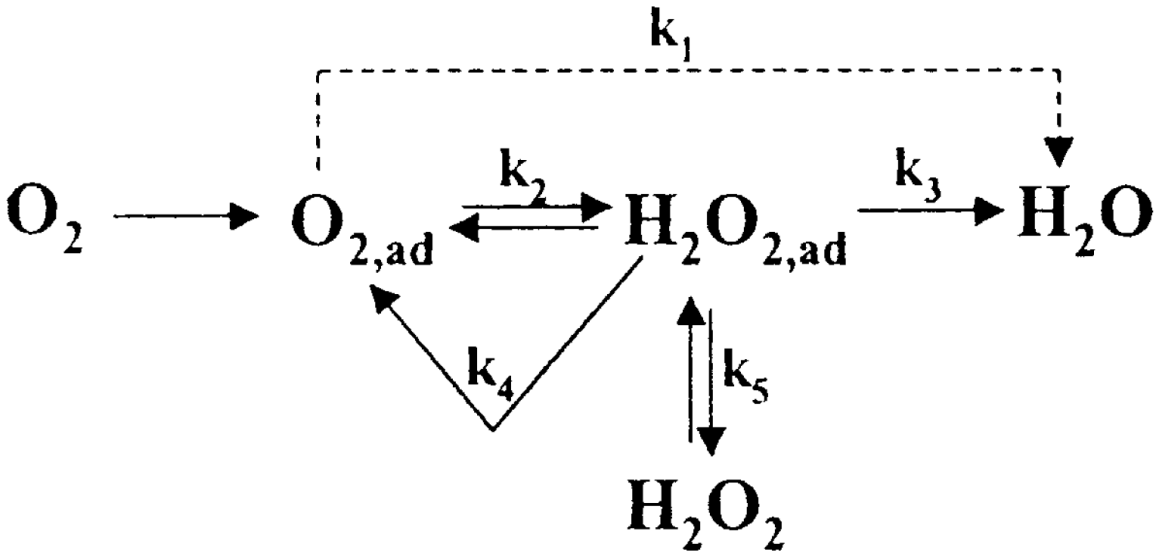

Figure 2.15 Simplified reaction pathway of ORR on metal surfaces[104, 105]

In early researches for ORR catalysts, various metals were investigated () and Pt was found to have the highest activity reported.[104, 107] There is tremendous progress in the recent development of electrocatalysts for ORR, including noble metals and their alloys, transition metals and their compounds (e. g. oxides, chacogenides, nitrides and carbides), metal-free catalysts and various single-atom catalysts.[106] The advantage of low cost for other electrocatalysts could not compensate their lower activities and the state-of-the-art electrocatalyst is still Pt-based nanomaterial.[108] For simplicity purpose, a Pt plate will be used as the cathode material in this project. The oxidation reaction occurring at the anode is EOR, and Au is chosen to be the electrocatalyst due to its performance to cost ratio.

Therefore in this project, the key focus and research interest will be the catalytic performance of Au and the strategies to bring about improvements. The main DEFC prototypes under current researches include the acidic PEM-DEFC and the alkaline DEFC with different pH values of electrolytes. Researches have shown that the former is suffering from quite a few issues, such as slow reaction kinetics that causes serious activation polarisation loss,[73, 109-111] possible corrosion problems in alloy catalysts,[109] as well as the high cost of polymer membrane materials.[109] Hence in this project, the research will be carried out based on the alkaline DEFC setup, and mainly works on the EOR reaction profiles at the anode.

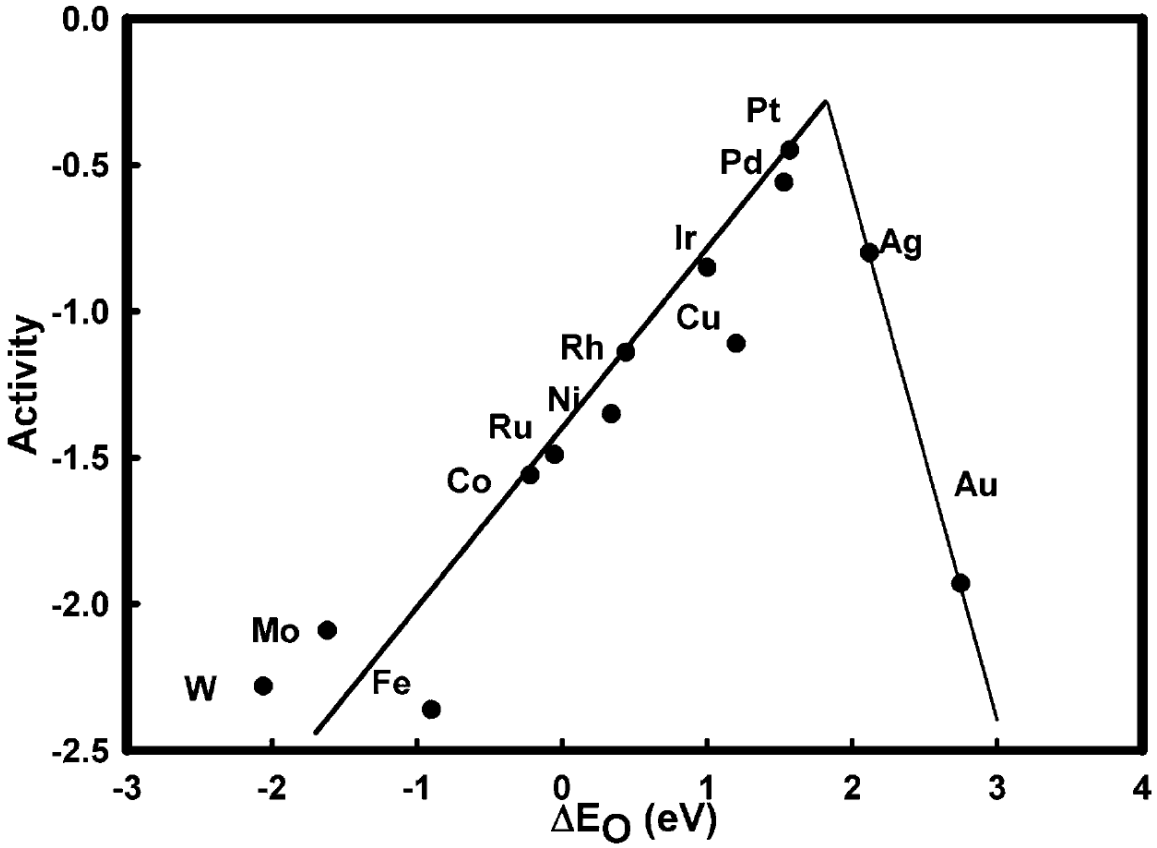

Figure 2.16 Volcano diagram showing ORR activity against O2 binding energy for metal catalysts[104, 107]

2.5 Fabrication of Au Electrocatalyst

Au electrocatalyst can be fabricated by many approaches, but the final appearance is usually classified as NPs or thin films. To carry out the fabrication, many methods have been reported, which generally include chemical synthesis of Au NPs, as well as deposition of Au thin films via electrochemical or physical approaches.

2.5.1 Synthesis of Au Nanoparticles

Compared to the bulk counterpart, nanomaterials are much smaller in size and therefore have much higher surface area to volume ratio, which in turn lead to higher catalytic performance. Due to the small size and ease of morphology control, there are plenty of researches on the fabrication of Au NPs as novel electrocatalysts, and most of them are solution-based syntheses.[112-115] Even though doping, shape control and special structures like core-shell could be achieved,[112, 116] hydrogen tetrachloroaurate ($HAuCl_4$, also known as chloroauric acid) is an essential chemical which is expensive. Therefore, this could be an efficient approach for small scale testing, but in large scale fabrication and industrial applications, deposition of thin films might be the better choice.

2.5.2 Deposition of Au Thin Films

When a layer of material is grown onto the surface of another, the grown layer is called a film and the process is known as deposition. Usually the film is considered "thin" if the deposited thickness is 100 nm or less. There are a library of well-developed techniques of deposition, which can be generally classified as vapour deposition, liquid phase and solid state deposition,[117-120] as shown in **Figure 2.17**. For the most commonly used techniques, some of their key indicators have been compared and listed in **Table 2.2**.

Solid state deposition is the most matured technique that is widely used in the industrial fabrication of ceramic coatings. Ceramic powders are usually dispersed homogeneously and made into a slurry or ink, which are then deposited by printing or casting.[121] It is a

fast and efficient method for low-cost large-scale fabrication, with a wide range of possible thicknesses from 1 μm to 3 mm.[122] However, this approach is strongly material-selective; it is excellent for ceramic powders with reasonably large zeta potentials,[123] but not really suitable for other materials.

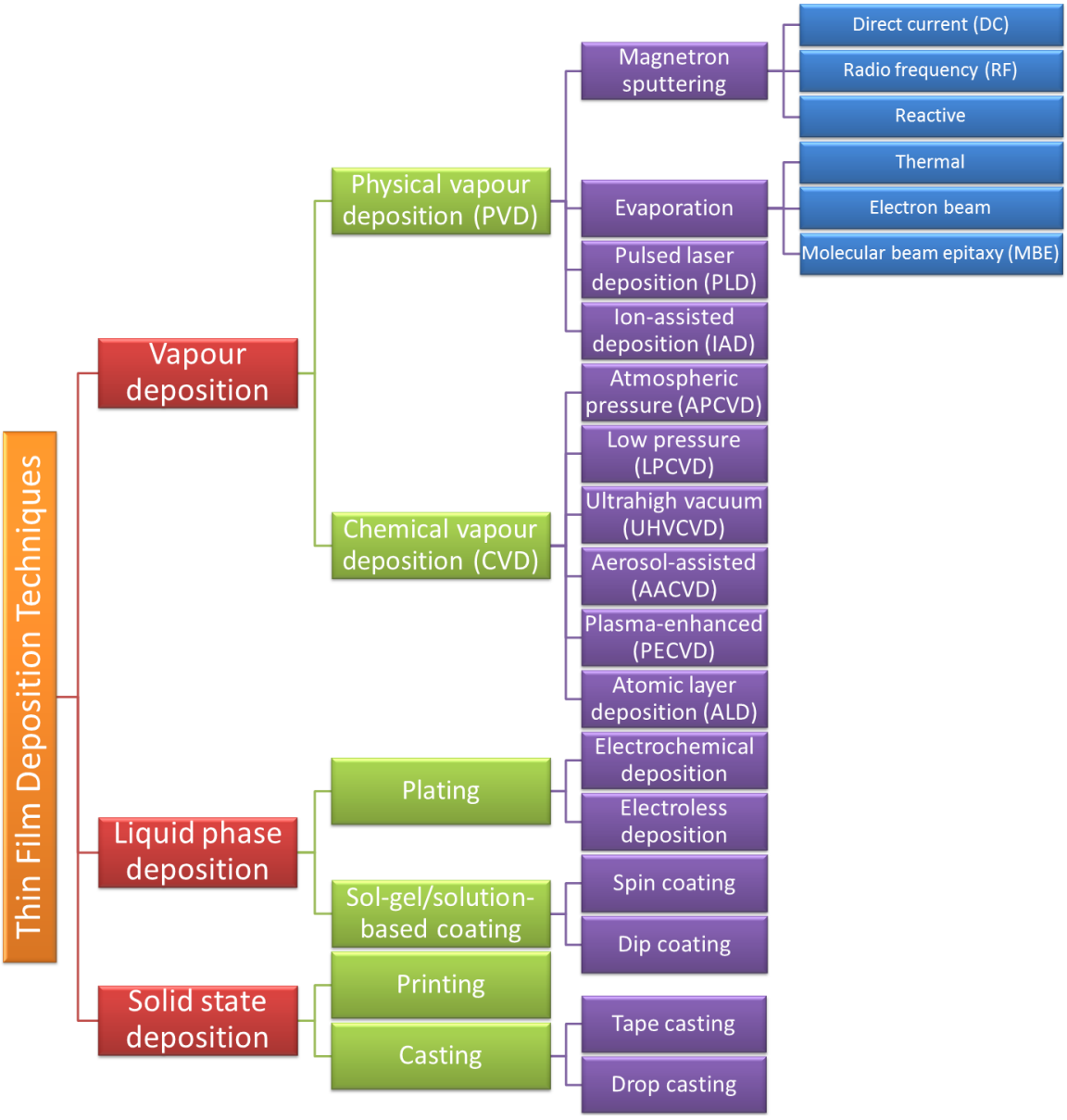

Figure 2.17 The library of well-developed thin film deposition techniques[117-120]

The liquid phase deposition mainly comprises of plating and coating approaches. The former is usually divided as electroplating and electroless plating; these electrochemical

processes require a solution (electrolyte) that contains ion species of the desired material. They are normally applied for metals/alloys[124] or metal-based semiconductors[125] by using suitable electrolytes, so it is generally limited for use with conductive substrates only.[126] However, its advantages include low requirement on physical conditions, simple one-step preparation and ability to cope with complex geometry of substrates. On the other hand, sol-gel or solution-based coating technique is usually done by synthesis of a precursor, followed by depositing it onto a substrate by spin coating or dip coating. Since the viscosity of the precursors is a key factor for successful deposition, this approach is generally used for deposition of organic thin films, or for inorganic thin films (usually compounds of metals) with the aid of heat treatment as a post-processing step.[117] The primary advantages of the sol-gel/solution-based coating technique are the high safety and ease of operation, as well as the excellent feasibility of morphology control,[127] but the thickness uniformity is a possible issue faced by both coating approaches.

The vapour deposition is divided into physical vapour deposition (PVD) and chemical vapour deposition (CVD) approaches, each of them have many sub-categories being well-developed and can be applied to suit different needs. In the PVD techniques, a target or source material is utilised which makes up the sample in whole or in part of the final composition. The ions formed by the deposition gas or laser beam provides sufficient energy, which vaporises the source material or the surface of the target, thus leads to the transfer of materials to the substrate as a thin film.[119] In comparison, the CVD technique realises a bottom-up growth of desired materials through chemical reactions of suitable precursors; during the deposition process, vapours of reactants are brought into the chamber by a carrier gas (usually an inert gas), and the chemical reactions take place on the surface of a heated substrate to form a thin film.[120] The advantages of the PVD mainly come from the controllability of the process parameters, possibility of epitaxial growth, as well as the ability to deposit almost any inorganic materials.[120] Certain organic materials could be deposited using PVD as well. The major advantages of CVD are the precise control of deposition rate,[128] possible production of single crystals, and the high selectivity of reaction pathway.[129] Nevertheless, the main disadvantages of the vapour deposition technique are the high cost of equipment setup, complexity in operation,

general requirement on high vacuum level, possible selectivity on the substrate materials in some particular approaches like magnetron sputtering, as well as potential high cost and toxicity of target/source materials and precursors.[118]

Table 2.2 Comparison of common thin film deposition techniques

	PVD	**CVD**	**Plating**	**Solution-based/sol-gel coating**	**Solid state**
Processing temperature	Room temperature or high temperature	High temperature	Room temperature	Room temperature	Room temperature
Processing pressure	Low pressure	Atmospheric pressure to low pressure	Atmospheric pressure	Atmospheric pressure	Atmospheric pressure
Cost	High cost of machine Possible high cost of target	High cost of machine Possible high cost of precursor	Low cost of machine Possible high cost of material	Low cost of machine Possible high cost of material	Low
Thickness uniformity	High	High	High	Spin coating: high to medium Dip coating: thickness has gradient	Medium
Compositional control	Excellent to medium	Excellent	Excellent to medium	Excellent to medium	Good to medium
Film purity	High	High	High	High	Medium
Film adhesion	Excellent to good	Excellent to good	Good to medium	Good to medium	Medium to poor
Substrate	Almost any substrate	Almost any substrate	Conductive substrate	Almost any substrate	Flat substrate

2.6 Enhancing Electrocatalytic Performance

The electrocatalytic performance of samples can be affected by several factors and some are quantifiable. Recent research works have shown that surface area to volume (SA/V)

ratio[124, 130-135] and surface energy content[134, 136-138] of samples, presence of active sites[139-141] and defects[134, 138, 140-142], as well as charge transfer rate[130, 132, 133, 135, 139] are some of the key parameters in electrochemical processes that influence the catalytic activities. For catalytic processes with noble metals, it is hard to alter the charge transfer rate by improving the conductivity, and difficult to induce defects in crystal structures due to single elemental composition. Therefore, the practical methods would be increasing the aspect ratio of the samples and raising the surface energy content during sample fabrication processes.

2.6.1 Increasing Aspect Ratio by Fabrication of Array Structures

To fabricate novel electrocatalysts, a smart way to enhance the efficiency of catalysis is to make array structures on electrode surfaces. Fabrication of arrays could be accomplished by various ways, including but not limited to focused ion beam (FIB) patterning,[143-148] lithography,[149-151] template-assisted method,[152-154] chemical etching [155-159] and so on. This section introduces the fundamentals of these techniques; the advantages and disadvantages will be compared as well.

2.6.1.1 FIB Patterning

Unlike scanning electron microscope (SEM) that uses a focused beam of electrons for imaging and analysis, FIB utilises a focused beam of ions, which could be functioned in imaging, analysis, patterning and special fabrications.[160] Modern FIB instruments usually integrate the liquid metal ion source (LMIS) to SEM column,[160, 161] so that site-specific requirements could be met. It should be noted that metal ions (usually Ga^{+}) have much larger mass than electrons and they are accelerated by a high voltage (usually up to 30 kV), FIB is inherently destructive to samples. As such, fabrication of nanostructural arrays becomes possible using FIB; the two patterning techniques are ion milling and FIB-induced chemical vapour deposition (CVD), as illustrated in **Figure 2.18**.

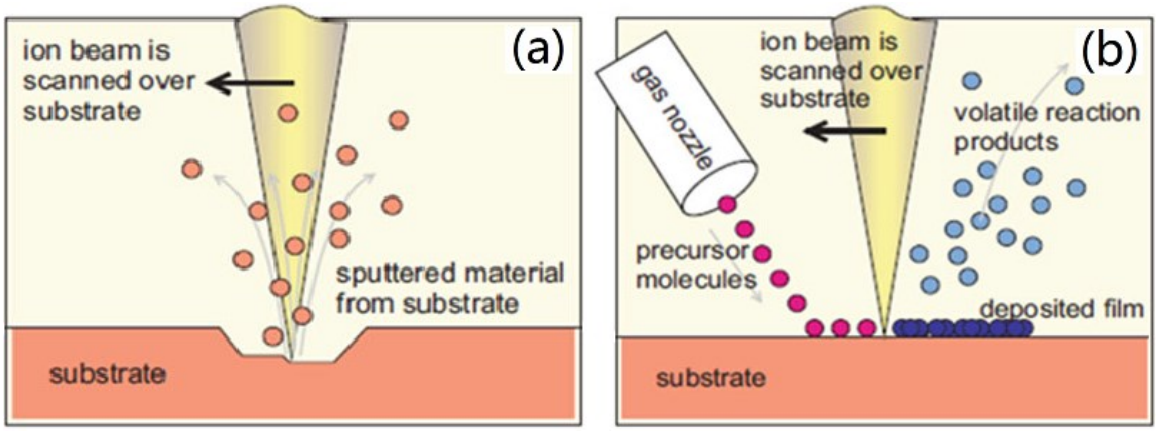

Figure 2.18 Comparison of (a) FIB milling and (b) FIB-induced CVD[161]

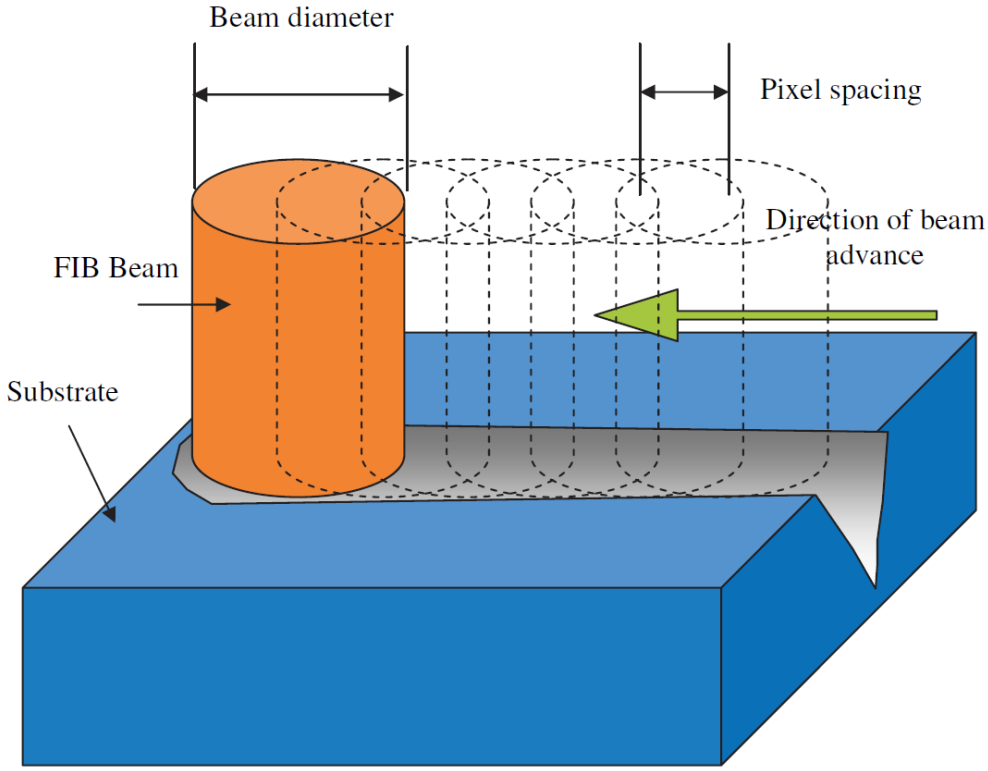

Figure 2.19 Schematic illustration of the working mechanism of FIB milling[162]

When a beam of ions is focused on the sample surface, a pre-set pattern could be introduced to guide the ion milling.[143-148] The focused beam scans along the designated paths and removes the surface particles due to ion bombardment,[161, 162] thus leaving the desired pattern at the end of operation (**Figure 2.19**). On the other hand, FIB-induced CVD requires the participation of specially made organometallic precursors, which are to

be installed on the instrument.[160, 161] The liquid precursors could be heated up to specific temperatures to get vaporised before the valve is opened after a command given by the software. The gaseous precursor will be delivered to the specific sites and chemically adsorbed onto the surface of the sample; at the same time, due to the interaction with the focused beam, the precursor decomposes into the desired deposition product in solid and volatile by-products which are removed by the vacuum system.[161]

2.6.1.2 Lithography

Lithography originated from ancient printing using lithographic limestone; images were created through chemical processes of etching and physical processes of adsorption due to differences in hydrophilicity.[163] In the present days, lithography is highly used to produce various kinds of publications, such as books, posters, newspapers and maps.[164]

Modern lithographic techniques have been widely used in materials science and semiconductor industries, and are often reduced to micrometre or even nanometre scales. In materials science, some of the common ways of nanolithography include nanoimprint lithography (NIL),[165-168] photolithography (PhL),[169-174] electron beam lithography (EBL),[175-179] nanosphere lithography (NSL)[152-154, 167, 180] and scanning probe lithography (SPL).[167, 181-183] **Figure 2.20** graphically illustrates these lithographic techniques, and **Table 2.3** lists their working principles, advantages and disadvantages.

Table 2.3 Comparison of common lithographic techniques[184]

Approach	Principle	Advantages	Disadvantages
NIL	Substrates are firstly softened and deformed, and then the patterns on moulds are mechanically replicated through the process of imprinting	Simple High throughput[165] High resolution[166]	High cost for stamps[167] Easy detachment of features and formation of defects[167, 168] Restricted by working temperature
PhL	The solubility of light-sensitive photoresist film[169] is selectively changed by exposure to light of various wavelengths[170-172] (usually UV light/X-ray), followed by positive or negative developing. The unprotected parts will be etched to obtain the desired pattern.	Customised patterns High resolution (sub-100 nm)[173]	Complex process Require expensive photomask[174] Instrumentation limitation (require high energy beam)[170-172]
EBL	The solubility of electron-sensitive resist film (usually PMMA[185] or HSQ[186, 187]) is selectively changed by exposure to electron beam,[175, 176] followed by positive or negative developing. The unprotected parts will be etched to obtain the desired pattern.	Customised patterns High resolution (sub-10 nm)[177, 178] No mask needed[179]	Complex process Low throughput Low production volume Instrumentation limitation (require electron beam)[175, 176]
NSL	Self-assembled monolayers (SAMs) of nanospheres (PS, PMMA or SiO_2)[167] serve as a protective mask, which could help to achieve precisely controlled nanolithography at the surface of substrates.	Simple Cost-effective[152-154] Precise control of periods[180]	Self-assembly must be monolayers
SPL	Scanning probe microscope (SPM)[181] characterises the surface of substrates; depending on the probe-surface interactions used,[182] materials can be site-specifically added onto or removed from the surface.	No mask needed High resolution (< 10 nm)[183] Atomic-level handling[167] Works in ambient environment[183]	Instrumentation limitation (require SPM)[167] Much slower process Difficult to scale up[167]

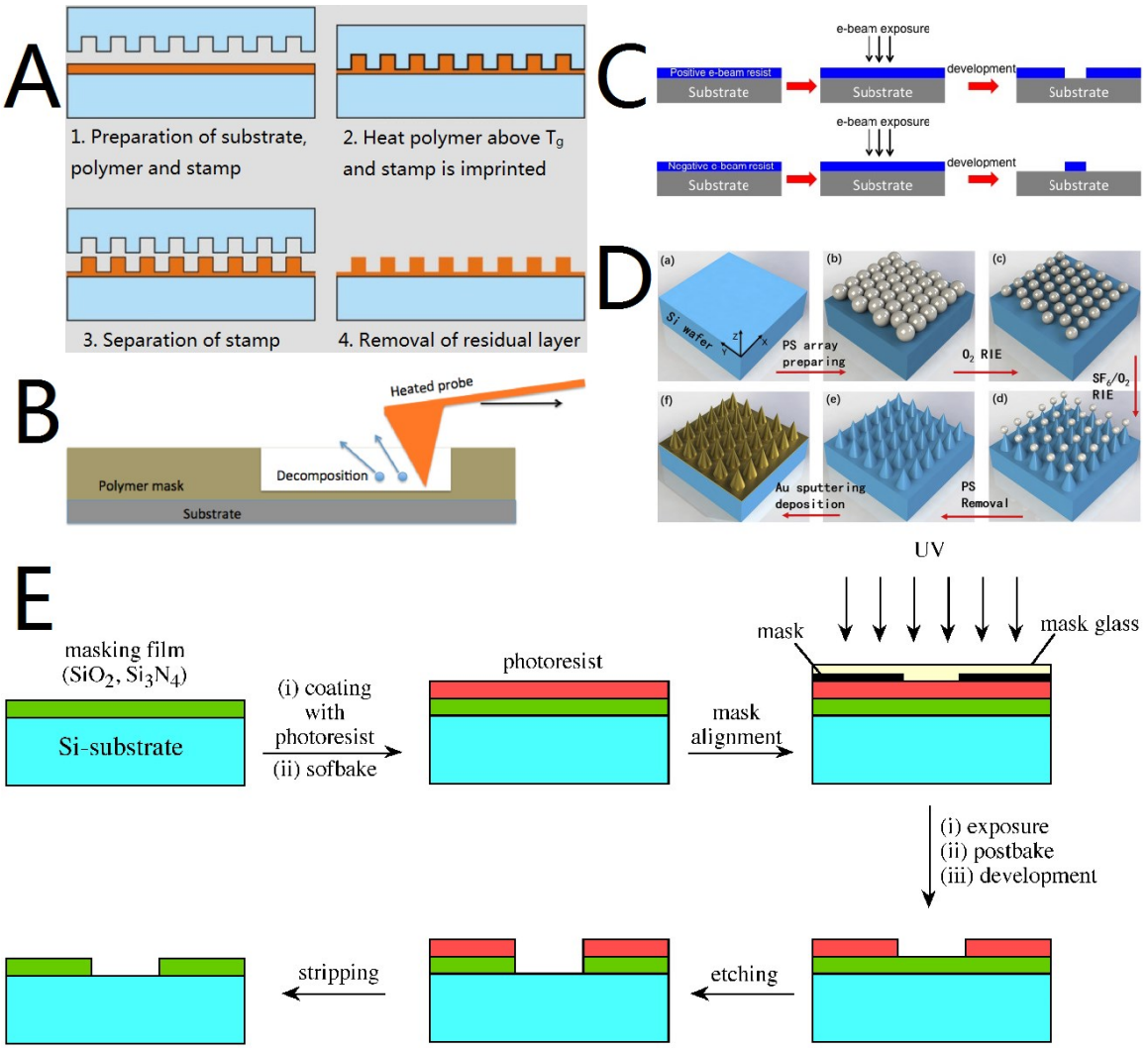

Figure 2.20 Illustration of some common techniques of nanolithography: (A) NIL;[188] (B) SPL;[189] (C) EBL;[187] (D) NSL[190] and (E) PhL.[191]

2.6.1.3 Template-Assisted Method

Template-assisted method is a simple bottom-up way to fabricate nanostructural arrays. Generally, a template is applied onto the surface of substrates, followed by an optional treatment of the template, and then deposition is performed with the protection of the template. After removal of the template, the desired pattern is obtained.[152-154] **Figure 2.21** shows the schematic illustration of template-assisted patterning method. This approach works by self-assembly of suitable materials to form the template, followed by deposition or casting of desired materials, and ends on removal of the template.[192, 193] Nevertheless,

it is important to note that this approach differentiates from NSL – the templates used in this method could be of any shape, and they are applied as deposition masks only. For example, the soft templates could be self-assembly of surfactants or liquid crystals, and the hard templates could be orderly arranged porous silica materials (**Figure 2.21**).

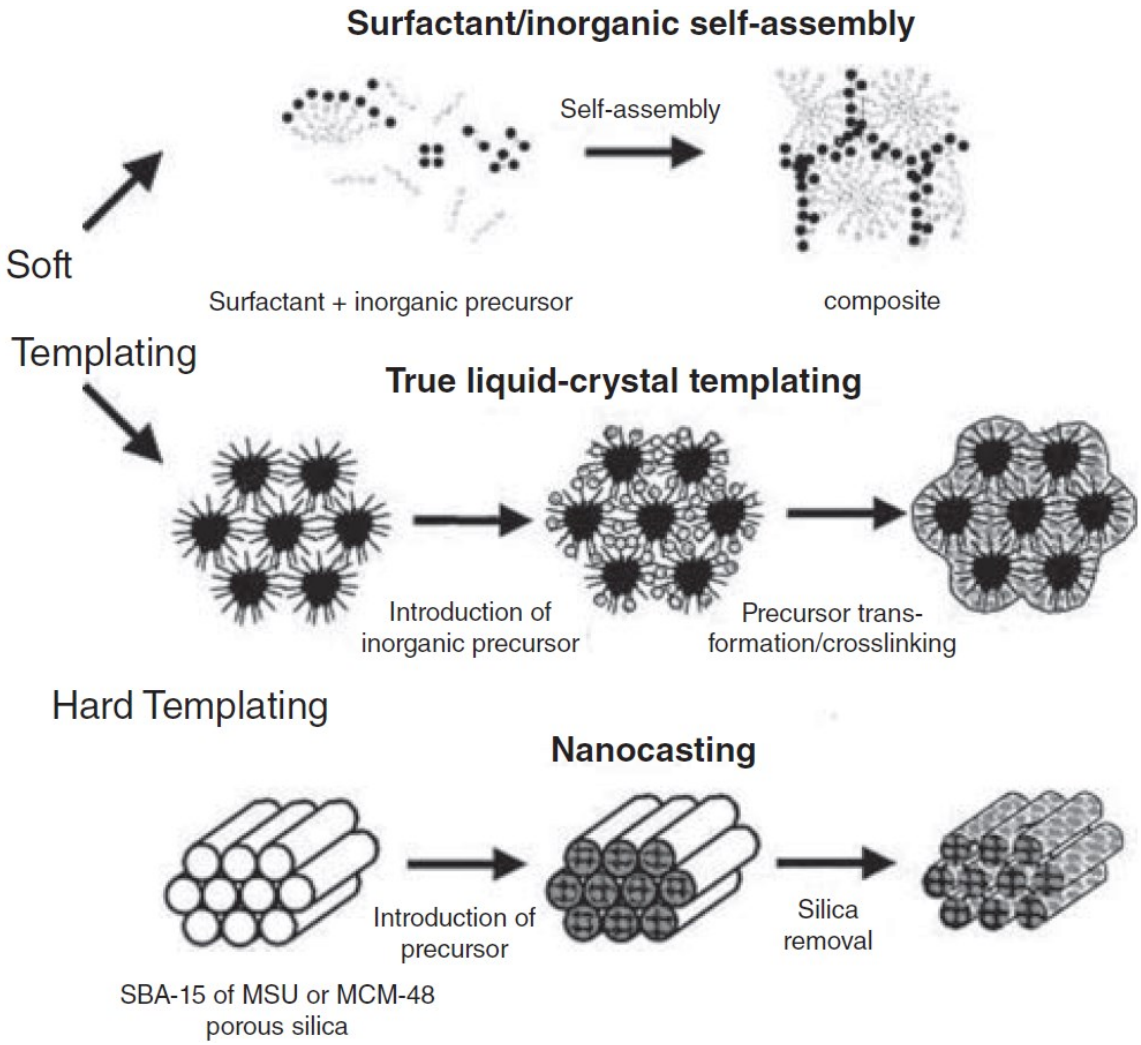

Figure 2.21 Illustration of template-assisted patterning method.[192, 193] SBA-15 and MCM-48 are the models of porous silica materials, while MSU stands for Michigan State University.

2.6.1.4 Chemical Etching

Chemical etching is a matured fabrication process that removes materials from the surface, so that objects of desired shapes can be produced. In industrial manufacturing,

chemical etching is mainly done with liquid-phase chemical baths; this process is alternatively known as wet etching.[157] In contrast, dry etching uses plasma to attack materials; a classic example of dry etching is reactive ion etching (RIE),[155, 158, 159] which ionises the etchant gases to form plasma; it is more commonly applied in semiconductor industries, where site-specific etching is needed. **Table 2.4** compares the advantages of wet and dry chemical etching processes.

Table 2.4 Advantages of wet and dry etching

Wet etching	Dry etching
High selectivity	Easy operation
Little damage to substrates	Lower temperature sensitivity
Cheap	High repeatability
Isotropic/anisotropic etching	Mainly anisotropic etching
Less shape-dependent	Fewer particles in environment

2.6.1.5 Summary for Array Structures Fabrication

In **Section 2.6.1**, various methods of fabricating array structures have been reviewed, and every method mentioned above has its advantages and disadvantages. In this project, these methods are to be compared in view of safe working and wide applications. PhL utilises hazardous UV/X-ray radiation, expensive photomasks and photoresists, whereas wet chemical etching usually makes use of strongly corrosive chemicals, they create potential chemical and physical hazards. On the other hand, FIB patterning, EBL and SPL could only work on limited small area that can hardly apply in industrial fabrication. In comparison, template-assisted method, NSL and NIL are the more desired approaches that possess low fabrication cost, small wastage of materials, large area fabrication, good controllability and utilisation of low-hazard materials.

2.6.2 Raising Surface Energy of Electrocatalyst

Surface area to volume ratio is also known as specific surface area. It could be increased by a sufficient amount through reducing the size of individual building blocks, or through creation of array structures if the former is not achievable.

Most of reported researches were focusing on morphology and size controlling, which would have neglected another key aspect. When materials are small enough in the nanometre scale, their physical and chemical properties would have changed and NPs possess huge amount of surface energy.[194] Usually the high surface energy is released through agglomeration of the NPs,[195, 196] which is one of the severe problems in using NPs as electrocatalysts. Therefore, it can be proposed that raising the amount of surface energy of NPs through mechanical straining would greatly improve their catalytic properties.[197-199] In contrast to most of the literatures in solution-based syntheses, some previous researches have demonstrated that ion bombardment of metal grid using a precision ion polishing system (PIPS) could produce sharp needles of the grid metal.[200, 201] It is believed that metals are removed in the form of NPs to finally create sharp-tipped needles with high crystallinity.[200-202] Characterisations have shown that the sharp needles display Moiré fringes,[202] which is a representation of partial lattice rotation. This marks the high surface energy content of the samples, which is believed to be transferred from the ions produced in the PIPS system.

References

1. M. Z. Jacobson, M. A. Delucchi, Z. A. F. Bauer, S. C. Goodman, W. E. Chapman, M. A. Cameron, C. Bozonnat, L. Chobadi, H. A. Clonts, P. Enevoldsen, J. R. Erwin, S. N. Fobi, O. K. Goldstrom, E. M. Hennessy, J. Liu, J. Lo, C. B. Meyer, S. B. Morris, K. R. Moy, P. L. O'Neill, I. Petkov, S. Redfern, R. Schucker, M. A. Sontag, J. Wang, E. Weiner and A. S. Yachanin, *Joule*, 2017, **1**, 108.
2. O. Ellabban, H. Abu-Rub and F. Blaabjerg, *Renewable Sustainable Energy Rev.*, 2014, **39**, 748.
3. N. Armaroli and V. Balzani, *Energy Environ. Sci.*, 2011, **4**, 3193.
4. M. Z. Jacobson, M. A. Delucchi, G. Bazouin, Z. A. F. Bauer, C. C. Heavey, E. Fisher, S. B. Morris, D. J. Y. Piekutowski, T. A. Vencill and T. W. Yeskoo, *Energy Environ. Sci.*, 2015, **8**, 2093.
5. E. F. Moran, M. C. Lopez, N. Moore, N. Müller and D. W. Hyndman, *Proc. Natl. Acad. Sci.*, 2018, **115**, 11891.
6. W. E. Glassley, *Geothermal Energy: Renewable Energy and the Environment*, CRC Press, 2nd Edition, 2014.
7. J. Liu, Y. Yao, S. Xiao and X. Gu, *J. Phys. D*, 2018, **51**, 123001.
8. M. A. Green, E. D. Dunlop, D. H. Levi, J. Hohl-Ebinger, M. Yoshita and A. W. Y. Ho-Baillie, *Prog. Photovoltaics: Res. Appl.*, 2019, **27**, 565.

9. A. A. F. Husain, W. Z. W. Hasan, S. Shafie, M. N. Hamidon and S. S. Pandey, *Renewable Sustainable Energy Rev.*, 2018, **94**, 779.
10. C. H. Ng, H. N. Lim, S. Hayase, Z. Zainal and N. M. Huang, *Renewable Sustainable Energy Rev.*, 2018, **90**, 248.
11. J. Yuan, Y. Zhang, L. Zhou, G. Zhang, H.-L. Yip, T.-K. Lau, X. Lu, C. Zhu, H. Peng, P. A. Johnson, M. Leclerc, Y. Cao, J. Ulanski, Y. Li and Y. Zou, *Joule*, 2019, **3**, 1140.
12. C. Liu, F. Li, L.-P. Ma and H.-M. Cheng, *Adv. Mater.*, 2010, **22**, E28.
13. X. Cao, N. Wang, S. Magdassi, D. Mandler and Y. Long, *Sci. Adv. Mater.*, 2014, **6**, 558.
14. C. Liu, X. Cao, A. Kamyshny, J. Y. Law, S. Magdassi and Y. Long, *J. Colloid Interface Sci.*, 2014, **427**, 49.
15. X. Cao, N. Wang, J. Y. Law, S. C. J. Loo, S. Magdassi and Y. Long, *Langmuir*, 2014, **30**, 1710.
16. X. Cao, M. N. Thet, Y. Zhang, S. C. J. Loo, S. Magdassi, Q. Yan and Y. Long, *RSC Adv.*, 2015, **5**, 25669.
17. N. Wang, M. Duchamp, R. E. Dunin-Borkowski, S. Liu, X. Zeng, X. Cao and Y. Long, *Langmuir*, 2016, **32**, 759.
18. M. S. Whittingham, *Proc. IEEE*, 2012, **100**, 1518.
19. J. M. Ogden, *Annu. Rev. Energy Env.*, 1999, **24**, 227.
20. W. G. Colella, M. Z. Jacobson and D. M. Golden, *J. Power Sources*, 2005, **150**, 150.
21. F. Wang, Y. Cao and J. Zhou, *Int. J. Energy Res.*, 2015, **39**, 418.
22. S. J. A. Moniz, S. A. Shevlin, D. J. Martin, Z.-X. Guo and J. Tang, *Energy Environ. Sci.*, 2015, **8**, 731.
23. H. Ahmad, S. K. Kamarudin, L. J. Minggu and M. Kassim, *Renewable Sustainable Energy Rev.*, 2015, **43**, 599.
24. Y. Lin, G. Yuan, R. Liu, S. Zhou, S. W. Sheehan and D. Wang, *Chem. Phys. Lett.*, 2011, **507**, 209.
25. J. Joy, J. Mathew and S. C. George, *Int. J. Hydrogen Energy*, 2018, **43**, 4804.
26. S. Anantharaj, S. R. Ede, K. Sakthikumar, K. Karthick, S. Mishra and S. Kundu, *ACS Catal.*, 2016, **6**, 8069.
27. Y. Yan, B. Y. Xia, B. Zhao and X. Wang, *J. Mater. Chem. A*, 2016, **4**, 17587.
28. I. Wierzba and Q. Wang, *Int. J. Hydrogen Energy*, 2006, **31**, 485.
29. C. Caucheteur, M. Debliquy, D. Lahem and P. Megret, *IEEE Photonics Technol. Lett.*, 2008, **20**, 96.
30. H. T. Hwang and A. Varma, *Curr. Opin. Chem. Eng.*, 2014, **5**, 42.
31. A. Contreras, S. Yiğit, K. Özay and T. N. Veziroğlu, *Int. J. Hydrogen Energy*, 1997, **22**, 1053.
32. S. Niaz, T. Manzoor and A. H. Pandith, *Renewable Sustainable Energy Rev.*, 2015, **50**, 457.
33. D. DeSantis, J. A. Mason, B. D. James, C. Houchins, J. R. Long and M. Veenstra, *Energy Fuels*, 2017, **31**, 2024.
34. *Fuel Cell Handbook*, EG&G Technical Services, Inc., 7th Edition, 2004.
35. M. C. Williams, in *Fuel Cells: Technologies for Fuel Processing*, Elsevier Amsterdam, 2011.

36. M. Z. F. Kamarudin, S. K. Kamarudin, M. S. Masdar and W. R. W. Daud, *Int. J. Hydrogen Energy*, 2013, **38**, 9438.
37. G. Hoogers, *Fuel Cell Technology Handbook*, CRC press, 2002.
38. Y. H. Chu and Y. G. Shul, *Int. J. Hydrogen Energy*, 2010, **35**, 11261.
39. A. Dessler, *Chemistry and Physics of Stratospheric Ozone*, Elsevier Science, 2000.
40. A. Cornish-Bowden, *Fundamentals of Enzyme Kinetics*, Elsevier Science, 4th Edition, 2014.
41. J. Matthiesen, S. Wendt, J. Ø. Hansen, G. K. H. Madsen, E. Lira, P. Galliker, E. K. Vestergaard, R. Schaub, E. Lægsgaard, B. Hammer and F. Besenbacher, *ACS Nano*, 2009, **3**, 517.
42. H. Lindlar and R. Dubuis, in *Organic Syntheses*, John Wiley & Sons, Inc., 2003.
43. H. Knözinger and K. Kochloefl, in *Ullmann's Encyclopedia of Industrial Chemistry*, Wiley-VCH Verlag GmbH & Co. KGaA, 2000.
44. A. Behr, in *Ullmann's Encyclopedia of Industrial Chemistry*, Wiley-VCH Verlag GmbH & Co. KGaA, 2000.
45. C. Elschenbroich, *Organometallics*, Wiley, 3rd Edition, 2016.
46. J. Kunze and U. Stimming, *Angew. Chem. Int. Ed.*, 2009, **48**, 9230.
47. A. J. Bard and L. R. Faulkner, *Electrochemical Methods: Fundamentals and Applications*, John Wiley and Sons, 2nd Edition, 2008.
48. D. N. Buckley, C. O'Dwyer, N. Quill and R. P. Lynch, in *Energy Storage Options and Their Environmental Impact*, The Royal Society of Chemistry, 2019.
49. K. Akihiko, K. Hideki and T. Issei, *Chem. Lett.*, 2004, **33**, 1534.
50. W. L. Kostedt IV, J. Drwiega, D. W. Mazyck, S.-W. Lee, W. Sigmund, C.-Y. Wu and P. Chadik, *Environ. Sci. Technol.*, 2005, **39**, 8052.
51. A. O. Kondrakov, A. N. Ignatev, V. V. Lunin, F. H. Frimmel, S. Bräse and H. Horn, *Appl. Catal. B*, 2016, **182**, 424.
52. A. O. Kondrakov, A. N. Ignatev, F. H. Frimmel, S. Bräse, H. Horn and A. I. Revelsky, *Appl. Catal. B*, 2014, **160-161**, 106.
53. T. P. T. Cushnie, P. K. J. Robertson, S. Officer, P. M. Pollard, R. Prabhu, C. McCullagh and J. M. C. Robertson, *J. Photochem. Photobiol., A*, 2010, **216**, 290.
54. D. L. Nelson and M. M. Cox, *Lehninger Principles of Biochemistry*, W. H. Freeman, 4th Edition, 2005.
55. Y. Sun and J. Cheng, *Bioresour. Technol.*, 2002, **83**, 1.
56. H. Guzmán-Maldonado, O. Paredes-López and C. G. Biliaderis, *Crit. Rev. Food Sci. Nutr.*, 1995, **35**, 373.
57. I. Alkorta, C. Garbisu, M. J. Llama and J. L. Serra, *Process Biochem.*, 1998, **33**, 21.
58. P. Molimard and H. E. Spinnler, *J. Dairy Sci.*, 1996, **79**, 169.
59. C. Dulieu, M. Moll, J. Boudrant and D. Poncelet, *Biotechnol. Progr.*, 2000, **16**, 958.
60. O. Kirk, T. V. Borchert and C. C. Fuglsang, *Curr. Opin. Biotechnol.*, 2002, **13**, 345.
61. S. P. S. Badwal, S. Giddey, A. Kulkarni, J. Goel and S. Basu, *Appl. Energy*, 2015, **145**, 80.
62. Y. Wang, S. Zou and W.-B. Cai, *Catalysts*, 2015, **5**, 1507.
63. S. Y. Shen, T. S. Zhao and Q. X. Wu, *Int. J. Hydrogen Energy*, 2012, **37**, 575.

64. R. R. Brooks, *Noble Metals and Biological Systems: Their Role in Medicine, Mineral Exploration, and the Environment*, Taylor & Francis, 1992.
65. *The Periodic Table of the Elements*, The International Union of Pure and Applied Chemistry (IUPAC), 2016.
66. *Indicative Prices of Noble Metals*, Heraeus Precious Metals, 2020.
67. Y. S. Jeong, J.-B. Park, H.-G. Jung, J. Kim, X. Luo, J. Lu, L. Curtiss, K. Amine, Y.-K. Sun, B. Scrosati and Y. J. Lee, *Nano Lett.*, 2015, **15**, 4261.
68. A. Borgschulte, R. J. Westerwaal, J. H. Rector, H. Schreuders, B. Dam and R. Griessen, *J. Catal.*, 2006, **239**, 263.
69. S. Yae, Y. Morii, N. Fukumuro and H. Matsuda, *Nanoscale Res. Lett.*, 2012, **7**, 352.
70. *Direct Alcohol Fuel Cells: Materials, Performance, Durability and Applications*, Springer, 2014.
71. W. J. Zhou, W. Z. Li, S. Q. Song, Z. H. Zhou, L. H. Jiang, G. Q. Sun, Q. Xin, K. Poulianitis, S. Kontou and P. Tsiakaras, *J. Power Sources*, 2004, **131**, 217.
72. S. Rousseau, C. Coutanceau, C. Lamy and J. M. Léger, *J. Power Sources*, 2006, **158**, 18.
73. S. Y. Shen, T. S. Zhao, J. B. Xu and Y. S. Li, *J. Power Sources*, 2010, **195**, 1001.
74. P. Gogoi, A. S. Nagpure, P. Kandasamy, C. V. V. Satyanarayana and T. Raja, *Sustainable Energy Fuels*, 2020, **4**, 678.
75. J.-Y. Jung, D. W. Kim, S. S. Shinde, S.-H. Kim, D.-H. Kim, C. Lin, T. J. Park and J.-H. Lee, *ACS Appl. Mater. Interfaces*, 2020, **12**, 16402.
76. C. Li, M. Yang, Z. Liu, Z. Zhang, T. Zhu, X. Chen, Y. Dong and H. Cheng, *Catal. Sci. Technol.*, 2020, **10**, 2268.
77. J. Kašpar, P. Fornasiero and N. Hickey, *Catal. Today*, 2003, **77**, 419.
78. G. Wang, Z. Zhou, X. Shen, S. Ivlev and E. Meggers, *Chem. Commun.*, 2020, **56**, 7714.
79. M. Cui, X. Guo, H. H. Y. Sung, I. D. Williams, Z. Lin and G. Jia, *Organometallics*, 2020, **39**, 2142.
80. M. Valencia, A. D. Merinero, C. Lorenzo-Aparicio, M. Gómez-Gallego, M. A. Sierra, B. Eguillor, M. A. Esteruelas, M. Oliván and E. Oñate, *Organometallics*, 2020, **39**, 312-323.
81. L. Zhou, X. Liu, K. Wang, X. Zhao, H. Pu, T. Zhang, J. Jia, K. Dong and Y. Deng, *Energy Fuels*, 2020, **34**, 9956.
82. R. Kanega, M. Z. Ertem, N. Onishi, D. J. Szalda, E. Fujita and Y. Himeda, *Organometallics*, 2020, **39**, 1519.
83. C. W. B. Bezerra, L. Zhang, K. Lee, H. Liu, A. L. B. Marques, E. P. Marques, H. Wang and J. Zhang, *Electrochim. Acta*, 2008, **53**, 4937.
84. A. L. Mohana Reddy, N. Rajalakshmi and S. Ramaprabhu, *Carbon*, 2008, **46**, 2.
85. S. Shahgaldi and J. Hamelin, *Carbon*, 2015, **94**, 705.
86. J. Stacy, Y. N. Regmi, B. Leonard and M. Fan, *Renewable Sustainable Energy Rev.*, 2017, **69**, 401-414.
87. X. Zhang, X. Cheng and Q. Zhang, *J. Energy Chem.*, 2016, **25**, 967.
88. X. Zhou, J. Qiao, L. Yang and J. Zhang, *Adv. Energy Mater.*, 2014, **4**, 1301523.
89. M. Haruta, *Nature*, 2005, **437**, 1098.
90. T. A. Baker, X. Liu and C. M. Friend, *Phys. Chem. Chem. Phys.*, 2011, **13**, 34.

91. P. Rodriguez, Y. Kwon and M. T. M. Koper, *Nat. Chem.*, 2012, **4**, 177.
92. G. J. Hutchings, M. Brust and H. Schmidbaur, *Chem. Soc. Rev.*, 2008, **37**, 1759.
93. T. Takei, N. Iguchi and M. Haruta, *New J. Chem.*, 2011, **35**, 2227.
94. P. Rodriguez, N. Garcia-Araez and M. T. M. Koper, *Phys. Chem. Chem. Phys.*, 2010, **12**, 9373.
95. H. Kita, H. Nakajima and K. Hayashi, *J. Electroanal. Chem. Interfacial Electrochem.*, 1985, **190**, 141.
96. P. Rodriguez and M. T. M. Koper, *Phys. Chem. Chem. Phys.*, 2014, **16**, 13583.
97. P. Rodriguez, J. M. Feliu and M. T. M. Koper, *Electrochem. Commun.*, 2009, **11**, 1105.
98. Y. Kwon, S. C. S. Lai, P. Rodriguez and M. T. M. Koper, *J. Am. Chem. Soc.*, 2011, **133**, 6914.
99. G. Tremiliosi-Filho, E. R. Gonzalez, A. J. Motheo, E. M. Belgsir, J. M. Léger and C. Lamy, *J. Electroanal. Chem.*, 1998, **444**, 31.
100. F. Ksar, L. Ramos, B. Keita, L. Nadjo, P. Beaunier and H. Remita, *Chem. Mater.*, 2009, **21**, 3677.
101. C. Fang, G. Zhao, Z. Zhang, J. Zheng, Q. Ding, X. Xu, L. Shao and B. Geng, *Part. Part. Syst. Char.*, 2018, **35**, 1800258.
102. L. Q. Wang, M. Bevilacqua, J. Filippi, P. Fornasiero, M. Innocenti, A. Lavacchi, A. Marchionni, H. A. Miller and F. Vizza, *Appl. Catal. B*, 2015, **165**, 185.
103. G. Andreadis and P. Tsiakaras, *Chem. Eng. Sci.*, 2006, **61**, 7497.
104. C. Song and J. Zhang, in *PEM Fuel Cell Electrocatalysts and Catalyst Layers: Fundamentals and Applications*, Springer London, 2008.
105. N. M. Marković and P. N. Ross, *Surf. Sci. Rep.*, 2002, **45**, 117.
106. Y. Li, Q. Li, H. Wang, L. Zhang, D. P. Wilkinson and J. Zhang, *Electrochem. Energ. Rev.*, 2019, **2**, 518.
107. J. K. Nørskov, J. Rossmeisl, A. Logadottir, L. Lindqvist, J. R. Kitchin, T. Bligaard and H. Jónsson, *J. Phys. Chem. B*, 2004, **108**, 17886.
108. M. Shao, Q. Chang, J.-P. Dodelet and R. Chenitz, *Chem. Rev.*, 2016, **116**, 3594.
109. Y. S. Li, T. S. Zhao and Z. X. Liang, *J. Power Sources*, 2009, **187**, 387.
110. A. D. Modestov, M. R. Tarasevich, A. Y. Leykin and V. Y. Filimonov, *J. Power Sources*, 2009, **188**, 502.
111. L. An and T. S. Zhao, *Int. J. Hydrogen Energy*, 2011, **36**, 9994.
112. J. Du, J. Qi, D. Wang and Z. Tang, *Energy Environ. Sci.*, 2012, **5**, 6914.
113. S. Anandan, F. Grieser and M. Ashokkumar, *J. Phys. Chem. C*, 2008, **112**, 15102.
114. P. Raveendran, J. Fu and S. L. Wallen, *Green Chem.*, 2006, **8**, 34.
115. Z. Peng, B. Spliethoff, B. Tesche, T. Walther and K. Kleinermanns, *J. Phys. Chem. B*, 2006, **110**, 2549.
116. M. Grzelczak, J. Pérez-Juste, P. Mulvaney and L. M. Liz-Marzán, *Chem. Soc. Rev.*, 2008, **37**, 1783.
117. S. Kassavetis, C. Gravalidis and S. Logothetidis, in *Nanostructured Materials and Their Applications*, Springer Berlin Heidelberg, 2012.
118. *Handbook of Deposition Technologies for Films and Coatings: Science, Applications and Technology*, Elsevier Science, 3rd Edition, 2010.
119. *Handbook of Thin-Film Technology*, Springer Berlin Heidelberg, 2015.

120. *Handbook of Thin Film Deposition*, William Andrew Applied Science Publishers, 4th Edition, 2018.
121. R. K. Nishihora, P. L. Rachadel, M. G. N. Quadri and D. Hotza, *J. Eur. Ceram. Soc.*, 2018, **38**, 988.
122. M. Jabbari, R. Bulatova, A. I. Y. Tok, C. R. H. Bahl, E. Mitsoulis and J. H. Hattel, *Mater. Sci. Eng., B*, 2016, **212**, 39.
123. L. H. Luo, A. I. Y. Tok and F. Y. C. Boey, *Mater. Sci. Eng., A*, 2006, **429**, 266.
124. K. Huang, D. Peng, B. Zhang, X. Cao, S. Hao, G. Yang, Y. Dong, J. Wu and Y. Huang, *Int. J. Hydrogen Energy*, 2018, **43**, 12596.
125. D. Peng, B. Zhang, J. Wu, K. Huang, X. Cao, Y. Lu, Y. Zhang, C. Li and Y. Huang, *ChemCatChem*, 2020, **12**, 2431.
126. S. Mersagh Dezfuli and M. Sabzi, *Ceram. Int.*, 2019, **45**, 21835.
127. H. K. Raut, V. A. Ganesh, A. S. Nair and S. Ramakrishna, *Energy Environ. Sci.*, 2011, **4**, 3779.
128. K. L. Choy, *Prog. Mater Sci.*, 2003, **48**, 57.
129. A. Rockett, in *The Materials Science of Semiconductors*, Springer US, Boston, MA, 2008.
130. Y. Zhang, X. Xia, X. Cao, B. Zhang, H. T. Nguyen, H. He, S. Chen, Y. Huang and H. J. Fan, *Adv. Energy Mater.*, 2017, **7**, 1700220.
131. M. Ma, G. Yang, H. Wang, Y. Lu, B. Zhang, X. Cao, D. Peng, X. Du, Y. Liu and Y. Huang, *Int. J. Hydrogen Energy*, 2019, **44**, 1544.
132. P. Zhu, Z. Zhang, P. Zhao, B. Zhang, X. Cao, J. Yu, J. Cai, Y. Huang and Z. Yang, *Carbon*, 2019, **142**, 269.
133. M. Wang, Y. Yu, M. Cui, X. Cao, W. Liu, C. Wu, X. Liu, T. Zhang and Y. Huang, *Electrochim. Acta*, 2020, **329**, 135181.
134. C. Li, B. Zhang, Y. Li, S. Hao, X. Cao, G. Yang, J. Wu and Y. Huang, *Appl. Catal. B*, 2019, **244**, 56.
135. G. Yang, H. Wang, B. Zhang, S. Foo, M. Ma, X. Cao, J. Liu, S. Ni, M. Srinivasan and Y. Huang, *Nanoscale*, 2019, **11**, 9556.
136. C. Li, X. Cao, W. Li, B. Zhang and L. Xiao, *J. Alloys Compd.*, 2019, **773**, 762.
137. C. Li, Y. Rao, B. Zhang, K. Huang, X. Cao, D. Peng, J. Wu, L. Xiao and Y. Huang, *Chemosphere*, 2019, **214**, 341.
138. Y. Rao, X. Cao, C. Li and L. Xiao, *Sep. Purif. Technol.*, 2019, **220**, 328.
139. B. Zhang, C. Li, G. Yang, K. Huang, J. Wu, Z. Li, X. Cao, D. Peng, S. Hao and Y. Huang, *ACS Appl. Mater. Interfaces*, 2018, **10**, 23807.
140. B. Zhang, B. Chen, J. Wu, S. Hao, G. Yang, X. Cao, L. Jing, M. Zhu, S. H. Tsang, E. H. T. Teo and Y. Huang, *Small*, 2017, **13**, 1603411.
141. X. Yao, X. Zhao, J. Hu, H. Xie, D. Wang, X. Cao, Z. Zhang, Y. Huang, Z. Chen and T. Sritharan, *iScience*, 2019, **19**, 976.
142. X. Zhao, Z. Zhang, X. Cao, J. Hu, X. Wu, A. Y. R. Ng, G.-P. Lu and Z. Chen, *Appl. Catal. B*, 2020, **260**, 118156.
143. H. Liu, J. Wu, Y. Wang, C. L. Chow, Q. Liu, C. L. Gan, X. Tang, R. S. Rawat, O. K. Tan, J. Ma and Y. Huang, *Small*, 2012, **8**, 2807.
144. H. Liu, B. Yadian, Q. Liu, C. L. Gan and Y. Huang, *Nanotechnology*, 2013, **24**, 175301.

145. H. Liu, C. Y. Khoo, B. Yadian, Q. Liu, C. L. Gan, X. Tang and Y. Huang, *Nanoscale*, 2014, **6**, 3078.
146. B. Yadian, H. Liu, Y. Wei, J. Wu, S. Zhang, L. Sun, C. Zhao, Q. Liu, R. V. Ramanujan, K. Zhou, C. L. Gan and Y. Huang, *Small*, 2014, **10**, 344.
147. Y. Z. Huang, S. G. Wang, C. Wang, Z. B. Xie, D. J. H. Cockayne and R. C. C. Ward, *Appl. Phys. Lett.*, 2006, **88**, 103104.
148. Y.-Z. Huang, D. J. H. Cockayne, J. Ana-Vanessa, R. P. Cowburn, S.-G. Wang and R. C. C. Ward, *Nanotechnology*, 2008, **19**, 015303.
149. Q. Chen, G. Hubbard, P. A. Shields, C. Liu, D. W. E. Allsopp, W. N. Wang and S. Abbott, *Appl. Phys. Lett.*, 2009, **94**, 263118.
150. W. Wei, H. Min, O. Fung Suong, L. Zhiyong and R. S. Williams, *Nanotechnology*, 2010, **21**, 255502.
151. H. Jung and K.-H. Jeong, *Appl. Phys. Lett.*, 2012, **101**, 203102.
152. C. Cong, W. Junus, Z. Shen and T. Yu, *Nanoscale Res. Lett.*, 2009, **4**, 1324.
153. L. Li, T. Zhai, H. Zeng, X. Fang, Y. Bando and D. Golberg, *J. Mater. Chem.*, 2011, **21**, 40.
154. Y. Li, G. Duan, G. Liu and W. Cai, *Chem. Soc. Rev.*, 2013, **42**, 3614.
155. R. M. Ranade, S. S. Ang and W. D. Brown, *J. Electrochem. Soc.*, 1993, **140**, 3676.
156. J. Zhu, Z. Yu, G. F. Burkhard, C.-M. Hsu, S. T. Connor, Y. Xu, Q. Wang, M. McGehee, S. Fan and Y. Cui, *Nano Lett.*, 2009, **9**, 279.
157. T. A. Green, *Gold Bull.*, 2014, **47**, 205.
158. S. Li, L. Ren, Z. Yang, Z. Zhang, F. Gao, J. Du and S. Zhang, *Microelectron. Eng.*, 2014, **113**, 143.
159. T.-S. Choi and D. W. Hess, *ECS J. Solid State Sci. Technol.*, 2015, **4**, N3084.
160. *Introduction to Focused Ion Beams: Instrumentation, Theory, Techniques and Practice*, Springer International Publishing, 2005.
161. *FIB Nanostructures*, Springer International Publishing, 2013.
162. A. T. Ampere, *J. Micromech. Microeng.*, 2004, **14**, R15.
163. P. Weaver, *The Technique of Lithography*, Batsford, 1964.
164. N. Howard, *The Book: The Life Story of a Technology*, Greenwood Press, 2005.
165. Y. Lu, J. Y. Huang, C. Wang, S. Sun and J. Lou, *Nat. Nanotechnol.*, 2010, **5**, 218.
166. S. Y. Chou, P. R. Krauss and P. J. Renstrom, *Science*, 1996, **272**, 85.
167. B. D. Gates, Q. Xu, M. Stewart, D. Ryan, C. G. Willson and G. M. Whitesides, *Chem. Rev.*, 2005, **105**, 1171.
168. N. Tucher, O. Höhn, H. Hauser, C. Müller and B. Bläsi, *Microelectron. Eng.*, 2017, **180**, 40.
169. C. G. Willson, R. R. Dammel and A. Reiser, *Proc. SPIE*, 1997, **3049**, 28.
170. K. Jain, *Excimer Laser Lithography*, SPIE Society of Photo-Optical Instrumentation Engineers, 1990.
171. D. Basting and G. Marowsky, *Excimer Laser Technology*, Springer Berlin Heidelberg, 2005.
172. K. Jain, C. G. Willson and B. J. Lin, *IEEE Electron Device Lett.*, 1982, **3**, 53.
173. B. L. Fontaine, *SPIE Professional, October*, 2010, DOI: 10.1117/2.4201010.09, 20.
174. M. Yoshizawa, V. Philipsen and L. H. A. Leunissen, *Proc. SPIE*, 2005, **5853**, 243.
175. G. Schell, H. Winter, H. Rietschel and F. Gompf, *Phys. Rev. B*, 1982, **25**, 1589.
176. L. W. Swanson, *J. Vac. Sci. Technol.*, 1975, **12**, 1228.

177. A. E. Grigorescu, M. C. van der Krogt, C. W. Hagen and P. Kruit, *Microelectron. Eng.*, 2007, **84**, 822.
178. A. T. K. G., S. N. Piramanayagam, M. Ranjbar, R. Sbiaa and T. C. Chong, *J. Vac. Sci. Technol., B*, 2011, **29**, 011035.
179. T. H. P. Chang, M. Mankos, K. Y. Lee and L. P. Muray, *Microelectron. Eng.*, 2001, **57-58**, 117.
180. A. Hatzor-De Picciotto, A. D. Wissner-Gross, G. Lavallee and P. S. Weiss, *J. Exp. Nanosci.*, 2007, **2**, 3.
181. O. C. Wells, United States Patent 4785189, 15 November 1988.
182. R. Garcia, A. W. Knoll and E. Riedo, *Nat. Nanotechnol.*, 2014, **9**, 577.
183. R. V. Martínez, N. S. Losilla, J. Martinez, Y. Huttel and R. Garcia, *Nano Lett.*, 2007, **7**, 1846.
184. X. Cao, C. Li, Y. Lu, B. Zhang, Y. Wu, Q. Liu, J. Wu, J. Teng, W. Yan and Y. Huang, *J. Catal.*, 2019, **377**, 389.
185. R. V. Lapshin, A. P. Alekhin, A. G. Kirilenko, S. L. Odintsov and V. A. Krotkov, *J. Surf. Invest.*, 2010, **4**, 1.
186. D. B. Cordes, P. D. Lickiss and F. Rataboul, *Chem. Rev.*, 2010, **110**, 2081.
187. A. E. Grigorescu and C. W. Hagen, *Nanotechnology*, 2009, **20**, 292001.
188. H. Yabu, Y. Saito, M. Shimomura and Y. Matsuo, *J. Mater. Chem. C*, 2013, **1**, 1558.
189. P. C. Paul, in *Frontiers of Nanoscience*, Elsevier, 2016.
190. Q. Li, J. Gao, Z. Li, H. Yang, H. Liu, X. Wang and Y. Li, *Opt. Mater.*, 2017, **70**, 165.
191. M. Madou and C. Wang, in *Encyclopedia of Nanotechnology*, Springer Netherlands, Dordrecht, 2012.
192. F. Schüth, *Chem. Mater.*, 2001, **13**, 3184.
193. D. Zhao, Y. Wan and W. Zhou, *Ordered Mesoporous Materials*, Wiley, 2012.
194. K. K. Nanda, A. Maisels, F. E. Kruis, H. Fissan and S. Stappert, *Phys. Rev. Lett.*, 2003, **91**, 106102.
195. B. Medasani, Y. H. Park and I. Vasiliev, *Phys. Rev. B*, 2007, **75**, 235436.
196. F. D. Fischer, T. Waitz, D. Vollath and N. K. Simha, *Prog. Mater Sci.*, 2008, **53**, 481.
197. J. R. Petrie, C. Mitra, H. Jeen, W. S. Choi, T. L. Meyer, F. A. Reboredo, J. W. Freeland, G. Eres and H. N. Lee, *Adv. Funct. Mater.*, 2016, **26**, 1564.
198. H. Li, C. Tsai, A. L. Koh, L. Cai, A. W. Contryman, A. H. Fragapane, J. Zhao, H. S. Han, H. C. Manoharan, F. Abild-Pedersen, J. K. Nørskov and X. Zheng, *Nat. Mater.*, 2016, **15**, 48.
199. H. Li, A. W. Contryman, X. Qian, S. M. Ardakani, Y. Gong, X. Wang, J. M. Weisse, C. H. Lee, J. Zhao, P. M. Ajayan, J. Li, H. C. Manoharan and X. Zheng, *Nat. Commun.*, 2015, **6**, 7381.
200. B. Zhang, J. Wu, X. Li, H. Liu, B. Yadian, R. V. Ramanujan, K. Zhou, R. Wu, S. Hao and Y. Huang, *J. Phys. Chem. C*, 2014, **118**, 9073.
201. B. Zhang, S. Hao, J. Wu, X. Li and Y. Huang, *RSC Adv.*, 2016, **6**, 19937.
202. J. Wu, X. Li, B. Yadian, H. Liu, S. Chun, B. Zhang, K. Zhou, C. L. Gan and Y. Huang, *Electrochem. Commun.*, 2013, **26**, 21.

Chapter 3

Experimental Methodology

This chapter introduces the materials and methods used for enhancing the electrocatalytic performance of the nanostructured Au in EOR, as well as the rationale for the selection. The processes and essential equipment settings are elaborated in details. Advanced materials characterisations and electrochemical property testing methods are also described, including the instruments used, the underlying theories, working principles and essential sample preparation techniques.

3.1 Selection of Methods and Rationale

In Au-catalysed EOR, the Au-ethanol interaction is the key to enhance the electrochemical performance. In this project, there are two general approaches to improve the surface activity of Au, which include increasing the surface area to volume ratio and raising the surface energy. Both are aiming to ramp up the number of active sites, which is the underlying factor to boosting the electrochemical activity.

Since the ultimate aim of the research is to apply the technology to industrial fabrication and real life applications, increasing the aspect ratio using methods with great potential in scaled production will be the top priority. As reviewed in **Section 2.6.1.5**, NSL and NIL are the selected approaches as they could easily cover large sample areas. The fabrication of NPs will not follow the traditional solution-based chemical synthesis; instead, ion bombardment using PIPS system is selected to induce stress and strain, so as to raise the surface energy content of the Au NPs.

3.2 Fabrication of Samples

3.2.1 Fabrication of Au Nano-Ring Arrays

Figure 3.1 shows a schematic illustration of the fabrication process, which depicts the whole work flow in both top view and side view. More principles and information can be found in the following sub-sections. P-type Si <1 0 0> wafers were treated in piranha solution and rinsed with ethanol before drying. Au thin film with the thickness of 100 nm was deposited by direct current (DC) magnetron sputtering using a homemade magnetron sputtering system, which is equipped with a DC power supply unit (Sorenson DCS600-1.7E, AMETEK, USA) as shown in **Figure 3.2**. Monodispersed commercial polystyrene (PS) colloidal spheres were self-assembled on Au thin film via the vapour-liquid-solid (VLS) method, which formed a close-packed monolayer. In order to obtain the Au nano-ring array structure, the samples were etched by a reactive ion etcher (ES371, Nippon Scientific Co. Ltd., Japan) as displayed in **Figure 3.3**.

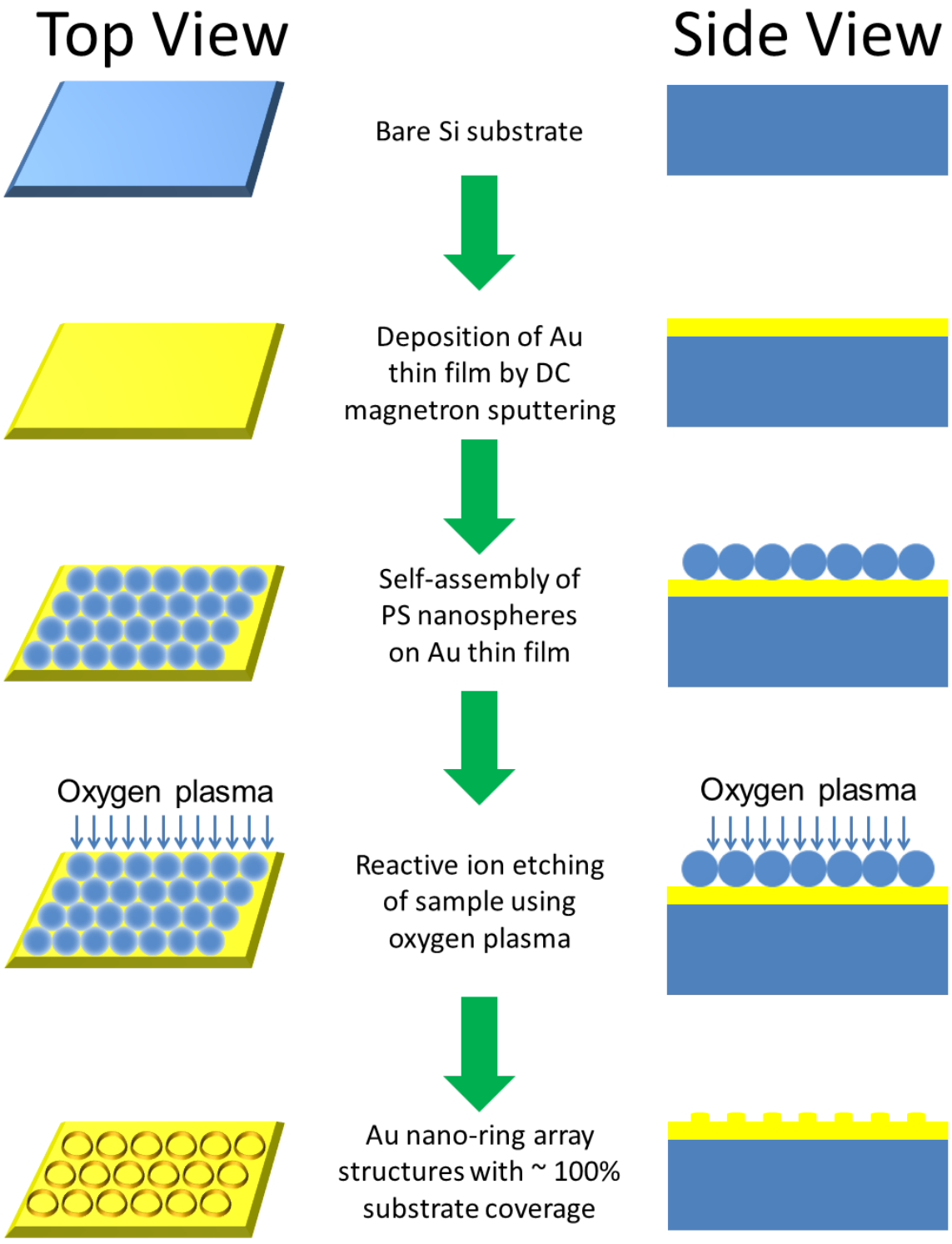

Figure 3.1 Schematic illustration of the fabrication process of Au nano-ring arrays on Si/SiO_2 substrate

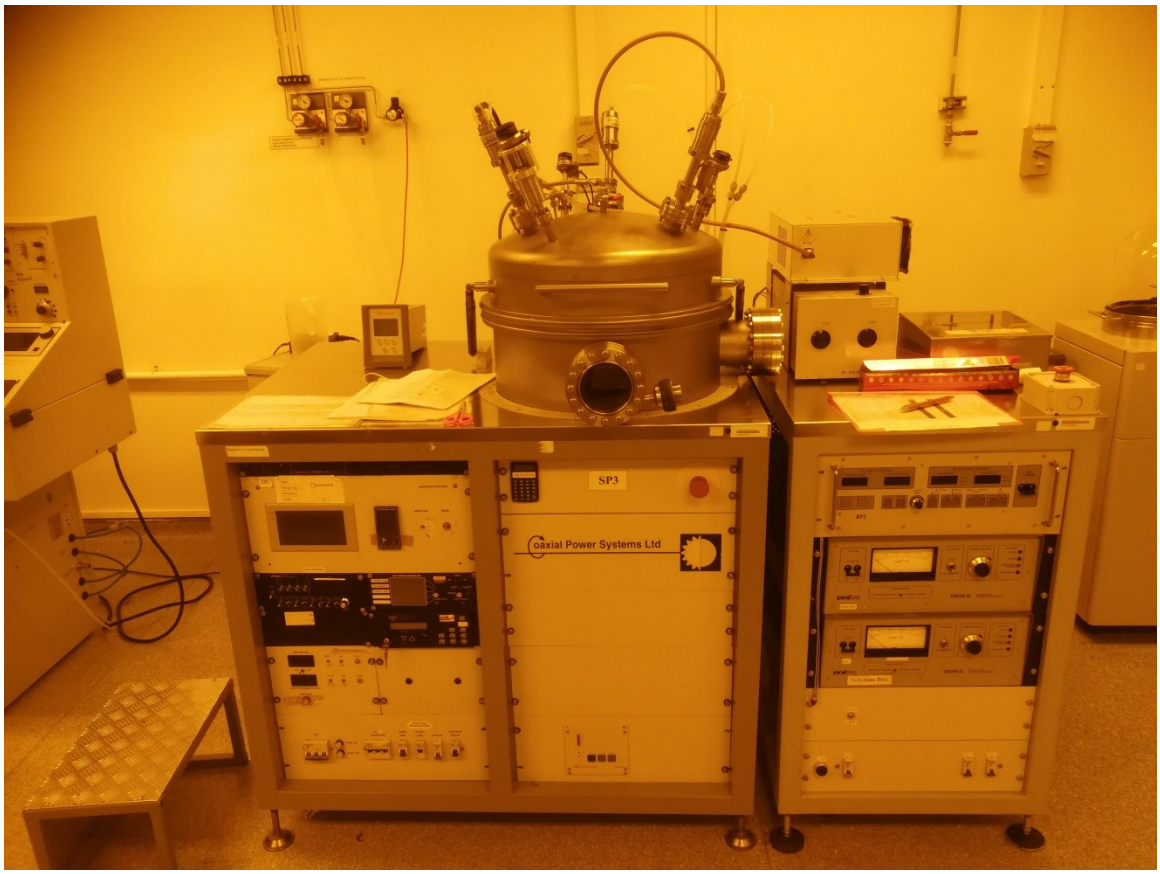

Figure 3.2 Photo of the homemade DC magnetron sputtering system with Sorenson DCS600-1.7E DC power supply unit used in this project

Figure 3.3 Photo of Nippon Scientific ES371 reactive ion etcher used in this project

3.2.1.1 Cleaning of Si p <1 0 0> Wafer

Si wafer was cut into 2 × 2 cm^2 squares, which were treated in piranha solution (H_2O_2 : H_2SO_4 = 1 : 3 by volume) for 30 min. Following that, the Si wafers were rinsed with absolute ethanol in a 300 W ultrasonic bath for 10 min to remove any residual piranha solution. Finally, the wafers were dried in an oven at 100 °C to completely evaporate the residual ethanol.

3.2.1.2 Deposition of Au Thin Film

The cleaned Si wafers will be fixed in a PVD chamber for DC magnetron sputtering. In order to obtain a smooth and homogeneous Au film, the target used was 99.99% Au and controlled deposition was carried out at the chamber pressure no more than 5.0×10^{-6} Torr, as this will reduce the scattering of plasma by the residual gas molecules. This process involves ionisation of a sputtering gas (typically an inert gas such as argon (Ar) or nitrogen (N_2)), in which the high-energy ions strike on the target and eject the material from its surface. Atoms ejected from the target have a wide energy distribution; typically only a small fraction of the ejected particles are ionised, which can fly from the target in straight lines and impact energetically on the substrates, thus causing the deposition of the desired material. The thickness of the Au thin film is controlled mainly by the power used, time of deposition and flow rate of sputtering gas; these parameters will be fine-tuned for the smooth and homogeneous deposition of Au thin film. In this research, the PVD instrument was operated at the DC power of 200 W and Ar flow rate of 20 sccm, and the deposition was held at room temperature for 2 min to get 100 nm Au thin film.

3.2.1.3 Self-Assembly of PS Colloidal Nanospheres

The Au-coated Si wafers will be placed into a plasma system (NT1, BSET EQ, USA) with an RF power of 300 W (**Figure 3.4**). The gas environment is a mixture of Ar and O_2 with 1:5 in pressure. The plasma treatment will be carried out for 10 s in order to make

the surface of the Au-coated Si wafers roughened and hydrophilic. The Ar^+ plasma could selectively attack Au and a mild treatment would not etch away the Au thin film. The oxygen on the surface of Au has higher electronegativity than hydrogen; it pulls electrons towards itself and away from hydrogen, leaving a slight positive charge near hydrogen and a slight negative charge near oxygen. Therefore, hydrogen bonding could be formed to create a polar effect, which tends to draw hydrophilic molecules/surfaces towards each other and away from other substances that do not exhibit this kind of non-symmetrical distribution of electron charge. Hydrophobic molecules group together in the presence of hydrophilic molecules, in order to minimise the surface area exposed to the hydrophilic regions. Thus, monodispersed commercial PS colloidal nanospheres of 500 nm diameter will be dispersed in ultrapure deionised water; due to its intrinsic hydrophobicity, PS spheres will form a close-packed monolayer under room temperature and pressure.

Figure 3.4 Photo of the BSET EQ NT1 plasma system used in this project

At this stage, the self-assembly of PS colloidal nanospheres on the surface of Au-coated Si wafers could be achieved via two different approaches. In the Langmuir-Blodgett (LB) method, the substrates would be placed slanted against the walls of the container, with the

Au-coated side facing up; the entire setup would then be transferred into an oven of ~ 60 °C to facilitate the self-assembly of PS colloidal nanospheres on the surface of Au-coated Si wafers. The deposition of an LB film relies on the liquid-solid interface.[1] When the solid substrate is immersed into the dispersion, the nanospheres tend to flow to the solid-liquid or liquid-air interface by convection. Evaporation of the liquid lowers the level of meniscus and leaves the nanospheres assembled on the surface of the solid substrate (**Figure 3.5**).[2] It should be noted that films deposited by the LB process could be influenced by a few factors, such as initial sphere volume fraction, temperature, relative humidity, substrate tilting angle, and the substrate material.[2] The LB process has several advantages like usage of small amount of coating material and low defect concentration.[2] However, due to the vertical orientation of the substrate, the deposited film usually renders a thickness gradient and it is hard to produce a fully monolayer self-assembly.[3-5] To avoid this, the VLS method could be interpreted as a special case of the LB process, during which the Au-coated Si wafers would be carefully immersed into the water/PS dispersion and slowly lifted out vertically,[6-8] so that the self-assembled monolayer PS colloidal nanospheres could stay on the surface of Au thin film. The samples will be dried with the aid of silica drying gel until the surface is water-free.

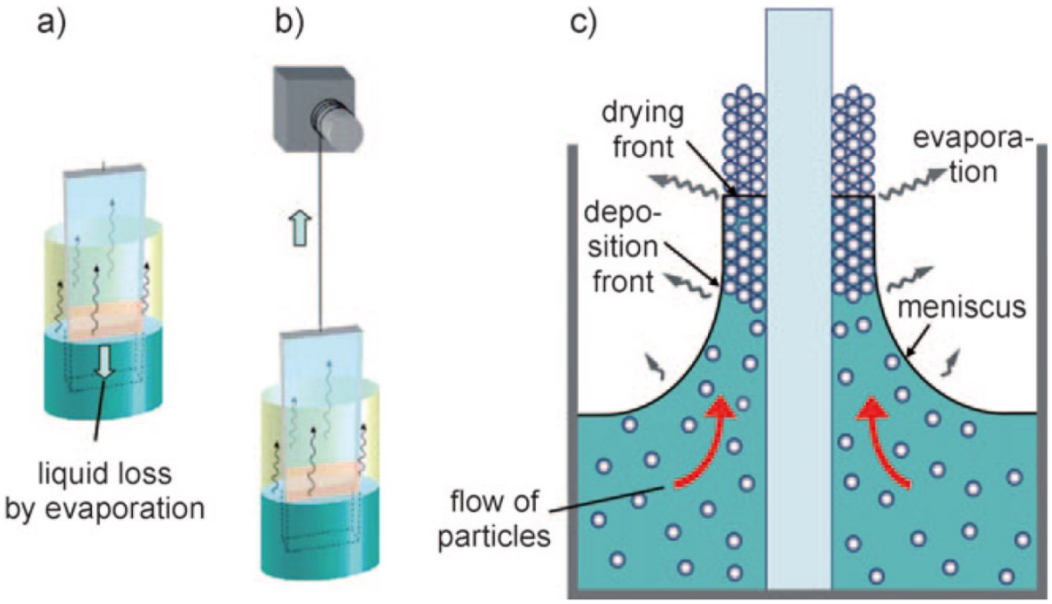

Figure 3.5 Illustration of the LB deposition process. (a) The traditional setup; (b) improved setup with integrated slow lifting; (c) the schematic process principle.[2]

3.2.1.4 RIE for Si/Au/PS Samples

The self-assembled PS colloidal nanospheres can serve as a protective mask, which helps to produce an orderly patterned structure on the Au surface. There are various ways to achieve this, but with the aid of a mask, RIE is a fast, convenient and efficient method. Plasma is initiated in the system by applying a strong radio frequency (RF) electromagnetic field to the wafer platter. The oscillating electric field ionises the etchant gas molecules by removing their electrons to form plasma. Because of the large voltage difference, the positive ions tend to drift towards the wafer platter, where they collide with the samples to be etched. The ions react chemically with the materials on the surface of the samples, but they can also knock off some materials by transferring some of the kinetic energy. Due to the mostly vertical delivery of reactive ions, RIE can produce very anisotropic etching profiles, which is in contrast with the typical isotropic profiles of wet chemical etching.

The samples were cut into small pieces (5×5 mm^2) and individually loaded into the chamber of the dry etching system, which was then pumped down before different etchant gases (Ar, CF_4 or O_2) were delivered one at a time at various flow rates (20 or 40 sccm). Following that, the system was maintained at different chamber pressures (ranging from 90 to 300 mTorr) and the etchant gas used in each run was ionised at various RF powers (ranging from 10 to 150 W) to etch the samples for different durations (ranging from 5.0 to 20.0 min).

3.2.2 Fabrication of Flexible Au Micro-Array (MA) Electrodes

The fabrication process of the patterned samples is following an earlier work.[9] PVC substrates were cut into 5.0×7.5 mm^2 or 10×15 mm^2 pieces. They were rinsed with deionised water and absolute ethanol in a 300 W ultrasonic bath for 10 min each to obtain a clean surface. Upon drying, one Ni grid was placed on a small (5.0×7.5 mm^2) piece of PVC substrate and loaded into a compact nanoimprinter (CNI, NIL Technology,

Netherlands) as displayed in **Figure 3.6**. Ni grids with a fixed mesh grade were used as the mould, and the PVC substrates were imprinted by the CNI system to obtain the micrometre scale array structure. The Ni grids were removed from the PVC substrates after cooling down to the room temperature. The nanoimprint conditions were varied based on three parameters (heating temperature, imprinting duration and operating pressure), and a set of optimum parameters were to be determined by these preliminary experiments.

Figure 3.6 Photo of NIL Technology compact nanoimprinter used in this project

With the application of the optimum parameters, the MA electrodes were fabricated in a similar way as abovementioned, except that Ni grids in 3 × 3 matrices were arranged on larger (10 × 15 mm^2) PVC substrates. The nine Ni grids in each set are of the same mesh grade and the different sets of electrodes are defined by the mesh grades of Ni grids (varied from 50-mesh to 400-mesh). Following this, Au thin film with the thickness of ~ 100 nm was deposited by electron beam evaporation using an electron beam evaporation system (ATC-ORION-8E UHV, AJA International Inc., USA) as illustrated in **Figure 3.7**.

A schematic illustration of the fabrication process for flexible Au MA electrodes is presented in **Figure 3.8**. More principles and information can be found in the following sub-sections.

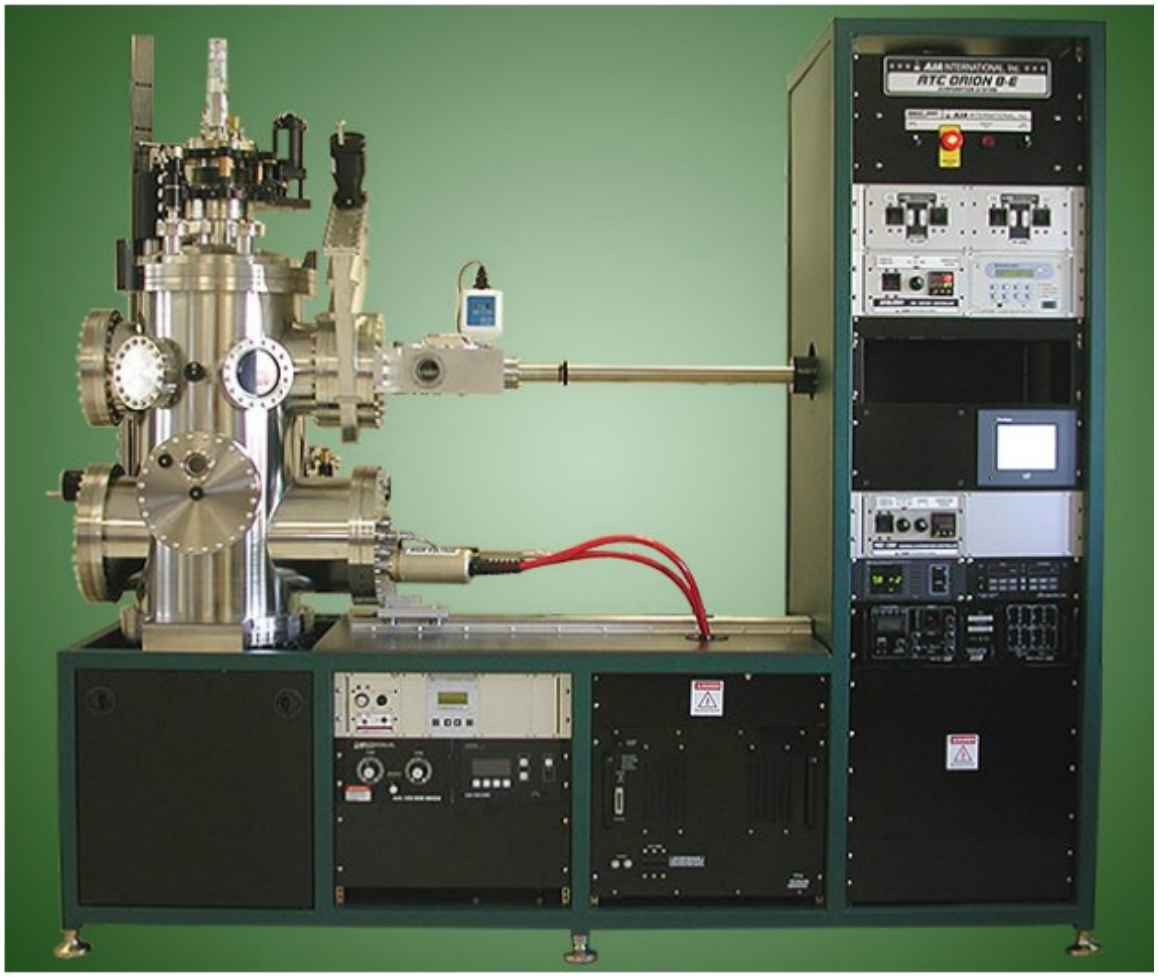

Figure 3.7 Photo of AJA ATC-ORION-8E UHV electron beam evaporation system used in this project

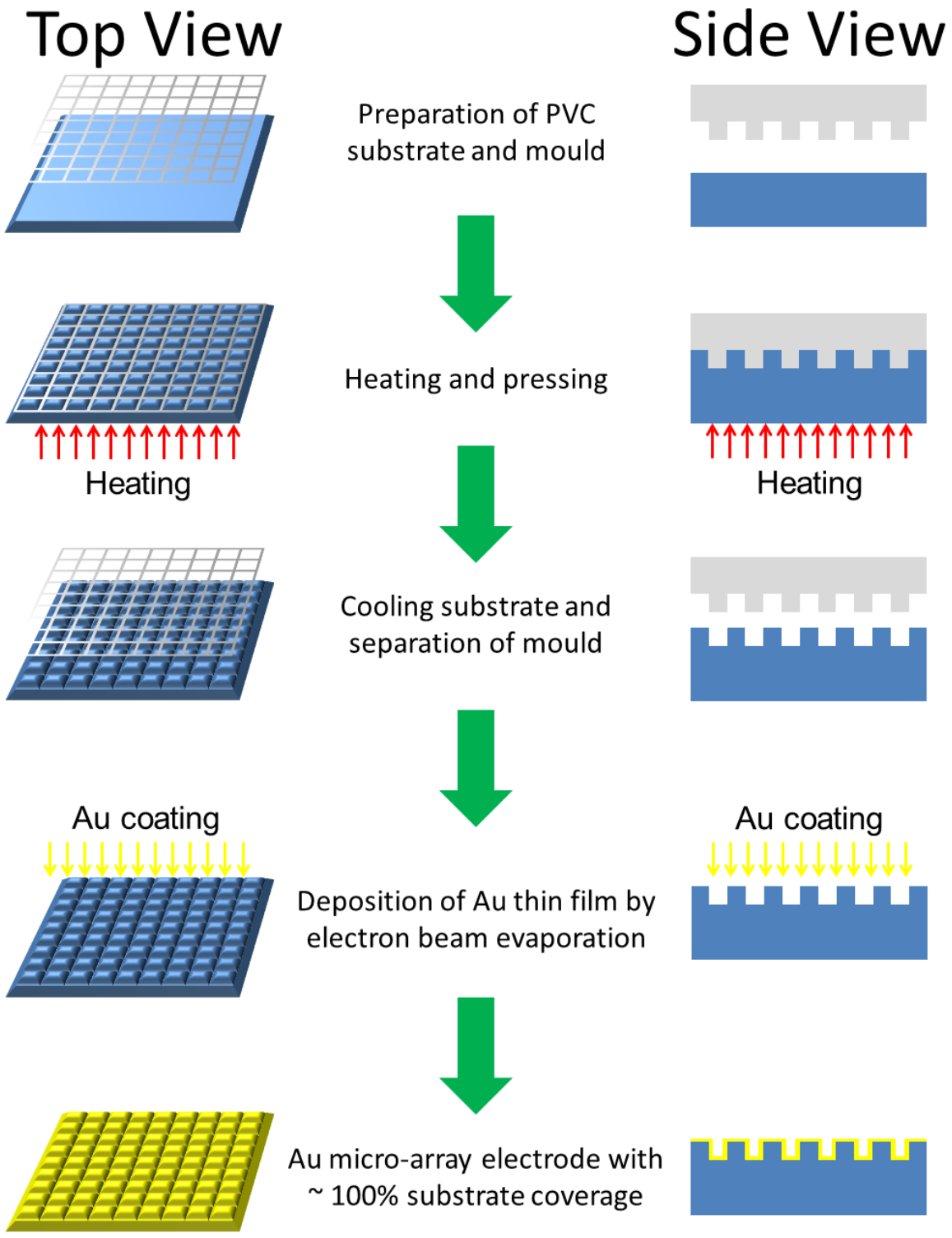

Figure 3.8 Schematic illustration of the fabrication process of flexible Au MA electrode on PVC substrate

3.2.2.1 Cleaning of PVC Substrates

PVC substrates were cut into small rectangular pieces (with the sizes being 5.0 × 7.5 mm^2 or 10 × 15 mm^2). They were rinsed with deionised water and absolute ethanol in a 300 W ultrasonic bath for 10 min each, and this process was repeated for several times to obtain a clean surface. Following that, the PVC substrates were dried in an oven at 70 °C for 30 min to completely remove any residual ethanol.

3.2.2.2 Determination of Phase Transition Profile of PVC

Since heating temperature is one of the key parameters of the imprint process, it is important to understand how PVC transforms upon heating, such that the parameter could be optimised. To achieve this, a small piece of PVC substrate was weighed by a high-accuracy electronic balance and loaded into a set of Al pans according to the standard solid-sample setup. Another set of empty Al pans was made in the same way as the reference. The samples were then transferred into a differential scanning calorimeter (DSC, Q10, TA Instruments, USA) and placed at the designated positions as instructed by the equipment. The system temperature was carefully calibrated prior to the measurement, which was carried out in a flowing N_2 environment. The PVC sample was heated from 25 °C to 200 °C at the ramping rate of 10 °C/min and the thermal phase transition profile was monitored.

3.2.2.3 Fabrication of Patterned PVC Substrates

Cleaned PVC substrates with the size of 5.0 × 7.5 mm^2 were used as the preliminary workpieces. 300-mesh Ni grids were used as the mould. A single Ni grid was placed on a PVC substrate and loaded into the CNI system. N_2 was used to apply pressure (ranging from 2 to 8 bar) and the PVC substrates were thermally imprinted (with heating temperature ranging from 70 °C to 150 °C) by the CNI system to obtain the micrometre scale array structure. The imprinting duration was varied from 1 to 5 min. The Ni grids were then removed from the PVC substrates after cooling down to the room temperature.

Upon determination of the optimum parameters, PVC substrates with the size of 10 × 15 mm^2 were used as the final workpieces. Ni grids of the same mesh grade were arranged into a 3 × 3 matrix on the PVC substrate for imprinting, and the samples were varied with Ni grids of different mesh grades (ranging from 50-mesh to 400-mesh).

3.2.2.4 Deposition of Au Thin Film

Compared to the fabrication of Au nano-ring arrays (**Section 3.2.1.2**), where the substrate (Si/SiO_2) is inorganic, the substrate for Au deposition now is a polymer; this has made magnetron sputtering unsuitable, because the highly energetic target materials could cause potential substrate heating and subsequently lead to melting of PVC. In contrast, electron beam evaporation is capable of avoiding such issue, and is thus chosen in this work. Its capability in coating complex geometries with precise control of deposition rate (as low as 1 nm/min) is an additional advantage. The patterned PVC substrates were cleaned again (as introduced in **Section 3.2.2.1**) to remove any residual contaminant and subsequently fixed in a PVD chamber (with the chamber pressure being 10^{-7} bar) for electron beam evaporation. Au particles (99.99% purity) were used as the source and evaporated at the voltage of 10 kV. The deposition rate was controlled as 0.5 Å/s and carried out at room temperature to produce 100 nm Au thin film.

3.2.3 Fabrication of Highly Strained Single Crystalline Au NPs

An Au grid was stacked on top of a conventional TEM Cu grid (with holey carbon support film facing up), and they were loaded into a PIPS system (Model 691, Gatan Inc., USA) as displayed in **Figure 3.9**. When the Ar^+ ions bombard onto the surface of the Au grid, they apply a shear force and remove the surface materials in the form of Au NPs. As such, the surface of the produced Au NPs would render some deformation which might be recovered from the stress/strain caused. If the shear force is strong enough, the deformation will break through the elastic limit, and thus the Au NPs produced are possible to be strained with high surface energy.

Figure 3.9 Photo of Gatan 691 precision ion polishing system used in this project

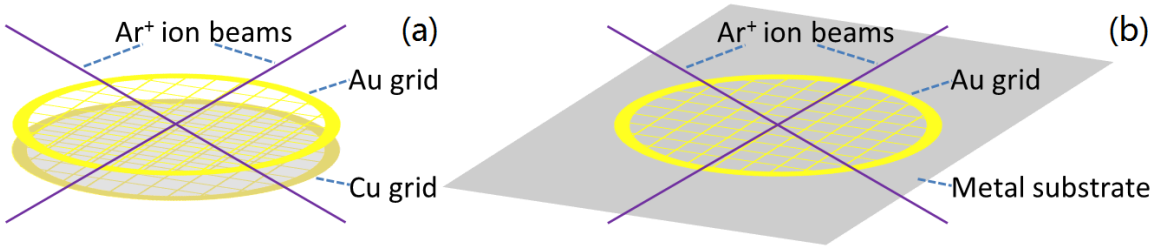

Figure 3.10 Schematic setup of sample preparation by PIPS: (a) for TEM characterisation and (b) for electrode preparation.

At the fixed Ar gas pressure of 2 bar, the two Ar^+ ion beams were produced with different energy levels (3 keV or 5 keV) and different inclined angles (1°, 3° or 5°) were set. A set of optimum parameters was to be determined. To prepare samples for further characterisations and electrochemical testing, Ti and brass substrates were cut into 6 × 4 mm^2 pieces and cleaned with absolute ethanol in an ultrasonic bath (of 300 W power) for 30 min. Upon drying, they were separately loaded into the PIPS system in the same way

with the aforementioned parameters. The mass loading of Au (~ 1.9 mg/cm^2) was obtained by weighing the substrate before and after deposition. The schematic setups for both are illustrated in **Figure 3.10**.

3.3 Characterisation and Testing Techniques

The characterisation and testing techniques used in this project are listed in this section. Basic theories and working principles are explained with schematic illustrations of key parts of the respective instrumentation. Following that, the common applications of each used in this project and the modes of operation are stated in details.

3.3.1 X-Ray Diffraction (XRD)

Electromagnetic (EM) waves comprise of a spectrum of waves with different wavelengths. Amongst these, the wavelengths of X-rays are typically in the order of angstroms (1 Å = 10^{-10} m), which are comparable to the radii of atoms. This allows a wide spectrum of applications of X-rays in modern technology, such as obtaining radiographs in medical science, radiation therapy, airport security checks and detection of counterfeit artworks. In the field of materials science and engineering, it is widely employed for the study of crystallography. Some of the most common applications of XRD include determination of crystallinity of materials, identification of phases and corresponding unit cells, measurement of crystallite size, as well as analysis of textures and strain mapping. Advanced application of XRD may assist in studying potential defects and phase transition of crystals, thereby helping in construction of phase diagrams in alloys and solid solutions.

In crystalline materials, atoms are orderly arranged in arrays with well-defined inter-atomic spacing (the d-spacing, denoted as $d_{(h\ k\ l)}$) between lattice planes. Since the wavelengths of X-rays have a comparable size to the d-spacing of crystals, the structures of materials could be revealed by precise matching of experimental results of XRD against a standard database.

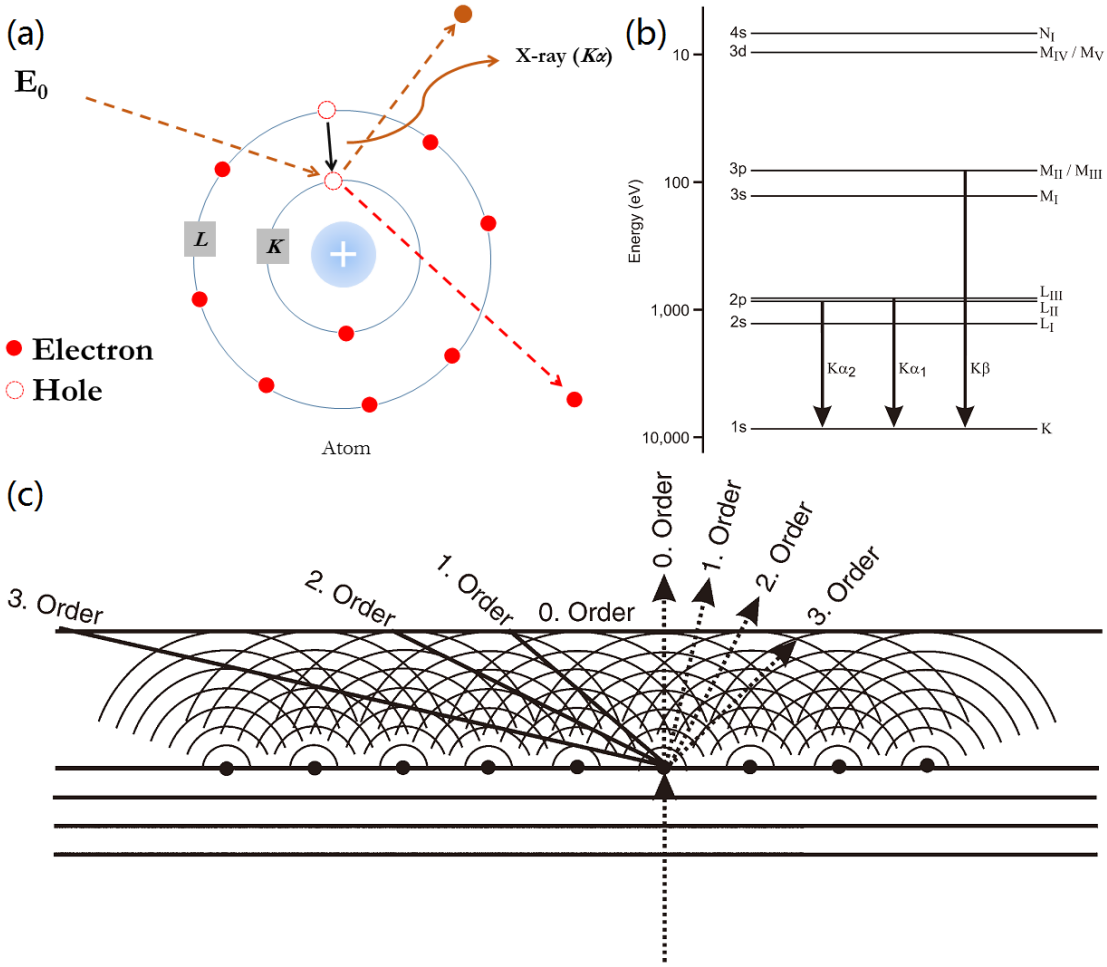

Figure 3.11 (a) Schematic illustration of the production of X-rays;[10] (b) energy level diagram showing electron transitions from different shells and orbitals, thereby producing X-rays of different wavelengths;[11] (c) schematic diagram of plane wave scattering by a one-dimensional chain of atoms.[12]

When electrons are accelerated from cathode by a high voltage and allowed to strike onto a metallic target (most commonly being Cu) at anode,[13] electrons from inner shell of atom are knocked out and electrons from outer shell fall into inner shell to reduce overall energy content. At the same time, the extra energy in this process is released as X-rays (**Figure 3.11 a**). Each element has its own characteristic X-ray pattern. For the same element, when the energy of incident beam varies, the electron transition process could occur from different shells and orbitals, thereby producing X-rays of different wavelengths (**Figure 3.11 b**). When the X-rays pass through a slit, diffraction will occur

due to the wave-particle duality of the EM radiation. If the radiation passes through multiple slits, the diffracted waves interfere with each other and maxima are produced upon constructive interference. The intensity of the maxima reduces with increasing order (**Figure 3.11 c**).

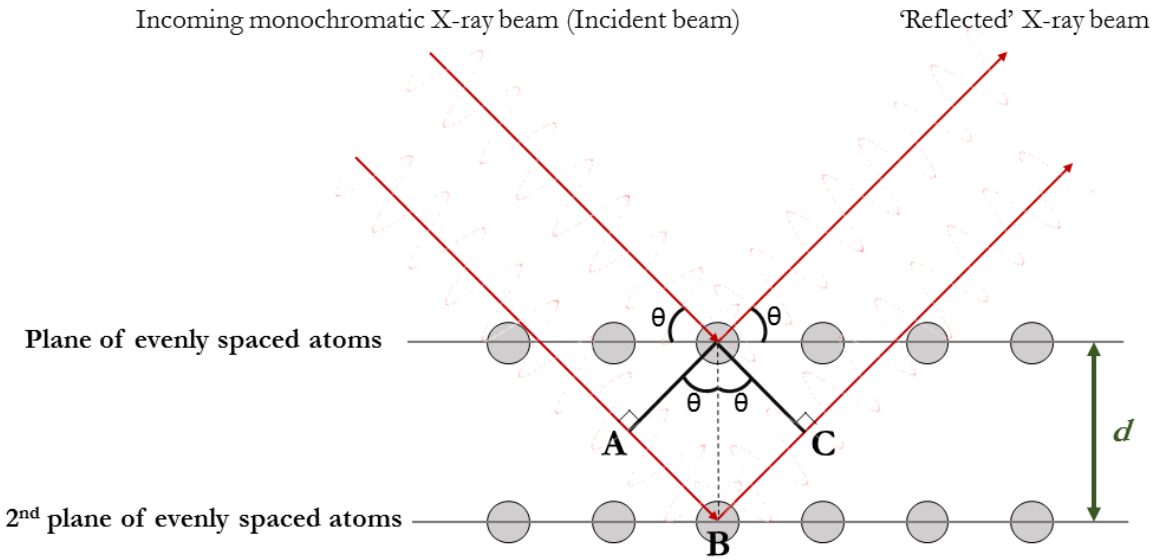

Figure 3.12 Schematic illustration of the interaction of X-ray with crystal planes, for the derivation of the Bragg's law of diffraction.[14]

By applying this theory to crystallography, when a beam of monochromatic X-rays is produced to strike a crystal lattice at an incident angle of θ, it will be reflected at the same angle (**Figure 3.12**). If the Ewald sphere intersects a reciprocal lattice point of the crystal, the Bragg's law is fulfilled (**Equation 3.1** as derived from **Figure 3.12**), and the constructive interference leads to the display of the characteristic patterns in the diffractogram. Some basic crystallographic information could thereby be determined, which includes the crystal structures, space groups and lattice constants of materials.

Equation 3.1 Bragg's law of diffraction[15]

$$n\lambda = 2d_{(h\,k\,l)} \sin\theta$$

where n is the diffraction order (and assumed to be 1), λ is the known wavelength of the produced X-rays, $d_{(h\,k\,l)}$ is the d-spacing of crystals to be determined, and θ is the angle of the scattered beam as measured.

In this project, all samples are in the form of thin films and therefore the XRD patterns of the samples were recorded on a thin film X-ray diffractometer (XRD-6000, Shimadzu, Japan) as shown in **Figure 3.13**. The Cu Kα1 radiation was produced at 40 kV and 30 mA with $\lambda \approx 1.5405986$ Å. All scans were performed under 2θ (thin film) mode at an X-ray grazing angle of 1.0°.

Figure 3.13 Photo of Shimadzu XRD-6000 thin film XRD used in this project

3.3.2 Electron Microscopies

Microscopies are the express ways to have an enlarged view of tiny features. Apart from light microscopes which use visible light as the incident beam, electron microscopes utilise a beam of accelerated electrons emitted from the electron gun. An electron gun contains a filament, which emits electrons upon heating or application of strong electric field. It could be classified into thermionic emission and field-emission guns (FEG), and

the FEGs can be further divided into cold and thermal FEGs. The mechanisms and performance of the three types of electron guns are compared as **Table 3.1**:

Table 3.1 Comparison of different types of electron guns[16]

	Thermionic emission	**Schottky-type thermal field-emission**	**Cold (cathode) field-emission**
Material	W or LaB_6 crystal	ZrO/W (1 0 0)	W single crystal
Mechanism of emission	Filament is heated with joule heat, causing the electrons to gain thermal energy and gets freed upon exceeding the work function of the material.	Strong electric field is applied to reduce the energy barrier of electron emission. Electrons are emitted due to Schottky effect upon thermal assistance (heating). Tip is coated with a thin layer of ZrO to enhance electrical conductivity at high temperature, so as to further reduce the energy barrier.	Strong electric field is applied to reduce the energy barrier of electron emission. Electrons are emitted due to tunnelling effect.
Electron beam size	~ 10-30 μm	< 10 nm	< 10 nm
Brightness	~ 10^5-10^6 A/cm^2·sr	Up to ~ 10^8 A/cm^2·sr	Up to ~ 10^9 A/cm^2·sr
Energy spread	A few eV	~ 0.7 eV	~ 0.3 eV
Stability	Stability depends on several external physical conditions	Very high stability, "flashing" of electron guns is not needed	High stability, "flashing" of electron guns is needed periodically
System requirement	High vacuum	Ultra-high vacuum	Ultra-high vacuum
Cost	Relatively cheap	Much more costly	Much more costly
Common applications	Entry level imaging and analyses	High resolution imaging and analyses	High resolution imaging and analyses

Equation 3.2 Calculation of wavelengths of incident beam in microscopes[16]

Wavelength of photons in EM,[17] including visible light $$\lambda = \frac{h \cdot c}{E}$$

Wavelength of electrons in motion[16] $$\lambda = \frac{h}{\sqrt{2m_e \cdot e \cdot V_{acc}}}$$

where λ is the wavelength of the incident beam, h is the Planck constant ($6.62607015 \times 10^{-34}$ J·s), c is the speed of light in vacuum (299792458 m/s), E is the energy of the incident light, m_e is the mass of a single electron ($9.10938356 \times 10^{-31}$ kg), e is the electron charge ($1.602176634 \times 10^{-19}$ C), and V_{acc} is the accelerating voltage of the incident electron beam.

Based on the wave-particle duality of electrons, accelerated electrons possess much higher energies and therefore have a much shorter wavelength compared to visible light (**Equation 3.2**). Since resolution is defined as the smallest separation at which two points can be seen as distinct entities, electron microscopes may resolve much smaller features which conventional light microscopes could not reach. Nevertheless, the resolution cannot be infinitely small and there is a limit, which is caused by aberrations.[18] The direct consequence of having aberrations is that beams could not be focused to one single image point as a perfect lens (**Figure 3.14 a**). The greatest contributions to the non-convergence of beams are from spherical aberration (**Figure 3.14 b**) and chromatic aberration (**Figure 3.14 b**). Aberrations cannot be avoided or totally removed, but minimising the aberrations could largely help in improving the resolution limit.

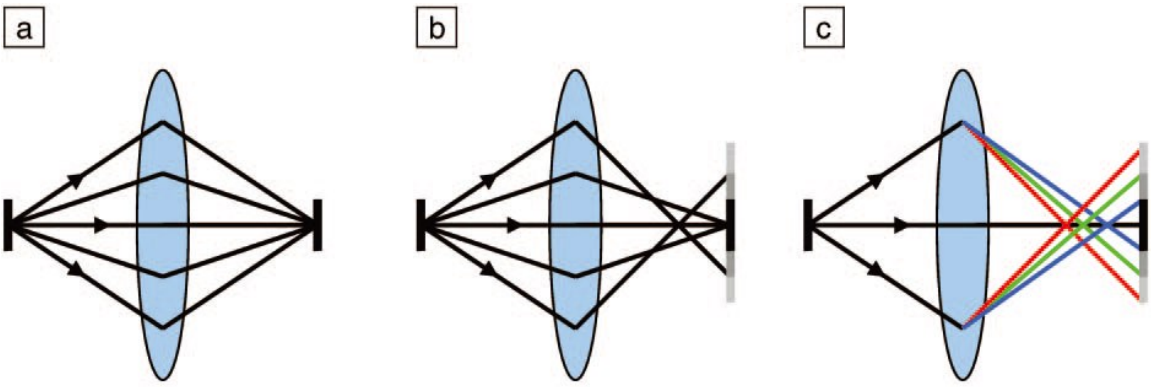

Figure 3.14 Schematic illustrations of common aberrations: (a) a perfect lens; (b) with spherical aberrations and (c) with chromatic aberrations.[18]

When electron beam is illuminated onto the surface of sample, there is a beam-specimen interaction, which will produce a series of possible signals (**Figure 3.15**). According to the pathways of the incident beam, common electron microscopies are generally divided

into two types, namely scanning electron microscopy (SEM) and (scanning) transmission electron microscopy ((S)TEM). The incident beam usually only scans on the surface of sample in SEM, while it may pass through the sample in TEM/STEM.

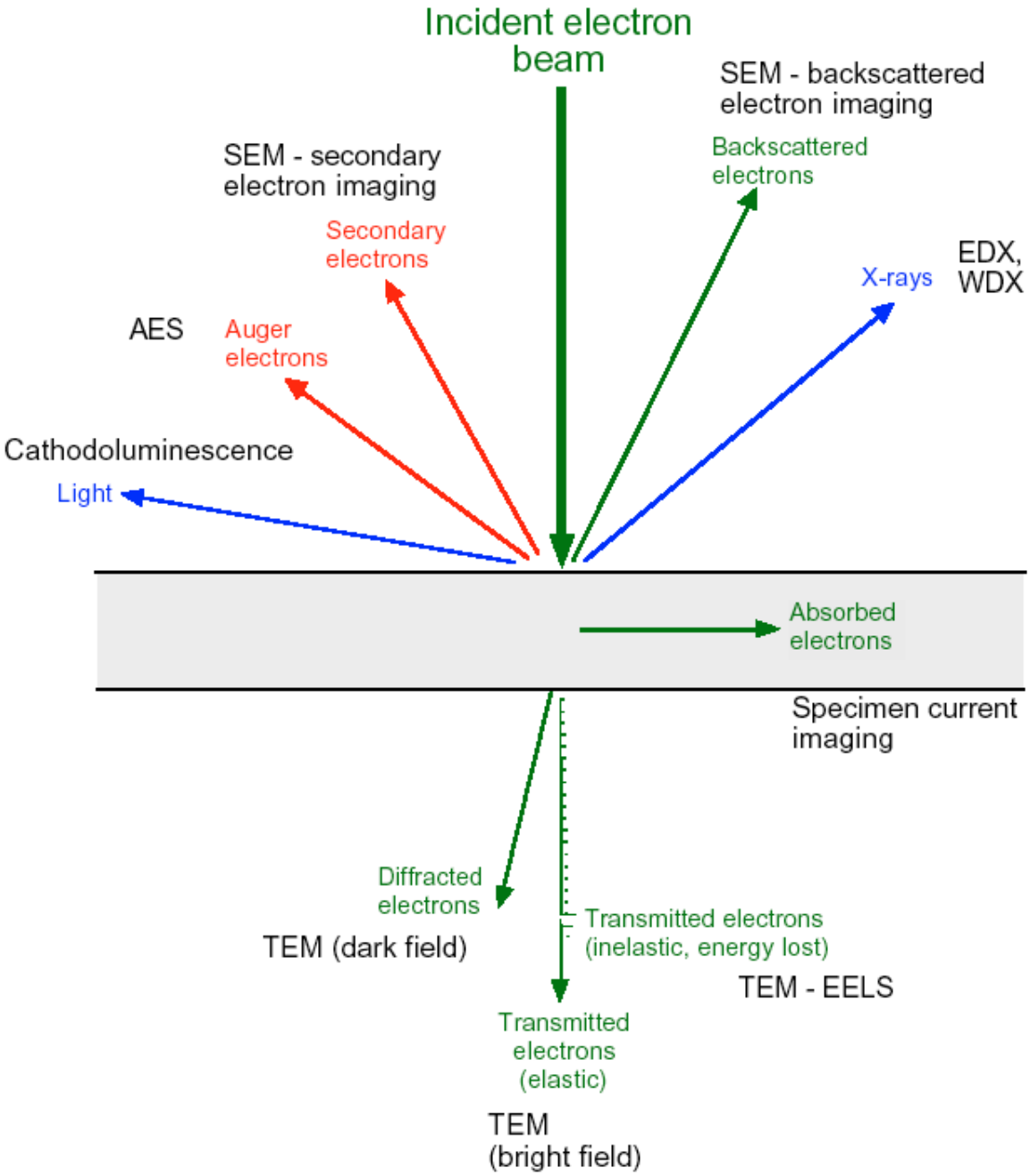

Figure 3.15 Schematic illustration of the beam-specimen interaction during electron microscopies and all possible signals being produced.[19]

The most commonly obtained signals include secondary electron imaging (SEI), backscattered electron imaging (BEI), elastically transmitted electrons (bright field TEM imaging), diffracted electrons (dark field TEM imaging) and X-rays (energy-dispersive X-ray (EDX) spectroscopy). These signals correspond to morphological observation, viewing of phase distribution, resolving the internal structures of materials and elemental analyses, respectively.

3.3.2.1 Field-Emission Gun (FEG) SEM

SEM is an efficient method to perform surface analysis on samples. When the electron beam is emitted from the electron gun and passes through the SEM column, the scanning coil controls the scanning pathway of the electrons. The magnification of an image is defined as the ratio between the area of screen and the area of scanned region. The accelerating voltage of SEM is normally up to 30 kV and the theoretical magnification is usually within the range of 25×to 1 M×.[20]

The beam-specimen interaction, as introduced previously, will lead to the creation of an interaction volume. As the beam energy increases, the depth of interaction may be ~ 0.5-2.0 μm down into the sample from its surface (**Figure 3.16 a**). Different signals are generated during this interaction. The most commonly received and interpreted signals are secondary electrons (SE), backscattered electrons (BSE) and characteristic X-rays respectively, along the beam pathway. **Figure 3.16 b** illustrates the production of these signals. When a primary electron (PE) interacts with the nucleus of a surface atom of the sample, elastic scattering results in backward bouncing of the PE and collected as the BSE. On the other hand, inelastic scattering will knock off an electron from the surface atom of the sample and collected as the SE; if an inner shell electron is knocked off, another electron from outer shell will fall into the inner shell and release the extra energy in the form of characteristic X-rays.[21]

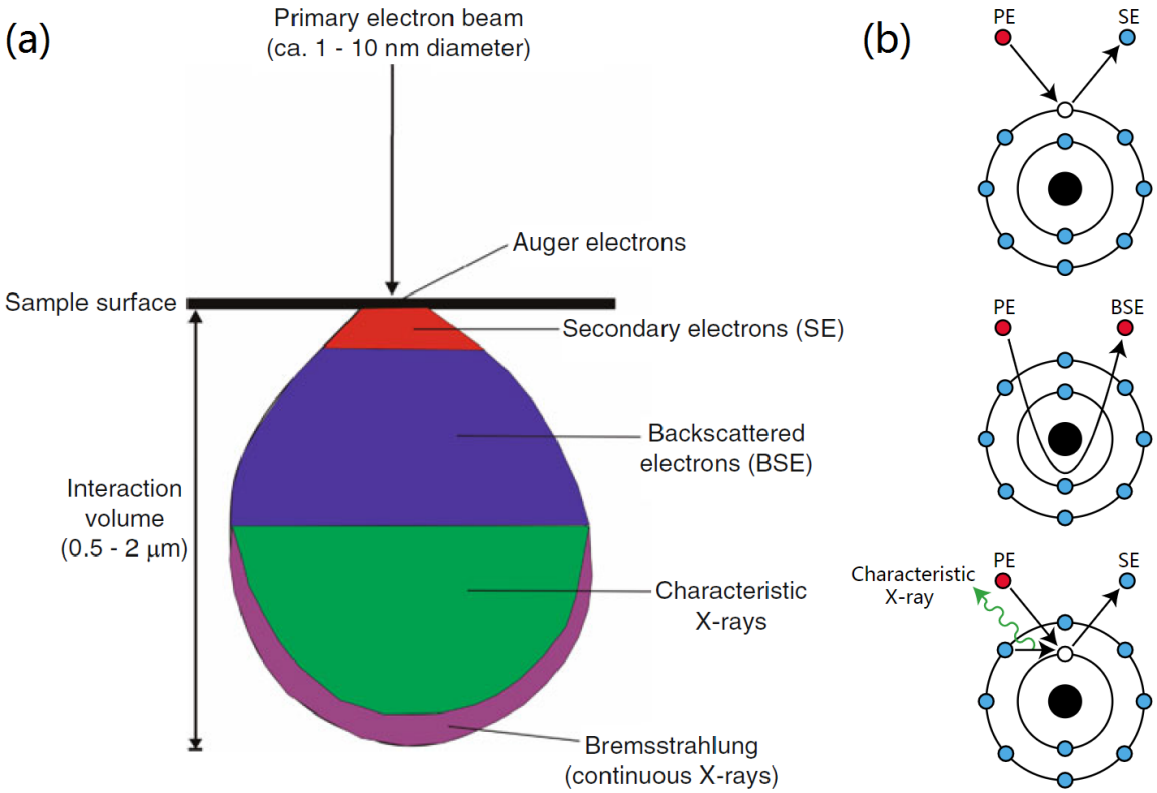

Figure 3.16 (a) Schematic diagram of interaction volume; (b) illustration of the production of various signals, (top) secondary electrons, (middle) backscattered electrons and (bottom) characteristic X-rays.[22]

In this project, FEG-SEM is mainly used to examine the surface morphologies of the microstructures and carry out elemental analyses. All operations for plane-view samples are performed in an in-lens Schottky plus FEG-SEM (JSM-7800F Prime, JEOL, Japan) as shown in **Figure 3.17**. The detailed internal structure and external attachment modules of the instrument are clearly illustrated in **Figure A.1**. The FEG-SEM was operated at the accelerating voltage of 5 kV for SEI, 20 kV for EDX and 30 kV for transmission electron detection (TED) mode.

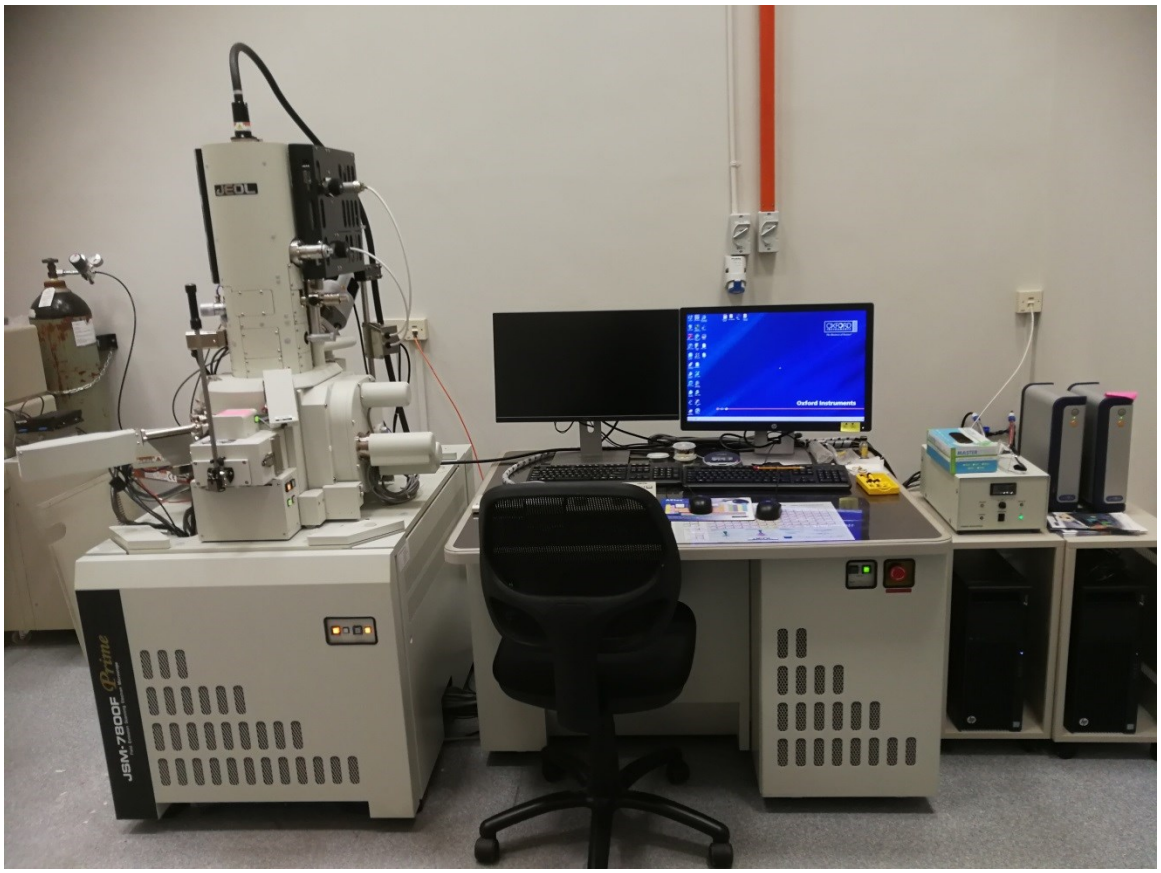

Figure 3.17 Photo of JEOL JSM-7800F Prime FEG-SEM used in this project

3.3.2.2 Dual-Beam FEG-SEM/FIB

FIB is a powerful tool in labs and industries across many fields. With the invention of LMIS, Ga metal is heated in the ion gun to molten state and gets ionised by field evaporation due to the application of a suitable voltage to the extractor.[23] Due to its low melting point (29.8 °C) and volatility, as well as low surface free energy and vapour pressure,[23] the Ga^+ ion beam could be focused and emitted into a sharp probe with an ultrafine radius (< 5 nm).[24]

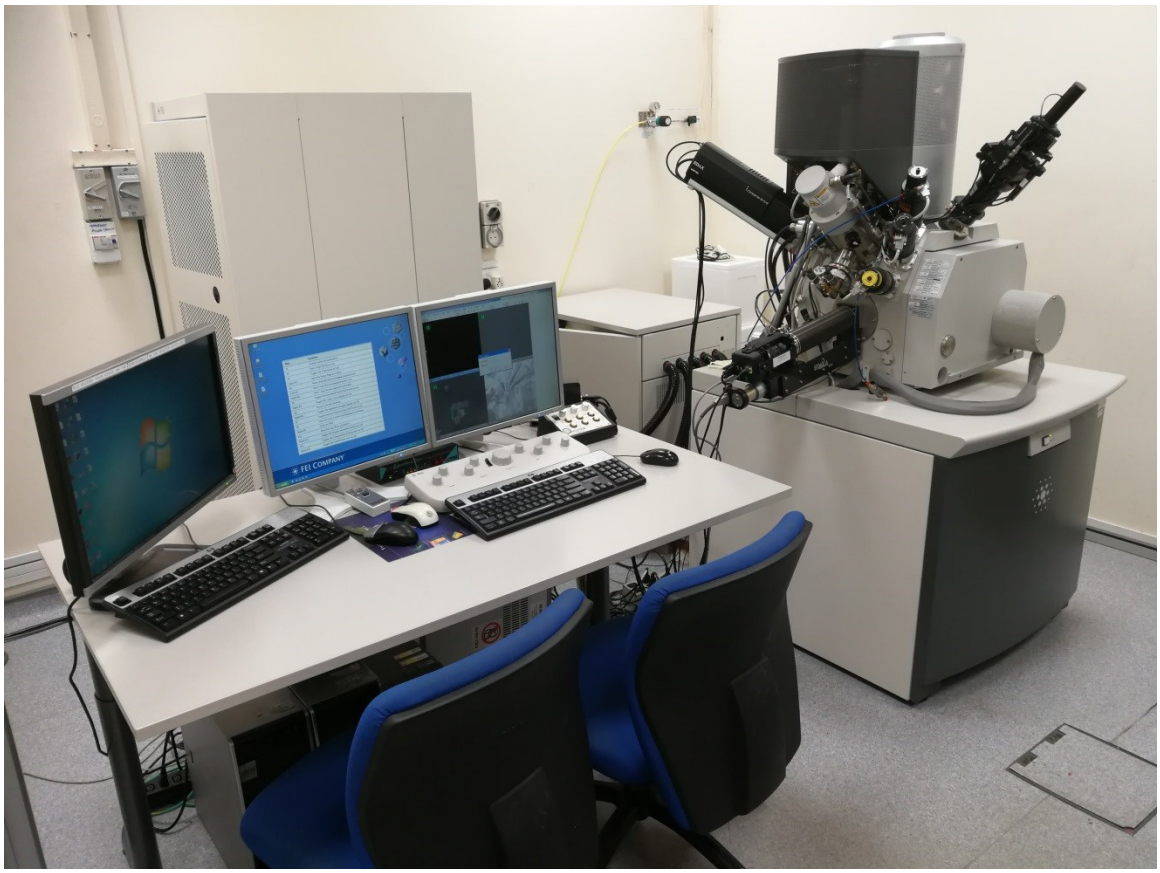

Figure 3.18 Photo of FEI Nova NanoLab 600i FEG-SEM/FIB used in this project

It was initially designed for semiconductor industries for circuit modification and failure analysis, and with the rise of nanotechnology, more capabilities of FIB have been unravelled. In modern days, the FIB column is usually integrated onto an FEG-SEM and makes it into a dual-beam system (**Figure 3.18**). There is an angle between SEM and FIB columns (usually 52°-54°), the site of interest on the surface of sample must be set at the correct eucentric height (usually ~ 5 mm), so as to view at the same point by SEM and FIB for *in-situ* observations and operations (**Figure 3.19**).[25]

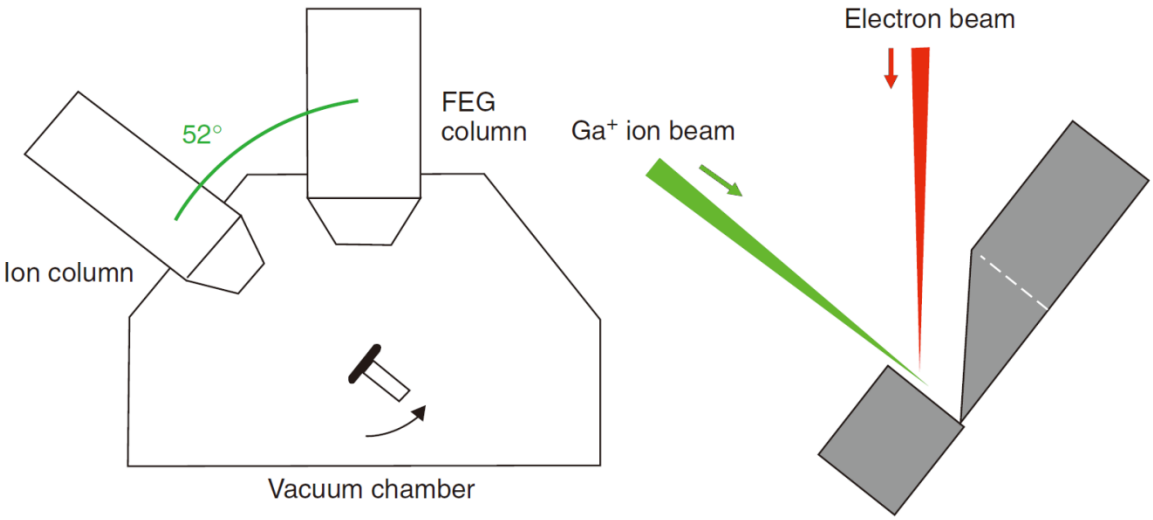

Figure 3.19 Schematic diagram showing the dual-beam system and the concept of eucentric height[25]

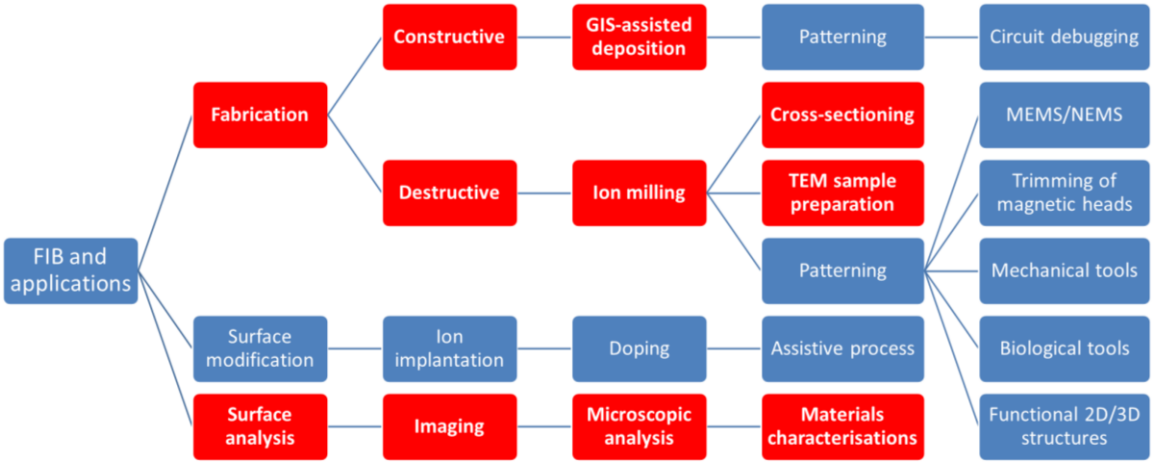

Figure 3.20 A panoramic view of the applications of FIB technology.[24] The techniques used in this project are highlighted in red.

With the aid of LMIS and gas injection system (GIS), the dual-beam FEG-SEM/FIB system may have vast range of applications. The main functionalities could be summarised into materials characterisation (imaging and analysis), nano-fabrication (deposition and milling), as well as surface modification (ion implantation). **Figure 3.20** shows the panoramic view of applications of FIB technology.[24] The general applications of FIB are classified into three types, namely fabrication, surface modification and surface analysis. The first two types are typically carried out using ion beam with various

beam currents (controlled by the aperture size); a special case is the GIS-assisted deposition, which could be done with the electron beam either alone or for enhancement. Surface analysis (especially imaging) is typically carried out by either electron beam or ion beam, with the respective signals forming the secondary electron/secondary ion (SESI) images. As its sub-category, microscopic analyses like electron backscatter diffraction (EBSD) or EDX have to be carried out using electron beam alone.

In this project, the key functions of FIB to be used include SESI imaging, EDX elemental analysis, GIS-assisted deposition and ion milling, as well as cross-sectional TEM sample preparation (X-TEM). Compared to the conventional way of X-TEM, FIB has many advantages and only a few shortcomings (**Table 3.2**). All operations are performed in a dual-beam FEG-SEM/FIB system (Nova NanoLab 600i, FEI, USA). The dual-beam FEG-SEM/FIB system was operated at electron accelerating voltage of 5 kV under field emission mode for SEI and EDX, and operated at ion accelerating voltage of 30 kV for milling/deposition and 2-5 kV for cleaning during X-TEM. The TEM thin lamellae are prepared by the *in-situ* lift-out method with the aid of an integrated nanomanipulator (OmniProbe 200, Oxford Instruments, UK), and transferred onto three-post TEM grids.

Table 3.2 Comparison of cross-sectional TEM sample preparation methods

Dual-beam FEG-SEM/FIB	**Traditional preparation method**
Single equipment	Multiple instruments required
Sample must fit in SEM/FIB chamber	No requirement on sample size
Sample must be electro-conductive, or coated with a conductive layer	No requirement on sample conductivity
Site-specific sample preparation	Random selection of preparation site
Extra protective layer and possible FIB-induced re-deposition of second phase	No extra materials other than sample
Multiple samples on one grid is possible	Only one sample on one grid

3.3.2.3 FEG-TEM/STEM

In the field of materials science, TEM and STEM are powerful and advanced analytical tools. In a modern TEM/STEM, three fundamental functions are provided – imaging,

diffraction and spectroscopy.[19] The modern TEM/STEM is usually operated at the accelerating voltage of 80-300 kV, according to **Equation 3.2**, the wavelength of incident electron beam could reach picometre scale and thus TEM/STEM is capable of presenting more information compared to SEM, for example, resolving much smaller features like crystal lattice and forming diffraction patterns of samples. On the other hand, the major limitation of TEM/STEM arises from the thickness of specimens – they need to be ~ 100 nm or less in order to be electron "transparent",[19] and that creates challenges in the sample preparation procedures.

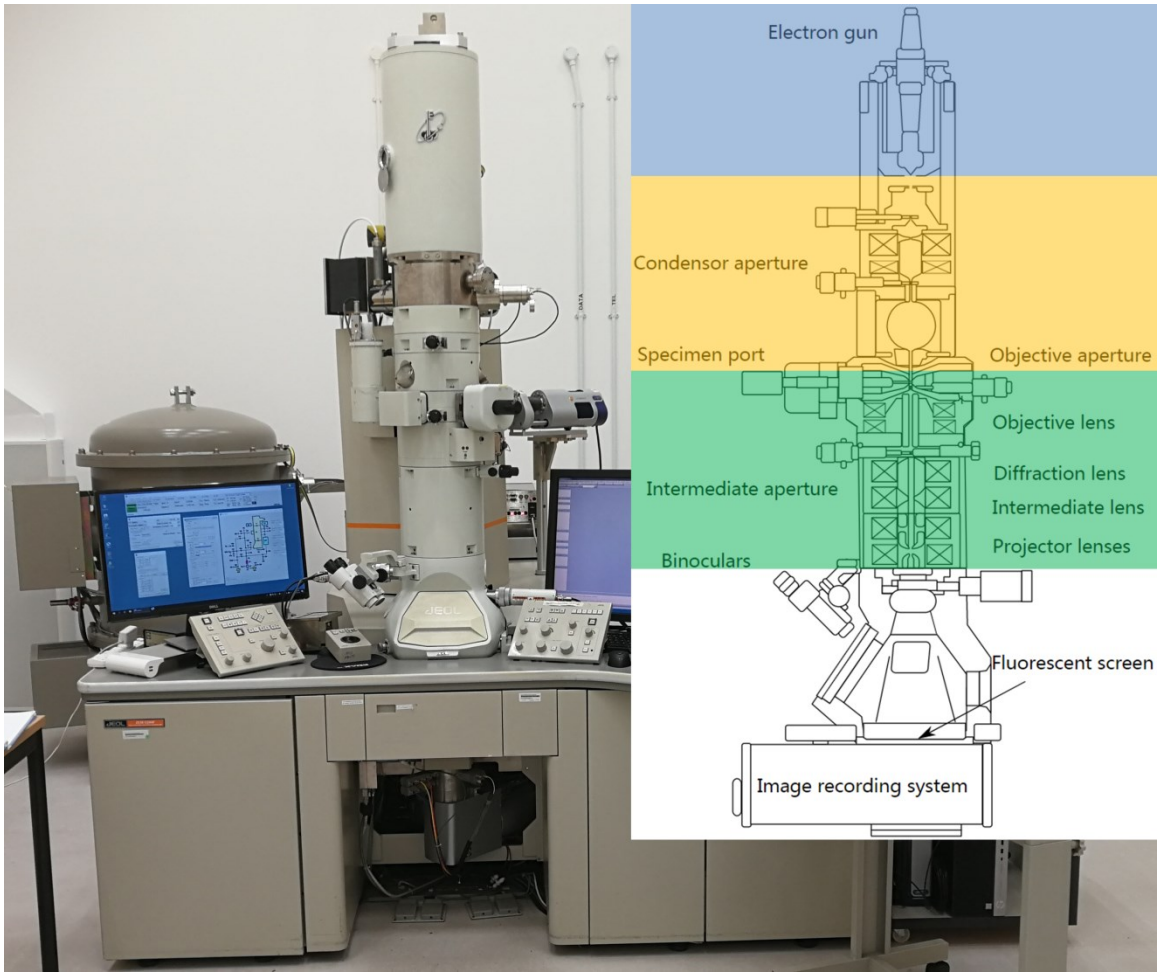

Figure 3.21 Photo of JEOL JEM-2100F FEG-TEM/STEM used in this project and the inset diagram is the schematic illustration of the instrument structure,[26] where blue marks the electron source part; yellow marks the illumination system and green marks the imaging system.

The TEM/STEM is a complex instrument with many sub-systems. As shown in **Figure 3.21**, the instrument can be generally divided as the vacuum system, the electron source, the illumination and imaging systems, the sample holder, as well as the recording system.[19] Similar to other electron microscope systems, the TEM/STEM also works in a vacuum environment; the electron beam is produced by the electron gun and first passes through the condenser lens and aperture in the illumination system, so as to get focused onto the specimen at the suitable stage height. There are many types of specimen holders for various applications. Conventional holders may have single/double-tilt configurations, such that the specimen could be oriented by tilting along either the X-axis or both X- and Y-axes (with Z-axis parallel to the optical axis) for study in crystal structures and diffractions. There are special holders for specific requirements, for example, low-background holders have Be windows for EDX analyses with minimum Bremsstrahlung and characteristic X-rays; multiple-specimen holders realises quick switching of samples without the need to remove the specimen holder; cryo-transfer holder ensures the transfer of cold specimens without the condensation of water vapour; tomography holder allows 360° tilting of specimen for 3D reconstruction purpose; *in-situ* holders could assist scientists in understanding the responses of specimens to external stimuli, such as heating, cooling, straining, probing, charging, being in liquid/gas environment, and so on.[19]

The imaging system is mainly comprised of objective lens and aperture, intermediate lens (also known as diffraction lens) and selected area (electron) diffraction (SA(E)D) aperture, as well as projector lens. When the incident beam passes through the thin specimen, it gets diffracted and focused by the objective lens; a diffraction pattern (DP) is formed on the back focal plane (BFP) and an intermediate image is generated on the image plane (**Figure 3.22**).[19] To switch between operational (imaging/diffraction) modes, simply adjust the strength of the intermediate lens and it will select either of the above as the object to form the second intermediate image. Below that, the projector lens operates with a fixed strength and projects the images onto the phosphor screen for viewing.[19] The beauty of electron microscopes is that all lenses are electromagnetic, thus the strength can be varied by the current passing through the coils. Weakening the lens leads to the lengthening of the focal length, thereby results in the magnification of object.[19]

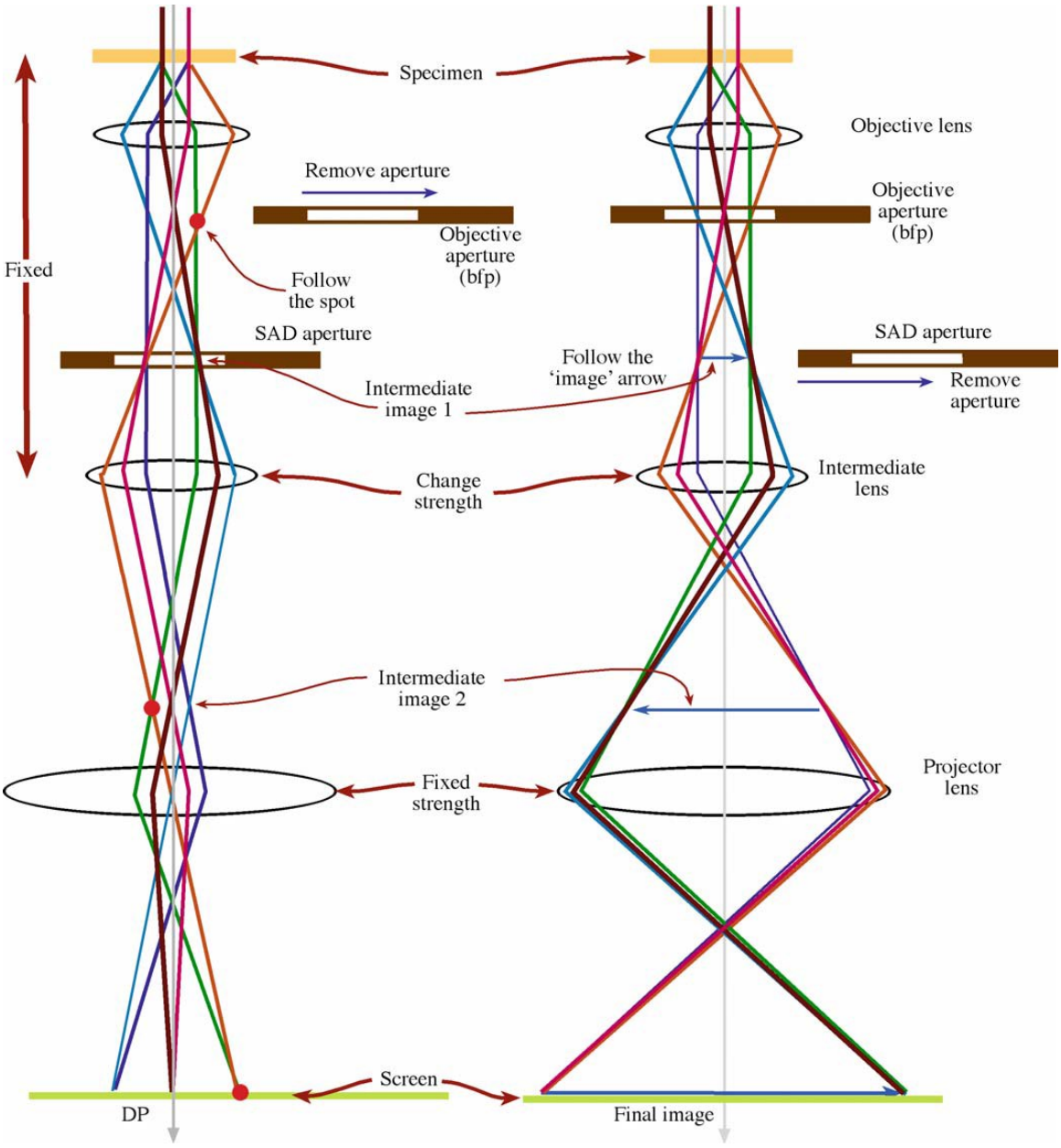

Figure 3.22 A simplified schematic illustration of operations in (left) diffraction and (right) imaging mode[19]

When there is a difference between electron densities of adjacent areas, a contrast can be detected.[19, 27-29] Contrast matters in the analysis of TEM/STEM images. Variation in atomic mass or thickness of sample or a combination of both causes mass-thickness contrast; it is exceptionally useful in high resolution (HR) STEM with high angle annular

dark field (HAADF) signals to distinguish heavy elements from the lighter ones, and that is specially named as the Z contrast. Apart from the abovementioned amplitude contrasts, crystalline regions could be separated from the amorphous ones by diffraction contrast, which utilises the differences between the DPs generated by these regions. Phase contrast arises from the interference of beams diffracted by the specimen; a region with constructive interference is different from that with destructive interference. This is commonly observed in both low magnification and HRTEM images.

In this project, while samples in the form of NPs were directly prepared to be deposited onto TEM copper grids, the cross-sectional samples were to be separately prepared. The TEM thin lamella was prepared by the *in-situ* lift-out method using the dual-beam FEG-SEM/FIB system with an integrated nanomanipulator (OmniProbe 200, Oxford Instruments, UK), and transferred onto a three-post copper grid. The surface and interfacial morphology, crystal structures and elemental distributions of the samples were examined under an ultra-high resolution Schottky FEG-TEM (JEM-2100F, JEOL, Japan), which was operated at the accelerating voltage of 200 kV (**Figure 3.21**).

3.3.2.4 Energy-Dispersive X-Ray (EDX) Spectroscopy

To analyse elemental compositions and distributions, EDX is an ideal technique with simple operations. The EDX spectrometer is usually attached to electron microscopes to provide *in-situ* analyses. The working principle of EDX is based on the beam-specimen interaction (**Figure 3.15**). With a suitable interaction volume, each element will give out characteristic X-rays with distinct energy levels (**Figure 3.16**), which generate individual peaks. The collection of all available peaks makes up a particular spectrum in an analysis. EDX is excellent in qualitative analysis to track the presence of chemical elements in a sample, but it has many limitations, such as the resolution to overlapping characteristic X-rays.[21] Furthermore, the isotropic emission of X-rays affects the signal detection,[21] thus EDX is often deemed as a semi-quantitative analytical technique.

In this project, the EDX analyses (including spectroscopy and elemental mapping) were performed by laser-cooled EDX spectrometers with silicon drift detector, which are attached to the individual electron microscopes of operation. The EDX spectrometer attached to the FEG-SEM (Ultim® Max 17, Oxford Instruments, UK) has a 170 mm^2 detector window and was operated at the electron accelerating voltage of 20 kV; the spectrometer attached to the FEG-SEM/FIB (Octane Elite Plus, EDAX, USA) has a 30 mm^2 detector window and was operated at the electron accelerating voltage of 5 kV; the spectrometer attached to the FEG-TEM (Ultim® Max TLE, Oxford Instruments, UK) has a 100 mm^2 detector window and was operated at the electron accelerating voltage of 200 kV. The elemental mapping for the X-TEM samples was only performed on the EDX attached to FEG-TEM under the STEM mode at the accelerating voltage of 200 kV.

3.3.3 Electrochemical Performance Testing

When an electrochemical process takes place, the chemical reaction could generate an electrical signal that can be monitored, captured and recorded by a computer-controlled electrochemical workstation. As illustrated in the schematic diagram (**Figure 3.23**), there are plenty of modules attached on the workstation, so various electrochemical processes can be carried out and recorded. A modern electrochemical workstation usually adopts the three-electrode setup. The electrolytic cell comprises of a working electrode (WE), a counter electrode (CE) and a reference electrode (RE), which are in contact with an electrically conductive electrolyte.[30] By setting an appropriate program, the polarity of WE and CE can be defined, thus the sample to be tested should be loaded onto the WE. On the other hand, the CE mainly serves to form a closed circuit in connection with the WE, as well as to host electrochemical reactions to balance those carried out at the WE. The popular choices of materials for CE are Pt, graphite and glassy carbon electrode.

The potentials at electrodes are not constant values; the measurement must be compared against the RE, of which the electrode potential is accurately known. When a particular electrode is connected to the RE to form a micro-cell, the electrode potential could be calculated by measuring the potential of the micro-cell. Therefore,

the RE serves as the standard in electrochemical measurements and is a very important component in testing. The electrode reaction on the RE must be a single and reversible redox reaction, such that the electrode potential is stable and reproducible.

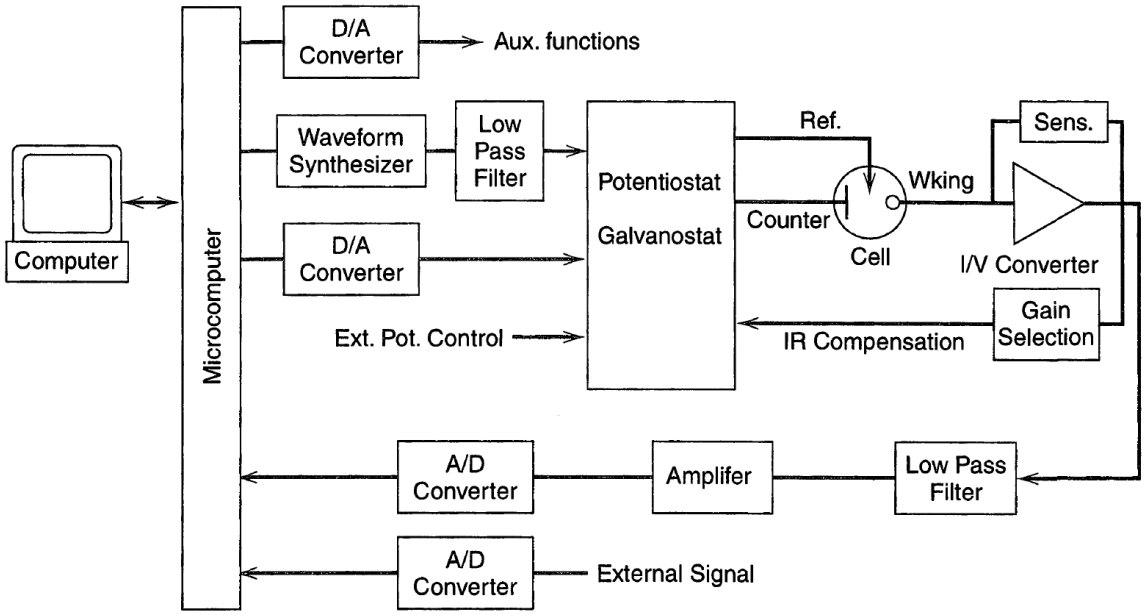

Figure 3.23 Schematic illustration of a computer-controlled electrochemical workstation with three-electrode setup, based on CH Instruments Model 600A.[30]

The standard hydrogen electrode (SHE) is a perfect RE but cannot be easily implemented for routine usage, hence it is often used as a comparative basis for other REs, and assumed to have a standard reduction potential (E^0) of 0 V at all temperatures. In contrast, the measured potential does not change with pH value of electrolyte.[31] Therefore a reversible hydrogen electrode (RHE) is more practical and reproducible, thus becoming a favourable standard for comparison. The frequently used REs in laboratories and industries include RHE, silver-silver chloride (Ag/AgCl) electrode, mercury-mercuric oxide (Hg/HgO) electrode, saturated calomel electrode (SCE), mercury-mercurous sulphate (Hg/Hg_2SO_4) electrode and copper-cupric sulphate ($Cu/CuSO_4$) electrode. Their equilibrium reactions and E^0 values against the SHE are listed in **Table 3.3**.

Table 3.3 List of commonly used reference electrodes[32]

Reference electrode	Equilibrium reaction	E^0 vs SHE†
SHE	$2H^+(aq) + 2e^- \rightleftharpoons H_2 \uparrow$	0 V
RHE*	$2H_3O^+(aq) + 2e^- \rightleftharpoons H_2 \uparrow + 2H_2O$	0 V
Ag/AgCl**	$AgCl + e^- \rightleftharpoons Ag \downarrow + Cl^-(aq)$	0.1976 V
Hg/HgO	$HgO + H_2O + 2e^- \rightleftharpoons 2Hg(l) + 2OH^-(aq)$	0.0977 V
SCE**	$Hg_2Cl_2 + 2e^- \rightleftharpoons 2Hg(l) + 2Cl^-(aq)$	0.2412 V
Hg/Hg_2SO_4	$Hg_2SO_4 + 2e^- \rightleftharpoons 2Hg(l) + {SO_4}^{2-}(aq)$	0.6125 V
$Cu/CuSO_4$	$Cu^{2+}(aq) + 2e^- \rightleftharpoons Cu \downarrow$	0.3419 V

* The electrolyte is set as pH = 0.

** The electrolyte is saturated KCl.

† In certain applications, the applied potential measured against REs other than hydrogen electrodes needs to be referenced against RHE. The conversion is based on **Equation 3.3**:

Equation 3.3 Conversion of potential between reference electrodes

$$E_{RHE} = E_{RE} + 0.059pH + {E^0}_{RE}$$

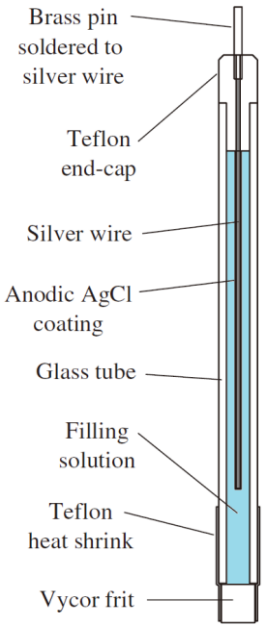

Figure 3.24 Schematic illustration of Ag/AgCl reference electrode[33]

Nowadays, the most commonly used RE in laboratories is Ag/AgCl,[34] primarily owing to its simplicity, stability, and capability of miniaturisation.[35] An Ag/AgCl electrode usually has an Ag wire coated with AgCl thin film (**Figure 3.24**), and the filling solution is usually saturated KCl because it does not interfere with the measurements of pH values. The mobility of the K^+ and Cl^- ions is nearly equal, so the liquid-junction potential is kept at the minimum.[35] According to the Nernst equation, as long as the concentration of Cl^- ions is consistent, the RE would produce a stable and reproducible electrode potential. Since AgCl is slightly soluble (~ 6×10^{-3} M at 25 °C) in concentrated KCl solution,[35] the KCl solution has to be frequently replaced as a common maintenance practice.

In this project, the electrocatalytic performance of the samples on EOR was tested using a computer-controlled electrochemical workstation (PGSTAT302N, Metrohm Autolab, Netherlands) via a three-electrode setup (**Figure 3.25**). The quartz electrolytic cell and all electrodes used were purchased from Tianjin Aida Hengsheng Technology Development Co. Ltd., PRC. Ag/AgCl (Model R0305) was used as the RE and a 10×10 mm^2 Pt foil (99.9% purity) was used as the CE. The samples were individually loaded onto the working electrode with Au facing the conductive Pt foil built in the WE. In cyclic voltammetry (CV) tests, two sets of electrolytes were prepared: for baseline scans, the electrolyte was OH^- aqueous solution, prepared by dissolving appropriate amount of NaOH pellets or KOH flakes in deionised water; for EOR scans, the electrolyte was prepared by mixing OH^- aqueous solution and absolute ethanol in appropriate volumetric ratios, such that the pH value and ethanol concentration in the final electrolyte is defined. All CV scans were carried out within a suitable potential range for 5 consecutive cycles and a step size of 0.00244 V; the scanning rate is set as 0.01 V/s unless otherwise needed. The obtained data were normalised with effective surface area exposed to the electrolyte, and only the data from the third cycles were selected and shown. Electrochemical impedance spectroscopy (EIS) was carried out with the applied AC frequency range being 10^5 Hz to 10^{-2} Hz, and CA was performed for 12 h or 15 h to test the stability

of the samples. The electrolyte for EIS and CA was OH^-/ethanol at pH = 13, with ethanol concentration being 1 M.

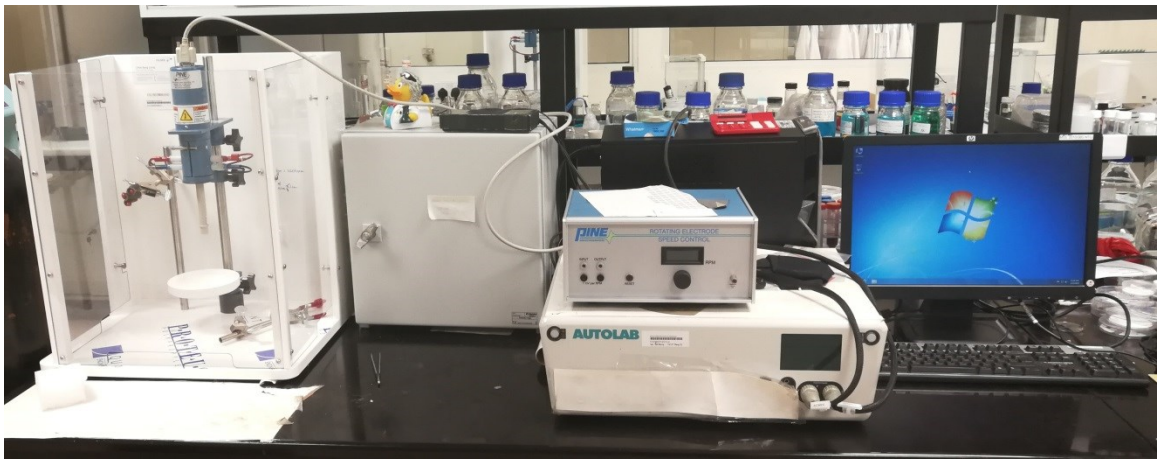

Figure 3.25 Photo of Metrohm Autolab PGSTAT302N electrochemical workstation used in this project

References

1. R. McGorty, J. Fung, D. Kaz and V. N. Manoharan, *Mater. Today*, 2010, **13**, 34.
2. F. Marlow, Muldarisnur, P. Sharifi, R. Brinkmann and C. Mendive, *Angew. Chem. Int. Ed.*, 2009, **48**, 6212.
3. L. M. Fortes, M. C. Gonçalves and R. M. Almeida, *J. Non-Cryst. Solids*, 2009, **355**, 1189.
4. L. Liu, S. K. Karuturi, L. T. Su and A. I. Y. Tok, *Energy Environ. Sci.*, 2011, **4**, 209.
5. S. K. Karuturi, J. Luo, C. Cheng, L. Liu, L. T. Su, A. I. Y. Tok and H. J. Fan, *Adv. Mater.*, 2012, **24**, 4157.
6. J. Rybczynski, U. Ebels and M. Giersig, *Colloids Surf., A*, 2003, **219**, 1.
7. Y. Li, J. Zhang, S. Zhu, H. Dong, F. Jia, Z. Wang, Z. Sun, L. Zhang, Y. Li, H. Li, W. Xu and B. Yang, *Adv. Mater.*, 2009, **21**, 4731.
8. M. Zhou, J. Bao, M. Tao, R. Zhu, Y. Lin, X. Zhang and Y. Xie, *Chem. Commun.*, 2013, **49**, 6021.
9. K. Huang, D. Peng, B. Zhang, X. Cao, S. Hao, G. Yang, Y. Dong, J. Wu and Y. Huang, *Int. J. Hydrogen Energy*, 2018, **43**, 12596.
10. C. Suryanarayana and M. G. Norton, *X-Ray Diffraction: A Practical Approach*, Springer Science & Business Media, 1st Edition, 1998.
11. I. C. Noyan and J. B. Cohen, in *Residual Stress: Measurement by Diffraction and Interpretation*, Springer New York, New York, NY, 1987.
12. *Powder Diffraction: Theory and Practice*, RSC Publishing, 2008.
13. T. Ryan, *J. Chem. Educ.*, 2001, **78**, 613.

14. B. B. He, *Two-dimensional X-ray diffraction*, Wiley Online Library, 2009.
15. W. H. Bragg and W. L. Bragg, *Proc. R. Soc. London, Ser. A*, 1913, **88**, 428.
16. T. Kogure, in *Developments in Clay Science*, Elsevier, 2013.
17. Y. Waseda, E. Matsubara and K. Shinoda, *X-Ray Diffraction Crystallography: Introduction, Examples and Solved Problems*, Springer Science & Business Media, 1st Edition, 2011.
18. S. J. Pennycook, M. Varela, C. J. D. Hetherington and A. I. Kirkland, *MRS Bull.*, 2006, **31**, 36.
19. D. B. Williams and C. B. Carter, *Transmission Electron Microscopy: A Textbook for Materials Science*, Springer, 2nd Edition, 2009.
20. P. J. Goodhew, J. Humphreys and R. Beanland, *Electron Microscopy and Analysis*, CRC Press, 2000.
21. J. I. Goldstein, D. E. Newbury, J. R. Michael, N. W. M. Ritchie, J. H. J. Scott and D. C. Joy, *Scanning Electron Microscopy and X-Ray Microanalysis*, Springer, 4th Edition, 2018.
22. B. D. Fahlman, *Materials Chemistry*, Springer Netherlands, 2nd Edition, 2011.
23. *Introduction to Focused Ion Beams: Instrumentation, Theory, Techniques and Practice*, Springer International Publishing, 2005.
24. *FIB Nanostructures*, Springer International Publishing, 2013.
25. P. R. Munroe, in *Encyclopedia of Materials: Science and Technology*, Elsevier, Oxford, 2010.
26. B. Fultz and J. M. Howe, *Transmission Electron Microscopy and Diffractometry of Materials*, Springer, Berlin, Heidelberg, 3rd Edition, 2008.
27. *Scanning Transmission Electron Microscopy: Imaging and Analysis*, Springer Science & Business Media, 1st Edition, 2011.
28. R. F. Egerton, *Physical Principles of Electron Microscopy*, Springer, 2nd Edition, 2016.
29. N. Tanaka, *Electron Nano-Imaging*, Springer, 2017.
30. A. J. Bard and L. R. Faulkner, *Electrochemical Methods: Fundamentals and Applications*, John Wiley and Sons, 2nd Edition, 2008.
31. Y. Cai and A. B. Anderson, *J. Phys. Chem. B*, 2004, **108**, 9829.
32. *CRC Handbook of Chemistry and Physics*, CRC Press, 97th Edition, 2016.
33. C. G. Zoski, *Handbook of Electrochemistry*, Elsevier B.V., 2007.
34. E. Bakker, in *Encyclopedia of Analytical Science (Third Edition)*, Academic Press, Oxford, 2019.
35. D. D. Zhou, in *Electrochemical Sensors, Biosensors and their Biomedical Applications*, Academic Press, San Diego, 2008.

Chapter 4

Catalysis of Au Nano-Pyramids Formed Across the Surfaces of Ordered Au Nano-Ring Arrays

In this work, a facile NSL-RIE approach has been developed to fabricate ordered Au nano-ring arrays with almost 100% substrate coverage. The preferential etching of {1 1 1} lattice planes of Au gives rise to the formation of a number of Au nano-pyramids across the entire surface of the nano-ring arrays. The sharp tips along with the Au atoms around the edges of these nano-pyramids provide active sites that perform strong catalysis. Meanwhile, Moiré fringes are observed over the etched Au surface due to the rotation of the partial Au lattice with respect to the original Au lattice, which provides high surface energy allowing significant improvement of the catalysis of Au nano-ring arrays. The direct evidence is proven by the enhanced electrochemical properties of the Au nano-ring array, which has high efficiency in EOR with low energy input requirement. Electrochemistry testing with various physical parameters shows that the detecting limit of ethanol is ~ 1.0 mM and strong signals come with high concentrations of mobile charge carriers at extreme pH values. Long continuous CV scans reveal that in alkaline medium, C1 pathway becomes increasingly preferential over C2 pathway, and thus making the Au nano-ring array structure useful in the application of DEFC.

---

*This chapter is published substantially as **X. Cao**, C. Li, Y. Lu, B. Zhang, Y. Wu, Q. Liu, J. Wu, J. Teng, W. Yan and Y. Huang, *J. Catal.*, 2019, **377**, 389.

4.1 Materials and Chemicals

The materials used in this work include p-type Si <1 0 0> wafers and Au target (99.99% purity). The chemicals used in this project include sulphuric acid (H_2SO_4, 98%), hydrogen peroxide (H_2O_2, 30 wt%, VWR), absolute ethanol (CH_3CH_2OH, 99.9%, Aik Moh), PS latex beads (500 nm diameter, 10 wt% colloid in deionised water, 5050C, Thermo Fisher Scientific), sodium dodecyl sulphate (SDS, 99%, Sigma-Aldrich) and sodium hydroxide pellets (NaOH, 98%, Sigma-Aldrich). All of the abovementioned chemicals were used as received without any further purification. The deionised water was made by the Millipore™ system, which has the resistivity of 18.2 MΩ·cm.

4.2 Parameter Control for Fabrication of Au Nano-Ring Arrays

The etching profiles in the RIE system strongly depend on the process parameters, such as etchant gas, flow rate, chamber pressure, RF power and etching duration. In the first set of experiments, the etchant gas was varied while all other parameters were strictly controlled to be the same (chamber pressure: 300 mTorr; etchant gas flow rate: 20 sccm; RF power: 100 W; etching duration: 5 min). **Figure 4.1** shows the FEG-SEM images of the samples before and after the RIE process.

Figure 4.1 (a) displays a single layer densely packed self-assembly of PS colloidal spheres on the surface of Au-coated Si substrate, which has highly ordered arrangement with few defects identified. After RIE with Ar for 5 min, most of Au was removed; the remaining Au could be found as the bright spots in image **Figure 4.1 (b)**, in which the Au nano-dots render a high level of orderliness, but are not uniform in size and having quite significant quantity of defects. Furthermore, non-continuous Au structures severely reduce the electrical conductivity of the sample, which is unfavourable in the electrochemical tests. RIE with tetrafluoromethane (CF_4) for 5 min produces regular nanoporous trough morphology as shown in **Figure 4.1 (c)**, Si substrate was etched to form large and deep valleys while many PS nanospheres were retained within these valleys; this is because the fluorine-containing etchant CF_4 is highly selective and it

chemically reacts with the Si substrate. However, a fatal problem is that the remaining PS hinders the proper functioning of the samples; when the sample was immersed in toluene to remove the remaining PS, Au coating gets easily detached from the substrate, and this is probably due to the high porosity of the structure. PS nipple array was formed after RIE with O_2 as shown in **Figure 4.1 (d)**, which has a similar orderliness as compared to **Figure 4.1 (b)**, but much more Au was kept on the substrate; this is because the O_2 plasma preferentially etches PS over Au and Si, and it could be determined from Z contrast and EDX analysis.

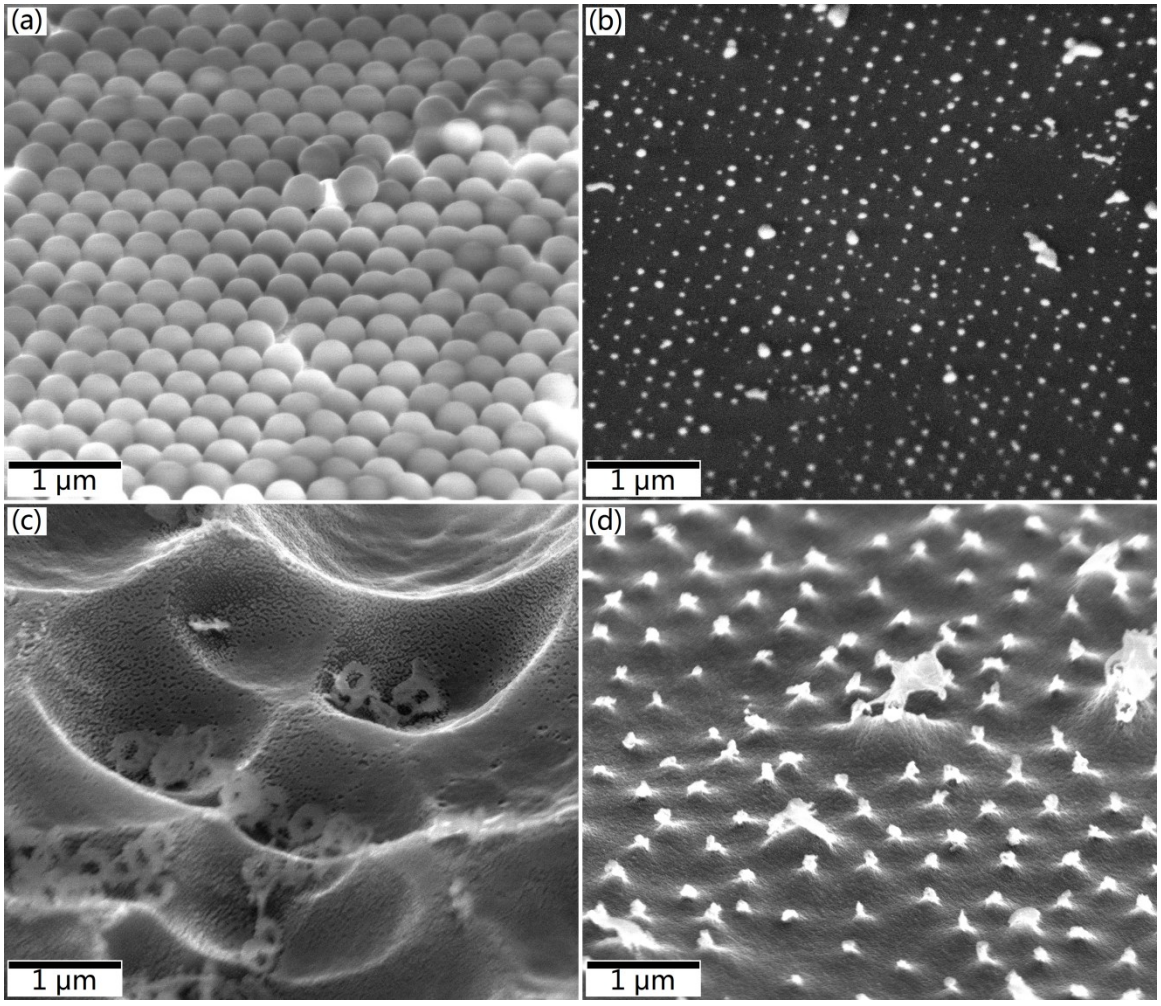

Figure 4.1 52° tilted FEG-SEM images of Si/Au/PS samples at 100 k×: (a) before and (b-d) after the RIE process. The etchant gas used was (b) Ar; (c) CF_4 and (d) O_2.

Being the electrocatalyst, Au is the core active material that facilitates the catalytic reactions, while a plane and smooth surface of Si substrate helps to support and maintain the Au thin film with patterns. As the targeted outcome is patterning of Au without sacrificing the Si substrate, the etchant gas is chosen to be oxygen, which has the least attacking effect on both Au and Si substrate.

Chamber pressure is another important factor that could affect the etching profiles, thus samples were individually loaded and the system was maintained at different chamber pressures before RIE, while all other parameters were kept constant (etchant gas: O_2; etchant gas flow rate: 20 sccm; RF power: 100 W; etching duration: 5 min). **Figure 4.2** demonstrates the polarised optical microscope (POM) and FEG-SEM images of these samples. In the POM images (**Figure 4.2 a-c**), the green spots are regions where ordered array structures could be found; it is obvious that as chamber pressure is reduced, more spots start to form arrays and they tend to aggregate to form larger continuous areas. Regions boxed up in red are further enlarged for FEG-SEM images.

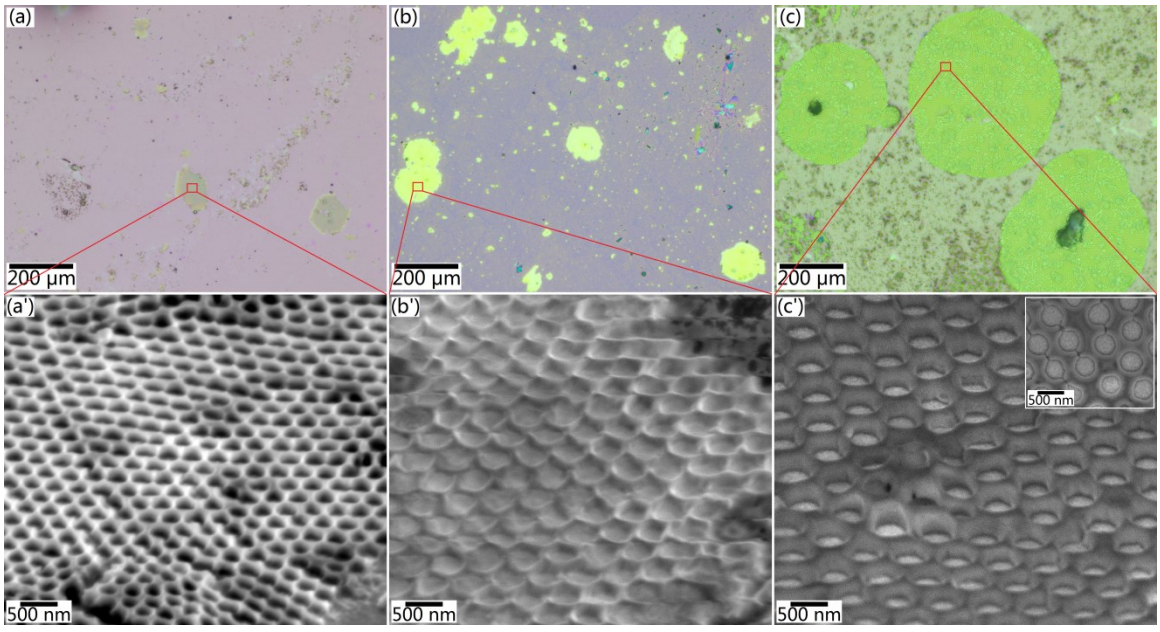

Figure 4.2 POM images taken at 1 k× (top) and 52° tilted FEG-SEM images taken at 50 k× (bottom) of Si/Au/PS sample after 5 min RIE. The chamber pressure was kept at (a-a') 300 mTorr; (b-b') 120 mTorr and (c-c') 90 mTorr. The inset of (c') is a top view FEG-SEM image taken at the magnification of 50 k×.

From the FEG-SEM images (**Figure 4.2 a'-c'**), it could be found that within the green spots in the POM images, all PS was etched away and Au array structures were nicely formed. When chamber pressure was kept at 300 mTorr, thick Au skeleton structure was obtained with its height almost being equal to that of the deposited Au thin film (**Figure 4.2 a'**); this might be because 300 mTorr is a relatively high chamber pressure and there is more scattering during the RIE process, thus leading to less effective etching and giving smaller continuous areas. When chamber pressure gets lowered to 120 mTorr, the skeleton structure becomes thinner (**Figure 4.2 b'**) and larger area could be found (**Figure 4.2 b**); this should be resulted by more effective etching due to less scattering by residual air molecules. With chamber pressure being further reduced to 90 mTorr (**Figure 4.2 c'**), extended etching brings about the formation of shallow bowl-shaped structure. The inset of **Figure 4.2 c'** shows the structure in its top view; the array forms a "ring" outside each individual feature, it is in fact the oblique inner wall of the bowl structure, which has a different contrast compared to the regions between the features.

In order to investigate the effect of RF power on feature size, the power was varied from 10 W to 150 W with all other parameters kept constant (chamber pressure: 100 mTorr; etchant gas: O_2; etchant gas flow rate: 20 sccm; etching duration: 5 min). **Figure 4.3** is a collection of the top view FEG-SEM images of this set of samples. **Figure 4.3 (a)** illustrates the state of the original sample without RIE, in which the PS spheres are in touch with each other and have a beautiful hexagonal arrangement. RIE using O_2 plasma etches PS spheres and they become more separated. When the RF power was set from 10 W up to 30 W (**Figure 4.3 b-d**), the size of PS sharply dropped from 500 nm to ~ 150 nm, and separation spacing increased quickly to ~ 280 nm (**Figure 4.3 i**); spherical shapes and spatial orderliness were well maintained as well.

As the power was increased from 30 W to 80 W (**Figure 4.3 d-f**), the sizes of remaining PS and separation spacing stayed steady and little variation could be observed (**Figure 4.3 i**); the only trend is that the shape of the remaining PS became less spherical, but the spatial orderliness was still good. Upon continued ramping of RF power from 80 W to

150 W (**Figure 4.3 f-h**), the size of remaining PS was further reduced down to ~ 60 nm and the separation spacing up was enlarged to ~ 350 nm (**Figure 4.3 i**); this again leads to the formation of the bowl structure shown previously (**Figure 4.2 c'**), but trace amount of PS is remained, possibly because the chamber pressure used in this set of experiment is a little higher (100 mTorr vs 90 mTorr).

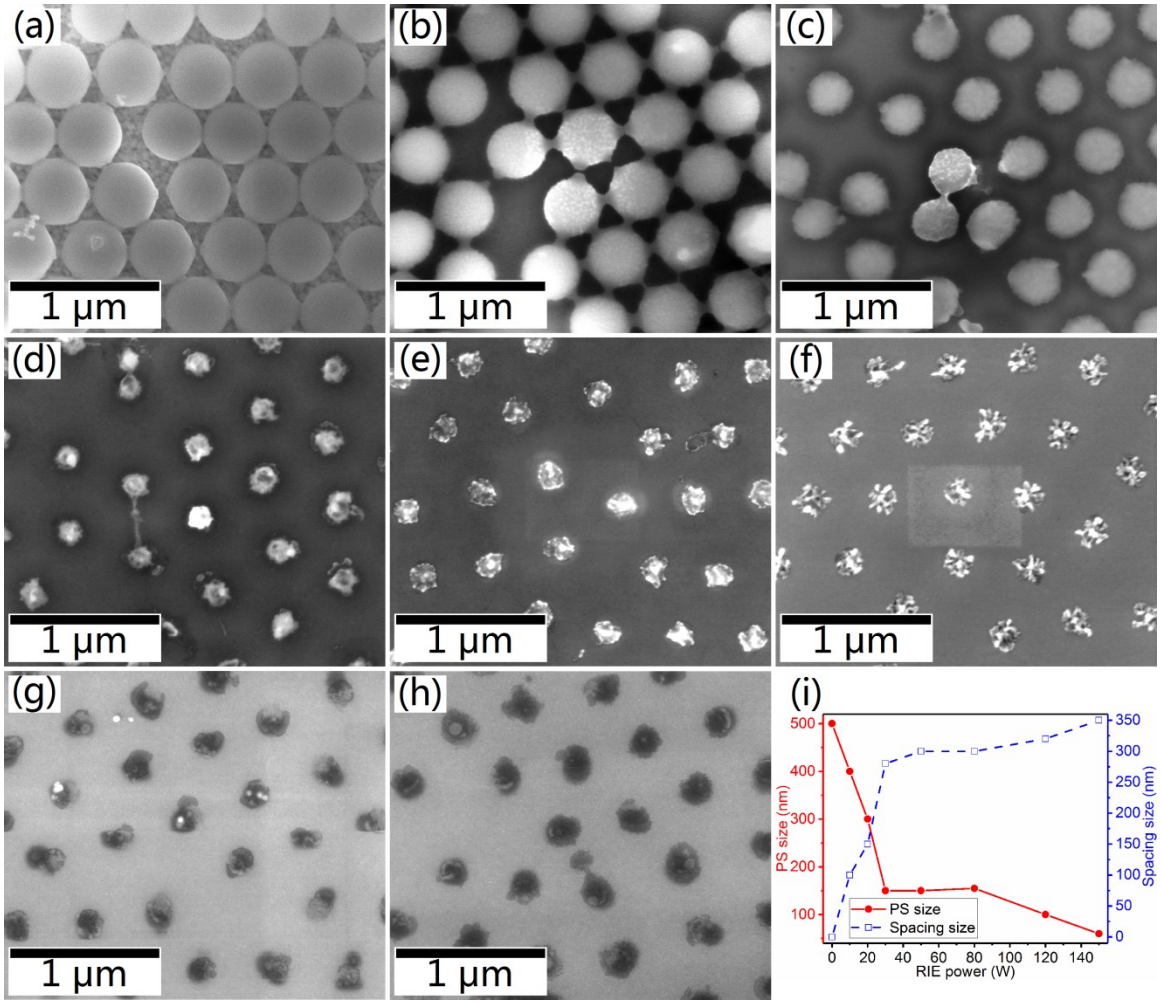

Figure 4.3 (a-h) Top view FEG-SEM images of Si/Au/PS sample taken at 100 k×: (a) before RIE; and after RIE for 5 min at the power of (b) 10 W; (c) 20 W; (d) 30 W; (e) 50 W; (f) 80 W; (g) 120 W and (h) 150 W. (i) A diagram showing the relationship of the remaining PS spheres and feature spacing sizes with RIE power.

To further manifest the formed array structures, the etchant gas flow rate was doubled from 20 sccm to 40 sccm, with all other parameters being fixed (etchant gas: O_2; chamber

pressure: 100 mTorr; RF power: 150 W; etching duration: 5 min). FEG-SEM images taken using the dual-beam FIB system (**Figure 4.4**) reveals that the fabricated array structures are in large area and well-aligned nicely in a hexagonal shape (**Figure 4.4 a**). Under a much larger etchant gas flow rate, the formed arrays are no longer having bowl-shaped structures, they turn to form rings instead, which protrude outwards from the surface of the Au thin film; the Au nano-rings are ~ 500 nm in outer diameter with wall thickness being ~ 25 nm (**Figure 4.4 b**), and the height of the rings is ~ 83 nm (**Figure 4.4 c**). This might be due to the upwards movement of the Au beneath the PS during RIE, or alternatively, Au might be softened by the plasma during RIE and PS nanospheres partially sink into the Au film at their original positions.

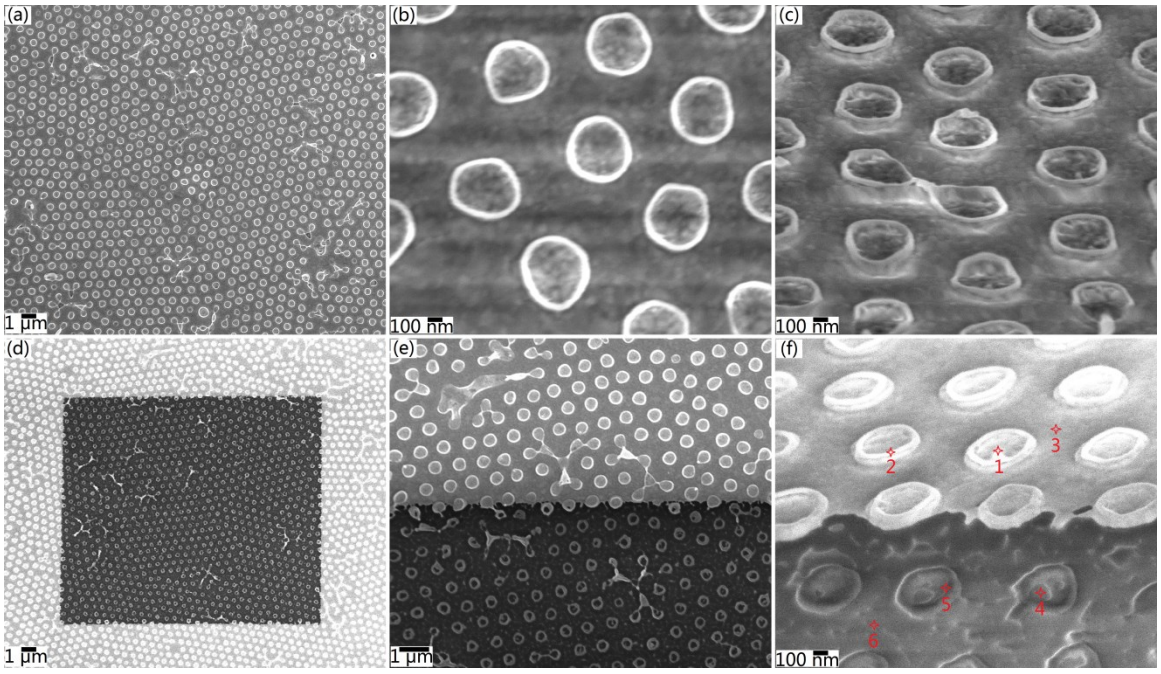

Figure 4.4 FEG-SEM images of Si/Au/PS sample after RIE taken using the dual-beam FIB system: (a-b) 10 k× and 100 k× top view and (c) 100 k× at 52° tilt; (d-e) 7 k× and 20 k× top view and (f) 100 k× at 52° tilt, showing contrast before and after irradiation by Ga^+ ion source at 30 kV and 0.46 nA for 30 s. The points in image (f) are the EDX analyses sites.

To investigate the physical stability of the Au nano-ring array upon external attacking, the ion beam was un-blanked and left unattended for 30 s ion illumination. The FIB system was operated at ion accelerating voltage of 30 kV and probe current of 0.46 nA.

Under the irradiation of Ga^+ ion beam, the illuminated area darkens out and the obvious contrast difference is contributed by height difference (**Figure 4.4 d**). Further magnifying (**Figure 4.4 e-f**) shows that the Au nano-rings are well kept in their original shape and alignment, which means the sample has high chemical inertness and could withstand strong external attacks. The elemental compositions of the surface microstructures were analysed by EDX, which was performed using an integrated laser-cooled EDX detector (Octane Elite Plus, EDAX, USA). From **Figure 4.4 f**, six individual points were selected and the EDX analyses (**Figure 4.5**) reveal that the nano-rings before and after Ga^+ ion beam irradiation, including the walls, regions inside and outside of the rings are gold, which have strong Au Mα intensity; signals of Si Kα and O K (contributed from substrate) appear to be stronger in the darkened area as Au becomes thinner after Ga^+ irradiation.

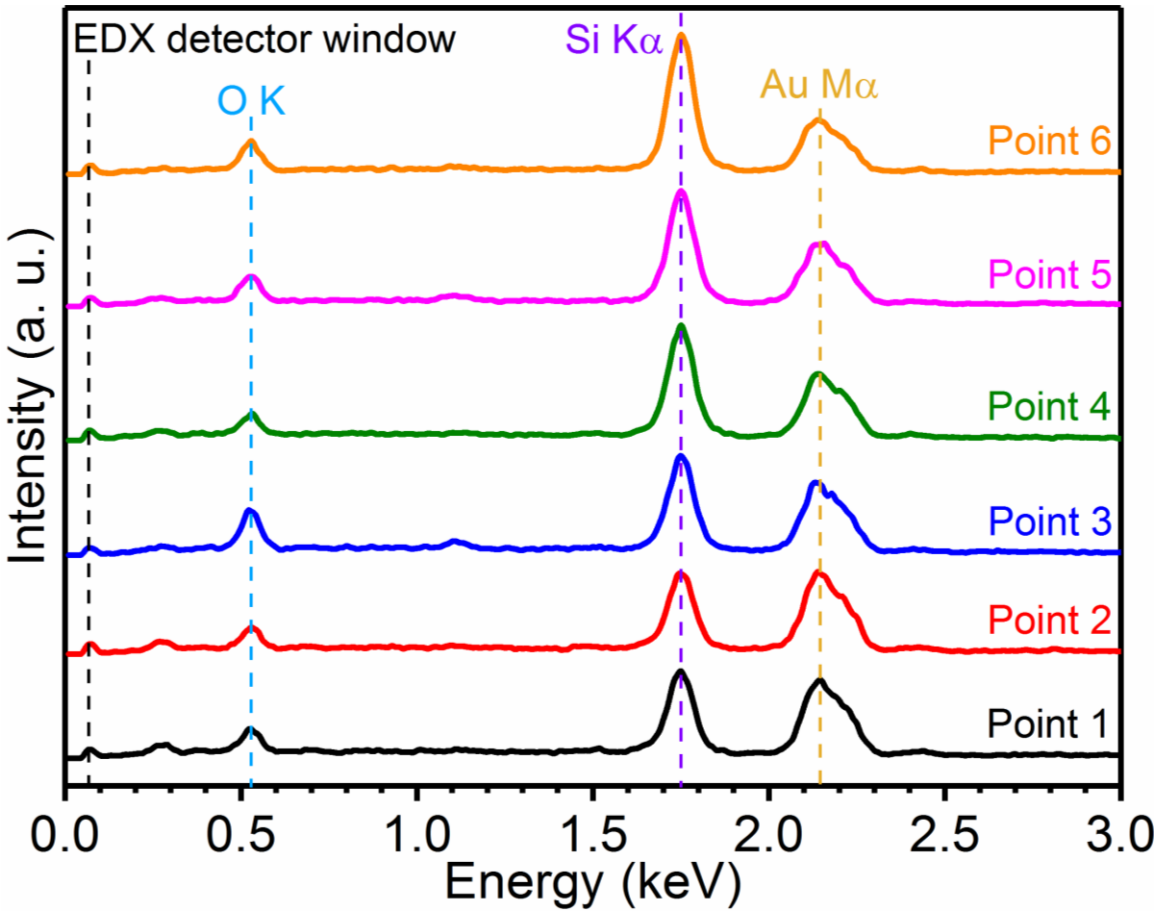

Figure 4.5 EDX spectra of different spots on the Si/Au/PS sample

4.3 Morphology and Crystallography of Au Nano-Ring Arrays

The crystalline phases of the samples were confirmed by thin film XRD. The thin film samples were scanned within the range of $10° \leq 2\theta \leq 120°$; all scans were performed under 2θ mode at an X-ray grazing angle of 1.0° with scanning rate of 2.0°/min and a step size of 0.02°. **Figure 4.6** shows the XRD patterns of the Si/Au/PS sample before (black) and after (red) RIE where most of the visible peaks could be ascribed to the face-centred cubic (FCC) pristine Au (JCPDS #04-0784). The peaks at $2\theta \approx 8.0°$ and $2\theta \approx 56.4°$ are contributed by the self-assembled PS nanospheres before the RIE process, as verified by the XRD pattern of the Si/PS sample, and they disappeared after the RIE process when PS was etched away by the O_2 plasma.

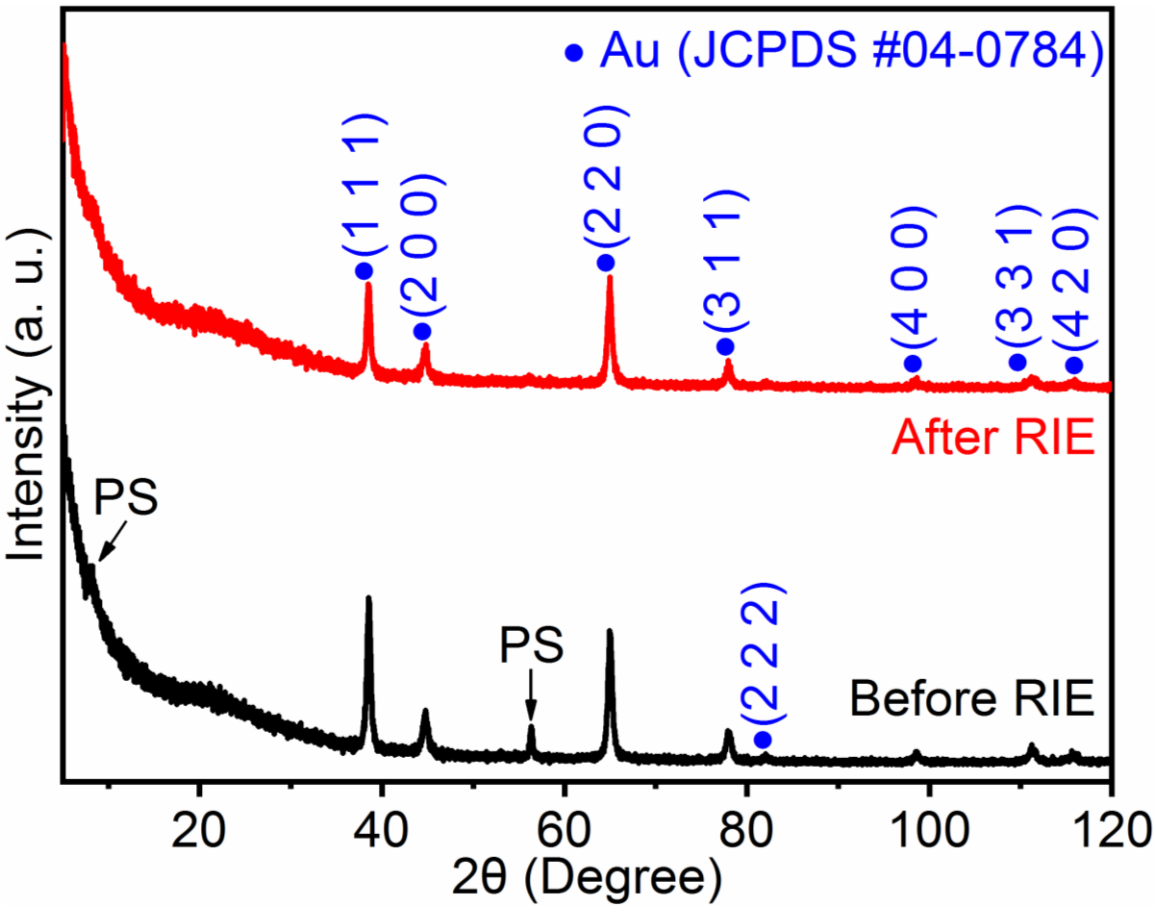

Figure 4.6 XRD patterns of the Si/Au/PS sample before (black) and after (red) RIE

XRD also shows anisotropic etching of Au thin film during the RIE process. The peak at $2\theta \approx 38.2°$, which represents the Au (1 1 1) orientation, is the highest before RIE, but it becomes much weaker (lower than (2 2 0) orientation) after the RIE process. On the other hand, the intensities of the other Au peaks remain relatively unchanged. This shows high selectivity of the O_2 plasma during RIE, which finally produced the Au nano-rings.

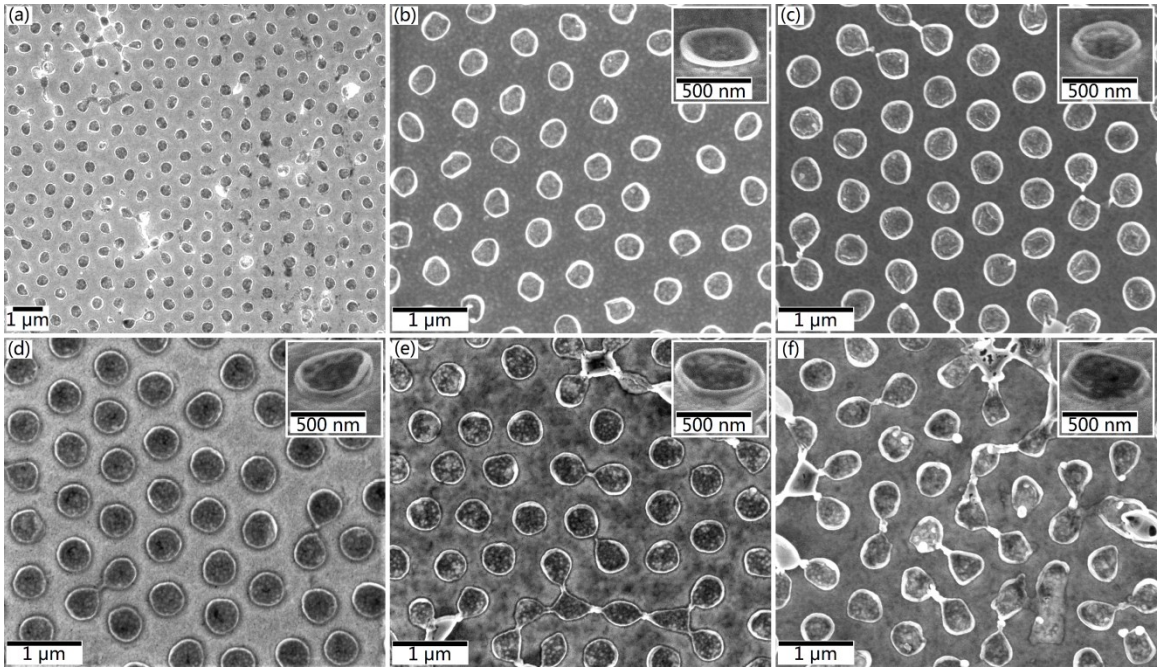

Figure 4.7 FEG-SEM image of Si/Au/PS samples taken under dual-beam SEM/FIB system. (a) Top view FEG-SEM images of Si/Au/PS samples, taken at a low magnification of 10 k×. (b-f) Top view FEG-SEM images of Si/Au/PS samples after different RIE durations: (b) 5.0 min; (c) 7.5 min; (d) 10.0 min; (e) 15.0 min and (f) 20.0 min, taken at the magnification of 50 k×. (Insets of b-f) 52° tilted FEG-SEM images of each sample showing one feature, taken at the magnification of 100 k×.

Based on the previous settings (etchant gas: O_2; etchant gas flow rate: 40 sccm; chamber pressure: 100 mTorr; RF power: 150 W), the last parameter was finely tuned and etching duration was varied from 5.0 to 20.0 min. The low magnification FEG-SEM image reveals that the fabricated array structures cover a large surface area over the Si substrate and are well-aligned in a hexagonal shape (**Figure 4.7 a**). FEG-SEM images of these samples at higher magnifications are depicted in **Figure 4.7 b-f**, which were taken both in

top view and at an inclined angle of 52°. Under a large etchant gas flow rate, the bowl-shaped arrays form ring structures, which protrude outwards from the surface of the Au thin film (**insets of Figure 4.7 b-f**). The Au nano-rings are ~ 500 nm in outer diameter with wall thickness of ~ 25 nm. This might be due to the upwards movement of the Au beneath the PS during RIE (as illustrated in **Figure 4.8**), which could be directly explained by the cross-sectional TEM lamella made by the dual-beam FEG-SEM/FIB system (**Figure 4.9 a-b**). Etching duration does not seem to have much effect in shape and ordered arrangement of the features, but longer etching time produces deeper etching and thus creates Au nano-rings with smaller heights. **Figure 4.10** shows the relationship of Au nano-ring height with etching duration. From the linear fit trend line, the etching rate under these settings is approximately 2.31 nm/min. After 20.0 min RIE, the Au nano-rings are still having a height of ~ 50 nm. The error analysis shows that the measurement of Au nano-ring height is quite precise and the error range is small.

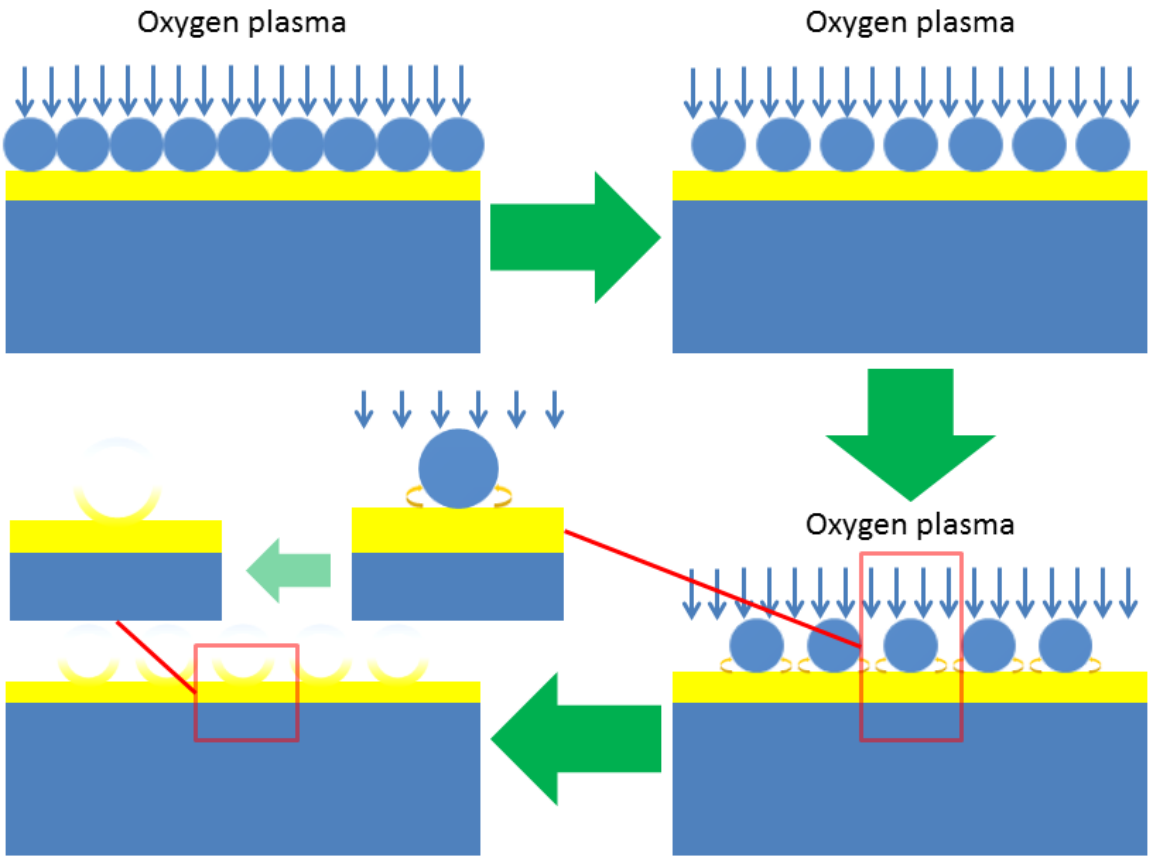

Figure 4.8 Schematic illustration of the formation mechanism of the Au nano-ring array, with inset being the magnified view of the boxed regions. The graphs are not drawn to scale.

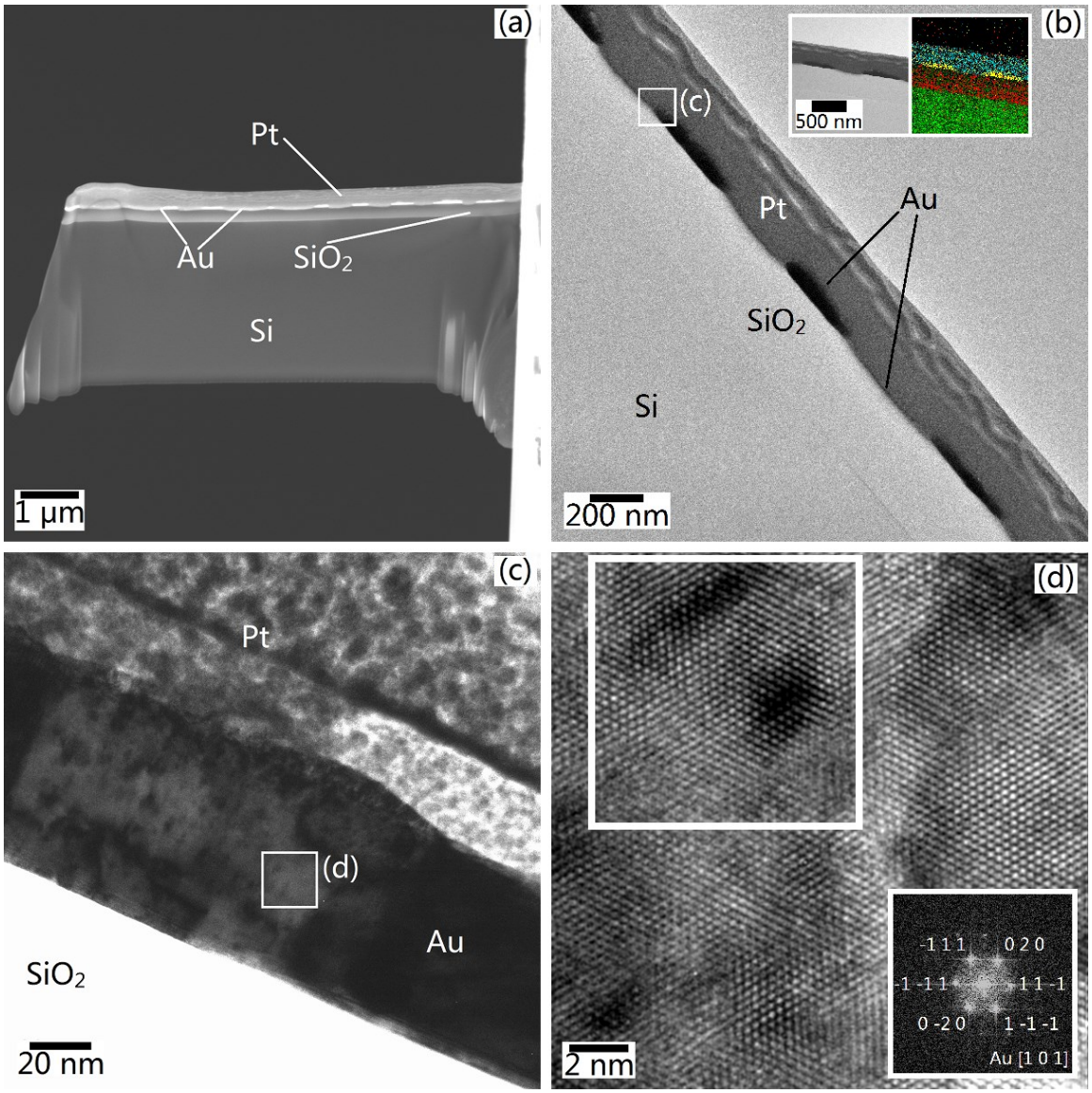

Figure 4.9 TEM and HRTEM images of Au nano-ring array. (a) The cross-sectional TEM lamella made by the dual-beam SEM/FIB system. (b) TEM image of the lamella at low magnification. (Inset of b) Low magnification bright field TEM image (left) and the corresponding EDX elemental mapping (right) of the sample performed using an EDX detector integrated on the FEG-TEM. Green: Si; red: O; yellow: Au; blue: Pt. (c) Magnified TEM image of the square region in (b). (d) HRTEM image of the square region in (c), and (inset) the FFT pattern of the square region in (d).

However, due to prolonged exposure to the bombardment from the reactive ions, the surfaces of the samples are inevitably degrading as well. By undergoing RIE for 10.0 min

or less (**Figure 4.4 b-c** and **Figure 4.7 b-d**), the samples have almost no defects. However, from 15.0 min onwards (**Figure 4.7 e-f**), some defective regions start to be visible, which usually present on the rings or between two rings. Apart from the intrinsic defects, these defects might be due to the lowered shielding effect resulted from reduced nano-ring height. **Figure 4.10** shows that the height of the Au nano-rings after 10.0 min RIE is ~ 75 nm, while it becomes ~ 60 nm after 15.0 min RIE. Etching beyond 10.0 min created more defective regions and thus the error in the measurements becomes slightly larger. This suggests that the height of the Au nano-rings needs to be at least ~ 83 nm in order to obtain enough shielding effect and to minimise the defects.

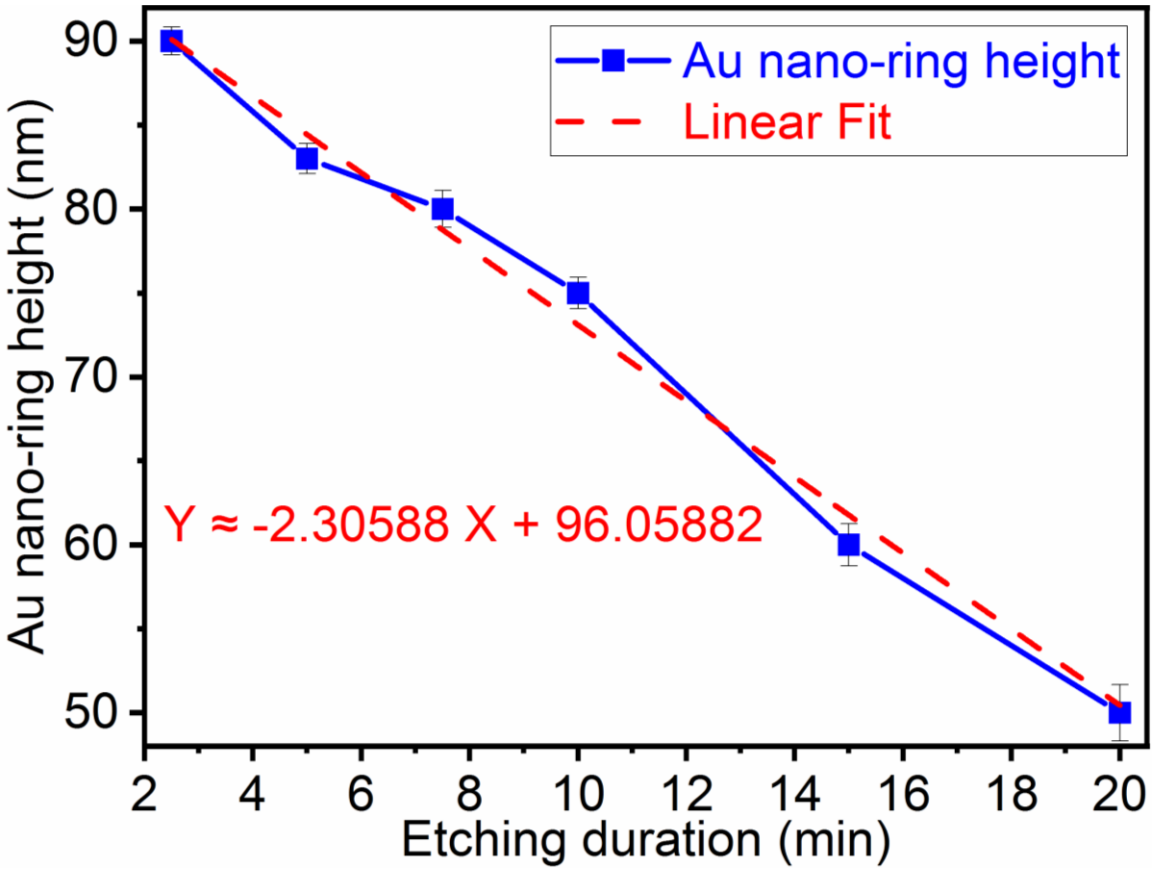

Figure 4.10 Relationship between Au nano-ring height and etching duration, as well as a linear fit trend line. The error analysis shows that the measurement of Au nano-ring height is quite precise and the error range is small.

The formation mechanism of the Au nano-ring array is deeply studied through cross-sectional TEM. A thin lamella was prepared by dual-beam SEM/FIB system (**Figure 4.9 a**) and characterised in FEG-TEM (**Figure 4.9 b-d**), which clearly show the interfacial structure of the sample being Si/SiO_2 (substrate) followed by Au nano-ring array and the Pt protection layer. The TEM-EDX elemental mapping (**inset of Figure 4.9 b**) could serve as a supplement to the interfacial structure. Under the mass-thickness contrast in the low-magnification bright field TEM image (**Figure 4.9 b**), the originally deposited Au film is found to be thinned during the RIE process and the upward flipping movement of the Au that wrapped around PS nanospheres could be explained by the round corners of the periodic features.

The square region marked in **Figure 4.9 b** was magnified and displayed as **Figure 4.9 c**, which shows only part of one nano-ring. The middle portion is the thinnest and has very little Pt re-deposition after FIB thinning, therefore the square region in **Figure 4.9 c** is further magnified for HRTEM shown in **Figure 4.9 d**. HRTEM shows that after RIE, Au is still having highly ordered lattice, which indicates very good crystallinity in the Au nano-ring. The FFT pattern (**inset of Figure 4.9 d**), which is the reciprocal lattice image converted from the square region in **Figure 4.9 d**, gives ordered array of sharp spots that corresponds to the FCC lattice of Au. Matching against the JEMS software (Electron Microscopy Software, Java Version 4.3905U2016, developed by Dr P. Stadelmann, Switzerland) shows that the Au nano-ring has a space group of *F*m-3m and crystallises along the zone axis of Au [1 0 1]; this is coherent with the XRD pattern (**Figure 4.6**) of the arrayed sample after RIE, in which the strongest crystalline peak is (2 2 0) instead of (1 1 1) before RIE.

The formation of Au nano-rings did not come with smooth surfaces and plenty active sites were produced during the RIE process. Direct evidence of forming the active sites was observed by TEM; many pyramids with sharp tips (with their bases not exceeding the size of 10 nm), are observed at the top surface of the Au nano-ring (interfacial positions between Au and deposited Pt) and are labelled with white arrows in **Figure 4.11 a**. The pyramids are uniform in size and do not differ from each other by a lot. However,

since the formation of the pyramids is random, the distribution of the pyramids on the top surface of Au nano-rings may not be very uniform. Pyramid 1, which is one of the active sites, is magnified and the HRTEM image is shown in **Figure 4.11 b**; the atomic sites of single crystalline Au can be clearly seen and they are orderly arranged with {1 1 1} family planes forming an angle of 120°. The surface atoms are marked as red dots, so as to show the interface between Au and Pt (deposited in the FIB during TEM lamella sample preparation in order to protect the Au surface from FIB sputtering). These surface atoms are exposed to the environment and therefore act as the active sites in atomic-scale. The red square marked in **Figure 4.11 a** is the edge of the body region of a nano-ring and its HRTEM image is displayed in **Figure 4.11 c**, which shows both a perfect lattice (red square) and a Moiré fringe lattice (blue square). The FFT patterns of the square regions in **Figure 4.11 c** are presented in respective colours and shown in **Figure 4.11 d**. There are two sets of blue spot arrays diffracted from the blue square region (i.e. the Moiré fringe region) in **Figure 4.11 c** taken at the zone axis of [1 0 1]. One blue spot array is in superposition with the red spot array that is generated from the original Au lattice. The other blue spot array is rotated with respect to the first blue spot array at a small angle of ~ 6° indicating the lattice distortion on the top surface of Au.

This lattice distortion at the edge is believed to originate from the formation of the nano-ring. When the sample was subjected to treatment during RIE, the self-assembled PS nanospheres served as a protective mask, and the unprotected Au was bombarded by the energetic reactive ions (**Figure 4.8**). Stress might be built up during the upwards movement of the Au exposed to oxygen plasma, and the edges of the as-formed Au nano-rings (including the active sites) tend to become stress centres, where the accumulated stress might be released upon reaching a threshold, which would finally lead to the partial lattice rotation as a result. From the reciprocal lattices in the FFT patterns (**Figure 4.11 d**), a partial lattice rotation of ~ 6° is observed along both the (1 1 -1) and (0 2 0) planes. It is expected that the presence of atomic-scale active sites and partial lattice rotation at the edges of Au nano-rings could produce outstanding performance in electrochemistry, because these lead to high surface energy at the active sites, which could attack the

covalent bonds in ethanol molecules and help to overcome the activation energy required for catalytic oxidation of ethanol with a voltage applied.

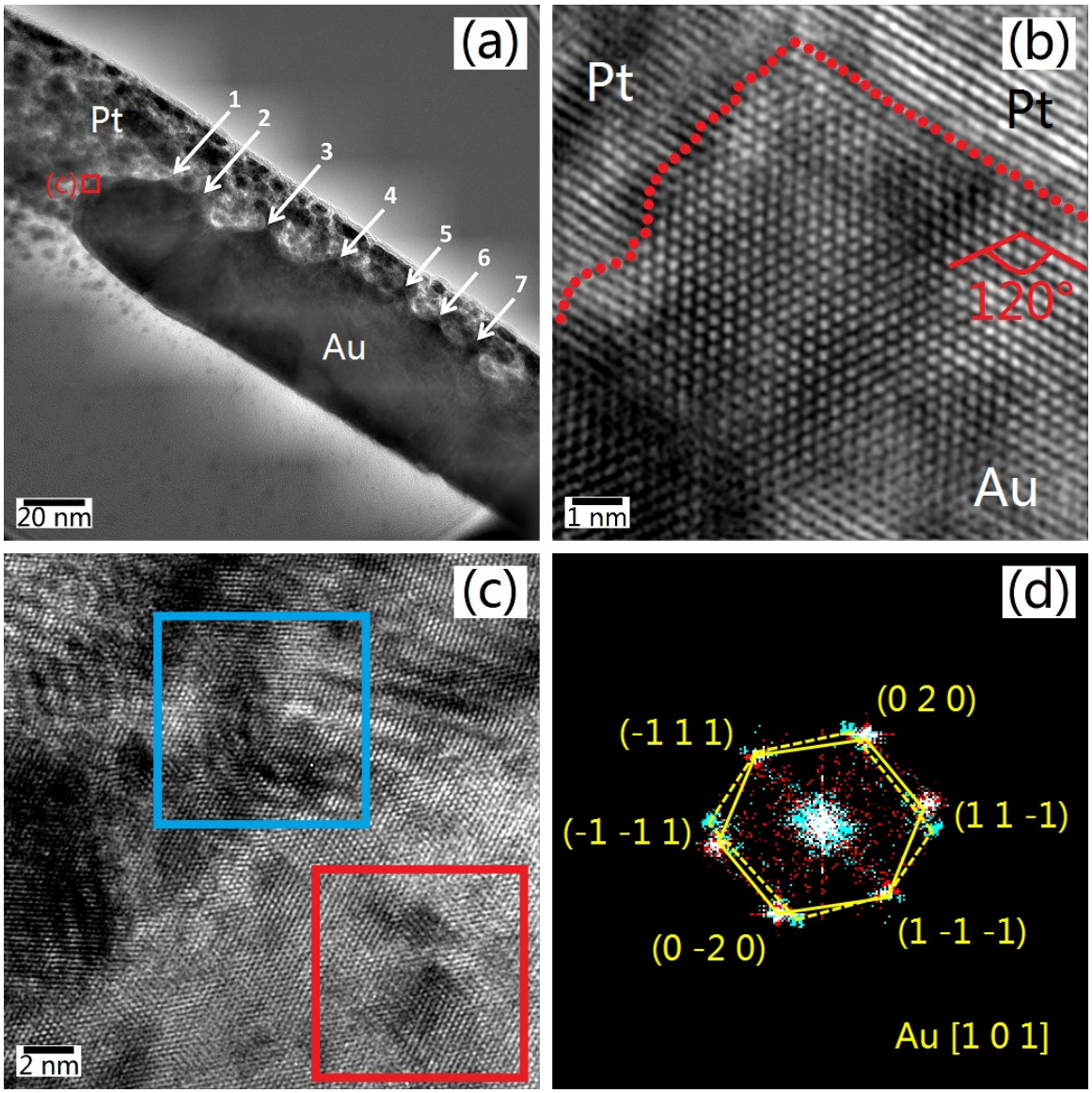

Figure 4.11 Direct observation of active sites through TEM and HRTEM images. (a) Part of one Au nano-ring imaged under TEM showing several pyramids across the surface. (b) HRTEM image taken at the tip of pyramid 1. (c) HRTEM image of the square region in (a). (d) The FFT patterns taken from the two square regions in (c) at the zone axis of [1 0 1], in which the red spot array is reflected from the red square area in (c). There are two sets of blue spot arrays diffracted from the blue square region (i.e. the Moiré fringe region) in (c). One blue spot array is in superposition with the red spot array. The other blue spot array is rotated with respect to the first blue spot array at a small angle of ~ 6°.

4.4 Catalytic Performance of Au Nano-Ring Arrays

4.4.1 Initial Testing and Evaluation of Turnover Frequency (TOF)

The electrochemical performance of the samples in EOR was studied using various ways (**Figure 4.12**), including CV, EIS and CA, with the electrolyte being 0.1 M NaOH and 1.0 M ethanol. In CV scans (**Figure 4.12 a**), strong oxidation peaks are observed at 0.3 V and -0.1 V, which correspond to reactions (a) and (b) in **Equation 2.8** respectively. The oxidation of ethanol to ethanal (occurs at E = 0.3 V) is the main reaction in EOR scans, it can be clearly observed that most of the arrayed samples (coloured curves) perform better than the planar sample (black curve) due to largely increased surface area and active sites. As the RIE duration lengthens, the Au nano-ring height gets lower, which shrinks the total surface area and reduces number of active sites. As a result, it gives a decreasing trend in the height of the peaks. The sample after 20.0 min RIE has abnormally lower performance than the planar sample; besides thinning of Au film and shortening of Au nano-ring height, this could also be due to the existence of large amount of defects on the surface (**Figure 4.7 f**), which may hinder the charge transfer during EOR.

Table 4.1 gives a list of the values of the working electrode current densities of the samples, which are in correspondence with **Figure 4.12 a**, at different oxidation peaks as shown. In the first oxidation reaction given in **Equation 2.8 a** ($CH_3CH_2OH \rightarrow CH_3CHO$), the ratio i/i_0 indicates that most samples with array structures show different degrees of enhancement in electrocatalysis of ethanol, except the sample after 20.0 min RIE which has too many defects that might have hindered the effect of arrays with limited increase in specific surface area. In the second oxidation reaction given in **Equation 2.8 b** ($CH_3CHO \rightarrow CH_3COOH$), the ratio j/j_0 gives a clear trend that the enhancement rises to the maximum at 5.0 min RIE, after which it quickly drops and falls below the performance of the sample without array structures (0.0 min RIE). This implies that the arrayed sample after 5.0 min RIE has the overall best catalytic activities in the EOR with the highest enhancement factor.

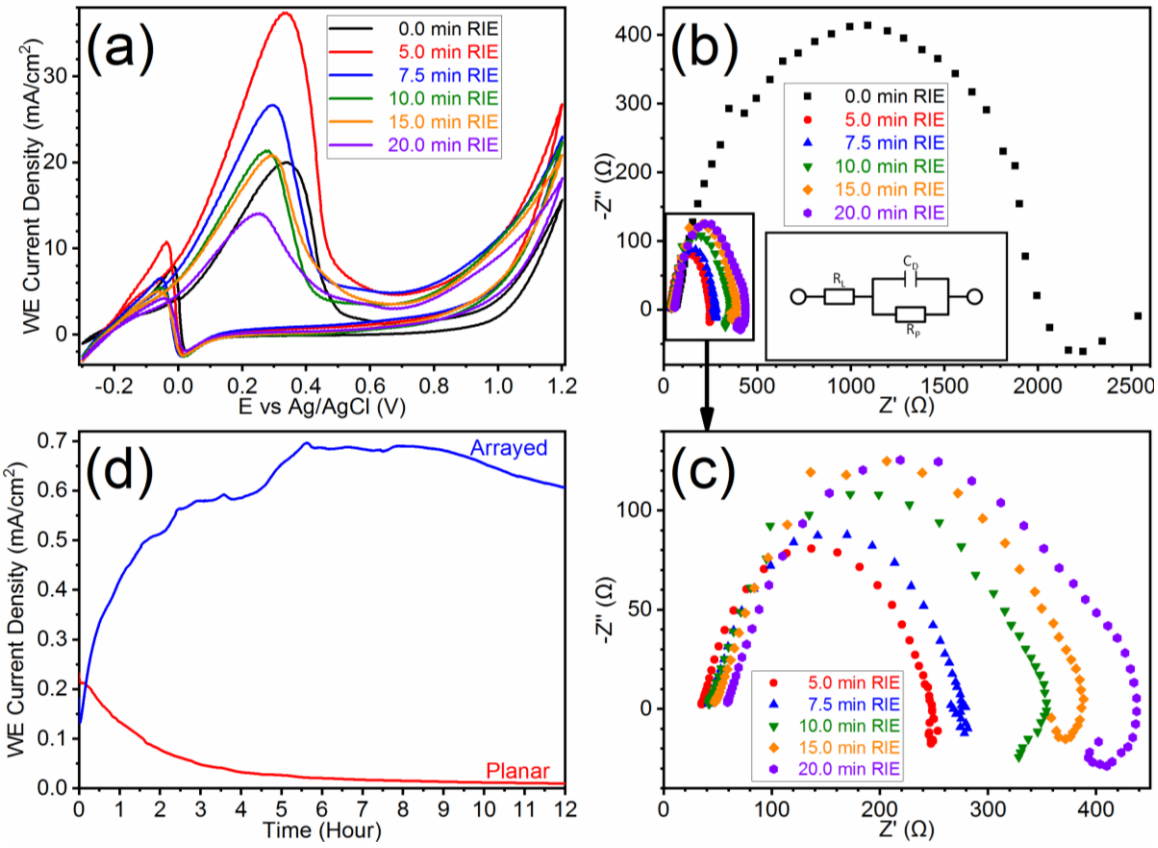

Figure 4.12 Electrochemical behaviours of the Si/Au/PS samples. (a) Cyclic voltammograms. (b) The Nyquist plots obtained from EIS, as well as the equivalent circuit diagram of the experimental setup (inset). R_L: electrolyte resistance; R_P: electrochemical impedance; C_D: double layer capacitance. (c) Magnified EIS of square region in (b) showing only the arrayed samples. (d) Chronoamperometry graph comparing the planar and arrayed samples. All testing was carried out in an electrolyte with 0.1 M NaOH and 1.0 M ethanol.

Table 4.1 WE current densities of the samples at different oxidation peaks

RIE duration	$CH_3CH_2OH \rightarrow CH_3CHO$			$CH_3CHO \rightarrow CH_3COOH$		
	WE current density j (mA/cm^2)*	j/j_0 *,**	TOF (s^{-1})*,†	WE current density j (mA/cm^2)*	j/j_0 *,**	TOF (s^{-1})*,†
0.0 min	20.00	1.00	0.69	7.94	1.00	0.28
5.0 min	37.40	1.87	2.87	10.80	1.36	0.83
7.5 min	26.65	1.33	1.53	6.59	0.83	0.38
10.0 min	21.36	1.07	1.02	5.49	0.69	0.26
15.0 min	20.90	1.05	0.85	5.07	0.64	0.21
20.0 min	14.10	0.71	0.44	4.27	0.54	0.13

* All values are corrected to the accuracy of two (2) decimal places.

** The value of j_0 is set to be that for the sample after 0.0 min RIE.

† The calculation of TOF is according to **Equation 4.1**:

Equation 4.1 Calculation of turnover frequency (TOF) values

$$TOF = \frac{J \times A}{n \times F \times m} \quad \text{(a)}^{1, 2}$$

$$slope = C_D = \frac{n^2 \times F^2 \times m}{4 \times R \times T} \quad \text{(b)}^{1, 2}$$

$$C_s = \frac{C_D}{ECSA} \quad \text{(c)}^{3}$$

$$TOF = \frac{J \times n \times F}{4 \times R \times T \times C_s} \quad \text{(d)}$$

where J is the maximum working electrode current density during each reaction, A is the coverage area of Au nano-ring arrays, n is the number of electrons transferred in each reaction to produce 1 mole of product, F is the Faraday constant (96485 C/mol), m is the amount of active sites within the coverage area of Au nano-ring arrays, R is the ideal gas constant (8.314 J/K·mol), and T is the environmental temperature during the reaction. **Figure 4.13** shows the CV profiles of the samples collected within the potential range between -0.07 V and +0.03 V (where no apparent Faradaic process occurs) under different scan rates; the dotted lines in each figure mark the potential where the values of working electrode current are measured. When the values of working electrode current are plotted against the scan rates, the gradients can be obtained from the linear fits of the plots which represent the values of C_D. The specific capacitance (C_s) is calculated as C_D per unit ECSA, and has a value of ~ 100 mF/cm^2 for Au.[4, 5] Substituting **Equation 4.1 b-c** into **Equation 4.1 a**, the TOF can be simply calculated as **Equation 4.1 d**.

EIS was carried out for all samples, with the AC frequency range being 10^5 Hz to 10^{-2} Hz. From the obtained Nyquist plots (**Figure 4.12 b-c**), it can be found that the planar sample has an impedance of ~ 2000 Ω in the low frequency range, which is almost five times that of the arrayed samples (~ 250-400 Ω). In the experimental setup, as the electrolyte has its intrinsic resistance (R_L), and electrochemical impedance (R_P) and double layer capacitance (C_D) play an important role during the EOR process, the equivalent circuit diagram is designed and shown in the **inset of Figure 4.12 b**. The obvious difference in

the R_P values mainly arises from the largely increased surface area and active sites due to the formation of the ordered Au nano-rings, from $R_{Au} = \rho_{Au} \cdot L/A$, it could be estimated that formation of the ordered Au nano-rings with 5.0 min RIE (red dots in **Figure 4.12 b-c**) brings about eight times increment in the total surface area. The square region in **Figure 4.12 b** is enlarged and displayed in **Figure 4.12 c**, so as to more clearly illustrate the trend of impedance of the arrayed samples. The low-frequency impedance shows an increasing trend as RIE duration lengthens, this is mainly because of thinning of Au film and shortening of Au nano-ring height. Nevertheless, the difference is only ~ 200 Ω, which is small enough as compared to the planar sample. This implies that the effect of having nano-ring arrays is much stronger and influential than thickness of Au film.

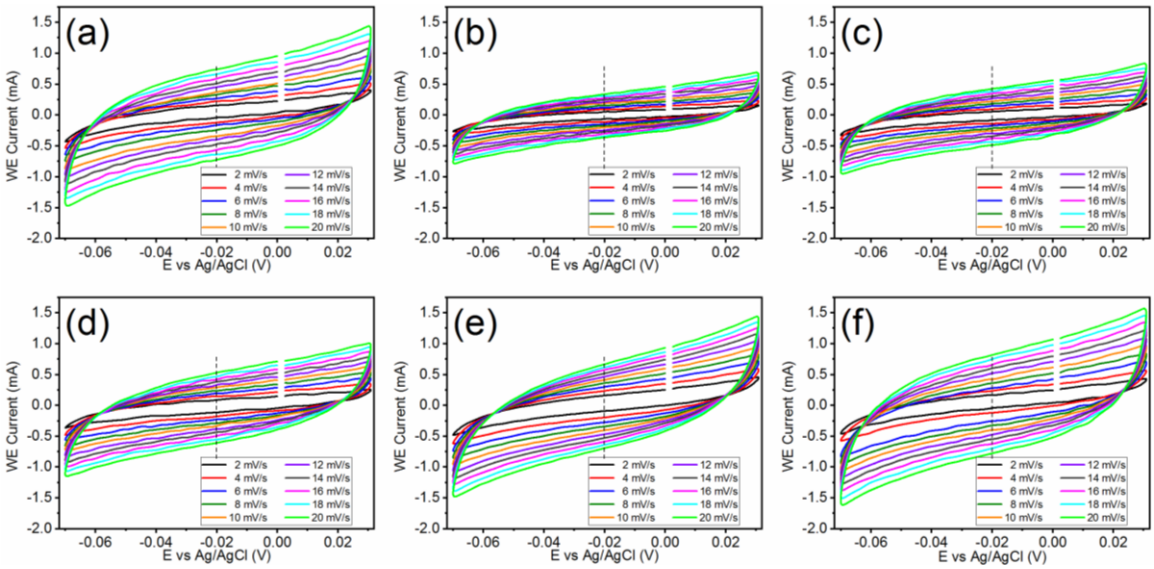

Figure 4.13 CV curves of the samples taken under different scan rates. (a) Original without RIE; as well as after (b) 5.0 min, (c) 7.5 min, (d) 10.0 min, (e) 15.0 min and (f) 20.0 min RIE.

CA was only carried out for planar sample and arrayed sample after 5.0 min RIE, so as to compare the stability of the planar and arrayed samples. **Figure 4.12 d** shows that the planar sample (red curve) gives a steadily decreasing performance (which is indicated by the working electrode current density), while for the arrayed sample (blue curve), there is an elevation of performance in the first 6 h, and then gradually reduces to a working electrode current density much higher than the initial value at the end of the 12-h test. This suggests that by creating nano-ring arrays, the sample could have much higher

specific surface area and more active sites, and thus lowers the activation energy of the EOR process. Both EIS and CA could serve as a supplementary explanation to the aforementioned observations in CV scans.

4.4.2 Performance under Different Physical Conditions

To reveal any hidden reactions which might be neglected in **Figure 4.12 a**, the samples were scanned within a wider potential range and the CV profiles were displayed in **Figure 4.14 a**. The two major oxidation peaks show no obvious difference as compared to **Figure 4.12 a**, except little deviation in the respective potentials. It also implies a general trend that samples with array structures perform much better than the planar (control) sample, except the sample underwent 20.0 min RIE which might have been greatly damaged due to prolonged exposure to the energetic reactive ions. The best performance is still given by the sample after 5.0 min RIE, which is in good agreement with **Figure 4.12**.

Since a larger potential range was used, extra oxidation peaks are therefore identified and clearly spotted with varying concentrations of ethanol. **Figure 4.14 b** shows the CV profiles of the sample after 5.0 min RIE, with ethanol concentrations varying from 1.0 M to 0.5 mM (the pH of electrolyte was held constant at 13). The intensity of the oxidation peak at E = 0.4 V displays an obvious reducing trend as the ethanol concentration gets lower, and the lowest concentration is 10 mM for this particular peak to be identifiable. A similar trend goes to the second strongest peak at E = 0.1 V, of which the detection limit is 50 mM ethanol. Another set of noticeable oxidation peaks is observed at E = 0.2-0.3 V and E = -0.3 V, which are suspected to be the EOR via C1 pathway (as shown in reactions (c) and (d) of **Equation 2.8** respectively).[6] These peaks are detectable down to the ethanol concentration of 5.0 mM and both show an increasing signal ratio to the two major oxidation peaks aforementioned with decreasing ethanol concentration. This suggests that at low ethanol concentration, the EOR would prefer to proceed via the C1 pathway, instead of producing acetic acid via C2 pathway.

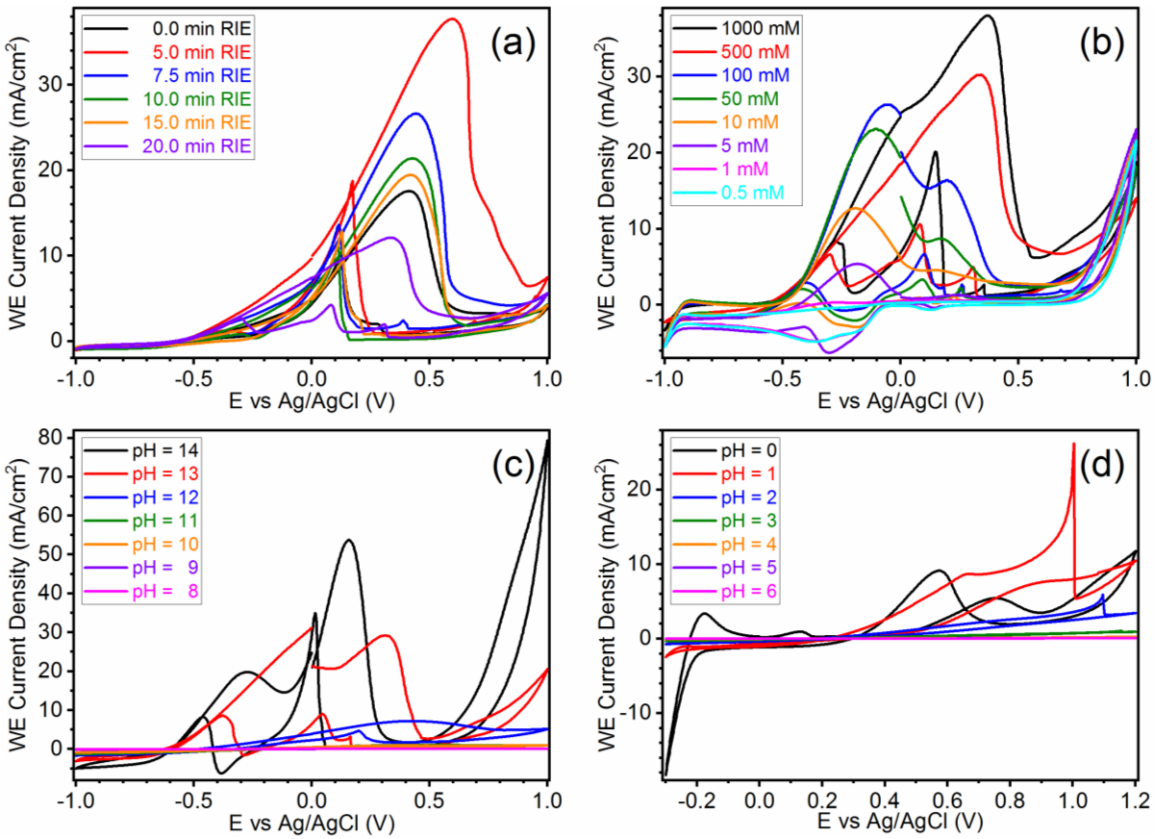

Figure 4.14 Cyclic voltammograms of the Si/Au/PS samples under different physical conditions. (a) All samples in 1.0 M ethanol at pH = 13; (b) the sample after 5.0 min RIE at pH = 13 with varying ethanol concentrations; (c-d) the sample after 5.0 min RIE in 1.0 M ethanol at different pH values.

The effect of pH values of electrolyte on EOR is separately displayed in alkaline/acidic conditions and shown in **Figure 4.14 c-d**. It can be found that at extreme pH values (pH = 14 or 0), the oxidation peaks are strong even with a high signal at upper or lower potential limit due to the evolution of oxygen or hydrogen. This is possibly because at extreme pH values, the concentration of mobile charge carriers (OH^- or H^+) is very high and thus the reactions could easily proceed under a high flux of charge transfer. When the electrolyte was diluted to the third grade (pH = 12 or 2), the concentration of mobile charge carriers is now three orders lower than that at extreme pH values, and this leads to significantly lower signals of the oxidation peaks. Further dilution makes the electrolyte even more neutral in pH value and the concentration of OH^-/H^+ gets even lower, this

would highly increase the electrolyte resistance (R_L as shown in **Figure 4.12 b**) and thus hinder the charge transfer process (lower C_D as shown in **Figure 4.12 b**).

4.4.3 Proposed Working Mechanism of Atomic-Scale Active Sites during EOR in Alkaline Medium

It seems that the EOR would occur via C1 pathway more preferentially in alkaline medium, in which more CO_2 could be produced and released as gas bubbles due to Le Chatelier's Principle, as alkaline electrolyte could help absorb and neutralise the released acidic CO_2. It is important to analyse the reaction products and any intermediate product, and this was performed by FTIR. The sample used was after 5.0 min RIE and the electrolyte had an ethanol concentration of 1.0 M at pH = 13.

Figure 4.15 shows the FTIR spectra of the electrolyte on KBr pellet after 5 (red spectrum) and 135 (blue spectrum) consecutive cycles of CV collected using transmission mode after the removal of background. There are several common peaks identified and they are important in reconstructing part of the EOR process. Peak (a) represents the O-H bond stretching from water (sourced from the electrolyte) and therefore both spectra show similar peak intensities (in terms of ΔT). Peaks (b) and (e) represents the O-H and C-OH bond stretching from ethanol and after 135 cycles of CV, the peaks are obviously weakened as much more ethanol has been oxidised during the EOR process. Peak (c) represents the C=O bond from ethanal and acetic acid; as the reaction from ethanol to ethanal is the major reaction in the entire EOR process, this peak has no obvious difference in intensities. Peak (d) represents the bending of CH_x species; as the EOR proceeds randomly via C1 or C2 pathway, more cycles will mean higher chance of production of CH_x species according to **Equation 2.8 c**, and therefore the blue spectrum shows a higher signal in this peak. Peak (f) represents the C-H bond bending; the signal again becomes much weaker in the blue spectrum, this could arise from the oxidation of the CH_x species to adsorbed CO, as displayed in **Equation 2.8 c**.

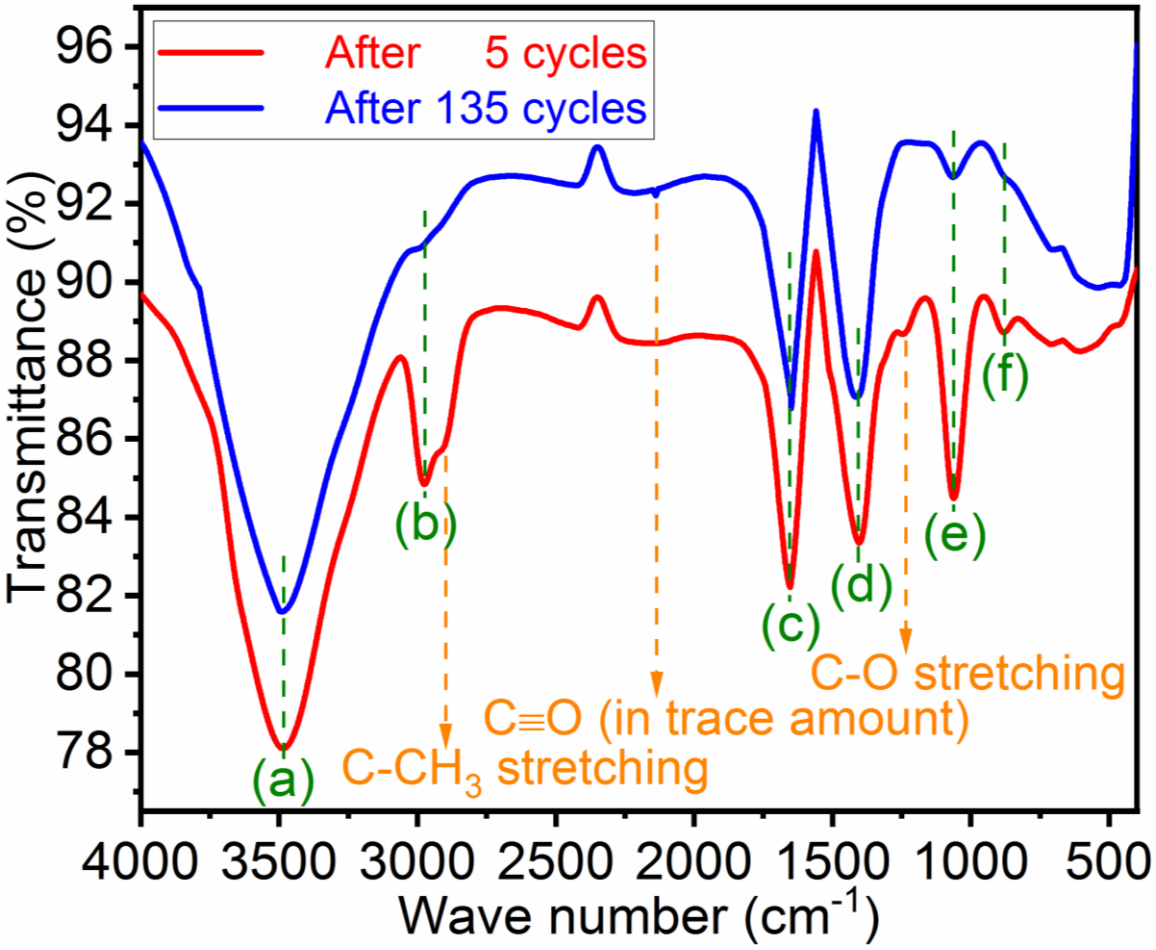

Figure 4.15 The FTIR spectra of the electrolyte on KBr pellet after 5 (red spectrum) and 135 (blue spectrum) consecutive cycles of CV collected using transmission mode after the removal of background

Figure 4.15 also displays three distinct differences in the peaks, which are marked in orange. At the wave number of 2910 cm^{-1}, the red spectrum shows a clear signal of C-CH_3 functional group and it becomes almost invisible in the blue spectrum; this signifies that more ethanol molecules has been converted into adsorbed CH_x and CO species via the C1 pathway. The appearance of the tiny peak in the blue spectrum at the wave number of 2140 cm^{-1} represents the C≡O functional group,[7] which could only originate from the adsorbed carbon monoxide according to **Equation 2.8 c**. These differences imply the occurrence of EOR via C1 pathway. The peak at the wave number of 1243 cm^{-1} in the red spectrum represents the C-O bond stretching from the ethanol molecules, and it becomes nearly invisible in the blue spectrum, this means that after 135 cycles of CV,

most of the ethanol molecules might have been reacted. The FTIR spectra have revealed that C1 and C2 pathways occur randomly and that they may happen at the same time.

The outstanding electrocatalytic activities observed above are mainly due to the largely increased number of active sites. With the first ever directly observed evidence of atomic-scale active sites for electrochemical activities, **Figure 4.16** gives a schematic illustration of the working principle during the electrocatalytic process of EOR. The yellow dots represent a single crystalline Au cluster, of which the surface atoms act as the active sites; when the sample (functioning as the working electrode) is inserted into the electrolyte, ethanol molecules are brought in close proximity to the atomic-scale active sites and get physisorbed as the first step.

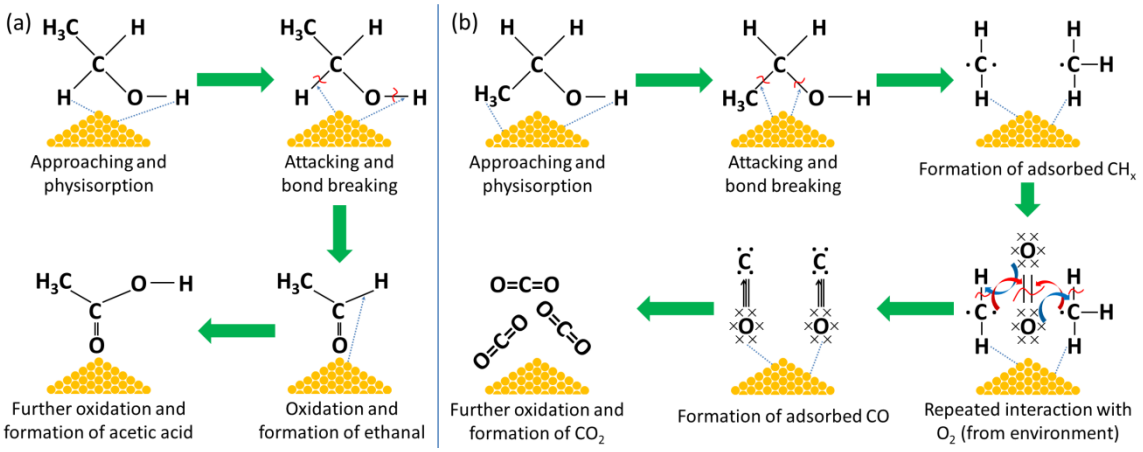

Figure 4.16 Schematic illustration of the working mechanism when the active sites are brought in close proximity to the ethanol molecules. The reactions are proceeding via (a) C2 and (b) C1 pathways, ending up with different intermediate and final reaction products.

The ethanol molecules tend to form dimers,[8] which may hinder the exposure of C-C bond to the Au nano-clusters, thus C2 pathway is the preferred reaction mechanism at the beginning of the EOR process. When the reaction goes via the C2 pathway (**Figure 4.16 a**), formation of the hydrogen bonds to gold (Au···H-X bonds)[9] leads to the attacking of the original H-C and/or H-O bonds of the ethanol molecules.[10] The direct intermediate product of this oxidation is ethanal, which is shown as reaction (a) in **Equation 2.8**. Following that, the Au···H-X bonds continue to form and cleavage of another H-C bond

leads to the formation of the new C-O-H bond, which finally produces molecules of acetic acid (displayed as reaction (b) in **Equation 2.8**). After completing these processes, the acetic acid molecules get desorbed from the active sites and new ethanol molecules may get adsorbed for another round of electro-oxidation. On the other hand, as the reactions proceed, the concentration of ethanol is slightly lowered in the electrolyte, and the ethanol-ethanol dimers progressively get transformed into ethanol-water dimers[11] via a different form of hydrogen bonding. With a lower bond dissociation energy compared to the C-H and O-H bonds, when the C-C bonds stand a higher chance of exposure to the Au nano-clusters, C1 pathway now gets increasing preference, and the reaction mechanism (**Figure 4.16 b**) is deduced from the reaction products (**Figure 4.15**).

In C1 pathway, with the physisorption of ethanol molecules on the surface of an Au nano-cluster, the active sites now attack the C-C bonds and this process is less energy-consuming. The ethanol molecules are broken down into intermediate CH_x with free radical sites (displayed as reaction (c) in **Equation 2.8**), which repeatedly interact with the oxygen molecules from the environment and then get oxidised into carbon monoxide molecules (adsorbed on the Au nano-clusters). Further oxidation will lead to the formation of carbon dioxide molecules (shown as reaction (d) in **Equation 2.8**), which would desorb from the Au nano-clusters and get released, thus allowing new rounds of electro-oxidation.

The drastic increase in the number of active sites benefits from the enhancement in total surface area brought by the nano-ring array structures. By calculations using theoretical values, sample with nano-ring arrays may achieve a maximum enhancement of ~ 15.6% in total surface area compared to the original planar sample before RIE. This is a great amount of increment in surface area, which provides plenty of rooms for the formation of active sites in both nano-scale and atomic scale as aforementioned.

4.5 Summary

The NSL-RIE approach is a fast and effective way to fabricate ordered Au nanostructured arrays on Si wafers. Compared to other methods, this approach is much safer and easier; the coverage of the Au nano-rings is almost 100% except intrinsic defective regions prior to the RIE process. Under the optimised RIE parameters with different etching durations, nano-ring array structure may result in a maximum of ~ 15.6% increase in total surface area compared to the planar sample, which provides substantial opportunity for the formation of active sites. Direct evidence of active sites in both micro-/nano-scale and atomic-scale has been first ever observed in TEM and HRTEM images. Electrochemistry tests have indicated that the Au nano-ring arrays have good electrocatalytic performance; samples with Au nanostructured arrays perform much better than the planar samples in EOR. This is probably because ordered nanostructures produced by RIE have much higher specific surface area and more active sites and therefore lowers the activation energy for EOR. Long continuous CV scans reveal that in alkaline medium, C1 pathway could become increasingly preferential over C2 pathway, and thus making the Au nano-ring array structure useful in the field of direct ethanol fuel cell.

References

1. Y. Yao, Z. Xu, F. Cheng, W. Li, P. Cui, G. Xu, S. Xu, P. Wang, G. Sheng, Y. Yan, Z. Yu, S. Yan, Z. Chen and Z. Zou, *Energy Environ. Sci.*, 2018, **11**, 407.
2. C. You, Y. Ji, Z. Liu, X. Xiong and X. Sun, *ACS Sustainable Chem. Eng.*, 2018, **6**, 1527.
3. Y. Li, F.-M. Li, X.-Y. Meng, S.-N. Li, J.-H. Zeng and Y. Chen, *ACS Catal.*, 2018, **8**, 1913.
4. M. B. Cortie, A. I. Maaroof and G. B. Smith, *Gold Bull.*, 2005, **38**, 14.
5. J. P. Carr and N. A. Hampson, *J. Electrochem. Soc.*, 1972, **119**, 325.
6. Y. Wang, S. Zou and W.-B. Cai, *Catalysts*, 2015, **5**, 1507.
7. P. A. Gerakines, W. Schutte, J. Greenberg and E. F. van Dishoeck, *Astron. Astrophys.*, 1994, **296**, 810.
8. V. Dyczmons, *J. Phys. Chem. A*, 2004, **108**, 2080.
9. H. Schmidbaur, H. G. Raubenheimer and L. Dobrzańska, *Chem. Soc. Rev.*, 2014, **43**, 345.
10. J. Cordón, G. Jiménez-Osés, J. M. López-de-Luzuriaga and M. Monge, *Nat. Commun.*, 2017, **8**, 1657.
11. I. A. Finneran, P. B. Carroll, M. A. Allodi and G. A. Blake, *Phys. Chem. Chem. Phys.*, 2015, **17**, 24210.

Chapter 5

Flexible Au Micro-Array Electrode with Atomic-Scale 3D Nanostructures for Enhanced Ethanol Oxidation Reaction

The catalysis of Au thin film could be improved by fabrication of nanostructured arrays with a large area. In this work, NIL approach has been developed to fabricate flexible Au micro-array (MA) electrodes on PVC substrates, which is safe, easy, fast and controllable. The coverage of Au MAs is nearly 100% with high tolerance to intrinsic defects (like scratches). Advanced electron microscopy has directly visualised the atomic-scale 3D nanostructures with a maximum depth of 6 atomic layers (ALs). In-situ observation unveils the crystal growth in the form of twinning. The concentric hexagonal pillars have increased the ECSA and brought about large number of active sites on the Au thin film, resulting in a higher C_D which is estimated to have a logarithmic relationship with mesh grade. Electrochemical testing reveals that MAs with higher mesh grade have a greater active site utilisation ratio (ASUR), which is important to build electrochemical double layer for efficient charge transfer. There are plenty of rooms for further improvements on the ASUR, which is expected to bring about greater electrocatalytic performance. Proceeding via C1 pathway reveals stronger signals in alkaline medium and makes the flexible Au MA electrode potentially useful in the application of DEFC.

---

*This chapter is submitted substantially as **X. Cao**, D. Peng, C. Wu, Y. He, C. Li, B. Zhang, C. Han, J. Wu, Z. Liu and Y. Huang, *Nano Res.*, submitted (revision in progress).

5.1 Materials and Chemicals

The materials used in this work include clear PVC sheets (0.2 mm thickness, Hongwang Moulds) as the substrates and Au source (99.99% purity, Sigma-Aldrich) for electron beam evaporation. Ni grids of different mesh grades (hexagonal mesh, 99% purity) were purchased from Electron Microscopy China, PRC. The chemicals used in this project include absolute ethanol (CH_3CH_2OH, 99.9%, Aik Moh) and potassium hydroxide flakes (KOH, 90%, Sigma-Aldrich). All of the abovementioned chemicals were used as received without any further purification. The deionised water was made by the Millipore™ system, which has the resistivity of 18.2 MΩ·cm.

5.2 Imprinting Parameter Optimisation

The thermal phase transition was determined by DSC and the profile is given in **Figure 5.1**. From 25 °C to 200 °C, PVC may have four distinct phases and undergoes three transitions as the temperature rises. PVC exists in its glassy state at room temperature; at the glass transition temperature (T_g) of ~ 74.2 °C, it undergoes the first thermal phase transition and steps into the rubbery state. Further heating to the heat deflection temperature (HDT) of ~ 92.5 °C leads to the thermal distortion of PVC, and the deformed state continues until reaching the melting temperature (T_m) of ~ 157.9 °C, at which PVC turns into its "liquidus" state and becomes completely amorphous. Based on the thermal analysis, the PVC substrates were first imprinted at the different working temperatures ranging from 70 °C to 150 °C at an interval of 20 °C. Each substrate was held at the setpoint for 5 min, with the N_2 gas pressure held constant at 8 bar. The working profile during the NIL process (steps 2-3 in **Figure 3.8**) is detailed in **Figure 5.2**.

The corresponding POM and top-view FEG-SEM images are displayed in **Figure 5.3 a-e**. It is clear that at 70 °C (**Figure 5.3 a**), no pattern could be formed on the substrate. This is because PVC was still in its glassy state and almost having no thermal phase transition at this temperature, which is in good agreement with the DSC profile. The glassy PVC has no fluidic nature and therefore thermal imprinting would not succeed. When the

temperature was raised to 90 °C (**Figure 5.3 b**), the first thermal phase transition had completed and the PVC was now in the rubbery state. Softening of PVC led to the successful imprinting and the grid pattern was generated.

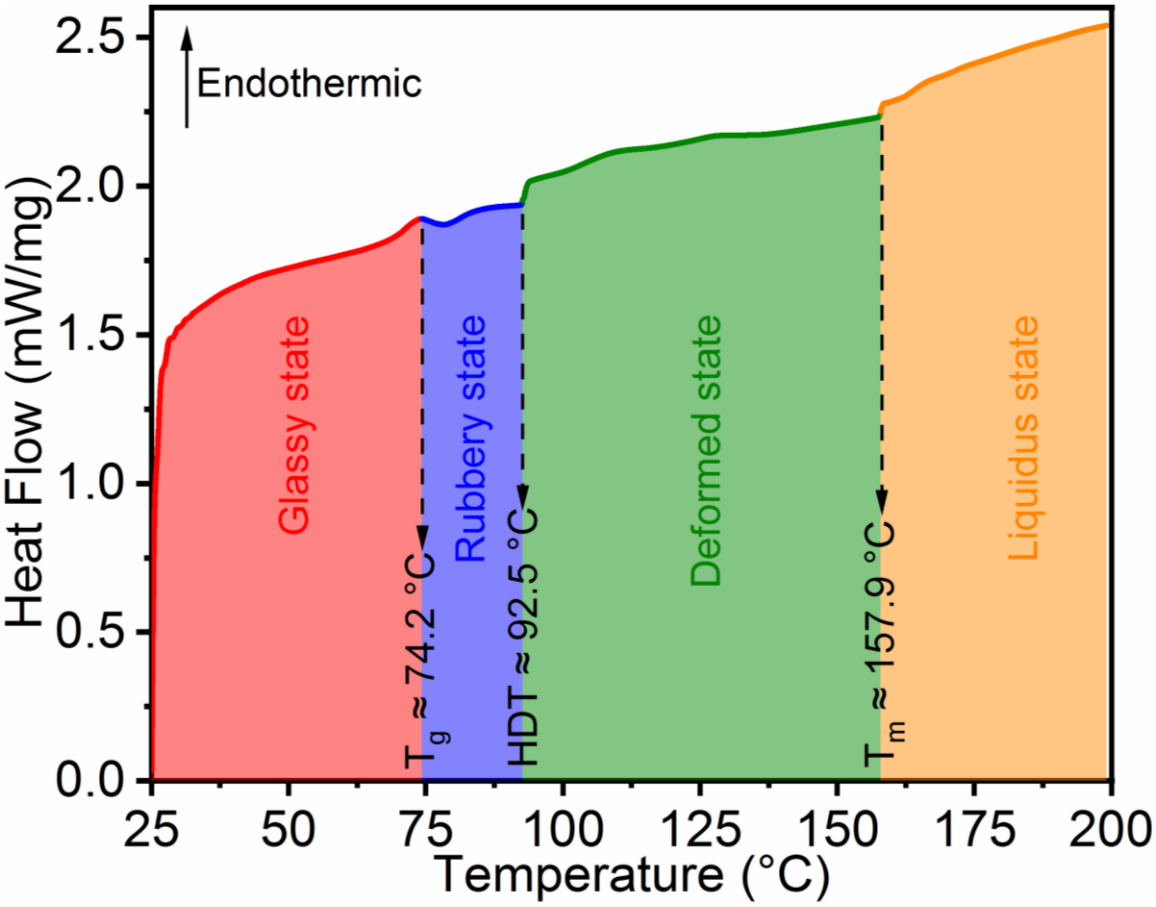

Figure 5.1 The thermal phase transition profile of the cleaned PVC substrate

When the PVC substrate was heated and softened, the suppression by the Ni grids created "aisles" surrounding the hexagonal features, which should have a lower altitude than both the hexagons (the main features in the figures) and regions outside the circular grids (the corners of the figures). However after imprinting at 90 °C, the hexagonal features were not distinct and the POM image appeared rough. The FEG-SEM image (**inset of Figure 5.3 b**) shows a junction between three hexagons. Many bulk pieces with various sizes could be observed, which are believed to be the residual PVC that did not spread out during the imprinting process. PVC in the rubbery state gets softened but its fluidity

might be poor, thus causing the residues to stay and that the hexagonal features could only be distinguished via phase contrast rather than amplitude contrast.

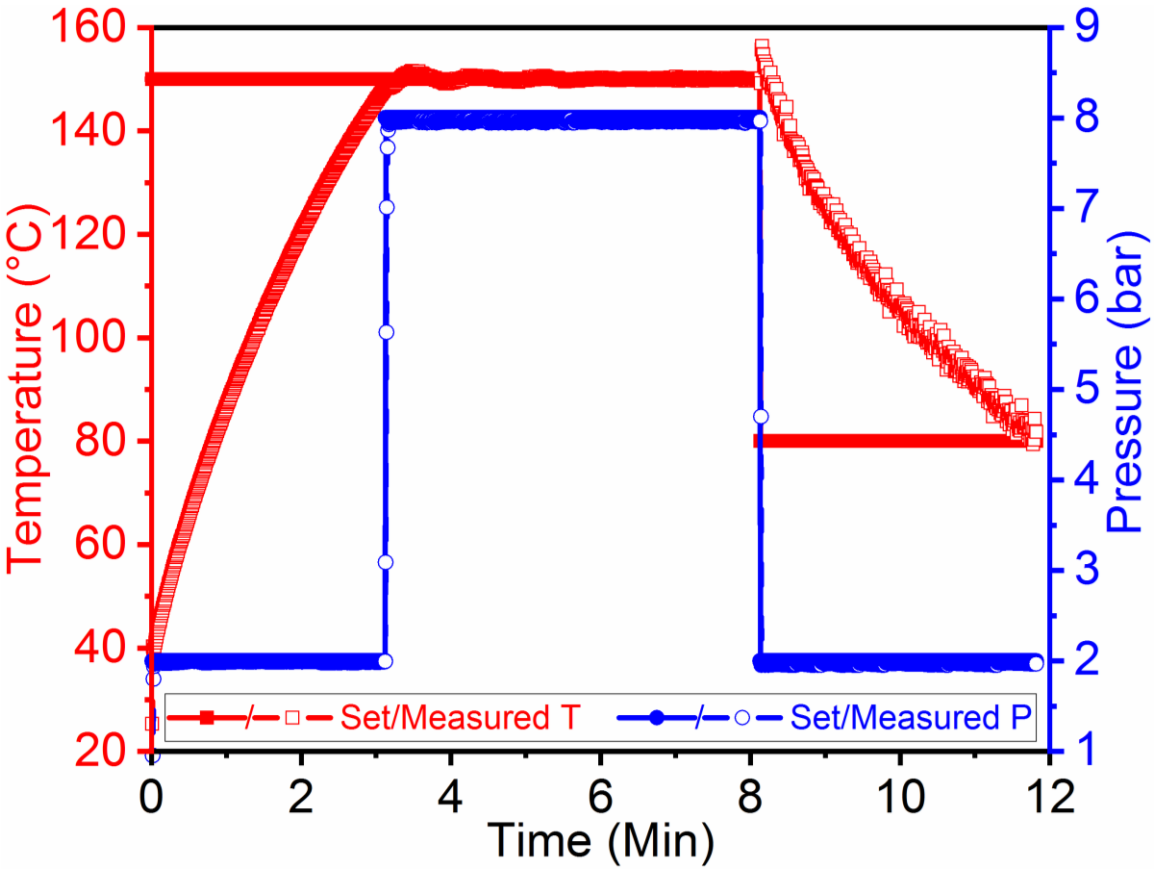

Figure 5.2 The working profile during the NIL process

Upon crossing the HDT, further heating to 110-150 °C brings the PVC into its deformed state. The softened PVC now has excellent fluidity and could be easily reshaped. The materials under the suppression regions spread out uniformly, thus forming hexagons in distinct pillar structures (**Figure 5.3 c-e**). Since the Ni grids have uniform thickness across the entire metallic regions, the pillars should have the same altitude as the regions outside the circular grids. The corresponding inset figures reveal that even within the deformed state, the working temperature still influences the geometry of the pillars. Each pillar has a double-layer structure (which cannot be observed in the **inset of Figure 5.3 b**), which is shallow after 110 °C imprinting and appears the most solid after 150 °C imprinting. This implies that higher temperature would lead to greater thermal distortion

of PVC; lower tackiness of the thermoplastic enhances the fluidity, and thus the pillars could protrude upwards with more solid double-layered structures.

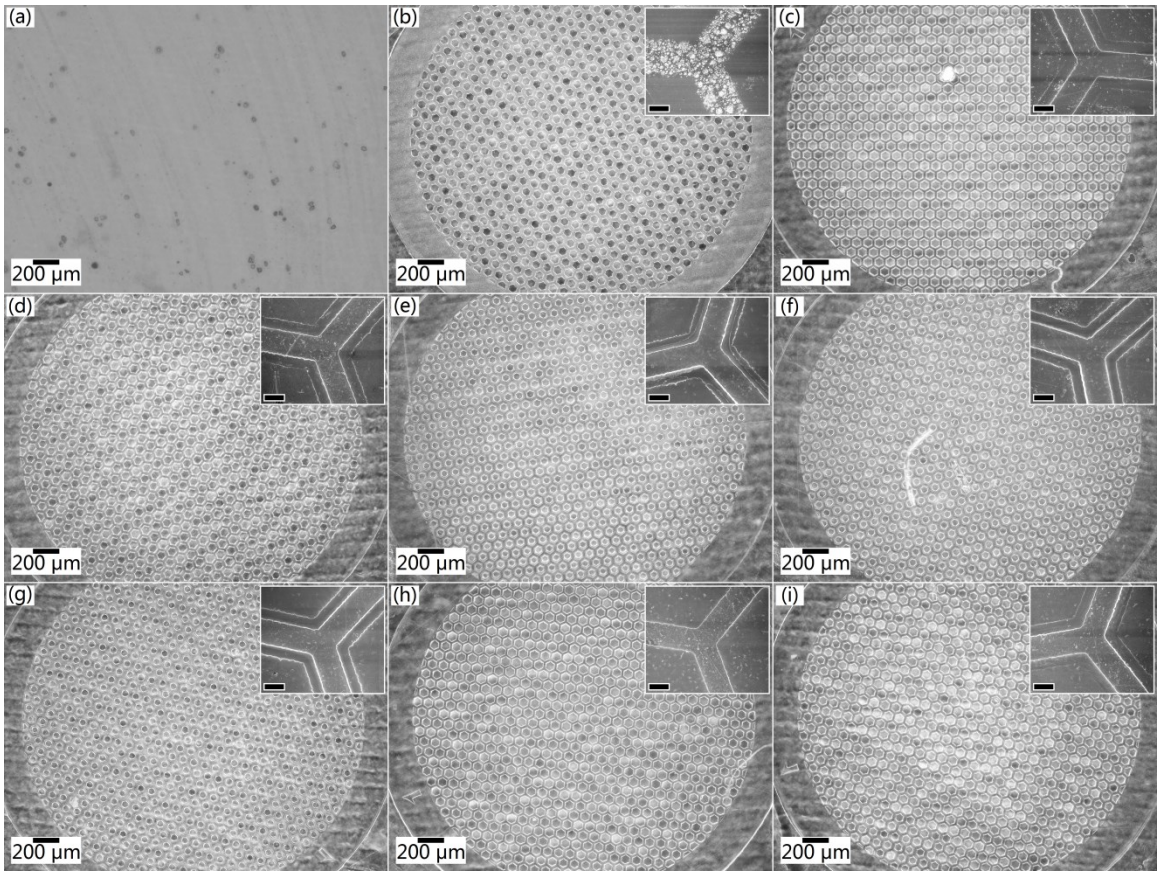

Figure 5.3 The POM and top-view FEG-SEM images of different samples. (a-e) Samples imprinted for 5 min under 8 bar pressure, at (a) 70 °C; (b) 90 °C; (c) 110 °C; (d) 130 °C and (e) 150 °C. (f-g) Samples imprinted at 150 °C under 8 bar pressure for (f) 1 min and (g) 3 min. (h-i) Samples imprinted at 150 °C for 5 min under (h) 2 bar and (i) 5 bar pressures. The inset figures of (b-i) show the top-view FEG-SEM images of a "junction" at the magnification of 2 k×, and the scale bar represents 10 µm.

The PVC substrate melts at ~ 157.9 °C, upon crossing the T_m, it turns into the "liquidus" state. The irreversible amorphisation would result in low dimensional stability (which means the material is easily deformed), therefore within the temperature limit (200 °C) of the instrument, the best imprinting temperature was confirmed to be 150 °C. Variation of imprinting durations was carried out as the next phase, the corresponding POM and FEG-SEM images are shown in **Figure 5.3 e-g**. No obvious difference could be identified

between the imprinted samples with 1-5 min holding time. This should be due to that the shaping of PVC is a fast process, such that 1 min of imprinting seems enough to produce good pillar structures. As such, the holding time for imprinting was chosen to be 1 min in a later stage of the study.

To understand the influence of pressure in the process, two extra samples were imprinted at 150 °C with 5 min holding time under different pressures (**Figure 5.3 h-i**). The effect is obvious from the inset FEG-SEM micrographs. Under 2 bar pressure (**Figure 5.3 h**), the pillar is uniform without the double-layer structure; double-layered pillars could be formed under 5 bar pressure (**Figure 5.3 i**), but they are much shallower compared to that formed under 8 bar pressure (**Figure 5.3 e**). As a result, the optimum imprinting parameters are set as 150 °C for 1 min under 8 bar pressure for the next stage of study.

5.3 Morphology and Crystallography of Au MA

Apart from the imprinting temperature, holding time and applied pressure, another key factor that affects the geometry of micro-arrays is the mesh grade of the mould (Ni grids). Based on the optimised parameters for imprinting, more samples were imprinted using Ni grids of different mesh grades (50, 150, 200, 300 and 400 mesh). Right after the NIL process, the overall appearance of the samples was first viewed under a POM, and the images of single-grids are displayed in **Figure 5.4 a-e**. They confirm that the micro-array samples are free of bulk defects (which could be caused by broken grids), and the hexagonal array structures are nicely arranged as a result of the NIL process. Defects such as scratches on the surface are unavoidable, but best efforts have been made to reduce them in quantity.

After Au-coating via electron beam evaporation, the samples were loaded into an FEG-SEM/FIB dual-beam system for further characterisation. Each sample was magnified such that one pillar structure can be clearly revealed. From the FEG-SEM images (**Figure 5.4 a'-e'**), it can be found that the width of the "aisles" (marked as the Y-shaped regions between the red parallel lines) decreases as the mesh grade increases, and the "aisles" are

getting rougher at higher mesh grade. The double-layered structure of the pillars is illustrated as a smaller hexagon sitting on top of a concentric larger one, and the size of the pillars shrinks as mesh grade increases (from ~ 500 μm for 50-mesh sample to ~ 60 μm for 400-mesh sample). The hexagonal pillar is viewed at an inclined angle of 52° and the high resolution FEG-SEM image is displayed in **Figure 5.4 f**. Cross-sectional measurements return a thickness of ~ 1.2 μm for the larger hexagon (bottom layer) and ~ 0.5 μm for the smaller hexagon (top layer), and multiple measurements have led to a small error range of ~ 1.6%. This in turn shows the homogeneity of the NIL process.

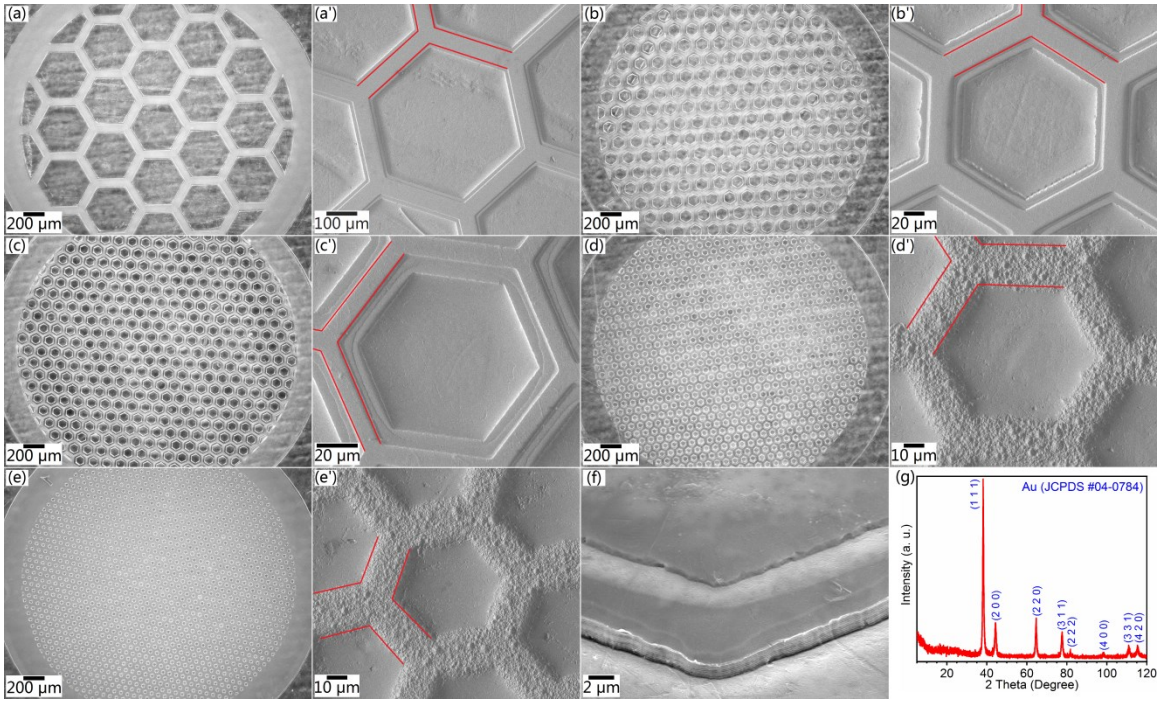

Figure 5.4 Characterisations of the PVC/Au samples. (a-e) The 50× POM images of the patterned samples with (a) 50-mesh, (b) 150-mesh, (c) 200-mesh, (d) 300-mesh and (e) 400-mesh MAs; (a'-e') the corresponding top-view FEG-SEM micrographs showing a single hexagonal pillar structure; (f) FEG-SEM micrograph of a pillar at its corner, taken at an inclined angle of 52° showing its height; (g) the XRD pattern of the samples after Au-coating.

The crystalline phase of the sample was confirmed by thin film XRD, and the diffraction pattern is shown in **Figure 5.4 g**. By matching against the standard database from the International Centre for Diffraction Data, the samples are highly polycrystalline FCC Au (JCPDS #04-0784), and the strongest diffraction line appears at $2\theta \approx 38.2°$, which should

be ascribed to the (1 1 1) crystal plane. The high crystallinity can be proven by the distinct diffraction lines at high 2θ angles, which represent high order crystal planes that usually have weak diffraction.

5.4 Direct Visualisation of Atomic-Scale 3D Nanostructures and Active Sites

To deeply investigate the details of the crystal structure, top-view TEM was performed to the Au thin film after it was transferred onto a Cu support grid. **Figure 5.5 a** is a bright-field TEM image taken at relatively low magnification, which shows part of an edge of the sample resting on a mesh opening of the Cu grid. The bright tip at the middle of the top edge (marked by the red circle) shows the amorphous PVC substrate covered by a thin layer of Au. The random-oriented dark fringes are wrinkles created during sample transfer due to folding and unevenness. The SAED pattern at this site (covering most of the area of **Figure 5.5 a**) is given in **Figure 5.5 b**, which suggests a highly polycrystalline nature of the Au thin film. All crystallographic planes, as per diffraction lines produced in XRD characterisation (**Figure 5.4 g**), are perfectly rendered in the SAED with similar ratios of intensities; the (4 2 2) crystal plane (diffracted at $2\theta \approx 135.4°$) and possible diffractions of even higher order planes that are beyond the capability of XRD, are shown with detectable intensities by the naked eye.

A thin square region with a side length of ~ 15 nm, which positions ~ 100 nm away from the edge and is free from folding, was imaged at high resolution in TEM (**Figure 5.5 c**). It is a highly single-crystalline region according to the FFT pattern (**Figure 5.5 d**) transformed from the entire HRTEM image of **Figure 5.5 c**. The strong diffraction spots are well matched against the JEMS software (Electron Microscopy Software, Java Version 4.3905U2016, developed by Dr. P. Stadelmann, Switzerland), and are ascribed to the {1 1 0} family of planes of the FCC-structured Au. The sample thus has a zone axis of [1 1 1] which is perpendicular to the PVC substrate, and is in alignment with the preferred growth orientation as presented by XRD. The FFT pattern was inversely transformed to present more information on crystallography by performing the IFFT imaging process (**Figure 5.5 e-i**) either in whole or along particular crystallographic

orientations. **Figure 5.5 e** (transformed in whole) shows an HRTEM image with a much better phase contrast compared to the originally captured (**Figure 5.5 c**).

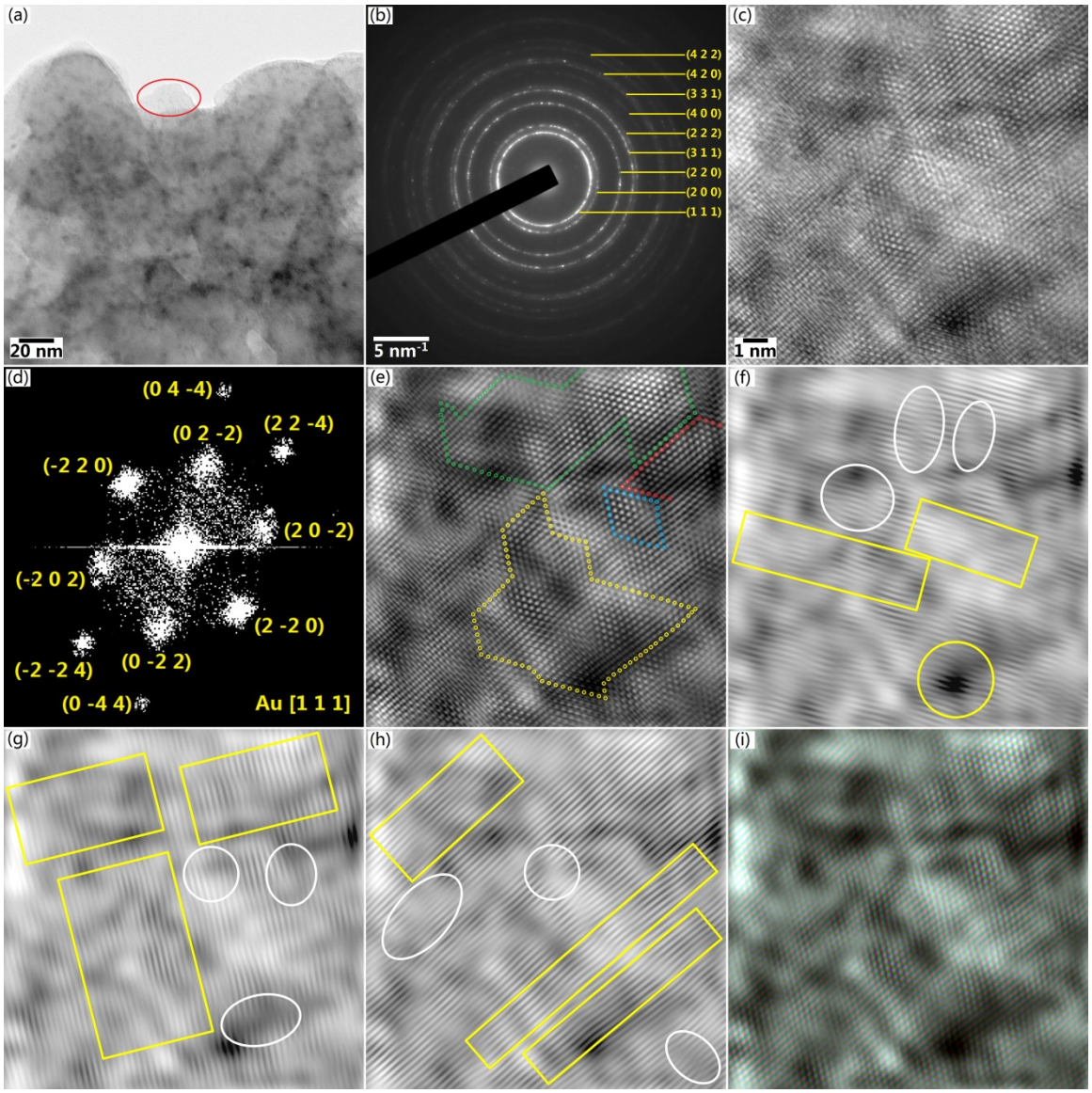

Figure 5.5 TEM characterisations of Au thin film with 400-mesh MAs. (a) Low magnification bright-field TEM image showing part of an edge. (b) The SAED pattern rendering strong diffraction of the sample. (c-d) The original HRTEM image (c) of an inner site (~ 100 nm away from the edge of sample), as well as the corresponding FFT pattern (d) of the entire HRTEM image. (e-i) The IFFT images of (d), transformed (e) in whole and (f-h) along <0 1 1>, <1 0 1> and <1 1 0> directions, respectively; (i) the RGB mapping of (f-h). (e-i) share the same scale bar as the HRTEM image shown in (c).

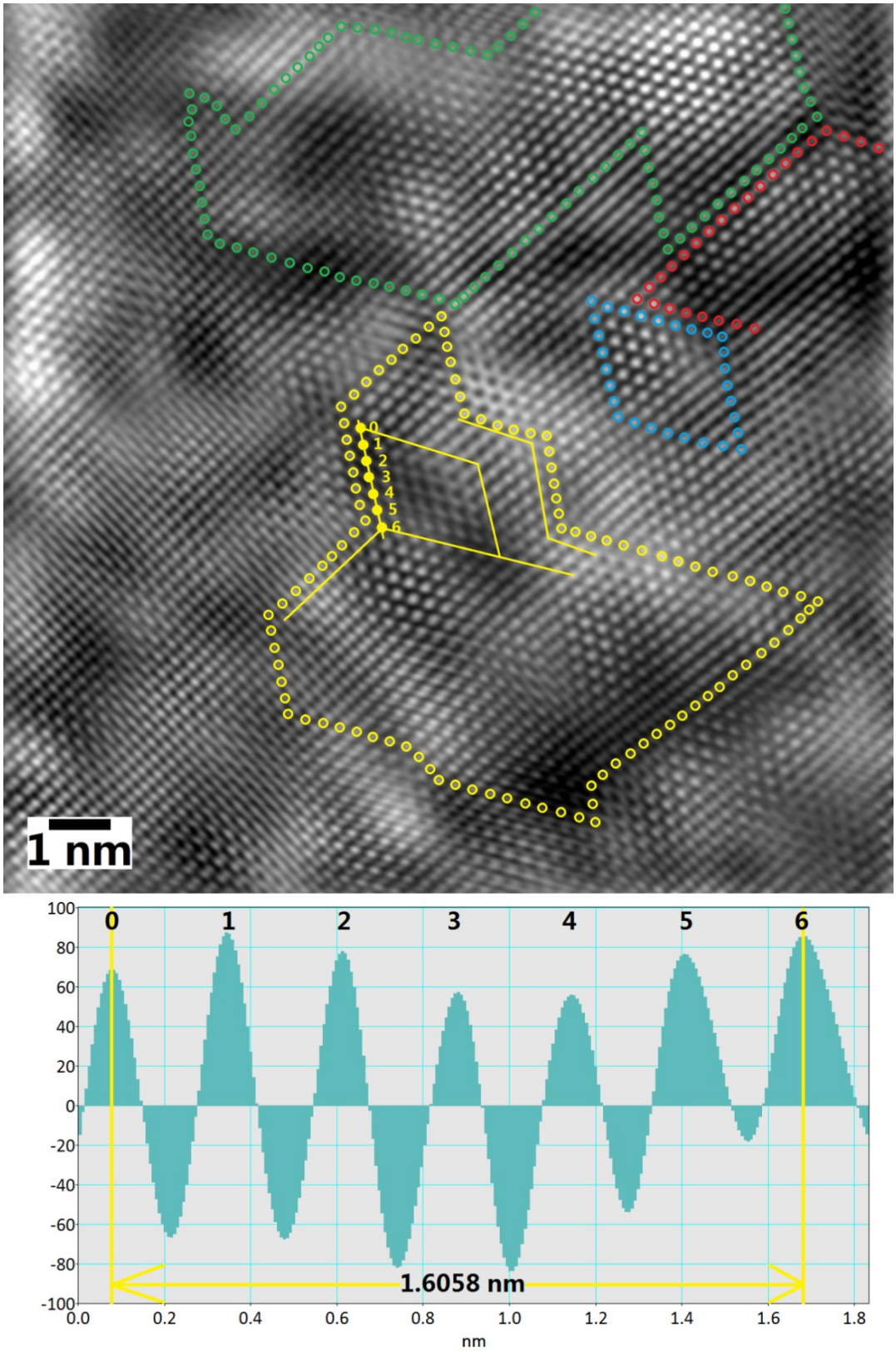

Figure 5.6 Marking of the atomic-scale 3D nanostructure (top), as well as the line measurement profile along the yellow line from atom #0 to atom #6 (bottom).

Increase in exposed surface area can now be clearly observed even at atomic scale – the single crystalline region reveals several parts (as enclosed by the coloured dots) with atomic-scale 3D nanostructures, with a maximum depth of 6 ALs (region bound by yellow dots) as accurately measured in **Figure 5.6**. The top shows part of the IFFT-HRTEM image as given in **Figure 5.5 e**. The open yellow circles mark the outer boundary of the region with the atomic-scale 3D nanostructure, and the yellow lines are the guidelines that mark the 3D structure. The solid yellow dots (from #0 to #6) form the z-axis of the 3D structure while dot #6 is in fact the origin point where x-, y- and z-axes converge. Line measurement was performed along the solid yellow dots and the corresponding profile is given at the bottom part of **Figure 5.6**. The peaks with negative values indicate atomic layers alternate to the labelled, therefore it can be found that the y-z plane has a maximum depth of 6 ALs (displayed as the region bound by the yellow lines) and the total depth is 1.6058 nm. The measured atomic size of Au is ~ 0.2676 nm, which is very close to the empirical value reported (~ 270 pm). The atomic-scale 3D nanostructures are believed to be formed as a result of the NIL process, during which strong force was applied to the small area of meshes and the great pressure led to the formation of the 3D nanostructures on the surface of the PVC substrates.

The subsequent Au deposition inherited the 3D nanostructures. The IFFT images transformed along <0 1 1>, <1 0 1> and <1 1 0> directions (**Figure 5.5 f-h**) render a number of defects (i.e. partial and edge dislocations spotted by the white circles), which carry considerable amount of energy driving efficient EOR process.[1] Apart from those, the yellow rectangles mark several wavy regions that are free from defects – the bright fringes are straight and continuous, but are bent only at junctions with a change in amplitude. The yellow circle in **Figure 5.5 f** identifies a site where the bright fringes gradually bend and weaken until break at a particular spot. Synchronisation to **Figure 5.5 e** shows that it is in fact at the lower corner of the region bound by the yellow dots, where an obvious valley could be observed. These ripple-like natures confirm the existence of the atomic-scale 3D nanostructures. The RGB mapping of **Figure 5.5 f-h** brings about **Figure 5.5 i**, in which clusters of bright atomic sites are clearly distinguished by some

dark spots and fringes. The surface atoms along the interfaces with the dark fringes, as well as those at the edge of the 3D nanostructures, serve as the atomic-scale active sites;[2] they are all along the <1 1 0> direction, indicating that more energy is stored at these active sites compared to any others that might be formed along the <1 0 0> and <1 1 1> directions.[1, 3] The large density of atomic-scale active site allows easier physisorption of ethanol molecules[2] and therefore will perform strong catalysis in EOR under the synergistic effect of the atomic-scale 3D nanostructures.

5.5 *In-Situ* Observation of Interactions between Atomic-Scale Active Sites

The interactions between atomic-scale active sites were investigated by *in-situ* TEM observations in the form of consecutive HRTEM imaging. A unique and easily identifiable nanostructure with atomic-scale active sites was first located and captured in TEM. **Figure 5.7 a** is an example where a triangular-shaped nano-flake is seen near the edge of the sample. The red lines mark the crystal twinning on the surface of the atomic-scale active site, where two parts of the crystal lattice show "mirror images" with each other along the twinning plane. The images in **Figure 5.7 a-f** were consecutively recorded at an interval of 30 s, and they visualise that the atomic-scale active site grows with time in the form of crystal twinning. **Figure 5.8** shows the time-resolved line measurement profiles along the twinning plane (as marked in **Figure 5.7 a**). At t = 0 s (corresponding to **Figure 5.7 a**), the twinning plane has 15 ALs; at t = 150 s (corresponding to **Figure 5.7 f**), it turns to be 21 ALs. The general growth rate is ~ 0.04 AL/s and the mechanism is following the Ostwald ripening phenomenon.[4, 5] The d-spacing between layers is ~ 2.2 Å, which is similar to the measured value given in the inset of **Figure 5.7 g**, and the crystallographic orientation is ascribed to the <1 1 1> plane as marked in **Figure 5.7 i**.

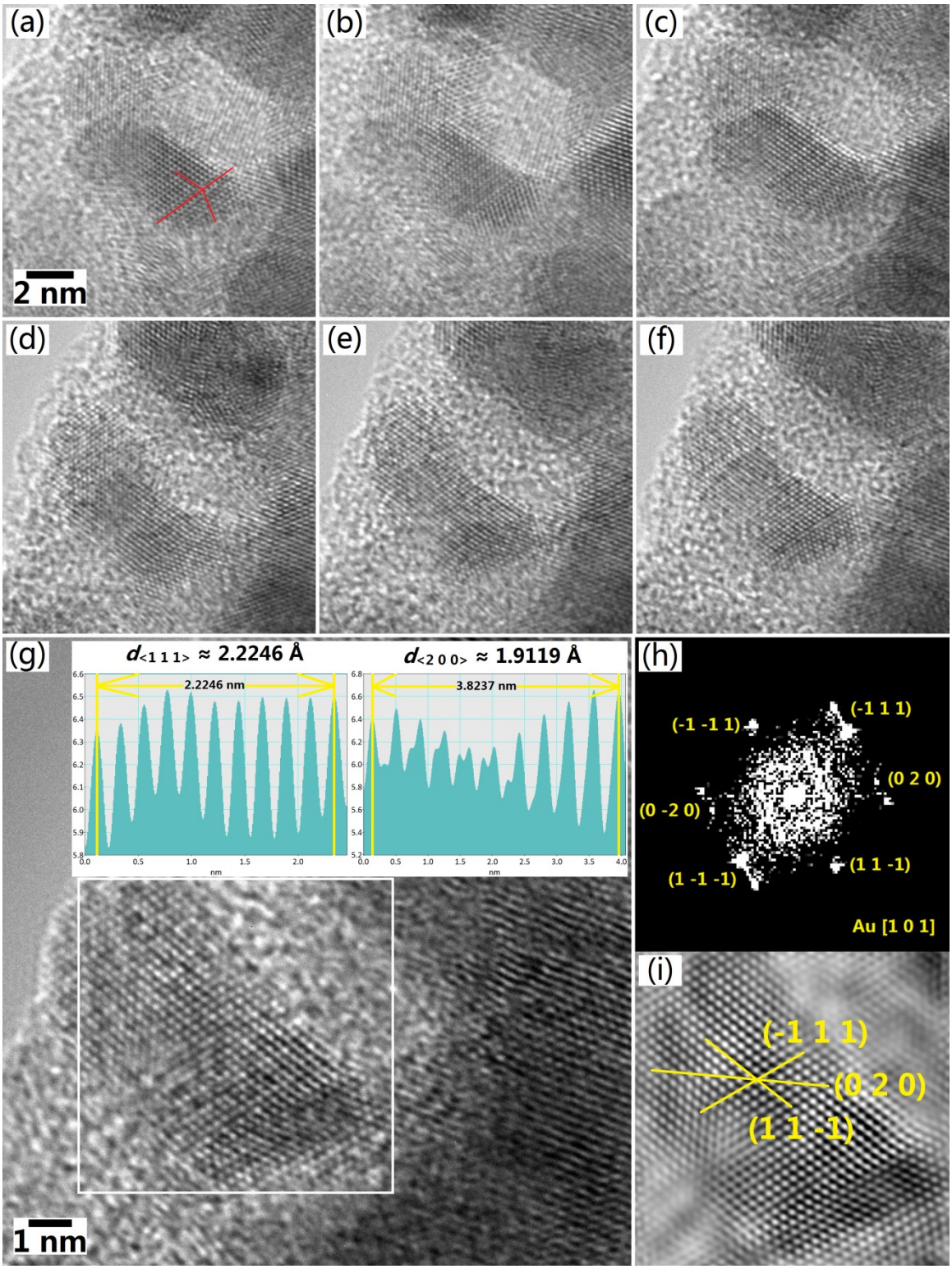

Figure 5.7 *In-situ* TEM observation of interactions between atomic-scale active sites. (a-g) HRTEM images of Au near the edge of sample, visualising the in-situ observation of the interactions between atomic-scale active sites; the images were consecutively captured at an

interval of 30 s. The red lines in (a) mark the crystal twinning on the surface of the atomic-scale active site which keeps its existence in (a-g). (h-i) The FFT pattern (h) and the corresponding IFFT image (i) of the white square region in (g); (inset of g) the line measurement profiles of the d-spacing values of <1 1 1> and <2 0 0> crystal planes as marked in (i). (b-f) share the same scale bar as (a), while (i) shares the same scale bar as (g).

Upon receiving energy from the electron beam, the nanostructures exhibit "self-motivated" re-crystallisation. Smaller crystals or less crystalline regions get dissolved and interlinked with larger crystals or more crystalline regions, and the process is usually multidirectional and isotropic. This first-ever observed phenomenon is believed to unveil part of the catalytic mechanism in EOR. During the "Ostwald ripening", a large number of free electrons (from the valence band of Au) causes high localised temperature and are subsequently discharged at the tips of the atomic-scale active sites within a very short period;[6-9] when the ethanol molecules are physisorbed onto the surface of the Au thin film (meaning sitting on top of these nanostructures since they are taken in plane-view), the lateral migrations of the nanostructures might act as scissors and help to break the incoming ethanol molecules into smaller fractions (i.e. the CH_x species) for more efficient oxidation, which in turn leads to the enhancement in the electrocatalytic performance in EOR. The crystalline nature of the active sites did not deteriorate after the observed growth, as illustrated in **Figure 5.7 g-i**; the white square region marked in **Figure 5.7 g** still shows strong crystallinity even at high magnification and the FFT pattern (**Figure 5.7 h**) reveals a perfect diffraction along the zone axis of [1 0 1], as a result of fusion with another nanocrystal near the edge of the sample (which is another case of Ostwald ripening). An interesting finding is that after the mergers of nanostructures, the d-spacing values of both <1 1 1> and <2 0 0> crystal planes (as marked in **Figure 5.7 i**) seem to become smaller (by ~ 0.1304 Å and ~ 0.1271 Å respectively) than the theoretical values (~ 2.3550 Å and ~ 2.0390 Å respectively) as shown in the line measurement profiles (**inset of Figure 5.7 g**). This means the crystal structure is subjected to compressive stress and is more compact. The interconnection of nanostructures upon more incident electron beam energy leads to the deposition of strain energy in crystals,1 and that could be one of the key sources for effective catalytic oxidation in EOR, which is proven by the performance evaluation experiments below.

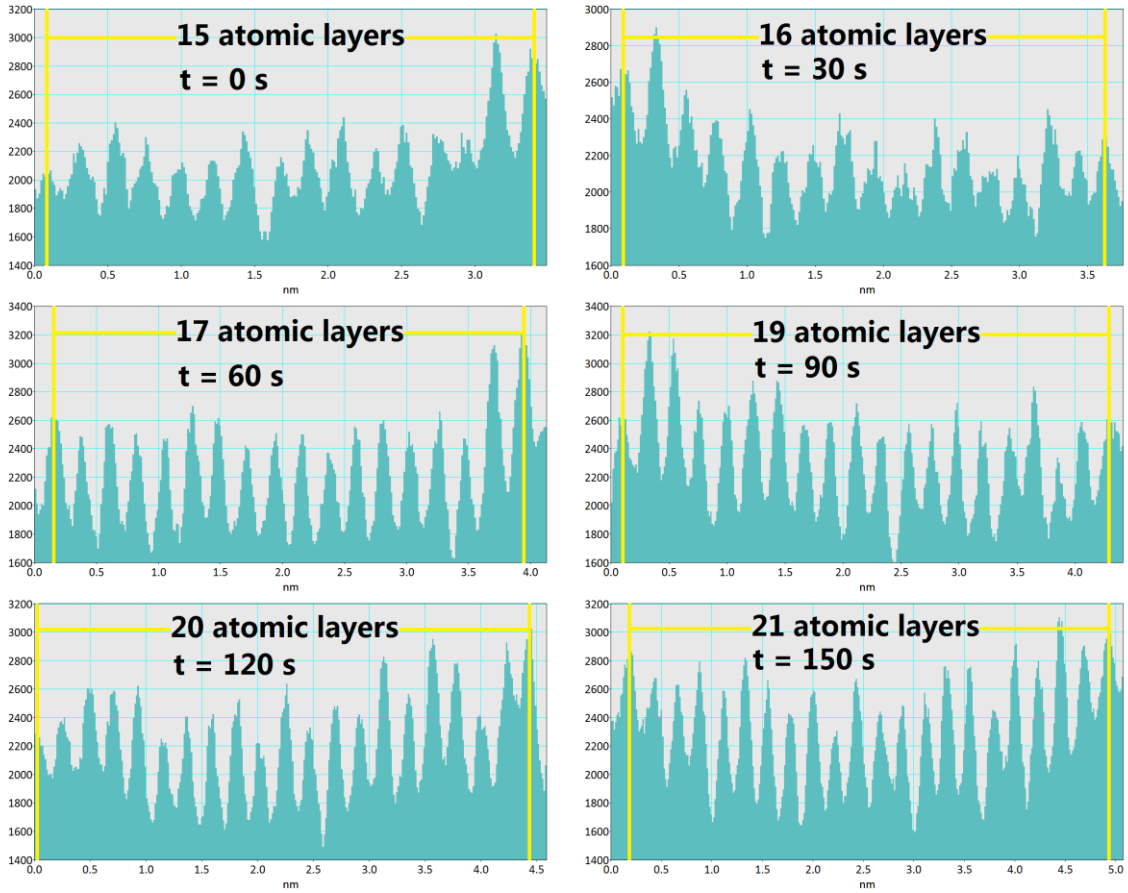

Figure 5.8 Time-resolved line measurement profiles along the twinning plane

5.6 Catalytic Performance of Au Micro-Arrays

The initial performance of the samples was investigated by testing under different physical conditions and the respective CV profiles are displayed in **Figure 5.9**. In a standard electrolyte (pH = 13) with 1 M ethanol, samples of different mesh grades (coloured solid curves) were first compared against each other with the planar sample (0 mesh, black solid curve) being the reference (**Figure 5.9 a**), and the baseline (black dashed curve) was collected with pure KOH solution electrolyte (pH = 13) for the identification of background signals. It can be found that the planar sample gives a strong and broad oxidation peak at E = 0.42 V, which is the oxidation of ethanol to ethanal and corresponds to **Equation 2.8 a**; following that, two extra oxidation peaks positioning at E = 0.15 V and E = 0 V are visible but much weaker, and they correspond to reactions (c)

and (b) in **Equation 2.8** respectively. This means by using the planar sample as the electrocatalyst for EOR, the major reaction would be $CH_3CH_2OH \rightarrow CH_3CHO$ (**Equation 2.8 a**), instead of breaking up the ethanol molecules into smaller hydrocarbons for further oxidation (**Equation 2.8 c-d**).[1, 2, 10, 11] In contrast, samples with mesh arrays reveal much stronger performance. This is evident from the much higher intensities of the oxidation peaks (**Equation 2.8 a-c**), as well as a shift of the peak position of the first oxidation reaction (**Equation 2.8 a**) to a lower potential of 0.25 V. This is mainly due to the presence of mesh arrays which considerably increase the ECSA exposed to the electrolyte, thus improving the efficiency of charge transfer during EOR. Furthermore, the intensities of the oxidation peaks corresponding to **Equation 2.8 c** have been greatly enhanced as demonstrated by the large increase of the ratio between the intensities of the MA samples to that of the planar sample. This signifies that with mesh arrays, the samples now could catalyse EOR much more via C1 pathway and more ethanol molecules would be broken into smaller hydrocarbons for further oxidation. Unfortunately, the oxidation peak corresponding to $CO \rightarrow CO_2$ (**Equation 2.8 d**) is not obviously observed in **Figure 5.9 a**, this is possibly due to the lower density of atomic-scale active sites compared to the Au nano-ring arrays reported in **Chapter 4**,[2] which could act as a strong driving force for full oxidation of ethanol in EOR.

From **Figure 5.9 a**, it can be understood that more electrochemical oxidation of ethanol could occur via C1 pathway (**Equation 2.8 c**) with mesh arrays, but the oxidation reactions via C2 pathway (**Equation 2.8 a-b**) are still the major reactions at the beginning.[10, 11] The peak current densities of these two reactions are listed in **Table 5.1** and the respective TOF values are calculated based on the experimental results.[12-15] The MA samples have much higher TOF values than the planar sample, and that is mainly affected by the oxidation peak current density (**Equation 4.1 d**). The sample with 400-mesh MAs has the overall best performance amongst the samples; it has TOF values for C2 oxidation reactions (**Equation 2.8 a-b**) that are ~ 4 times and ~ 14 times higher than that of the planar sample respectively. This signifies that even within C2 pathway, much more complete oxidation is only feasible with MA samples which provide increased surface area and amount of active sites (labelled as m in **Equation 4.1 a-b**).

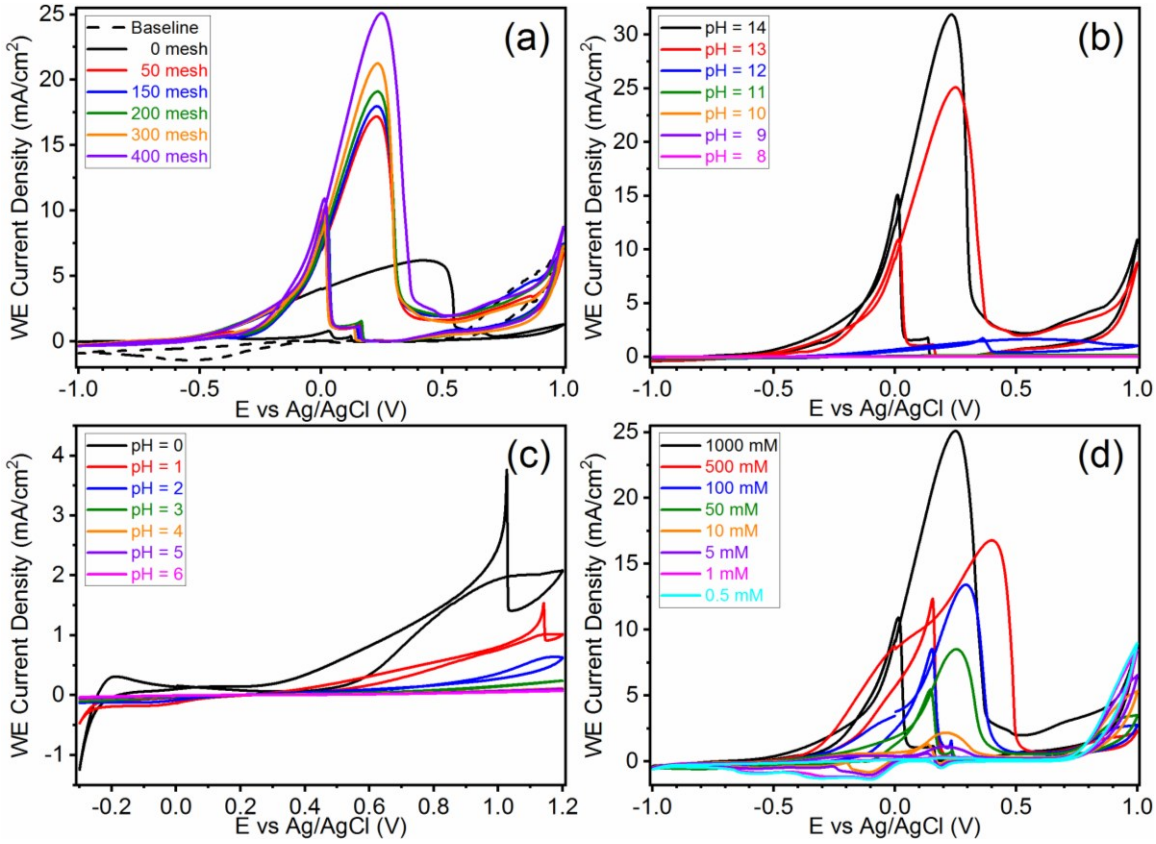

Figure 5.9 Cyclic voltammograms of the samples in EOR showing their electrochemical behaviours. (a) Comparison of MA samples of different mesh grades against the planar sample; (b-c) performance of the sample with 400-mesh MAs in (b) alkaline and (c) acidic electrolytes of varying pH values; (d) performance of the sample with 400-mesh MAs in alkaline electrolytes (pH = 13) with different ethanol concentrations.

Since the sample with 400-mesh array has the best initial performance in EOR, it was subjected to more detailed electrochemical tests for deeper understanding of the mechanism. Testing in electrolytes of different pH values (**Figure 5.9 b-c**) reveal much stronger catalytic performance in EOR at extreme pH values (0, 1 or 13, 14). This is evident from the distinct oxidation peaks shown in the CV profiles, in which the intensities of the oxidation peaks decrease exponentially as the pH values get closer to neutral. This is probably because at extreme pH values, high concentrations of mobile charge carriers are present in the electrolyte, which brings about a small R_L in the equivalent circuit diagram (**inset of Figure 5.10 b**). This may also lead to the boosting of

charge transfer efficiency, which reduces R_P as displayed in the equivalent circuit diagram. The sample with 400-mesh array (as in **Figure 5.9 a**) was again set as a new reference, and the electrocatalytic performance was further tested in electrolytes of different ethanol concentrations (**Figure 5.9 d**). The CV profiles show a gradual weakening in the intensities of the oxidation peaks as the concentration of ethanol gets lower. For reactions corresponding to **Equation 2.8 a-b**, the intensities reduce almost linearly against ethanol concentration and the oxidation peaks are observable down to 5 mM ethanol. This implies that with 400-mesh array, the sensitivity of Au micro-array electrocatalyst is much more competitive compared to the planar sample and the bulk counterparts. However, since the size of single building blocks of the MAs is obviously large (in the range of micrometres for both lateral and height dimensions), the density of atomic-scale active sites would inevitably drop, thus the detecting limit is still higher than the Au nano-ring arrays (the detecting limit is ~ 1 mM) reported in **Chapter 4**.[2]

Table 5.1 WE current densities of the samples at different oxidation peaks

Mesh grade	$CH_3CH_2OH \rightarrow CH_3CHO$			$CH_3CHO \rightarrow CH_3COOH$		
	WE current density j (mA/cm^2)*	j/j_0 *, **	TOF (s^{-1})*, †	WE current density j (mA/cm^2)*	j/j_0 *, **	TOF (s^{-1})*, †
0 mesh	6.20	1.00	0.60	0.79	1.00	0.08
50 mesh	17.18	2.77	1.67	8.75	11.11	0.85
150 mesh	19.98	2.90	1.75	9.72	12.34	0.95
200 mesh	19.10	3.08	1.85	10.08	12.80	0.98
300 mesh	21.25	3.43	2.07	10.47	13.30	1.02
400 mesh	25.10	4.05	2.44	10.93	13.88	1.06

* All values are corrected to the accuracy of two (2) decimal places.

** The value of j_0 is set to be that for the planar sample (0-mesh).

† The calculation of TOF is according to **Equation 4.1**.

EIS was carried out at the fixed potential of 0.25 V (which is the potential of reaction (a) in **Equation 2.8**) to investigate the detailed reaction processes during EOR. **Figure 5.10 a** displays the Nyquist plots of the samples, which clearly shows that the electrochemical impedance of the planar sample (~ 700 Ω) is almost 4-8 times higher than those of the MA samples (~ 80-140 Ω). This is because the PVC electrode with MAs has a pillar-

structured surface, which in turn leads to a larger surface area for Au coating compared to the planar sample. According to $R_{Au} = \rho_{Au} \cdot L/A$, larger area will bring about a smaller resistance at a constant length L. The details of the arrayed samples are enlarged and shown in the **inset of Figure 5.10 a**. All Nyquist plots show a single semicircle shape, indicating that $CH_3CH_2OH \rightarrow CH_3CHO$ (**Equation 2.8 a**) is a single process without any intermediate product. The equivalent circuit diagram (**inset of Figure 5.10 b**) is obtained through the fitting of the Nyquist plots, which is comprised of R_L, R_P and C_D. With the fixation of pH value at 13 and ethanol concentration at 1 M, the values of R_L (taken as the first intersect of the horizontal axis) are quite close to each other. The diameter of the semicircle, which could be estimated as the difference between the two intersects of the horizontal axis, is taken as the value of R_P. From the **inset of Figure 5.10 a**, it is obvious that R_P is inversely proportional to the value of mesh grade, thus suggesting that the mesh grade of the MAs is an important factor influencing R_P.

Another influencing factor for the ramping of performance would be the value of C_D. As given in the equivalent circuit diagram, a resistor and a capacitor (representing R_P and C_D respectively) are in parallel connection. In unit amount of time, larger C_D value will definitely lead to a smaller total resistance (assuming R_L and R_P are constant). Therefore, in order to quantify the values of C_D, CV profiles were first collected within the potential range between -0.07 V and +0.03 V (where no apparent Faradaic process occurs) under different scan rates (**Figure 5.11**). The values of working electrode current are plotted against the scan rates (**Figure 5.10 b**) and the gradients of the plots represent the values of C_D (according to **Equation 4.1**).

Table 5.2 summarises the values of each individual component in the equivalent circuit diagram for all samples, and the experimentally measured data are compared against those from software fitting. It can be perceived that while the values of R_L stay nearly consistent, the values of R_P drop with increasing mesh grades and the opposite happens to the values of C_D, which coincides with the trend demonstrated in **Figure 5.10 b**. It should be noted that there are several fitted values differing a lot from the measured data, they could be due to the presence of anomalous points in the experimentally measured data

and further analyses should be carried out with experimental data. As such, the correlation of experimentally measured C_D (as given in **Figure 5.10 b** and **Table 5.2**) with mesh grades and sizes of MAs is fitted in **Figure 5.10 c**. The equations of the fitted curves reveal that the value of C_D is proportional to the natural logarithm of mesh grade G, and has a quadratic relationship with the inverse of array size S. This implies that the value of C_D still has plenty of rooms for improvement, as long as the size of MAs could be tuned down till the limit of the NIL process.

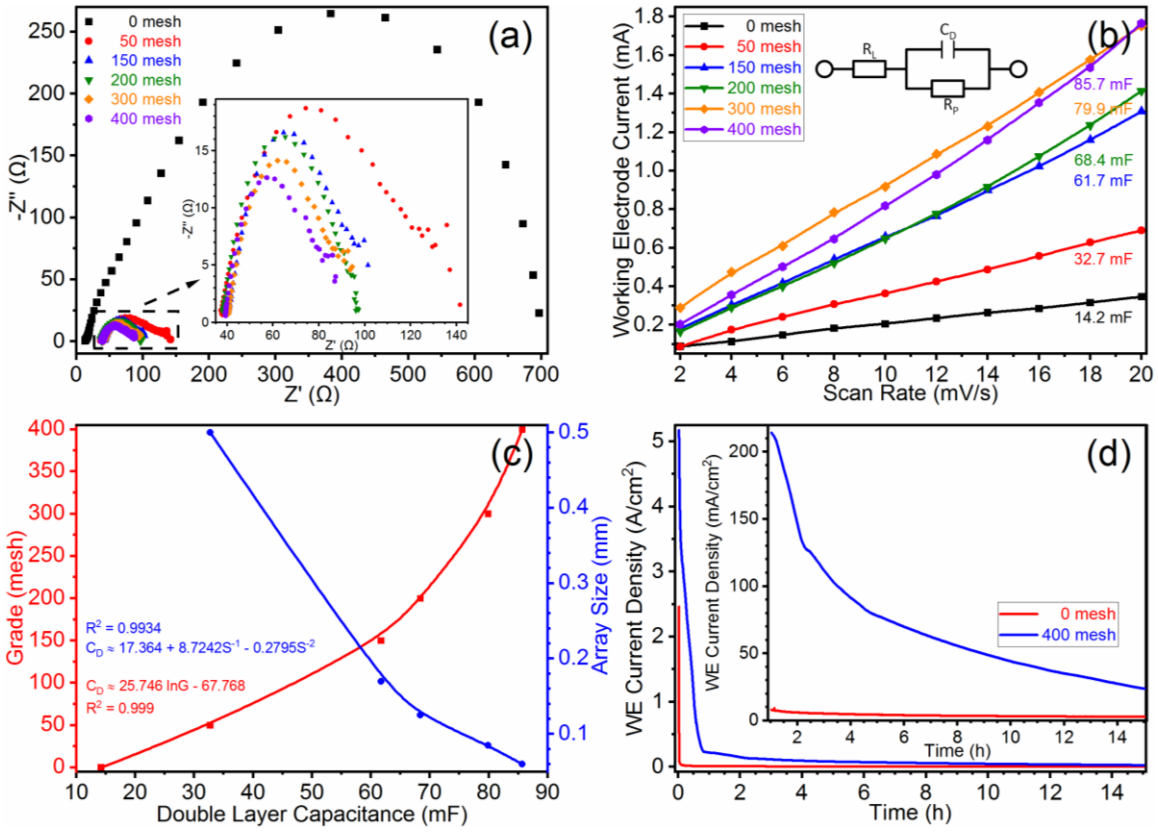

Figure 5.10 (a) The Nyquist plots of the samples obtained from EIS, with the enlarged plots for the samples with MAs (inset); (b) plot of WE current against scan rate for the calculation of C_D as displayed in the equivalent circuit diagram (inset); (c) plots and fitting of C_D in relationship with mesh grade and array size; (d) CA profiles of planar and MA samples with amplification of their difference (inset).

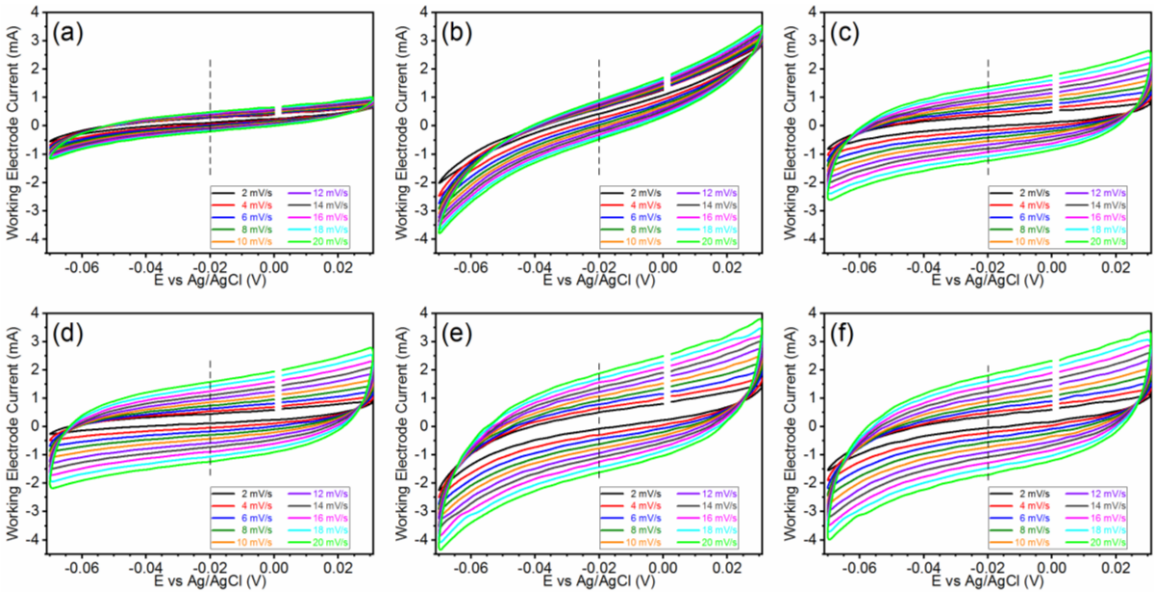

Figure 5.11 CV curves of the samples taken under different scan rates. (a) Planar sample; as well as samples with (b) 50-mesh, (c) 150-mesh, (d) 200-mesh, (e) 300-mesh and (f) 400-mesh MAs.

Table 5.2 Summary of measured and fitted data of individual components in the equivalent circuit diagram

Mesh grade	R_L (Ω)*		R_P (Ω)*		C_D (mF)*	
	Measured	Fitted**	Measured	Fitted**	Measured***	Fitted**
0 mesh	13.3	15.0	709.2	712.0	14.2	13.4
50 mesh	38.1	37.1	106.1	97.9‡	32.7	43.7‡
150 mesh	41.1	43.1	62.0	58.7‡	61.7	60.9
200 mesh	38.3	54.1‡	61.1	59.5	68.4	62.8
300 mesh	40.7	40.0	58.6	56.7	79.9	68.4‡
400 mesh	39.5	41.5	53.0	46.8	85.7	87.7

* All values are corrected to the accuracy of one (1) decimal place.

** Fitted values were obtained by fitting the original data using the NOVA software version 1.11.

*** The measured CD values were obtained by calculation according to **Equation 4.1 b** and **Figure 5.11**.

‡ These values differ a lot from the measured data, possibly due to the presence of anomalous points.

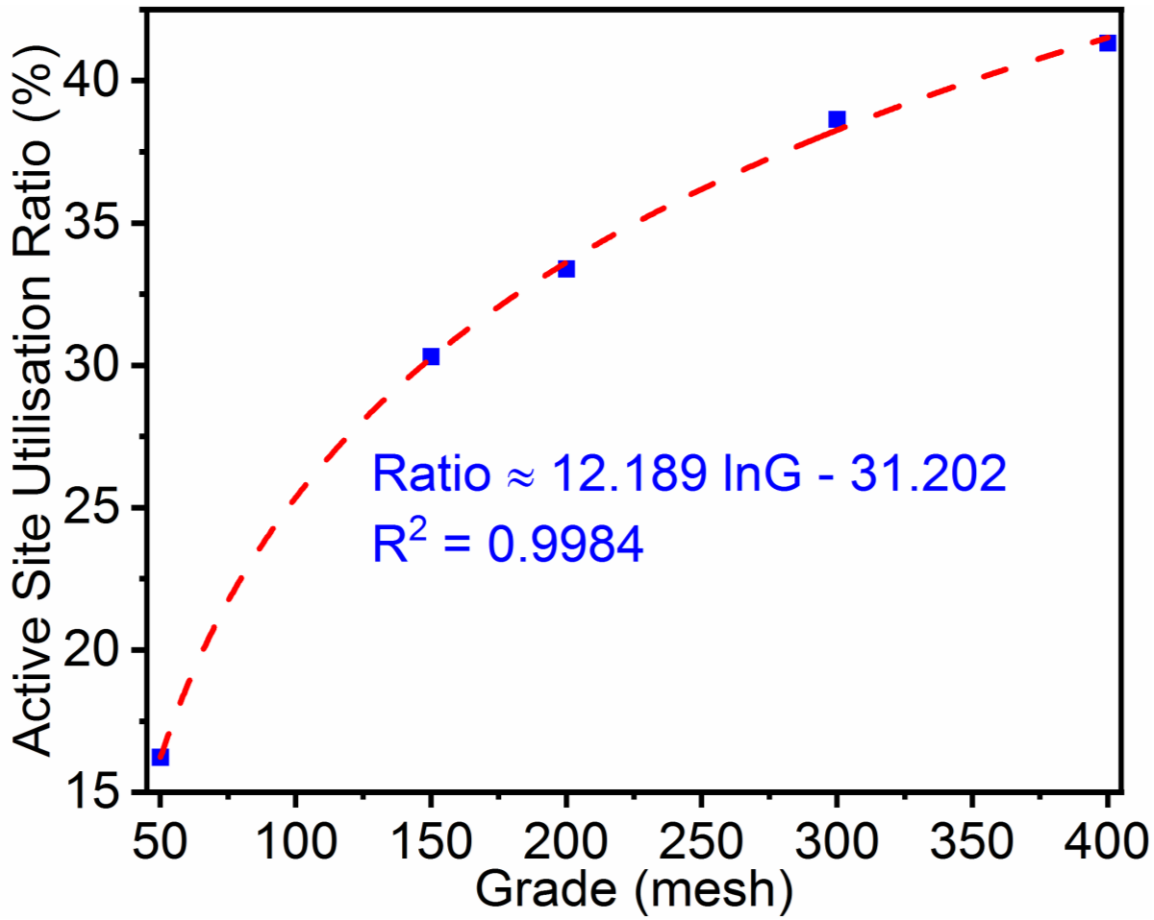

Figure 5.12 Simple simulation of the relationship between active site utilisation ratio and mesh grade

According to **Equation 4.1 b**, a higher value of C_D will lead to a larger amount of active sites as confirmed by **Equation 4.1 c**, in which higher value of C_D brings about a larger ECSA with more active sites (assume homogeneous distribution). However, the values of m based on the two calculations (**Equation 4.1 a-b**) are not consistent with each other, and the value of TOF-based m is in larger amount. Nevertheless, by taking the ratio of the two values (C_D-based m to TOF-based m) for each sample, a significant improvement is unravelled – the ratio for the planar sample is only 7.10%, but ramps up to 41.32% for the sample with 400-mesh MAs. This means for the electrodes with MA structures, the higher active site utilisation ratio (ASUR) renders a much greater efficiency in the first step of reaction mechanism (physisorption of ethanol molecules), thus ensuring a more efficient charge transfer process through building of the electrochemical double layer.

Simple simulation via correlations (**Figure 5.12**) shows that the ASUR is expected to reach > 50% and ~ 61.5% respectively with 800-mesh and 2000-mesh MAs (almost the highest mesh grade in commercial products), and if the ratio were to reach the theoretical 100%, it needs nearly 50000-mesh MAs (which is not possible, at least for now) in just one single Ni grid (of 3.05 mm diameter)!

The stability of the planar and 400-mesh arrayed samples is tested via CA, in an electrolyte with 1 M ethanol at the pH of 13 for consecutive 15 hours without physical disturbance. **Figure 5.10 d** shows the CA profiles, in which the majority of the catalysis occurred within the first hour (according to the drastic decrease of the WE current density). After that, the catalytic process slows down and gets stabilised. An enlarged profile is illustrated in the **inset of Figure 5.10 d**, which amplifies the difference between the planar and arrayed samples. The catalytic activity of the planar sample became stable and low after ~ 30 min stability test, whereas that of the arrayed sample was still much higher and gradually reducing at the end of the 15-h stability test. This reiterates the much stronger catalytic performance of the samples with micro-array structures.

5.7 Summary

The catalysis of Au thin film could be improved by fabrication of array structures in large area. In this work, NIL has been developed to fabricate flexible Au MA electrodes with ~ 100% coverage. Advanced electron microscopy characterisations have directly visualised the atomic-scale 3D nanostructures with a maximum depth of 6 ALs. *In-situ* observation unveils the crystal growth in the form of twinning. Large C_D value brings about large number of active sites on the Au thin film and has a logarithmic relationship with mesh grade. Electrochemistry testing shows that the Au MAs perform much better ethanol oxidation reaction than the planar sample; MAs with higher mesh grade have a greater ASUR, which is important to build electrochemical double layer for efficient charge transfer. Further improvement on ASUR is expected for greater electrocatalytic performance and potential application in direct ethanol fuel cell.

References

1. X. Cao, C. Li, D. Peng, Y. Lu, K. Huang, J. Wu, C. Zhao and Y. Huang, *J. Phys. Chem. Lett.*, 2020, **11**, 3005.
2. X. Cao, C. Li, Y. Lu, B. Zhang, Y. Wu, Q. Liu, J. Wu, J. Teng, W. Yan and Y. Huang, *J. Catal.*, 2019, **377**, 389.
3. L. Vitos, A. V. Ruban, H. L. Skriver and J. Kollár, *Surf. Sci.*, 1998, **411**, 186.
4. P. W. Voorhees, *J. Stat. Phys.*, 1985, **38**, 231.
5. B. Jia and L. Gao, *Cryst. Growth Des.*, 2008, **8**, 1372.
6. C. Li, X. Cao, W. Li, B. Zhang and L. Xiao, *J. Alloys Compd.*, 2019, **773**, 762.
7. C. Li, Y. Rao, B. Zhang, K. Huang, X. Cao, D. Peng, J. Wu, L. Xiao and Y. Huang, *Chemosphere*, 2019, **214**, 341.
8. C. Li, B. Zhang, Y. Li, S. Hao, X. Cao, G. Yang, J. Wu and Y. Huang, *Appl. Catal. B*, 2019, **244**, 56.
9. Y. Rao, X. Cao, C. Li and L. Xiao, *Sep. Purif. Technol.*, 2019, **220**, 328.
10. Y. Wang, S. Zou and W.-B. Cai, *Catalysts*, 2015, **5**, 1507.
11. Y. Zhao, X. Li, J. M. Schechter and Y. Yang, *RSC Adv.*, 2016, **6**, 5384.
12. Y. Yao, Z. Xu, F. Cheng, W. Li, P. Cui, G. Xu, S. Xu, P. Wang, G. Sheng, Y. Yan, Z. Yu, S. Yan, Z. Chen and Z. Zou, *Energy Environ. Sci.*, 2018, **11**, 407.
13. C. You, Y. Ji, Z. Liu, X. Xiong and X. Sun, *ACS Sustainable Chem. Eng.*, 2018, **6**, 1527.
14. Y. Li, F.-M. Li, X.-Y. Meng, S.-N. Li, J.-H. Zeng and Y. Chen, *ACS Catal.*, 2018, **8**, 1913.
15. M. B. Cortie, A. I. Maaroof and G. B. Smith, *Gold Bull.*, 2005, **38**, 14.

Chapter 6

Highly Strained and Single-Crystalline Au Nanoparticles for Improved Electrocatalysis of Ethanol Oxidation Reaction

The Au catalyst usually exists in the form of NPs for high aspect ratio. In this work, a non-traditional physical approach has been developed to fabricate ultra-small and homogeneous single crystalline Au NPs by simple ion bombardment in a PIPS system. TEM characterisations show that the Au NPs produced with 5 keV Ar^+ are growing along the [1 1 1] zone axis, and the {1 1 0} family planes with highest energy are highly strained to form twinned crystals, which give rise to the accumulation of large amount of surface energy, and this was found to be an underlying reason causing strong catalysis. The direct evidence is proven by the enhanced electrochemical properties of the as-produced Au NPs, which has much higher efficiency in EOR compared to the normal Au NPs. Electrochemistry testing with varying physical parameters shows that the detecting limit of ethanol can be as low as 0.5 mM and strong signals come with high concentrations of mobile charge carriers at extreme pH values. CV scans reveal that in alkaline medium, C1 pathway occurs much more preferentially in the strained Au NPs than the normal Au NPs, thus showing that in the Au NPs-catalysed EOR, the surface energy content might play a more important role than aspect ratio in enhancing the catalytic activities.

---

*This chapter is published substantially as **X. Cao**, C. Li, D. Peng, Y. Lu, K. Huang, J. Wu, C. Zhao and Y. Huang, *J. Phys. Chem. Lett.*, 2020, **11**, 3005.

6.1 Materials and Chemicals

The chemicals used in this study include KOH flakes (90%, Sigma-Aldrich) and absolute ethanol (CH_3CH_2OH, 99.9%, Aik Moh), both chemicals were used as received without any further purification. Au grids (200/inch square mesh, 99% purity) were purchased from Electron Microscopy Sciences, USA. Ti (99% purity) and brass (64%Cu-36%Zn) foils were purchased from Hongwang Moulds, PRC. The deionised water was made by the Millipore™ system, which has the resistivity of 18.2 MΩ·cm.

6.2 Morphology and Crystallography of Au NPs

Figure 6.1 shows the TEM images of the samples. During the 1-min PIPS processing, Au grid is bombarded by Ar^+ ion beams which apply a shear force on its surface. As a result, Au NPs are removed from the surface of the Au grid and collected by the Cu grid. It can be found that most of the NPs produced by each set of parameters are highly homogeneous and all are within the range of 3-20 nm. Measurements reveal that with 3 keV Ar^+ ion beams, the size of the Au NPs increases from ~ 3 nm (1°) to ~ 8 nm (5°), at the rate of ~ 2.5 nm per degree of inclination angle (**Figure 6.1 a-c**). Similarly for 5 keV Ar^+ ion beams, the Au particle size increases from ~ 10 nm (1°) to ~ 20 nm (5°), at the rate of ~ 5 nm per degree of inclination angle (**Figure 6.1 a'-c'**). Corresponding vertical comparisons show that at each inclination angle, the NPs produced by 5 keV Ar^+ are ~ 2.5 times larger than those produced by 3 keV Ar^+. The above were recorded as the mean values from multiple measurements and the error is relatively small (~ 5%).

The Au NPs were further magnified and the HRTEM images are displayed in **Figure 6.2**. They are highly crystalline and each is determined to be a single crystal. In 1 min of ion bombardment, only very limited amount of Au could be detached from the surface of the Au grid. At a lower ion beam energy (3 keV Ar^+), the particle size is much smaller compared to those produced with a higher ion beam energy (5 keV Ar^+). **Figure 6.2 a-c** also show that the crystallinity of the Au NPs is not affected by the inclination angle. On

the other hand, NPs produced under more energetic ion beams are larger in size and have higher crystallinity as a result of absorption of energy from higher-voltage ion beams.

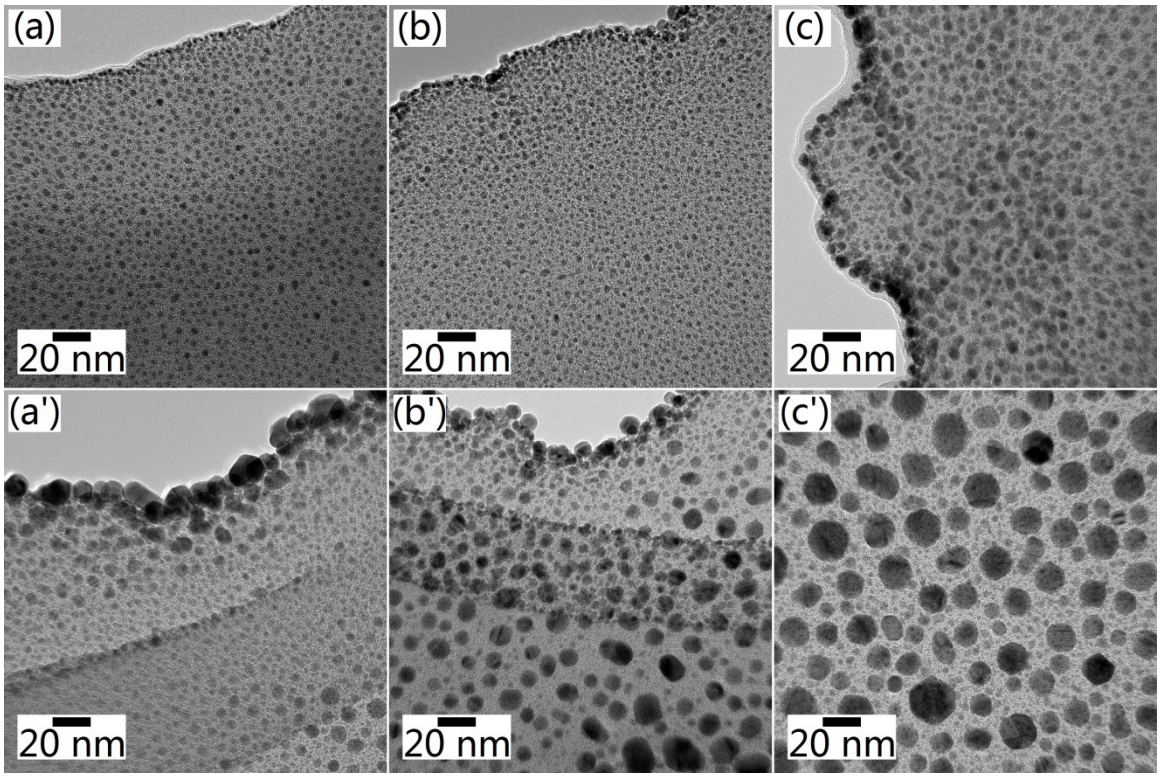

Figure 6.1 TEM images of the Au NPs: (a-c) Samples produced with 3 keV Ar^+ beams set at an inclined angle of 1°, 3° and 5° from top; (a'-c') samples produced with 5 keV Ar^+ beams set at an inclined angle of 1°, 3° and 5° from top.

Apart from that, it is noteworthy that when the Ar^+ ions apply a shear force on the Au grid and remove the surface materials in the form of Au NPs, the surface of the produced Au NPs would render some deformation which might be recovered from the stress/strain caused. When the shear force is strong enough, the deformation will break through the elastic limit, and therefore the Au NPs produced with 5 keV Ar^+ are highly strained to form twinned crystals (**Figure 6.2 a'-c'**) with high surface energy. **Figure 6.2 a'** is a classic example of crystal twinning. In a crystalline region (such as the one in the white square), there is at least one interface that forms mirror images of the lattice on both sides of the interface. As such, the FFT of the square region may be formed and overlapped by at least two sets of diffraction spots (in this case, there are three sets), and some may look

distorted due to the high stress and strain applied onto the NPs (**Figure 6.2 d**). The same could be observed in **Figure 6.2 b'-c'**, they might appear different, but this should be due to the random orientation of the collected single-crystalline NPs. Rotating the sample stage might reveal a more panoramic structure of a single NP together with the crystal twinning nature. Nevertheless, crystal twinning due to high strain gives rise to a much higher content of surface energy, and in the previous research (reported in **Chapter 4**), high surface energy has been found to be one of the underlying reasons in enhancement of electrocatalytic performance in EOR.[1]

The FFT reveals that the Au NPs are growing along the [1 1 1] zone axis (**Figure 6.2 d**). By matching against the JEMS software (Electron Microscopy Software, Java Version 4.3905U2016, developed by Dr P. Stadelmann, Switzerland), the diffraction spots are ascribed to the {1 1 0} family of planes of the FCC structured Au, which possesses the highest energy compared to {1 0 0} and {1 1 1} families.[2] This explains why the Au NPs are highly strained to form twinned crystals and the (1 1 1) crystal plane is the most frequently being exposed during characterisations. The FFT pattern was further transformed inversely, either in whole or along one of the crystallographic orientations, to obtain the IFFT images (**Figure 6.2 d'-h**). **Figure 6.2 d'** is the IFFT image of the entire FFT pattern, and the red lines mark the existence of the crystal twinning effect. The two parallel lines represent the twinning plane, whereas the zig-zag lines show the "mirror images" of the crystal lattice formed along the twinning plane. The IFFT images transformed along each of the crystallographic orientations (**Figure 6.2 e-g**) reveal several defects as highlighted in white circles, which include partial and edge dislocations, they are believed to carry large amount of energy that could perform strong catalysis in EOR. The parts with intense contrasts between the bright and dark fringes signify the stress centres, and most of the defects exist around or near to these stress centres. **Figure 6.2 h** displays the RGB mapping of **Figure 6.2 e-g**; by matching against the IFFT image in **Figure 6.2 d'**, it can be deduced that crystal twinning would preferentially occur around the stress centre of a crystalline particle. The above can be cross-referenced from XRD (**Figure 6.3**), which confirms the crystalline phases of the samples. Therefore, the TEM Cu grid was replaced by a piece of thin Ti foil substrate and the NPs were collected

to make electrodes with catalyst loading. By taking into account of the surface area to volume ratio (**Equation 6.1**), one sample was produced at each ion beam energy level, and the beam inclination angle was fixed to 1° from top as that will produce Au NPs with the smallest size. In order to have enough loading of the NPs, the PIPS processing time was lengthened to 30 min for each sample.

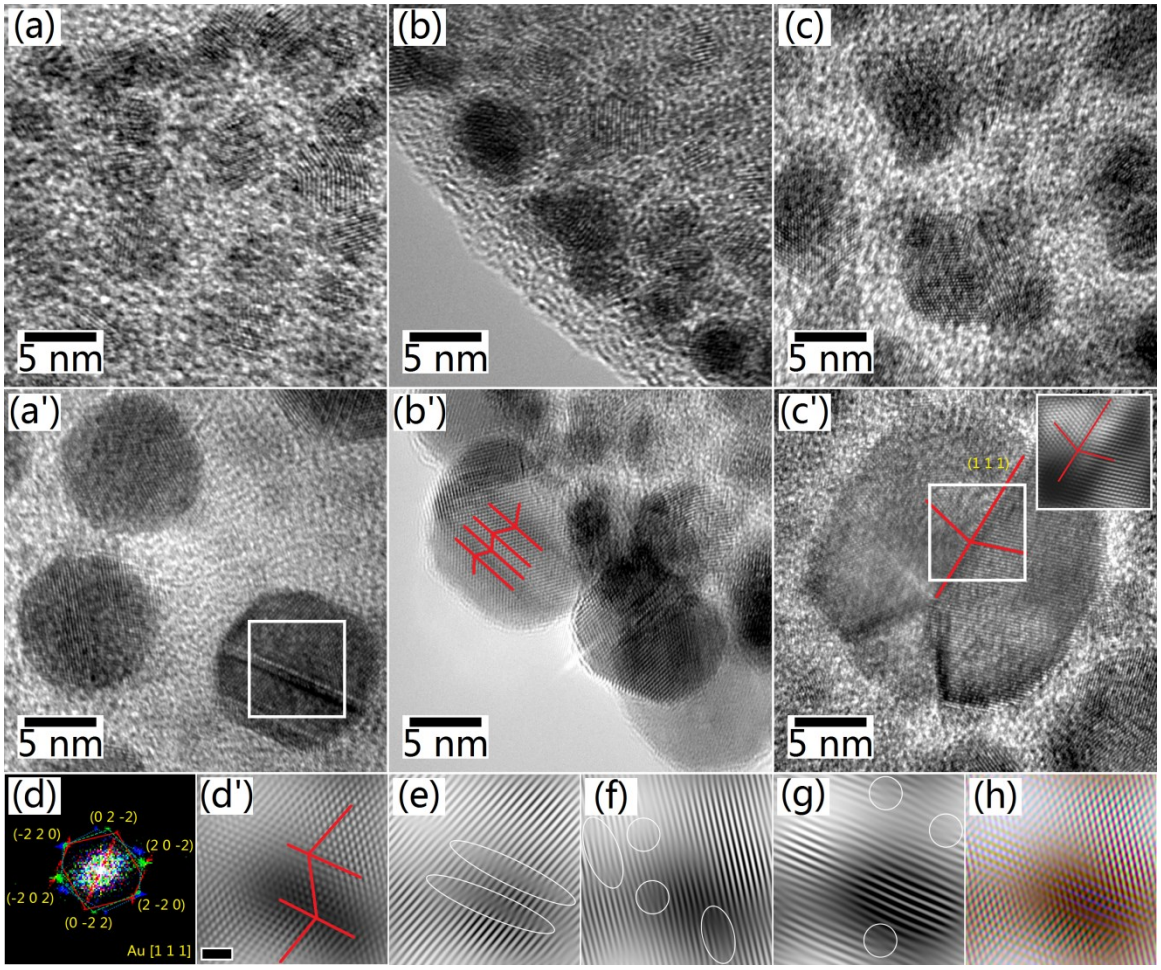

Figure 6.2 HRTEM images of the Au NPs. (a-c) Samples produced with 3 keV Ar^+ beams set at an inclined angle of 1°, 3° and 5° from top. (a'-c') Samples produced with 5 keV Ar^+ beams set at an inclined angle of 1°, 3° and 5° from top; the red lines mark the existence of crystal twinning; (inset of c') the magnified image of the square region in (c'). (d) The FFT pattern of the square region marked in (a'). Note that samples produced with 5 keV Ar^+ beams are highly strained to form twinned crystals. (d'-h) The IFFT images of (d), transformed (d') in whole; (e-g) along <1 1 0>, <1 0 1> and <0 1 1> directions respectively; (h) the RGB mapping of (e-g). The images of (d'-h) share the same scale bar as (d'), which represents 1 nm.

Equation 6.1 Detailed estimation of atomic exposure and SA/V ratios

$$V_{NP} = \frac{4}{3}\pi R^3 \qquad V_{atom} = \frac{4}{3}\pi r^3$$

$$Total\ number\ of\ atoms\ N = \frac{V_{NP}}{V_{atom}} = (\frac{R}{r})^3$$

$$Surface\ area\ of\ nanoparticle\ S_{NP} = 4\pi R^2$$

$$Exposed\ surface\ area\ of\ a\ surface\ atom\ S_{atom} = 2\pi r^2$$

$$Total\ number\ of\ surface\ atoms\ n = \frac{S_{NP}}{S_{atom}} = 2 \cdot (\frac{R}{r})^2$$

$$Atomic\ exposure\ ratio = \frac{Total\ number\ of\ surface\ atoms}{Total\ number\ of\ atoms\ in\ NP} = \frac{n}{N} = \frac{2r}{R} \propto \frac{1}{R}$$

$$SA/V\ ratio = \frac{Total\ exposed\ surface\ area}{Total\ volume\ of\ NP} = \frac{4\pi R^2}{\frac{4}{3}\pi R^3} = \frac{3}{R}$$

where r is the atomic radius of Au (with the value of ~ 135 pm) and R is the radius of Au NPs (~ 1.5 nm for 3 keV Ar^+ sample, ~ 5 nm for 5 keV Ar^+ sample and ~ 2.5 nm for commercial Au NPs), assuming a spherical form factor. The mean particle sizes, as well as the calculated atomic exposure and SA/V ratios for these samples, are listed in **Table 6.1**. Both ratios are inversely proportional to the dimensions of the NPs, therefore, with a smaller particle size, the specific surface area will increase and that brings about a boost in the amount of active sites for effective catalysis in the electrochemical testing.

Table 6.1 Summary of calculated atomic exposure and SA/V ratios

Sample	Mean particle size	Atomic exposure ratio	SA/V ratio
Commercial Au NPs	~ 5 nm	10.8%	1.2 nm^{-1}
3 keV Ar^+ sample	~ 3 nm	18.0%	2.0 nm^{-1}
5 keV Ar^+ sample	~ 10 nm	5.4%	0.6 nm^{-1}

According to the standard database from the International Centre for Diffraction Data, the strongest diffraction line of the FCC Au (JCPDS #04-0784) appears at $2\theta \approx 38.2°$, which should be ascribed to the (1 1 1) orientation; however, this may be overlapping with the strongest diffraction line of the hexagonal close-packed (HCP) Ti (JCPDS #44-1294) at $2\theta \approx 38.5°$, which should be ascribed to the (1 1 0) orientation. Therefore, to avoid possible confusion, the samples were prepared on two different kinds of substrates (Ti

and brass foils) for analyses. The crystalline phases of the samples were confirmed by thin film XRD, and the diffraction patterns are shown in **Figure 6.3**.

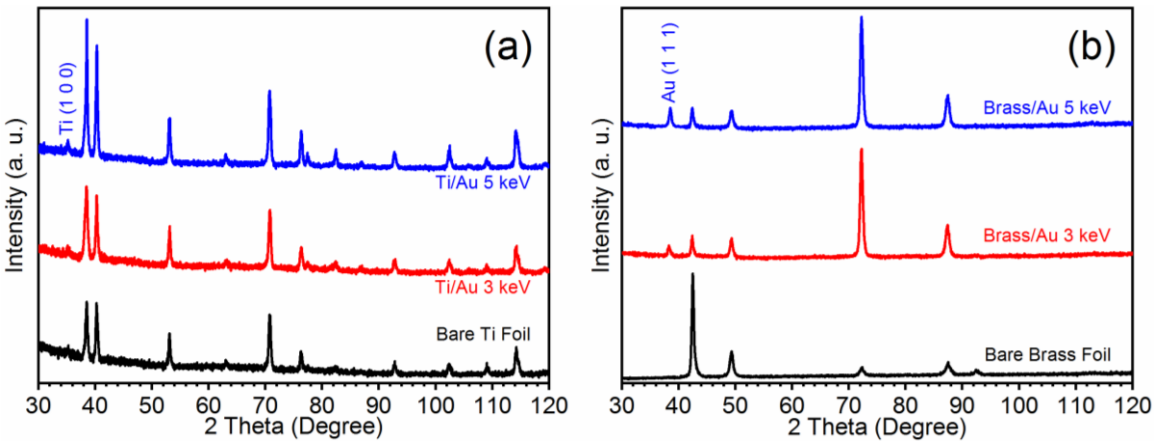

Figure 6.3 XRD patterns of the Au NPs on (a) Ti foil and (b) brass foil substrates

In **Figure 6.3 a** (Ti foil system), Au (1 1 1) is severely overlapping with Ti (1 1 0), and there is hardly any other signals for Au, despite that Au forms a ring with 3 mm diameter (obviously seen by the naked eye). Hence, to confirm the crystallinity of Au, the diffraction is compared against the brass foil system (**Figure 6.3 b**), in which Au (1 1 1) is clearly distinguished from all diffraction lines of brass. The stronger signal of Au (1 1 1) indicates higher crystallinity when PIPS was carried out with 5 keV Ar^+. Within a fixed duration, bombardment using more energetic ion beams could facilitate greater efficiency in energy transformation; with a similar mass loading of Au NPs, the extra amount of energy from the ion beams has to be utilised in the crystallisation of the as-produced Au NPs.

Equation 6.2 Estimation of crystallite size using the Scherrer equation[3]

$$\tau = \frac{K \cdot \lambda}{\beta \cdot cos\theta}$$

where K is the dimensionless shape factor of the crystallites and has a value of 0.9, λ is the wavelength of the incident X-ray (which is ~ 1.5405980 Å in this work), θ is the Bragg angle (at which the diffraction would occur), β is the full width at half maximum

(FWHM) of the diffraction peak (which is calculated as $\Delta 2\theta$), and τ is the calculated crystallite size.[3] Therefore, a reduction in crystallite size will lead to broadening of the diffraction peaks.[4]

The crystallite sizes for both samples are predicted using the Scherrer equation (**Equation 6.2**). From the XRD patterns, the FWHM values for both samples are ~ 0.60° (3 keV Ar^+) and ~ 0.52° (5 keV Ar^+) respectively, thus the corresponding crystallite sizes are calculated to be ~ 13.7 nm (3 keV Ar^+) and ~ 15.8 nm (5 keV Ar^+). With reference to the TEM (**Figure 6.1 a-a'**) and HRTEM (**Figure 6.2 a-a'**) images, it can be found that the experimental particle sizes of both samples are actually smaller than the theoretical crystallite size, so each NP must be one crystallite. This further confirms that the NPs are single crystalline and this is in good agreement with the FFT pattern (**Figure 6.2 d**).

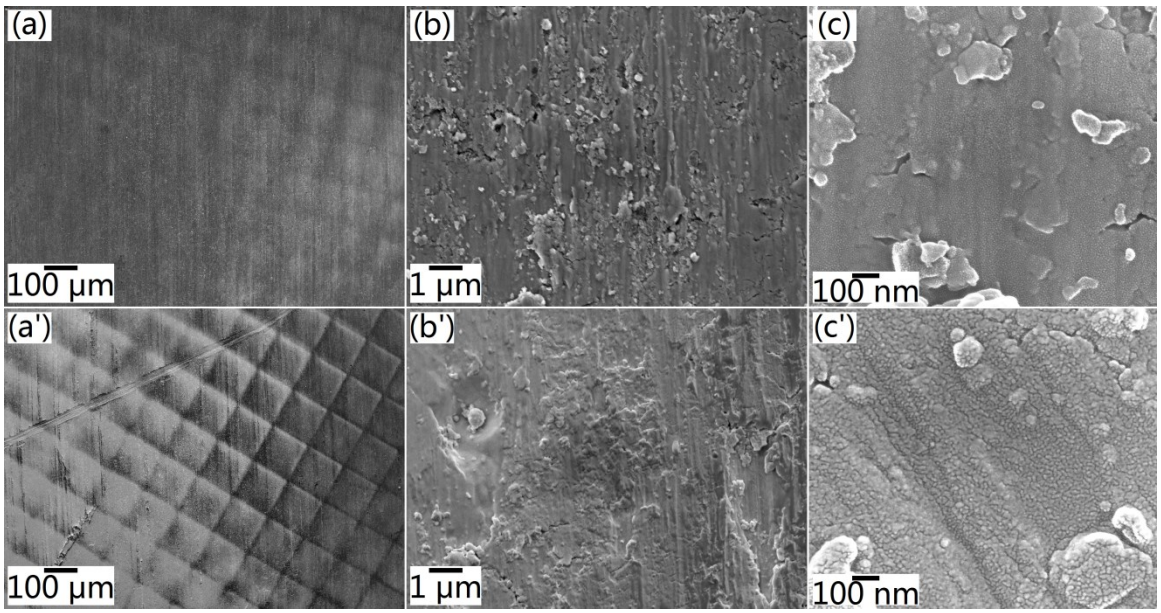

Figure 6.4 Surface morphology of the Au NPs on Ti foils with increasing magnifications taken under FEG-SEM and FIB systems: (a-c) Sample produced with 3 keV Ar^+ ion beams and (a'-c') sample produced with 5 keV Ar^+ ion beams. The images were taken in increasing magnifications, from left to right: 100 ×, 10 k× and 100 k×.

The surface morphology of the samples is displayed in **Figure 6.4**. At the low magnification of 100 ×, an ordered array structure (**Figure 6.4 a-a'**) is observed due to

the masking effect of the Au grids, and is much more obvious in the sample underwent 5 keV ion bombardment in PIPS. Zooming in to any of the squares will render **Figure 6.4 b-b'**; at the magnification of 10 k×, Au is seen to form a layer and the film has totally covered the Ti substrate. The surface is never flat and the height profile has very large deviations; this is mainly due to that the samples were subjected to the bombardment of energetic Ar^+ ions, even if the Ti substrate was polished prior to PIPS. Further enlarging to 100 k× shows that the as-deposited Au NPs are ultrafine and having the particle size of a few tens of nanometres (**Figure 6.4 c-c'**), which agrees with the TEM images (**Figure 6.1**); some are inevitably aggregated (to reduce total surface energy) into large chunks, which are readily observable in **Figure 6.4 b-b'**.

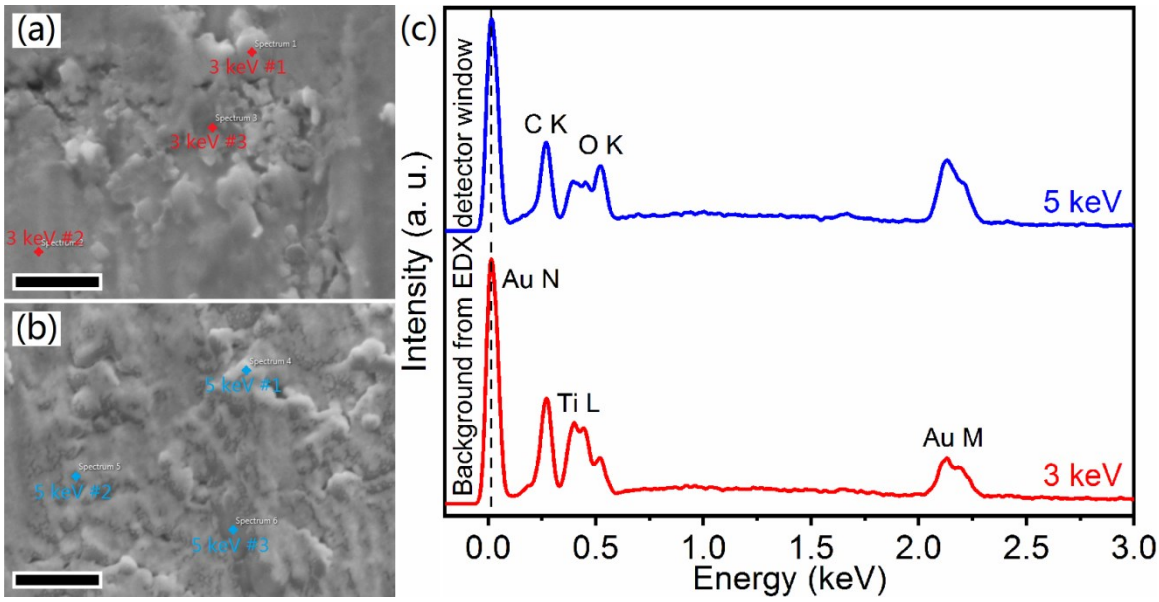

Figure 6.5 FEG-SEM images (taken at the magnification of 50 k×) of the samples produced with (a) 3 keV and (b) 5 keV Ar^+ ion beams, the scale bar represents 500 nm; (c) the EDX spectra of the Au NPs on Ti foil.

The amount of Au NPs on Ti foil substrates was semi-quantified by EDX (**Figure 6.5**). Both samples were imaged at the magnification of 50 k× under SEI mode (**Figure 6.5 a-b**). In each micrograph, the EDX spectra were taken at three distinct points and the average spectra are displayed. With the accelerating voltage of 5 kV, the beam-sample interaction volume is small, such that the signal of substrate (Ti) will not be substantially

larger than the signal of sample (Au). From the as-obtained spectra (**Figure 6.5 c**), a strong signal from Au N (~ 0.2 keV) is observed from both samples, indicating the abundance of Au NPs after 30 min PIPS processing. Furthermore, Au M signals can be spotted at ~ 2.12 keV (Au Mα) and ~ 2.20 keV (Au Mβ), and they could be clearly distinguished. The sample produced with 5 keV Ar^+ has a stronger Au M signal in terms of its ratio against that of Ti L, this implies that a thicker film of Au NPs has been deposited onto the Ti substrate.

6.3 Catalytic Performance of Au NPs

The catalytic performance of the Au NPs on EOR was examined using various ways of electrochemical testing. The cyclic voltammograms with variation in different parameters are displayed in **Figure 6.6**. First of all, samples produced with 3 keV and 5 keV Ar^+ are compared against the commercial Au NPs on glassy carbon electrode and the CV profiles are given in **Figure 6.6 a**. All profiles (including that for a bare Ti foil to determine background signals) were obtained in an alkaline electrolyte at pH = 13 with the concentration of ethanol being 1 M. As the profiles start from 0 V and proceed to +1.0 V, followed by returning backwards to -1.0 V and finally getting back to 0 V, there are four major oxidation peaks for EOR, which correspond to **Equation 2.8 a-d** respectively. In **Figure 6.6 a**, it can be found that the commercial Au NPs only produce two EOR oxidation peaks (which correspond to the oxidation via C2 pathway according to **Equation 2.8 a-b**), while both the Ti/Au samples show all four oxidation peaks. This signifies that the PIPS-fabricated Au NPs have more competitive performance in EOR than the commercial catalyst due to the ability of oxidising ethanol more completely. The commercial Au NPs have a mean size of ~ 5 nm, which is comparable to the sample produced with 3 keV Ar^+ (~ 3 nm), and they produce oxidation peaks of similar intensities. This implies that for pristine Au NPs with minimal strain, particle size matters in terms of electrocatalytic performance. The relative intensities of all EOR peaks are much stronger in Au NPs produced with 5 keV Ar^+, indicating that besides SA/V ratio, surface energy is another key factor affecting the electrocatalytic performance. With a small compensation in SA/V ratio, Au NPs produced with 5 keV Ar^+ are highly strained,

therefore the surface energy content should be much higher than those produced with 3 keV Ar^+.

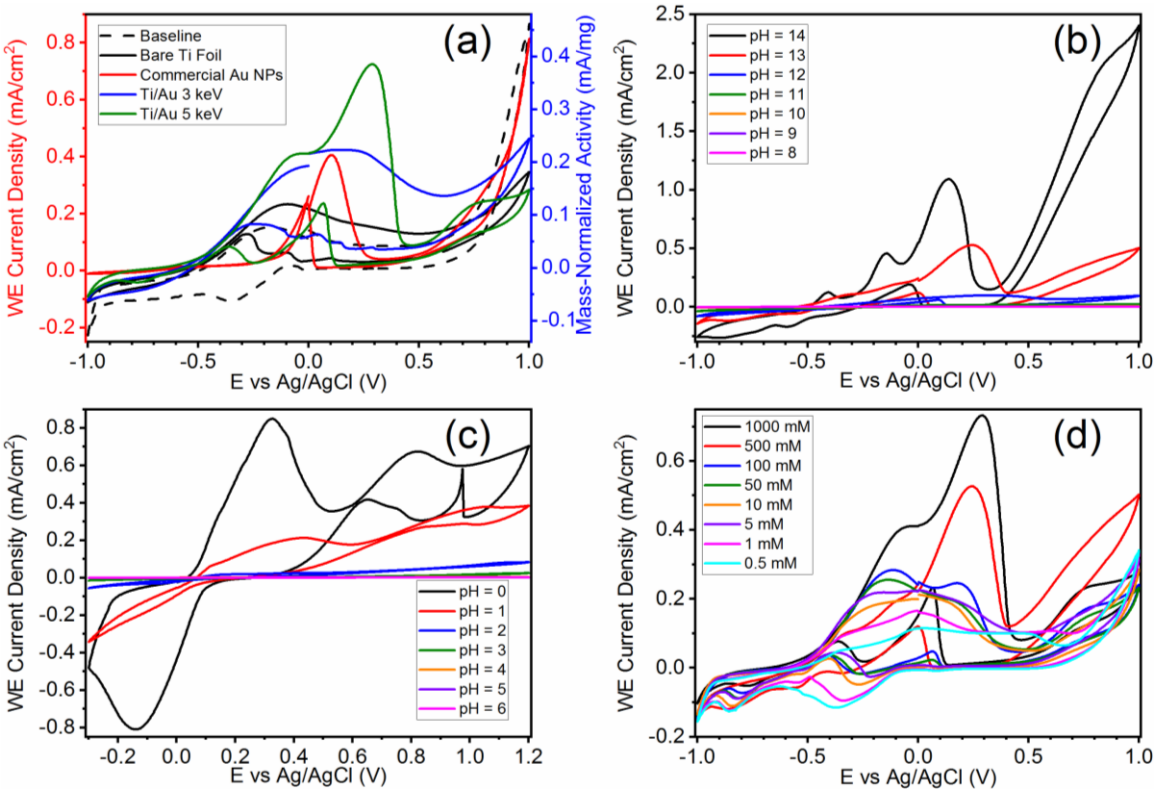

Figure 6.6 Cyclic voltammograms of the samples in EOR showing their electrochemical behaviours. (a) Comparison of the samples in terms of catalytic performance in EOR; (b-c) catalytic performance of the sample produced with 5 keV Ar^+ ion beam in electrolytes of different pH values; (d) catalytic performance of the sample produced with 5 keV Ar^+ ion beam in electrolytes of different ethanol concentrations. The mass loadings for Ti/Au samples and commercial Au NPs are ~ 1.9 mg/cm^2 and the graphs are plotted based on mass activities. The commercial Au NPs serve as a reference sample for comparison purpose.

The strained Au NPs produced with 5 keV Ar^+ were further tested by varying more parameters. Testing in electrolytes of different pH values (**Figure 6.6 b-c**) reveal that the EOR catalytic performance is much better at extreme pH values (0, 1 or 13, 14), and this should be due to the high concentration of mobile charge carriers (especially free electrons). Testing with varying ethanol concentration was carried out using electrolyte at

pH = 13. **Figure 6.6 d** shows that the intensity of almost all oxidation peaks decreases with the concentration of ethanol in the electrolyte; however, they do not seem to obey the same linearity in the intensity-concentration relationship. This should be due to that EOR may occur via two distinct pathways (C1 and C2) which do not form intermediate products of the same species.[5, 6]

The oxidation peaks at E = 0.3 V and E = 0.1 V represent EOR via C2 pathway, which oxidises ethanol to ethanal and further oxidises it to acetic acid/acetate (**Equation 2.8 a-b**). They are identifiable at 1 mM and 50 mM ethanol respectively. The signals of these two oxidation peaks decrease obviously with the concentration of ethanol, indicating that only at high concentrations of ethanol, EOR is preferred to occur via C2 pathway. The oxidation peaks at E = -0.3 ~ -0.7 V and E = -0.1 V represent EOR via C1 pathway, which includes the breaking of C-C bond in ethanol molecules and further oxidation to carbon oxides respectively (**Equation 2.8 c-d**). They are found to decrease at a much smaller rate as compared to the reactions in C2 pathway, and are detectable at very low ethanol concentration. To be specific, the oxidation peak at E = -0.7 V still remains obvious even when the concentration of ethanol is as low as 0.5 mM, this means not only EOR preferentially occurs at low ethanol concentrations, but also that the highly strained Au NPs have super high sensitivity in EOR.

The performance stability of the strained Au NPs was tested in an electrolyte with 1 M ethanol at the pH value of 13. CA tests were set at the constant potential of 0.3 V (vs Ag/AgCl) for a consecutive period of 15 h without any physical disturbing. **Figure 6.7 a** shows the CA profiles of both a bare Ti substrate and one with strained Au NPs. It is clear that Ti almost contributes no signal in the performance stability test; on the other hand, the intensity of signals contributed by the strained Au NPs gradually drops and reaches a steady minimum after ~ 7 h of testing. An interesting finding is that from 7 h onwards, strong signals suddenly appear with periodicity in decrease of interval time, and the peak intensities of the sudden strong signals also show an exponential reduction over time (**inset of Figure 6.7 a**). This should be due to the pitting corrosion of Ti after long time of stability test, and it is suspected that the pitting corrosion occurs at the sites with

imperfections (such as surface roughening due to exposure to the energetic Ar^+ ion beams or simply having scratches). These imperfections lead to a partial localisation of stress which is enlarged during the electrochemical testing. After 7 h accumulation, the strain energy is high enough to initiate the pitting corrosion as a result of the galvanic setup at the working electrode. Based on the exponential fitting of the peak signals, the rate of pitting corrosion is estimated to be ~ 0.17585 h^{-1} with an extrapolated initial intensity (WE current density) of 0.42965 mA/cm^2.

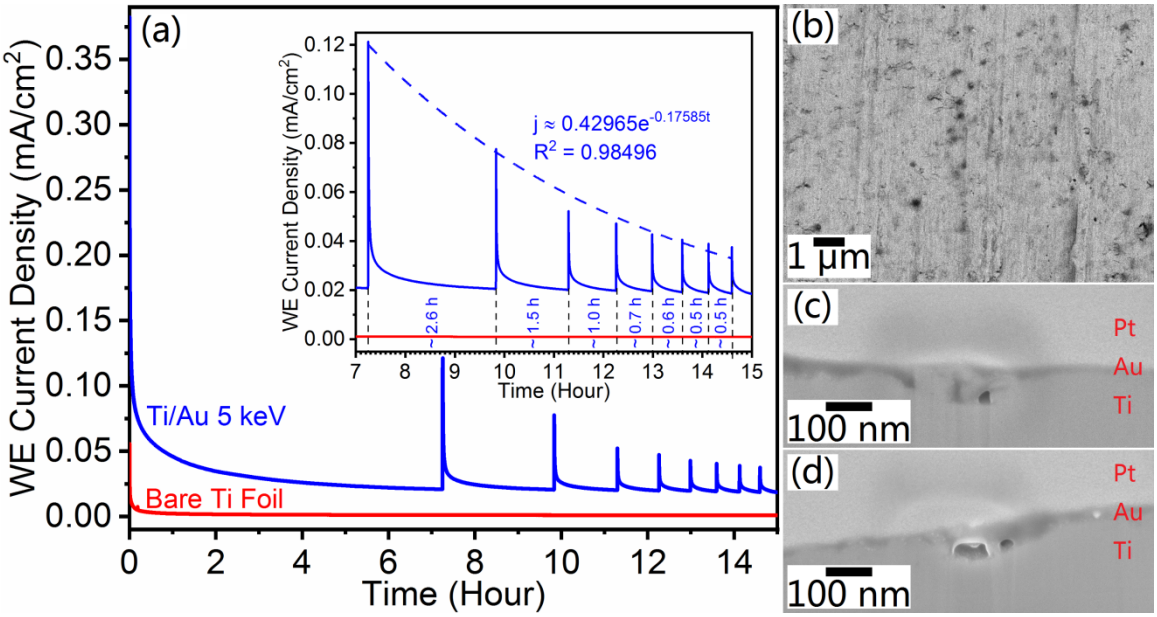

Figure 6.7 (a) CA profiles of bare Ti foil and Ti/Au sample in EOR, showing their stability during electrochemical testing; (inset of a) enlarged graph showing the pitting corrosion, with an exponential fit of the rate of corrosion. (b-d) The morphology of the Ti/Au sample after CA test, with the top-view image (b) shows many pits formed across the surface and the cross-sectional images (c-d) show some of the pits formed in an enlarged view.

The morphology of the Ti/Au sample was viewed after the CA test. **Figure 6.7 b** shows the top-view FEG-SEM image of the Ti/Au sample with many pits formed across the surface. Two distinct sites were randomly selected for cross-sectioning (with FIB-deposited Pt as the protective layer), and the 52°-tilted images are displayed in **Figure 6.7 c-d**. Measurements have shown that the lateral size of the pits formed after the 15-h CA test is ~ 30 nm; the large pit shown in **Figure 6.7 d** is suspected to be two adjacent pits

joined together. The depth of the pits might not be homogeneous; this should be due to the variation in stress and surface energy of the Au NPs covering the surface.

6.4 Summary

This research has shown that PIPS can be a fast and effective approach to fabricate homogeneous and ultra-small single crystalline Au NPs, which is much easier and free of chemical synthesis. With a suitable set of parameters, the Au NPs can be highly strained to form twinned crystals, which have high surface energy content. Theoretically, this approach could produce Au NPs on almost any substrate material. Electrochemistry tests have indicated that the Au NPs have good electrocatalytic performance due to having a high SA/V ratio; the strained Au NPs produced with 5 keV Ar^+ perform much better than the normal sample produced with Ar^+ in EOR. This draws a conclusion that at the compensation of SA/V ratio of no more than an order, strained Au NPs have much higher surface energy content and therefore lowers the activation energy for EOR.

References

1. X. Cao, C. Li, Y. Lu, B. Zhang, Y. Wu, Q. Liu, J. Wu, J. Teng, W. Yan and Y. Huang, *J. Catal.*, 2019, **377**, 389.
2. L. Vitos, A. V. Ruban, H. L. Skriver and J. Kollár, *Surf. Sci.*, 1998, **411**, 186.
3. A. L. Patterson, *Phys. Rev.*, 1939, **56**, 978.
4. C. Liu, X. Cao, A. Kamyshny, J. Y. Law, S. Magdassi and Y. Long, *J. Colloid Interface Sci.*, 2014, **427**, 49.
5. Y. Wang, S. Zou and W.-B. Cai, *Catalysts*, 2015, **5**, 1507.
6. Y. Zhao, X. Li, J. M. Schechter and Y. Yang, *RSC Adv.*, 2016, **6**, 5384.

Chapter 7

Implications/Impact/Outstanding Questions

This chapter draws together the threads of the thesis. Reconnaissance studies on optical and Raman properties of Au nano-ring arrays (which did not warrant a complete chapter) are also included. Apart from the summary of results for the current research works, the opportunities and strategies for future work are elaborated. The extent to which the original hypothesis was proven is adequately addressed.

7.1 General Discussions

This project focuses on the fabrication of nanostructured Au and its relationship with the improvement in the catalytic performance on EOR. Three sets of results were produced, namely the ordered Au nano-ring arrays, the flexible Au MA electrode, as well as the highly strained Au NPs with crystal twinning. In the field of EOR, the state-of-the-art catalyst material is Pt-based, and reported as carbon-supported PtRuSn alloy NPs.[1] Based on various aspects ranging from fabrication and structure to performance and mechanism, **Table 7.1** summarises the results produced in this project and compares with the state-of-the-art material (PtRuSn/C).

The samples produced in this project are in two forms, namely thin films and NPs. The electrocatalytic performance of nanostructured Au thin films cannot be directly compared with that of the Au NPs, because there is a difference in mass loadings (with the unit being mg/cm^2). In unit area of sample, the loading of NPs is much lower than the thin films and thus the WE current density (with the unit being mA/cm^2) is almost two orders smaller. Therefore, thin films with nanostructured Au are compared with the planar Au thin film; the highly strained Au NPs are compared with the commercial Au NPs, and could be compared with the PtRuSn/C NPs reported.

To improve the electrocatalytic performance, an efficient way is to increase the SA/V ratio, and this has been illustrated by the thin film samples reported in **Chapter 4** and **Chapter 5**. A slight increase in the SA/V ratio could bring about large enhancement in the electrocatalytic performance of the Au thin films. The key point being elaborated in this project is that, besides SA/V ratio, surface energy is another significant factor which could play a more important role in enhancing the catalytic activities. Therefore, a common feature in this project is the high surface energy content across the studies and the samples, and their fabrication methods are related with the high-energy feature. For example, in the fabrication of the ordered Au nano-ring arrays, the NSL-RIE approach was using highly energetic O_2 plasma; in the fabrication of the flexible Au MA electrode,

the NIL process utilised high pressure; and in the fabrication of the highly strained Au NPs, the PIPS method used Ar^+ ions which bombarded on a bulk (Au grid).

Table 7.1 Summary and comparison of the works over various aspects

	Ordered Au nano-ring arrays[2]	**Flexible Au MA electrode**	**Highly strained Au NPs[3]**	**State-of-the-art sample[1]**
Material and structure	Au Thin film on Si/SiO_2	Au Thin film on PVC	Strained Au NPs with crystal twinning	PtRuSn/C
Fabrication method	NSL-RIE	NIL	PIPS	Chemical synthesis
Reference sample	~ 100 nm Au thin film on plain Si/SiO_2	~ 100 nm Au thin film on plain PVC	~ 5 nm Au NPs (commercially available)	~ 5 nm Pt NPs (chemically synthesised)
Feature size of best-performance sample	~ 500 nm diameter; ~ 83 nm height	~ 60 μm lateral; ~ 1.7 μm height	~ 10 nm diameter	~ 5 nm diameter
Active sites	Micro-/nano-scale and atomic-scale	Nano-scale and atomic-scale	Nano-scale	Nano-scale
SA/V ratio vs reference sample	↑ by ~ 15.6%	↑ by ~ 2.3%	↓ by ~ 50%	Same
Electrocatalytic performance vs reference sample	↑ by ~ 87%	↑ by ~ 305%	↑ by ~ 81%	↑ by ~ 50%
Lower limit of ethanol detection	~ 1 mM	~ 5 mM	~ 0.5 mM	N. A.†
Catalytic processes	Both C1 & C2 pathways*	Both C1 & C2 pathways*	Both C1 & C2 pathways*	Both C1 & C2 pathways
Possible mechanism	Higher SA/V ratio for more physisorption; large surface energy for C-C bond breaking	Higher SA/V ratio for more physisorption; large surface energy for C-C bond breaking	Large surface energy for C-C bond breaking	Noble metal alloy creates active sites for C-C bond breaking
Stability	Excellent	Excellent	Medium**	Excellent
Scalability in application	High	High	Low***	Medium‡

* C1 pathway is desired and can be more preferential with time.

** Pitting corrosion of Ti substrate was observed after 7 h of stability test.

*** Limited by the PIPS fabrication equipment and process.

† This type of values was not reported prior to the works in this project.

‡ Limited by the fabrication cost of noble metals.

As reported in the literature, the EOR catalysis could proceed via two pathways (namely C1 and C2), with C1 pathway being the desired one due to the full oxidation of ethanol. Unfortunately, there is no full oxidation of ethanol by electrochemistry method to date, and the most efficient EOR process is always a mixture of both pathways – this could be confirmed by the PtRuSn/C NPs as listed in **Table 7.1**, and this is the case of the three sets of results produced in this project. In this project, atomic-scale active sites were first ever directly visualised and this brings about advancement in the field of research. The WE current density of the samples may not be as large as the PtRuSn/C NPs, but the works have shown that C1 pathway could be the more preferential one upon fulfilment of certain criteria, for example, long cycling durations or high surface energy content.

In this project, another new idea was proposed, which is the lower detection limit of ethanol. This is exceptionally important for EOR-based ethanol sensors, and is believed to be useful in high-sensitivity hand-held detectors for drunk driving. As such, no data could be found for other samples, including the state-of-the-art material. The best-performance samples were compared with their respective reference samples instead.

7.1.1 Discussion on Ordered Au Nano-Ring Arrays

Other reported morphology on Au pyramids are usually nanosphere lithography (NSL) alone for large-scale or by FIB for small-scale fabrication. For Au nano-ring arrays, this morphology is by far unique and not reported by others yet. There was only one similar structure reported,[4] which was done by electron beam lithography (EBL) for small-scale fabrication. In this particular work, the Au nano-ring arrays are the base structure with Au nanopyramids being the sub-features on the surface of the Au nano-rings, which has not been reported by others yet.

The NSL-RIE approach is a fast and effective way to fabricate ordered Au nanostructured arrays on Si wafers. Compared to other methods, this approach is much safer and easier;

the coverage of the Au nano-rings is almost 100% except intrinsic defective regions prior to the RIE process. It can be confirmed that O_2 is the most suitable etchant gas in controlling the surface morphology; chamber pressure needs to be kept low, in order to obtain the ordered Au nanostructured arrays. The shape of the samples and distribution of features could be controlled by changing the RF power, which is the one of the key underlying factors in the RIE process; the structure of the samples can be fine-tuned through variation of the etchant gas flow rate. Under the optimised RIE parameters with different etching durations, experiments have revealed that the height of Au nano-rings has a reduction rate of ~ 2.31 nm/min.

Electrochemistry tests have indicated that the Au nano-ring arrays have good electrocatalytic performance; samples with Au nanostructured arrays perform much better than the normal samples in EOR. This is probably because ordered nanostructures produced by RIE have much higher specific surface area and more active sites and therefore lowers the activation energy for EOR. Based on the calculated TOF values, the sample after 5.0 min RIE gives the best electrocatalytic activity in EOR, which has the strongest oxidation signals in working electrode current density. Electrochemical testing with varying physical parameters shows that the detecting limit of ethanol is ~ 1.0 mM and strong signals come with high concentrations of mobile charge carriers at extreme pH values. Long continuous CV scans reveal that in alkaline medium, C1 pathway could become increasingly preferential over C2 pathway, and thus making the Au nano-ring array structure useful in the field of direct ethanol fuel cell.

Nano-ring array structure may result in a maximum of ~ 15.6% increase in total surface area compared to the planar sample, which provides substantial opportunity for the formation of active sites. Direct evidence of active sites in both micro-/nano-scale and atomic-scale has been first ever observed in TEM and HRTEM images. Overlapped FFT patterns prove that the Au nano-rings have distorted lattice at the top surface, possibly due to the accumulated stress during its formation process. This in turn explains the outstanding electrochemical performance of the Au nano-ring arrays in EOR.

A key part in the fabrication process is the optimisation of parameters. As the template-assisted method has quite some similarities to NSL, most reported literatures were in fact performing the former with the use of PS nanospheres as the sacrificial mask. In the end, the nanostructured materials actually underwent a bottom-up growth followed by the removal of the mask, instead of going through the top-down treatment using high energy plasma as it was introduced in **Chapter 4**. The main difference between these two modes is that, bottom-up growth simply increases the surface area, whereas the top-down treatment brings about an extra increase in the stress and strain as observed from the partial lattice rotation given by the HRTEM/FFT image. At the same time, the formation of atomic-scale active sites could be an added advantage of the process, which can be hardly achieved by the template-assisted method.

7.1.2 Discussion on Flexible Au MA Electrode

NIL was another approach used to quickly and effectively fabricate ordered arrays with pillar structures on PVC substrates. Electron beam evaporation ensured homogeneous deposition of Au on the MAs. This approach is safe and easy to operate; by ignoring the regions between the grids, the coverage of the Au MAs is nearly 100%, and can be controlled and manipulated. Intrinsic defects (like scratches) prior to the thermal imprinting process have little impact on the final outcome of the fabrication. It can be confirmed that temperature and applied pressure are the underlying factors that influence the geometry of MAs. Since holding time does not really affect the structure, the most suitable set of parameters is 150 °C for 1 min under 8 bar pressure.

Under the optimised imprinting parameters, MAs were fabricated with different mesh grades. The concentric hexagonal pillars with double-layered structures have increased the specific surface area by a maximum of ~ 2.3%. With advanced electron microscopy characterisations, the atomic-scale 3D nanostructures are directly visualised with a maximum depth of 6 ALs, which largely increases the specific surface area of the electrode samples. *In-situ* observation unveils the interactions of atomic-scale active sites,

during which crystal grows along the twinning plane of the highly strained twinned crystals, thus building and storing large amount of energy to drive efficient EOR catalysis.

Electrochemistry tests have shown that a larger amount of active sites on the Au thin film brings about improved electrocatalytic performance in EOR. The value of C_D is directly proportional to ECSA, and is estimated to have a logarithmic relationship with mesh grade and a quadratic relationship with the inverse of array size. Increased C_D brings about a larger amount of active sites on the Au thin film, and therefore electrochemistry testing shows that the Au MAs perform much better EOR than the planar sample. The Au MAs with higher mesh grade have a greater ASUR, and that plays an important role in building the electrochemical double layer for efficient charge transfer. There are plenty of rooms for further improvements on the ASUR, which is expected to bring about much more improved electrocatalytic performance. Variation in physical parameters reveals that the detecting limit of ethanol is ~ 5.0 mM and strong signals come with high concentrations of mobile charge carriers at extreme pH values. Proceeding via C1 pathway shows stronger signals in alkaline medium and makes the Au MA structure potentially useful in DEFC.

7.1.3 Discussion on Highly Strained Au NPs

In comparison to the traditional methods, PIPS can be a fast and effective approach to fabricate homogeneous and ultra-small single crystalline Au NPs, which is much easier and free of chemical synthesis. With a suitable set of parameters, the Au NPs can be highly strained to form twinned crystals, which have high surface energy content. Theoretically, this approach could produce Au NPs on almost any substrate material.

Electrochemistry tests have indicated that the Au NPs have excellent electrocatalytic performance due to having a high surface area to volume ratio; the strained Au NPs produced with 5 keV Ar^+ perform much better than the normal sample produced with Ar^+ in EOR. This draws a conclusion that at the compensation of aspect ratio of no more than an order, strained Au NPs have much higher surface energy content and therefore lowers

the activation energy for EOR. In other words, aspect ratio is no longer the only factor that affects the electrochemical performance of Au NPs; instead, the surface energy content might be a more impactful element to take into account.

Stability tests via CA show that the strained Au NPs could last for more than 7 h before reaching a steady minimum performance. In this work, due to the galvanic setup at the working electrode, pitting corrosion occurred after 7 h of test, which had an estimated rate of ~ 0.17585 h^{-1} and an extrapolated initial intensity (WE current density) of 0.42965 mA/cm^2 through exponential fitting. Suitable corrections may be carried out in the future works and the strained Au NPs are believed to have even longer stability in the electrochemical testing.

7.2 Outstanding Questions

The current researches accomplish most of the works in the initial proposal. In spite of the achievement made, this project can be further carried out by the following means:

7.2.1 The Temperature-Dependency of EOR

One of the outstanding issues to address is the temperature-dependency of the EOR process. According to literatures, the working temperature might be a possible factor that affects the rate of ethanol oxidation and the reaction pathway. In this project, the working temperature was assumed to be constant at room temperature and this issue was not addressed. In the future works, this is an interesting point to research on, which will make the research on EOR more complete and systematic.

7.2.2 Other Approaches to Fabricate Flexible Electrodes

There could be another way to fabricate flexible electrode with ordered nanostructured Au arrays. In NIL, the substrate must be a thermoplastic, so as to feature a glass transition for thermal imprinting. As derived from **Chapter 4**, SiO_2 nanospheres could be self-

assembled on Au-coated flexible substrates more than just PVC; it can extend out to almost any substrate even it is a thermoset. The RIE process in this case could be carried out using CF_4, which is an excellent etchant for Si-based materials.

7.2.3 Combination of Approaches

The electrocatalytic activities of nanostructured Au has been greatly improved by either increasing the specific surface area or raising the surface area. With the successful fabrication of flexible electrodes with thin substrates, a combination of both approaches is suggested. The flexible electrodes could be loaded into the PIPS system to collect the highly strained Au NPs with crystal twinning effect. This should bring about a much more enhanced electrochemical performance, and at the same time, avoiding the problem of pitting corrosion as found in **Chapter 6**.

7.2.4 Future Works for Practical Applications

This thesis has reported two fabrication approaches of Au thin films with nanostructured arrays via lithography. These approaches are easy in operation and capable of large-scale production. The active material has a thickness of ~ 100 nm. For samples with 1.5 cm^2 surface area, the cost of Au electrocatalyst is less than 0.02 USD/sample (based on the recent price of Au according to **Figure 2.8**). Apart from these advantages, the materials used have low hazard and the Ni grids can be reusable for multiple times. This in turn ensures the safety of the operators and saves material cost in industrial fabrications. The excellent controllability and repeatability will guarantee the yield rate of products.

This thesis has also reported the fabrication of highly strained Au NPs by PIPS. The PIPS system tends to be used for small TEM sample preparation, so the scaling up of this method does not seem realistic, unless the issue of instrument/sample size could be solved. In this particular research (with the use of Gatan Model 691 PIPS), there is limitation in the size of sample and/or substrate, both in lateral dimensions and thickness. The limitation in lateral size is approximately a rectangle with the size of ~ 6 × 4 mm^2 (as

indicated in **Section 3.2.3**), exceeding this will lead to being either unable to get into the sample chamber or unable to fit into the sample clamp. The limitation in thickness is ~ 6 pieces of TEM grids (stacked), exceeding this will lead to loosening of the sample clamp and subsequently might damage the entire instrument due to dropping of grids.

In order to translate the research outcomes into practical applications, the entire setup has to be a full fuel cell (the current works are just half-cell reactions). More research works will need to be conducted on the cathodic ORR. On the other hand, materials technology for the ion-conducting membranes should also be developed, so as to further strengthen the durability of the membranes to prevent the ethanol crossover issue and to cater to DEFCs with different electrolyte types.

7.3 Conclusions

In conclusion, the research works in this project have concluded that increasing the aspect ratio or raising the surface energy could largely increase the amount of exposed active sites and/or bring about stress centres, and thus provides great contribution to the enhancement of nanostructured Au in the electrocatalysed EOR. The original research outcomes have successfully proven the hypothesis stated at the beginning of this thesis.

References

1. M. Z. F. Kamarudin, S. K. Kamarudin, M. S. Masdar and W. R. W. Daud, *Int. J. Hydrogen Energy*, 2013, **38**, 9438.
2. X. Cao, C. Li, Y. Lu, B. Zhang, Y. Wu, Q. Liu, J. Wu, J. Teng, W. Yan and Y. Huang, *J. Catal.*, 2019, **377**, 389.
3. X. Cao, C. Li, D. Peng, Y. Lu, K. Huang, J. Wu, C. Zhao and Y. Huang, *J. Phys. Chem. Lett.*, 2020, **11**, 3005.
4. M. Zheng, X. Zhu, Y. Chen, Q. Xiang and H. Duan, *Nanotechnology*, 2017, **28**, 045303.

Appendix

Supplementary Information

The Appendix furnishes some supplementary information to the thesis. Reconnaissance studies on optical and Raman properties of Au nano-ring arrays (which did not warrant a complete chapter) are also included.

A.1 Schematic Diagram of JEOL JSM-7800F Prime

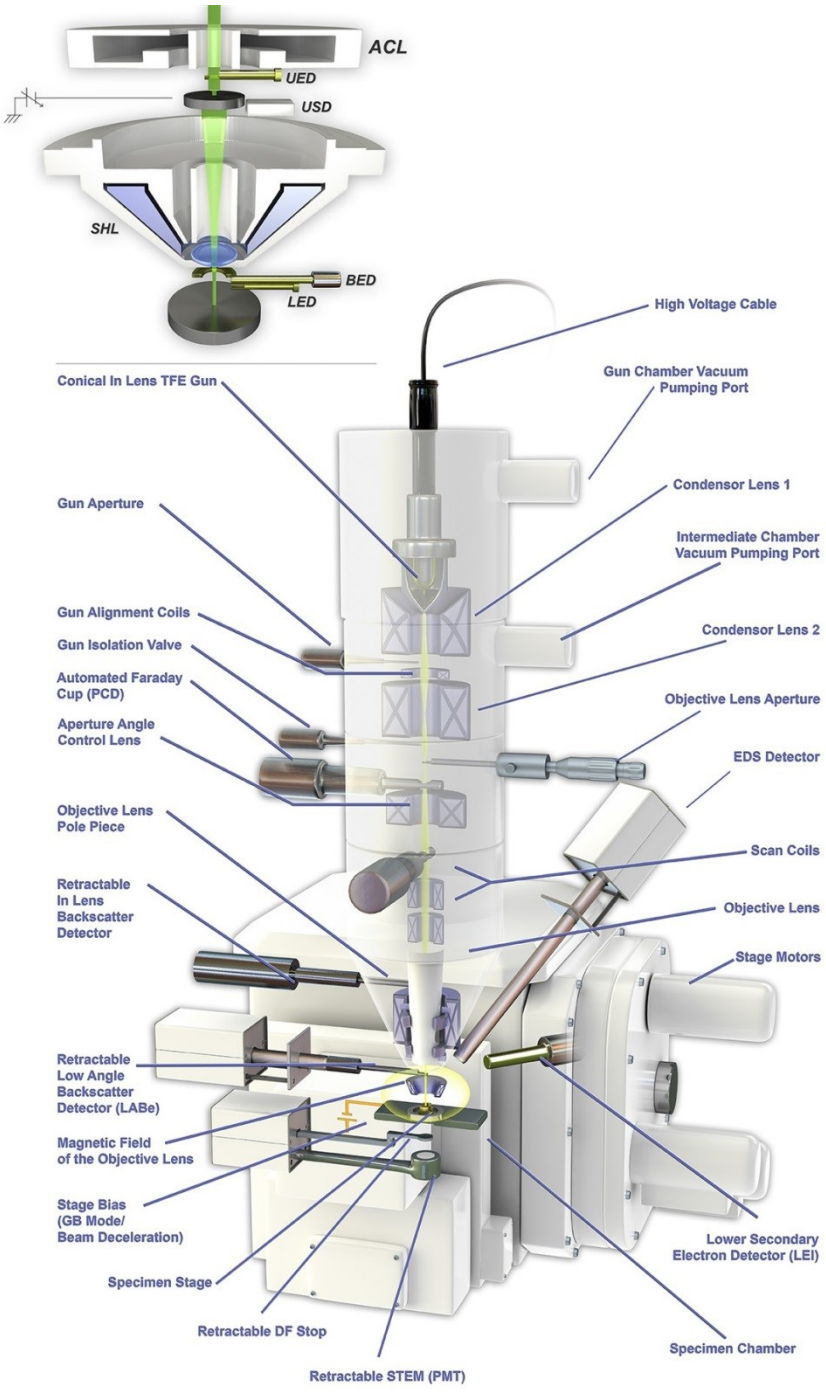

Figure A.1 The detailed internal structure and external attachment modules of JEOL JSM-7800F Prime FEG-SEM used in this project

A.2 Raman Properties of Au Nano-Ring Arrays

Apart from the electrochemical properties in EORs, the samples were also tested for their ability in the detection of rhodamine 6G (R-6G) molecules through surface-enhanced Raman spectroscopy (SERS). Prior to SERS, possible LSPR effect of the samples was studied through ultraviolet-visible light-near infrared (UV-Vis-NIR) spectroscopy, which is one of the most common methods used to study the optical properties of many samples. In this study, the spherical reflectance spectra of the samples were collected using a UV-Vis-NIR spectrophotometer (Lambda 950, Perkin Elmer, USA).

A.2.1 Optical Properties of Au Nano-Ring Arrays

When a beam of light is shone onto the surface of a sample, it can record the transmittance (%T) and reflectance (%R) of light within a continuous spectrum at defined temperatures, thereby the absorptance (%A) of light could be obtained by applying the formula %T + %R + %A = 100%. Since the samples are having Si substrates and thus %T = 0, the absorptance spectra were calculated as %R + %A = 100%. A bare Si substrate was firstly fixed onto a piece of clean microscopic glass slide with double-side tape, mounted onto the instrument by mechanical clipping and a baseline spectrum was collected based on spherical reflectance correction. Following that, each individual sample was loaded in the same way to collect their respective %R spectra. All measurements were performed at room temperature.

Spherical reflectance and absorptance of the samples were first measured within the wavelength range of $250 \leq \lambda \leq 800$ nm. **Figure A.2 a** shows the %A spectra based on the collected %R measurements, which display very obvious absorption peaks at $\lambda \approx 500$ nm contributed by Au. While for $\lambda < 400$ nm, the signals are contributed from the double-side tape, the absorption peaks at $\lambda \approx 500$ nm display a widening and weakening trend. However, from **Figure A.2 b**, the only peak at $\lambda \approx 500$ nm contributed by Au indicates that localised SPR effect of the samples seems to be not obvious. No shifting of peak position is observed yet, this might be due to the change in size of the Au nano-rings is

too little, which could not trigger any peak shift in light absorption. Further experiments with various PS sphere sizes are planned to study how LSPR could be rendered in the patterned Au.

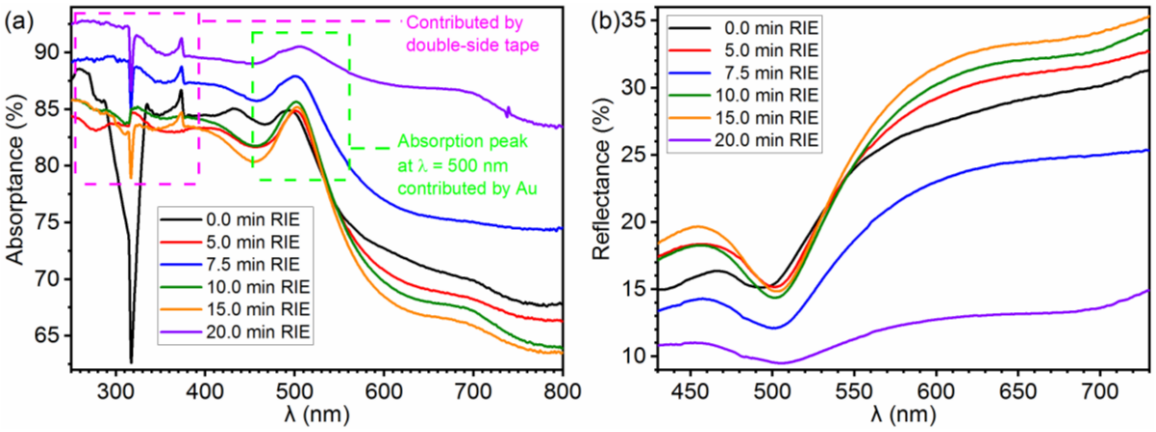

Figure A.2 (a) Absorptance and (b) spherical reflectance spectra of the Si/Au/PS samples measured using UV-Vis-NIR: (black) original before RIE; (red) after 5.0 min RIE; (blue) after 7.5 min RIE; (green) after 10.0 min RIE; (orange) after 15.0 min RIE and (purple) after 20.0 min RIE.

Nevertheless, the emission profile of the arrayed samples was measured by a spectrofluorophotometer (Cary Eclipse, Agilent, USA) with an excitation wavelength of 320 nm, which determines that the emission peak of the samples at λ = 650 nm (please refer to **Figure A.3**). Since the excitation and emission profiles of R-6G molecules ($\lambda_{excitation}$ = 525 nm, $\lambda_{emission}$ = 555 nm as from the database) are within this range, the excitation wavelength of 457 nm was chosen for the Raman spectroscopy.

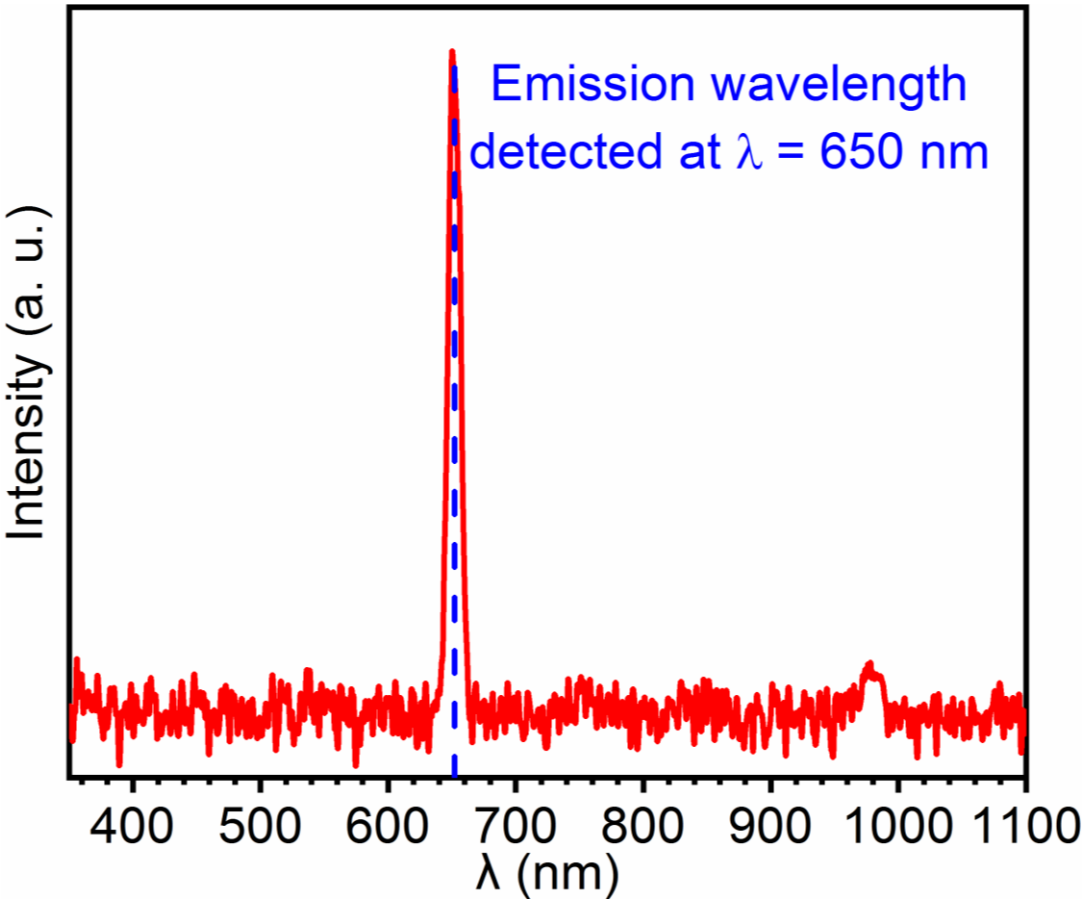

Figure A.3 Emission profile of the arrayed Si/Au sample measured using spectrofluorophotometer, with excitation wavelength being 320 nm.

A.2.2 SERS Detection Properties of Au Nano-Ring Arrays

In order to study the enhancement by Au nano-ring array structures, plain Si (bare Si substrate without Au thin film), plain Si/Au (original sample before RIE) and Si/Au sample patterned by 5.0 min RIE were separately immersed in 1 ppm R-6G solution and dried in air, after which Raman spectroscopy was carried out using 457 nm laser source (**Figure A.4 a**). The spectrum of commercial R-6G powder serves as the reference to indexing the peaks of R-6G. On plain Si and plain Si/Au surfaces, signals of R-6G can hardly be detected; on patterned Si/Au surface, four peaks can be clearly identified and they perfectly match those given by the commercial R-6G powder. This implies that with ordered nanostructured arrays, Au thin film could serve as a good SERS substrate in detecting R-6G molecules at low concentrations.

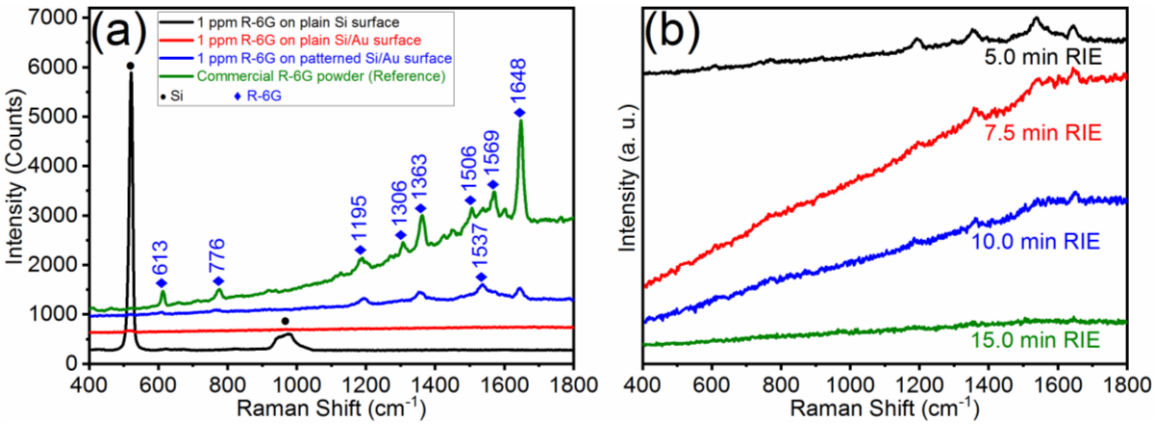

Figure A.4 (a) Raman spectra of R-6G powder and 1 ppm R-6G solution on different surfaces; (b) Raman spectra of 0.01 ppm R-6G solution on different samples.

To determine the lowest detection limit, the R-6G solution was then further diluted and different patterned samples were immersed. **Figure A.4 b** shows that at the concentration of 0.01 ppm, the sample after 15.0 min RIE could not render identifiable signals, while others could give at least one peak. The sample after 5.0 min RIE has the best detecting ability, as it gives the highest number of identifiable peaks with enough intensity as compared to the rest. The intensity of R-6G peaks shows a reducing trend as RIE duration increases, this implies that the height of nanostructured arrays plays an important role in the detection. When the concentration reaches 1 ppb, no peak could be detected even by the sample after 5.0 min RIE.

LIST OF PUBLICATIONS

Research papers as first or co-first author:

1. **X. Cao**, C. Li, Y. Lu, B. Zhang, Y. Wu, Q. Liu, J. Wu, J. Teng, W. Yan and Y. Huang, *J. Catal.*, 2019, **377**, 389.
2. **X. Cao**, C. Li, D. Peng, Y. Lu, K. Huang, J. Wu, C. Zhao and Y. Huang, *J. Phys. Chem. Lett.*, 2020, **11**, 3005.
3. **X. Cao**, D. Peng, C. Wu, Y. He, C. Li, B. Zhang, C. Han, J. Wu, Z. Liu and Y. Huang, *Nano Res.*, submitted (revision in progress).
4. C. Li, **X. Cao**, W. Li, B. Zhang and L. Xiao, *J. Alloys Compd.*, 2019, **773**, 762.
5. Y. Rao, **X. Cao**, C. Li and L. Xiao, *Sep. Purif. Technol.*, 2019, **220**, 328.

Research papers as collaborative author:

6. N. Wang, M. Duchamp, R. E. Dunin-Borkowski, S. Liu, X. Zeng, X. Cao and Y. Long, *Langmuir*, 2016, **32**, 759.
7. B. Zhang, B. Chen, J. Wu, S. Hao, G. Yang, X. Cao, L. Jing, M. Zhu, S. H. Tsang, E. H. T. Teo and Y. Huang, *Small*, 2017, **13**, 1603411.
8. G. Yang, J. Feng, B. Zhang, V. Aravindan, D. Peng, X. Cao, H. Yu, M. Srinivasan and Y. Huang, *Int. J. Hydrogen Energy*, 2017, **42**, 22167.
9. Y. Zhang, X. Xia, X. Cao, B. Zhang, H. T. Nguyen, H. He, S. Chen, Y. Huang and H. J. Fan, *Adv. Energy Mater.*, 2017, **7**, 1700220.
10. K. Huang, D. Peng, B. Zhang, X. Cao, S. Hao, G. Yang, Y. Dong, J. Wu and Y. Huang, *Int. J. Hydrogen Energy*, 2018, **43**, 12596.
11. B. Zhang, C. Li, G. Yang, K. Huang, J. Wu, Z. Li, X. Cao, D. Peng, S. Hao and Y. Huang, *ACS Appl. Mater. Interfaces*, 2018, **10**, 23807.
12. C. Li, Y. Rao, B. Zhang, K. Huang, X. Cao, D. Peng, J. Wu, L. Xiao and Y. Huang, *Chemosphere*, 2019, **214**, 341.
13. P. Zhu, Z. Zhang, P. Zhao, B. Zhang, X. Cao, J. Yu, J. Cai, Y. Huang and Z. Yang, *Carbon*, 2019, **142**, 269.
14. C. Li, B. Zhang, Y. Li, S. Hao, X. Cao, G. Yang, J. Wu and Y. Huang, *Appl. Catal. B*, 2019, **244**, 56.

15. M. Ma, G. Yang, H. Wang, Y. Lu, B. Zhang, X. Cao, D. Peng, X. Du, Y. Liu and Y. Huang, *Int. J. Hydrogen Energy*, 2019, **44**, 1544.
16. G. Yang, H. Wang, B. Zhang, S. Foo, M. Ma, X. Cao, J. Liu, S. Ni, M. Srinivasan and Y. Huang, *Nanoscale*, 2019, **11**, 9556.
17. Q. Zeng, B. Sun, K. Du, W. Zhao, P. Yu, C. Zhu, J. Xia, Y. Chen, X. Cao, Q. Yan, Z. Shen, T. Yu, Y. Long, Y. K. Koh and Z. Liu, *2D Mater.*, 2019, **6**, 045009.
18. X. Wang, P. Yu, Z. Lei, C. Zhu, X. Cao, F. Liu, L. You, Q. Zeng, Y. Deng, C. Zhu, J. Zhou, Q. Fu, J. Wang, Y. Huang and Z. Liu, *Nat. Commun.*, 2019, **10**, 3037.
19. X. Zhao, Z. Zhang, X. Cao, J. Hu, X. Wu, A. Y. R. Ng, G.-P. Lu and Z. Chen, *Appl. Catal. B*, 2020, **260**, 118156.
20. X. Yao, X. Zhao, J. Hu, H. Xie, D. Wang, X. Cao, Z. Zhang, Y. Huang, Z. Chen and T. Sritharan, *iScience*, 2019, **19**, 976.
21. M. Wang, Y. Yu, M. Cui, X. Cao, W. Liu, C. Wu, X. Liu, T. Zhang and Y. Huang, *Electrochim. Acta*, 2020, **329**, 135181.
22. J. Xie, X.-F. Cheng, X. Cao, J.-H. He, W. Guo, D.-S. Li, Z. J. Xu, Y. Huang, J.-M. Lu and Q. Zhang, *Small*, 2019, **15**, 1903188.
23. Y. Lin, G.-P. Lu, X. Zhao, X. Cao, L. Yang, B. Zhou, Q. Zhong and Z. Chen, *Mol. Catal.*, 2020, **482**, 110695.
24. Y. Huang, F. Yu, X. Cao, L. Nie, P. Zhang, F. Xu, Q. Gong, X. Zhan, K. Zhao, Y. Huang, Y. Mai and Q. Zhang, *Nanoscale*, 2020, **12**, 3058.
25. J. S. J. Tan, X. Cao, Y. Huang and Z. Chen, *Colloids Surf., A*, 2020, **589**, 124460.
26. S. Hao, C. Li, B. Ouyang, B. Zhang, X. Cao, D. Chen and Y. Huang, *Nanotechnology*, 2020, **31**, 215602.
27. D. Peng, B. Zhang, J. Wu, K. Huang, X. Cao, Y. Lu, Y. Zhang, C. Li and Y. Huang, *ChemCatChem*, 2020, **12**, 2431.
28. Q. Guo, Y. Wu, L. Xu, Y. Gong, Y. Ou, Y. Liu, L. Li, Y. Yan, G. Han, D. Wang, L. Wang, S. Long, B. Zhang, X. Cao, S. Yang, X. Wang, Y. Huang, T. Liu, G. Yu, K. He and J. Teng, *Chin. Phys. Lett.*, 2020, **37**, 057301.
29. H. Wang, A. Artemova, G. Yang, H. Wang, L. Zhang, X. Cao, E. Arkhipova, J. Liu, Y. Huang, J. Lin and Z. Shen, *J. Power Sources*, 2020, **466**, 228303.

30. S. Guo, J. Di, C. Chen, C. Zhu, M. Duan, C. Lian, M. Ji, W. Zhou, M. Xu, P. Song, R. Long, X. Cao, K. Gu, J. Xia, H. Liu, Y. Zhao, L. Song, Y. Xiong, S. Li and Z. Liu, *Appl. Catal. B*, 2020, **276**, 119156.
31. M. Wang, Y. Zhang, T. Zhang, Y. Li, M. Cui, X. Cao, Y. Lu, D. Peng, W. Liu, X. Liu, T. Wang and Y. Huang, *Nanoscale*, 2020, **12**, 11887.
32. K. Huang, B. Zhang, J. Wu, T. Zhang, D. Peng, X. Cao, Z. Zhang, Z. Li and Y. Huang, *J. Mater. Chem. A*, 2020, **8**, 11938.
33. M. Wang, Y. Zhang, M. Cui, Y. Lu, D. Peng, X. Cao, C. Wu, J. Zhou, Y. Feng, W. Liu, Z. Chen, X. Liu, T. Wang, P. Song and Y. Huang, *Biosens. Bioelectron.*, 2020, **165**, 112373.
34. P. Song, J. Di, H. Chen, S. Zhao, C. Wu, X. Cao, M. Wang, J. Xiong and X. Ye, *Mater. Adv.*, 2020, **1**, 760.
35. L. Kang, C. Ye, X. Zhao, X. Zhou, J. Hu, Q. Li, D. Liu, C. M. Das, J. Yang, D. Hu, J. Chen, X. Cao, Y. Zhang, M. Xu, J. Di, D. Tian, P. Song, G. Kutty, Q. Zeng, Q. Fu, Y. Deng, J. Zhou, A. Ariando, F. Miao, G. Hong, Y. Huang, S. J. Pennycook, K.-T. Yong, W. Ji, X. Renshaw Wang and Z. Liu, *Nat. Commun.*, 2020, **11**, 3729.
36. J. A. S. Oh, H. He, J. Sun, X. Cao, B. Chua, Y. Huang, K. Zeng and L. Lu, *ACS Appl. Energy Mater.*, 2020, **3**, 6870.
37. C. Wu, Z. Chen, M. Wang, X. Cao, Y. Zhang, P. Song, T. Zhang, X. Ye, Y. Yang, W. Gu, J. Zhou and Y. Huang, *Small*, 2020, **16**, 2001686.
38. H. Liu, X. Cao, H. Wu, B. Li, Y. Li, W. Zhu, Z. Yang and Y. Huang, *Sens. Actuators B*, 2020, **324**, 128743.
39. T. Rui, G. Lu, X. Zhao, X. Cao and Z. Chen, *Chin. Chem. Lett.*, 2020, (Accepted). DOI: https://doi.org/10.1016/j.cclet.2020.06.027